



Imaging Microglia and Astrocytes *In Vivo* and Non-Invasively: An MRI-Histology Study

Doctoral Thesis presented by

Raquel García Hernández

Thesis Director:

Dr. Santiago Canals Gamoneda

PhD Program in Neuroscience

Neurosciences Institute

Miguel Hernández University of Elche

- 2024 -



This Doctoral Thesis, entitled "Imaging Microglia and Astrocytes *In Vivo* and Non-Invasively: An MRI-Histology Study" is presented as a compendium of the following publications:

Garcia-Hernandez, R., Cerdán Cerdá, A., Trouve Carpena, A., Drakesmith, M., Koller, K., Jones, D. K., Canals, S., & De Santis, S. (2022). Mapping microglia and astrocyte activation in vivo using diffusion MRI. *Science advances*, 8(21), eabq2923.

PMID: 35622913

DOI: 10.1126/sciadv.abq2923



Sant Joan d'Alacant, 12th of June 2024

Dr. D. Santiago Canals Gamoneda, Director of the doctoral thesis entitled *“Imaging Microglia and Astrocytes In Vivo and Non-Invasively: An MRI-Histology Study”*

Report that:

That Mr/Mrs "Raquel García Hernández" has carried out under our supervision the work entitled *“Imaging Microglia and Astrocytes In Vivo and Non-Invasively: An MRI-Histology Study”* in accordance with the terms and conditions defined in his/her Research Plan and in accordance with the Code of Good Practice of the Miguel Hernández University of Elche, satisfactorily fulfilling the objectives foreseen for its public defence as a doctoral thesis.

I sign for appropriate purposes, at Sant Joan d'Alacant, on the 12th of June, 2024

Thesis supervisor

Dr. D. Santiago Canals Gamoneda



Sant Joan d'Alacant, 12th of June 2024

Ms. Cruz Morenilla Palao, Coordinator of the Neurosciences PhD programme at the Institute of Neurosciences in Alicante, a joint centre of the Miguel Hernández University (UMH) and the Spanish National Research Council (CSIC),

Report that:

That Mr/Mrs "Raquel García Hernández" has carried out under our supervision the work entitled "*Imaging Microglia and Astrocytes In Vivo and Non-Invasively: An MRI-Histology Study*" in accordance with the terms and conditions defined in his/her Research Plan and in accordance with the Code of Good Practice of the Miguel Hernández University of Elche, satisfactorily fulfilling the objectives foreseen for its public defence as a doctoral thesis.

I sign for appropriate purposes, at Sant Joan d'Alacant, on the 12th of June, 2024

And for the record, for all due purposes, I sign this certificate.

Dra. Cruz Morenilla Palao

Coordinator of the PhD Programme in Neurosciences

E-mail: cruz@umh.es
www.in.umh.es

Tel: +34 965 919229
Fax: +34 965 919229

Av Ramón y Cajal s/n
SANT JOAN CAMPUS
03550 SANT JOAN D'ALACANT- SPAIN

Acknowledgements

Necesitaría otra tesis para expresar solo un pequeño porcentaje de cuánto amor siento y lo agradecida que estoy por las personas que siempre me apoyan y me quieren. Pero lo voy a intentar.

Empezando por mis padres. Desde que era muy pequeña, siempre me habéis permitido soñar y ser curiosa... Y siempre en un entorno lleno de amor. Me enseñasteis lo importante que es el conocimiento y la educación, y ahora, después de años intentando contribuir un poquito al conocimiento global, me doy cuenta, una vez más, de lo sabios que sois. Gracias mamá, y gracias papá, por amarme e impulsarme a ser como soy. Gracias por todos los momentos vividos y los que nos quedan. Sois una inspiración en mi vida y os quiero muchísimo, y más. Y me faltan palabras...

A mis dos hermanos... ¿qué puedo decir? Como papá y mamá, críticos en mi vida. Desde chica siempre estáis conmigo, enseñándome, queriéndome y apoyándome. Gracias a vosotros soy lo que soy ahora también, y os quiero infinito (y me quedo corto). Es increíble que somos hermanos y más que eso, compartiendo tanto, desde jugar a la consola hasta ir a un circuito de carreras, pasando por tantas fiestas familiares y Nochebuenas en el sofá. Me encantáis... Y a mis cuñadas, que también han confiado en mí siempre, gracias mil por todo. También gracias a mis sobrinos, Candela y Lucas, que me alegráis el día solo con veros en una foto. También al resto de la familia. Os quiero mucho.

And maybe you think I am forgetting you... but not. Adam. An incredible researcher who has taught me everything I know about programming and hardware (and more!), and the owner of a part of my heart... my husband and the father of our soon-to-arrive babies :D, or "dragoncillos" as I like to call them (a nickname that only I like). Thank you, husband and Dr. Matić, for everything. I am very happy we found each other and we are building a life together. I love you more everyday. Also thank you, dragoncillos, for letting me write this thesis. How is it possible that I love you without knowing you? And of course, Flufli and Negri, our little cats. You had to be mentioned somehow... :)

También quiero señalar otro pilar importante en mi vida: mis amigos. Soy muy afortunada por tenerlos. Puedo decir que tengo más amigos que dedos en las manos, y sois verdaderos buenos amigos. Mis amigos de Librilla, de biología, mis chicas (¡y sus esposos!) y chicos de Alicante... Os debo tanto por confiar en mí, no juzgarme y apoyarme. En los buenos y malos momentos; en fiestas, amaneceres y en mis quejas por pensar que llevo mal un examen... Os quiero, de verdad, y sé que, aunque no sea un vínculo de sangre, también durará para siempre.

Finalmente, pero no menos importante (de hecho, sin ellos esta página ni siquiera existiría), Santiago y Silvia. Santiago, mi supervisor de tesis, me dijiste que no me querías en tu laboratorio tres veces... (¿pensabas que no iba a dejar esto escrito en algún lado? :)) pero aquí estamos. Me has enseñado muchas cosas y, muy importante, me has dejado equivocarme y explorar mis ideas, enseñándome aún más. No tengo palabras para agradecerte por todo este tiempo, tu conocimiento, y... tu paciencia. Silvia, también quería agradecerte por tu confianza, apoyo y por hacerme crecer. Os admiro a ambos y espero poder llegar en el futuro a donde estáis ahora. Respecto a los demás compañeros y autores del artículo de la presente tesis, muchas gracias, no habría sido posible sin el fantástico trabajo en equipo de todos. A los demás compañeros del laboratorio y del instituto, team engram, club de la una, team VR, y el resto... gracias, ha sido un viaje muy bonito y didáctico junto a vosotros.

Muchas gracias a todos. Vosotros también sois mis gigantes.

“If I have seen further, it is by standing
on the shoulders of giants”

Isaac Newton

Index

List of abbreviations.....	1
List of figures and tables.....	3
Abstract.....	9
Resumen.....	10
I. Introduction.....	13
1.1 Neuroinflammation: a timeline.....	13
1.1.1. Origin, function and main characters.....	13
1.1.2. Current view: dynamism and new (undesired) roles.....	16
1.2. Imaging Neuroinflammation.....	19
1.2.1. Magnetic resonance imaging and water diffusion.....	20
1.2.1.1. (Lack of) Cell specificity of dw-MRI.....	23
II. Hypothesis.....	27
2.1. Integrating MRI and histology for <i>in vivo</i> analysis.....	27
2.1.1. dw-MRI multicompartiment models: in search of cell specificity.....	28
2.1.2. Histology of neuroinflammation: characterising glia morphology.....	29
2.1.3. Animal models of neuroinflammation: targeting specific cell populations.....	31
2.2. Translatability of the framework.....	32
III. Objectives.....	35
IV. Methods.....	39
4.1. Animal inflammation models: experimental design.....	39
4.2. Magnetic Resonance Imaging.....	44
4.2.1. Rats Acquisition.....	44
4.2.2. Humans Acquisition.....	44
4.2.3. Analysis and statistics.....	45
4.2.3.1. Diffusion Weighted Multi-compartment model (dw-MRI model).....	45
4.2.3.2. Conventional MRI data.....	47
4.2.3.3. Human patient data.....	47
4.3. Histological Analysis of Inflammation.....	48
4.3.1. Tissue processing and immunohistochemistry (IHC).....	48
4.3.2. Imaging and data extraction.....	49
4.4. Statistics and graphical representation.....	53
V. Results.....	57
5.1. Characterising glia reaction with histology and MRI.....	57
5.1.1. Histological glial response to LPS immunological challenge.....	57
5.1.2. Microglia reaction characterised using Iba-1 staining and MRI.....	59
5.1.2.1. Microglia reaction on PLX-LPS animals.....	61
5.1.3. Astrocyte reaction characterised using GFAP staining and MRI.....	62
5.1.3.1. Astrocyte reaction on PLX-LPS animals.....	63

5.1.4. LPS protocol preserves neuronal and myelin integrity.....	65
5.2. Distinguishing glia reaction with concomitant neurodegeneration.....	66
5.2.1 Neuronal death with microglia reaction characterised using NeuN staining and MRI.....	66
5.2.2. Isolated neuronal death characterisation.....	68
5.3. Specificity of the model in the presence of demyelination.....	69
5.3.1. Myelin reaction characterised using MBP staining and MRI.....	70
5.4. Translation to human patients.....	73
5.4.1. Quantifying human microglia density at whole brain <i>in vivo</i>	73
5.5. Comparison with conventional MRI techniques.....	74
VI. Discussion.....	79
6.1. Animal models of inflammation.....	80
6.2. Imaging Neuroinflammation non invasively <i>in vivo</i>	82
6.2.1. The value of our model and the emergence of new ones.....	84
6.3. Implications and perspectives from our evidences: from research to clinical purposes.....	85
6.4. Limitations.....	87
6.5. Future lines.....	88
VII. Conclusions.....	93
VII. Conclusiones.....	94
VIII. Bibliography.....	97
IX. Annex.....	123

List of abbreviations

a.u.	Arbitrary Units
CHARMED	Composite Hindered and Restricted Model of Diffusion
CSF1R	Colony-Stimulating Factor 1 Receptor
DAPI	4',6-Diamidine-2'-phenylindole dihydrochloride
DTI	Diffusion Tensor Imaging
dw-MRI	Diffusion-weighted Magnetic Resonance Imaging
FOV	Field of View
GFAP	Glial Fibrillary Acidic Protein
Iba-1	Ionised calcium-binding adapter molecule 1
IHC	Immunohistochemistry
LPS	Lipopolysaccharide
MD	Mean Diffusivity
MRI	Magnetic Resonance Imaging
NMDA	N-methyl-D-aspartate
NODDI	Neurite Orientation Dispersion and Density Imaging
PBS	Phosphate Buffered Saline
PFA	Paraformaldehyde
ROIs	Regions Of Interest
TE	Echo Time
TR	Repetition Time

List of figures and tables

Introduction

- Figure I.1: Historical timeline of neuroinflammation.
- Figure I.2: Microglia and Astrocytes current view; an update.
- Figure I.3: dw-MRI; conceptual explanation of isotropy vs anisotropy.
- Figure I.4: Examples of diffusion MRI applications.
- Figure I.5: White versus Grey Matter: cell units presence.

Methods

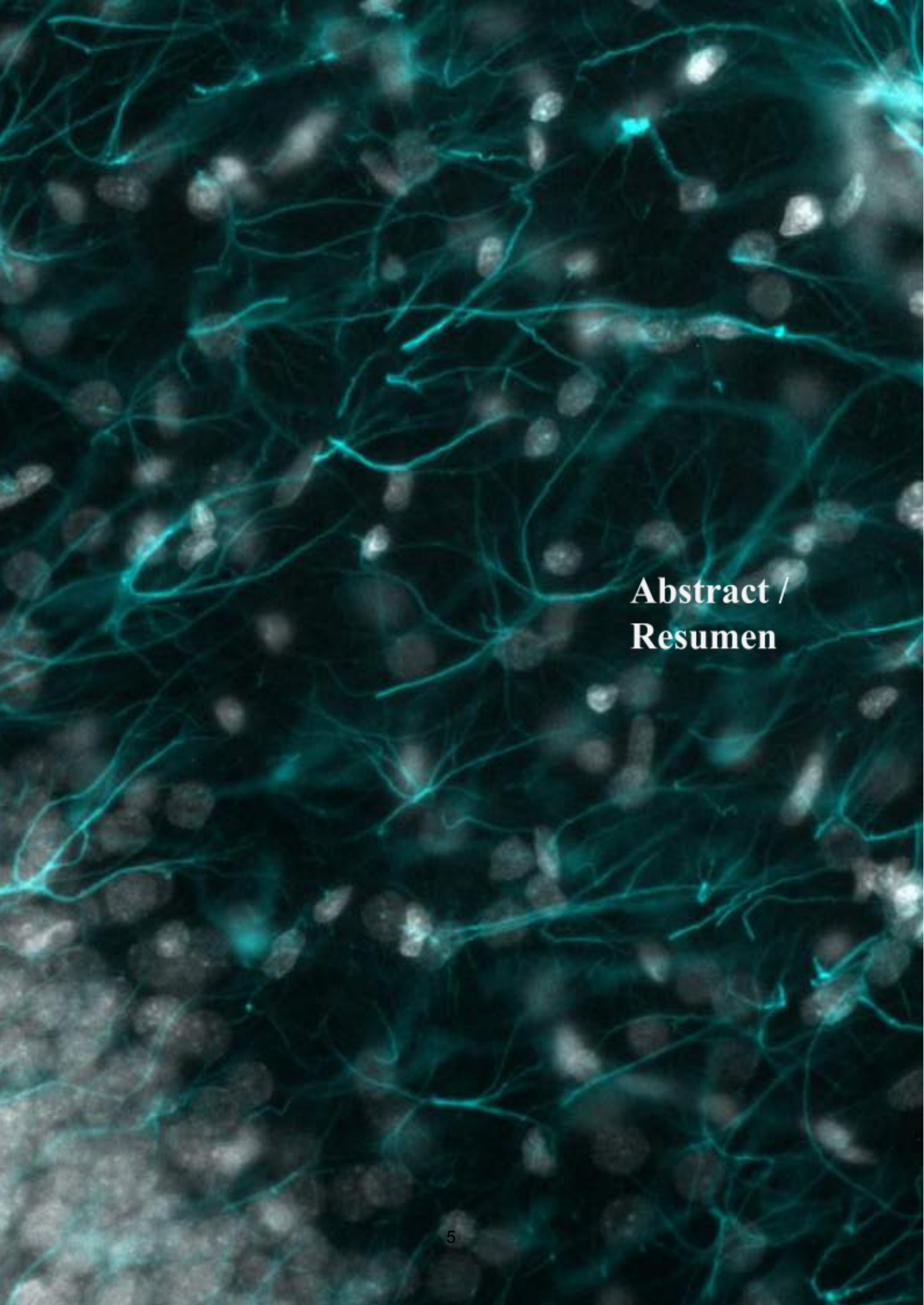
- Figure. M1: Animal inflammation models.
- Figure. M2: Multi-compartment tissue model.
- Figure. M3: Microglia analysis workflow.
- Figure. M4: Astrocyte analysis workflow.
- Figure. M5: Density analysis pipeline
- Figure. M6: Intensity analysis pipeline.
- Table M.1: Table summary comparing dw-MRI model measurements and histological measurements.

Results

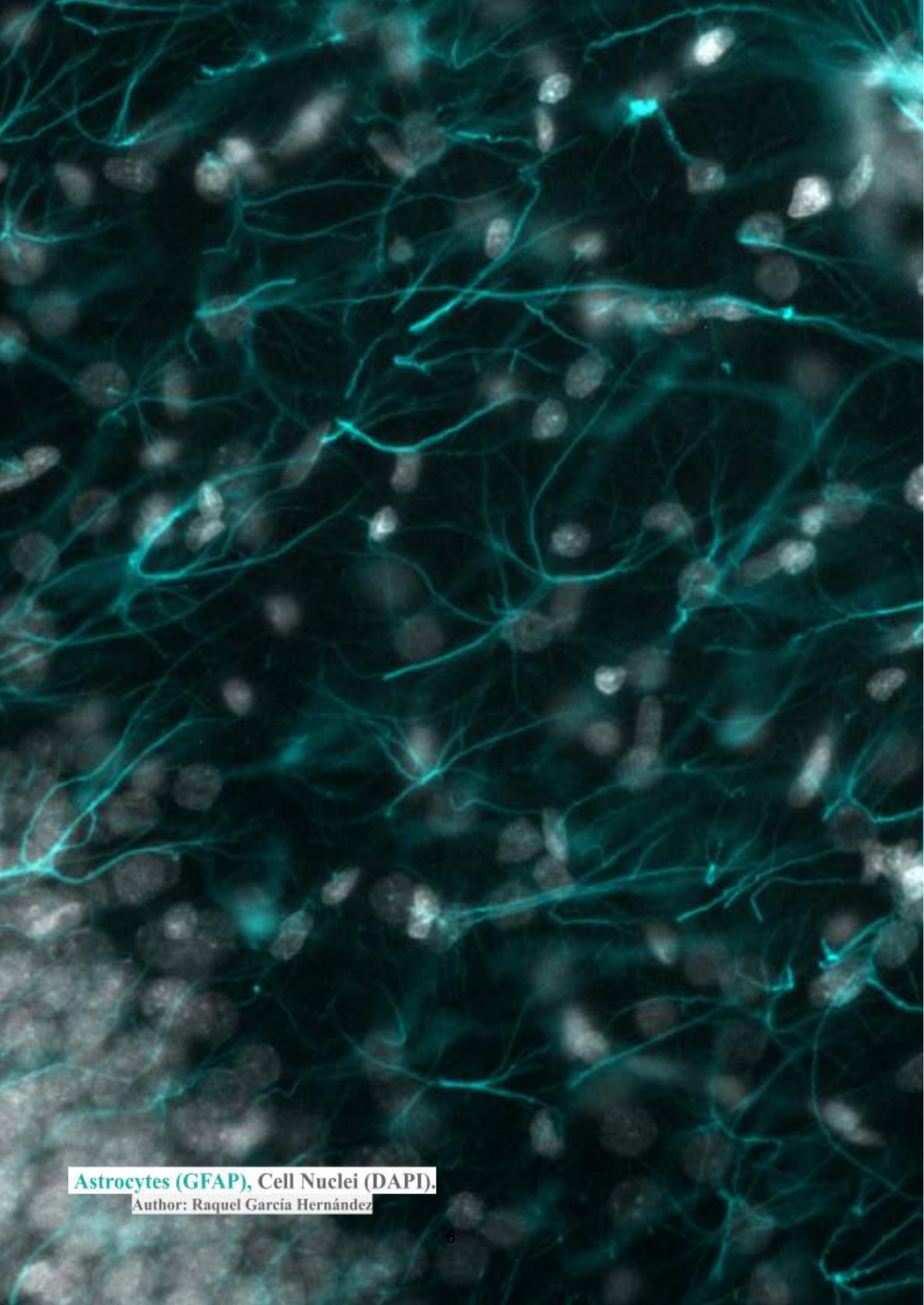
- Figure R.1: Microglia and astrocytes main results.
- Figure R.2: Microglia reaction characterization with dw-MRI and histology.
- Figure R.3: Microglia in PLX animals.
- Figure R.4: Astrocyte reaction characterization with dw-MRI and histology.
- Figure R.5: LPS protocol preserves neuronal and myelin integrity.
- Figure R.6: Neuronal death characterization with dw-MRI and histology.
- Figure R.7: Isolated neuronal death characterisation.
- Figure R.8: Myelin reaction characterised using MBP staining and MRI.
- Figure R.9: Dispersion parameter at different *in silico* scenarios.
- Figure R.10: Quantifying human microglia density at whole brain *in vivo*.
- Figure R.11: Comparison with conventional MRI techniques.

Discussion

- Figure D.1: Imaging Neuroinflammation non invasively and *in vivo*, an MRI-histology approach.
- Figure D.2 Imaging microglia and astrocyte *in vivo*, from research to clinical purposes

A microscopic image of a neural network. The image shows a dense network of thin, cyan-colored axons and dendrites. The cell bodies (soma) are stained in a light grey or white color, appearing as small, rounded structures scattered throughout the network. The background is dark, making the stained structures stand out. The overall appearance is that of a complex, interconnected neural circuit.

**Abstract /
Resumen**



Astrocytes (GFAP), Cell Nuclei (DAPI).

Author: Raquel García Hernández

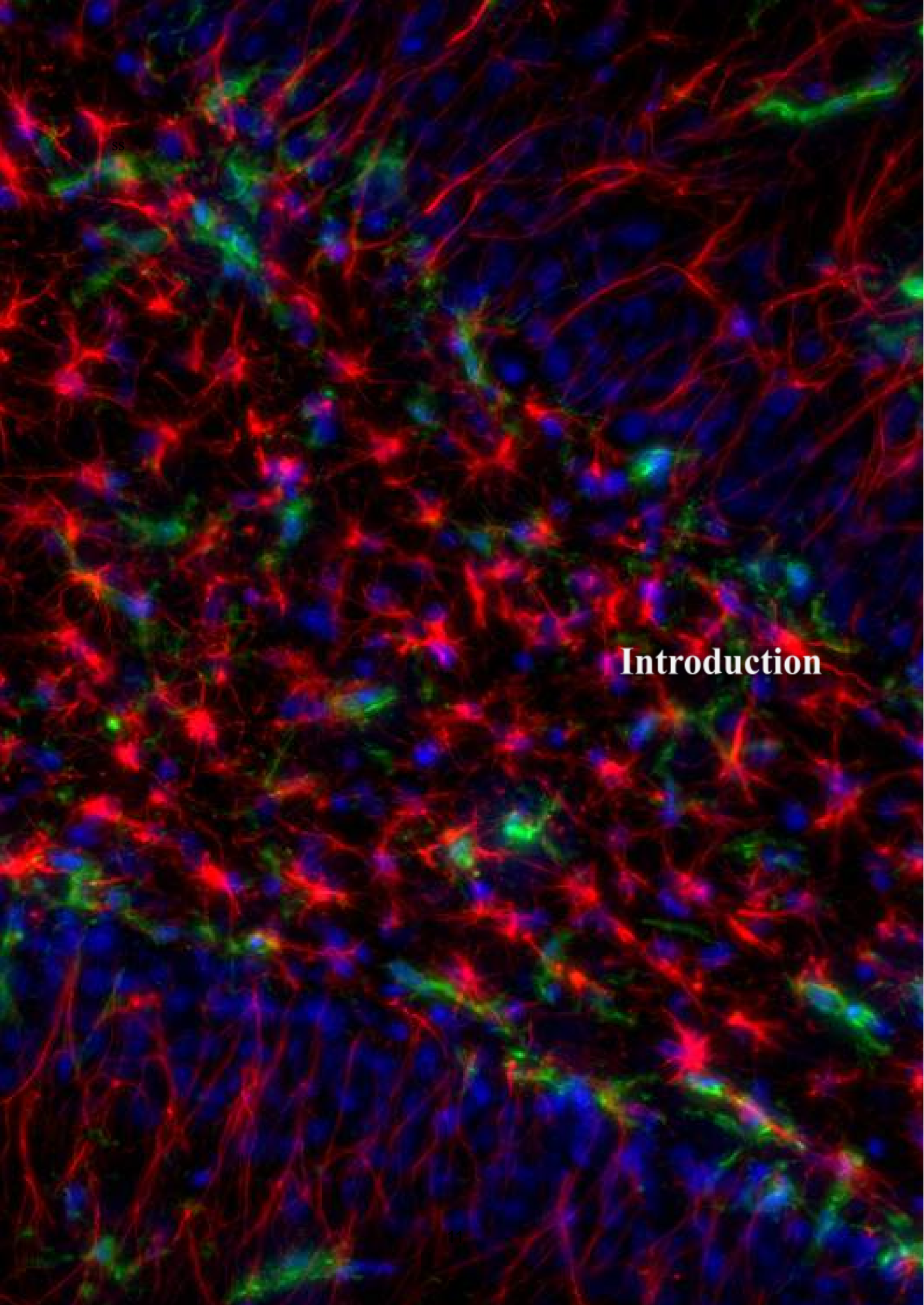
Abstract

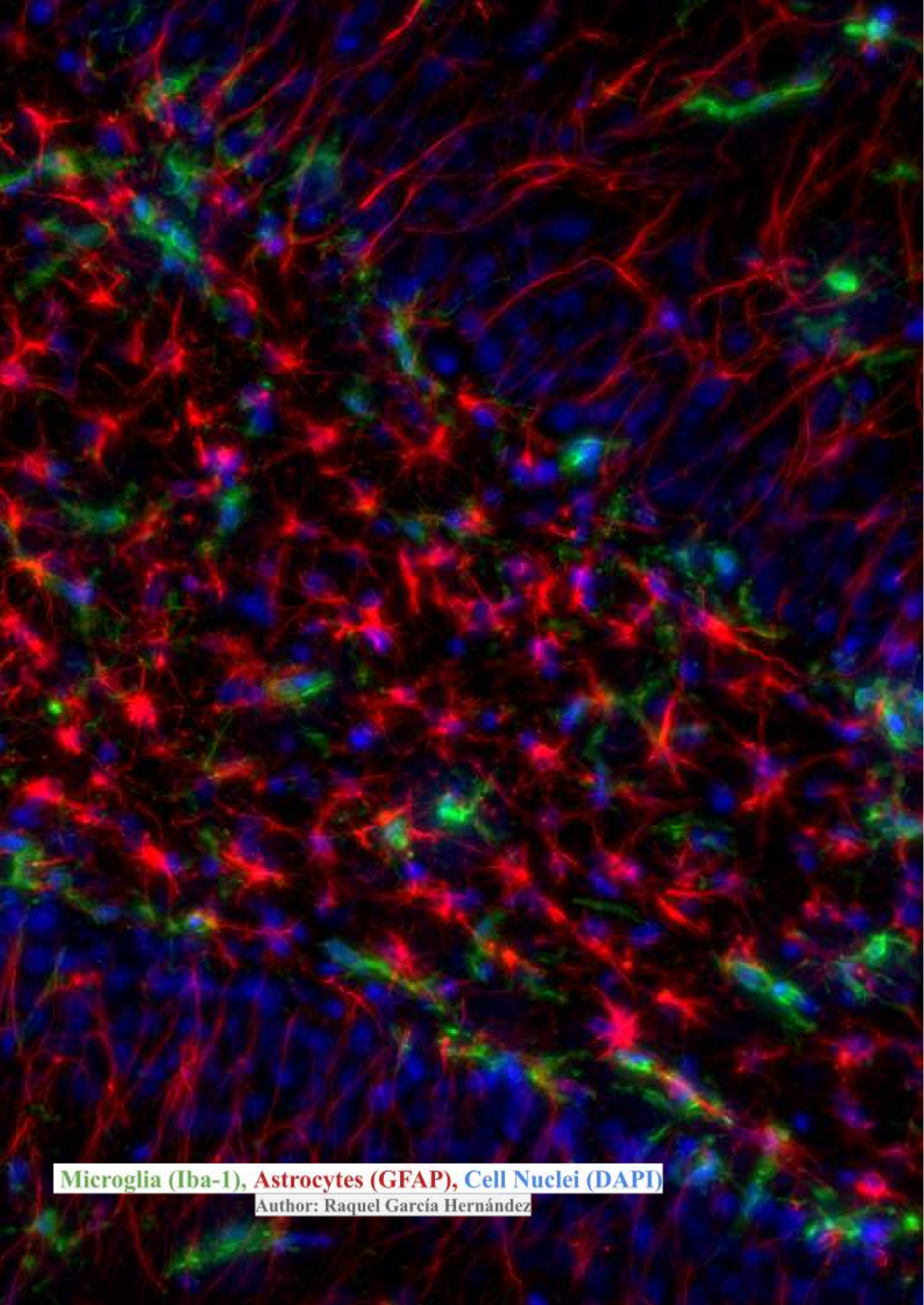
Neuroinflammation is a central topic of research in neuroscience due to its implication in the development of numerous neurological and psychiatric disorders. However, to date, there are no imaging techniques capable of characterising brain inflammation *in vivo* and non-invasively. In this study, we propose a novel approach to visualise microglial and astrocytic reactions in the gray matter using diffusion-weighted magnetic resonance imaging (dw-MRI). To demonstrate it, we employed various animal models in rats and conducted a pilot study in humans to explore its clinical utility. The study is based on 1) the ability of dw-MRI to study structural changes in different cellular compartments, 2) the characteristic morphology of glial cells, and 3) their known morphological change in response to an inflammatory process. The available animal models allowed us to generate time windows to distinguish the microglial response from the astrocytic response (longitudinal study after lipopolysaccharide treatment), as well as to induce inflammatory responses in the absence (lipopolysaccharide) or presence (ibotenic acid) of neurodegeneration or demyelination (lyssolecithin). Finally, the specific footprint left by microglial reaction in dw-MRI could be verified in experiments with PLX5622, a compound that produces almost complete microglia depletion in the tissue. The combination of dw-MRI and histological studies in the same animals allowed us to demonstrate a high correlation between cell type-specific histological measurements and specific compartments defined in dw-MRI. Overall, our experiments with animal models demonstrate that 1) it is possible to non-invasively measure the reaction of microglia and astrocytes in an inflammatory process, 2) the reaction of both cell types can be distinguished and quantified separately, even though both occur simultaneously, and 3) this capability of dw-MRI is not affected in cases of neuronal death or axonal demyelination, two alterations that themselves modify water diffusion in the tissue. Finally, we adapted our dw-MRI protocol to a human research scanner and demonstrated its ability to estimate microglial density in several brain regions in six healthy human patients, corroborated by *post mortem* data from the literature. These results underscore the potential of our approach to obtain non-invasive images of microglia and astrocytes *in vivo*. We anticipate that this model will significantly contribute to our understanding of glial functions in both health and disease.

Resumen

La neuroinflamación es un tema central de investigación en neurociencia por su implicación en el desarrollo de numerosos trastornos neurológicos y psiquiátricos. Sin embargo, hasta la fecha, no hay técnicas de imagen capaces de caracterizar la inflamación cerebral *in vivo* y de forma no invasiva. En este estudio, proponemos un enfoque novedoso para visualizar las reacciones microgliales y astrocitarias en la sustancia gris mediante imagen por resonancia magnética ponderada en difusión (IRMd). Para demostrarlo, empleamos varios modelos animales en rata y realizamos un estudio piloto en humanos para explorar su utilidad clínica. El estudio se basa en 1) la capacidad de la IRMd para estudiar cambios estructurales en distintos compartimentos celulares, 2) la morfología característica de las células gliales, y 3) su conocido cambio morfológico en respuesta a un proceso inflamatorio. Los modelos animales disponibles nos permitieron generar ventanas de tiempo donde distinguir la respuesta microglial de la astrocitaria (estudio longitudinal tras tratamiento con lipopolisacárido), así como inducir respuestas inflamatorias en ausencia (lipopolisacárido) o presencia (ácido iboténico) de neurodegeneración o desmielinización (lisolecitina). Finalmente, la huella específica que deja la activación de la microglia en la IRMd pudo ser verificada en experimentos con PLX5622, un compuesto que produce la depleción casi completa de la microglía en el tejido. La combinación, en los mismos animales, de los estudios de IRMd e histológicos, nos permitió demostrar una alta correlación entre las mediciones histológicas específicas de tipo celular y los compartimentos específicos definidos en la IRMd. En conjunto, nuestros experimentos con los modelos animales demuestran que, 1) es posible medir de forma no invasiva la reacción de la microglia y los astrocitos en un proceso inflamatorio, 2) que la reacción de ambos tipos celulares se puede distinguir y cuantificar separadamente, aunque ambas sucedan de forma simultánea, y 3) que esta capacidad de la IRMd no se ve alterada en caso de muerte neuronal o desmielinización de los axones, dos alteraciones que de por sí modifican la difusión del agua en el tejido. Por último, adaptamos nuestro protocolo de IRMd a un escáner de investigación humano y demostramos su capacidad para estimar la densidad microglial en varias regiones cerebrales en seis pacientes humanos sanos, corroborado por datos *post mortem* de la literatura. Estos resultados subrayan el potencial de nuestro enfoque para obtener imágenes no invasivas de la microglía y los astrocitos *in vivo*. Anticipamos que este modelo contribuirá significativamente a nuestra comprensión de las funciones de la glía tanto en la salud como en la enfermedad.

Introduction





Microglia (Iba-1), Astrocytes (GFAP), Cell Nuclei (DAPI)

Author: Raquel García Hernández

I. Introduction

1.1 Neuroinflammation: a timeline

The central nervous system, a marvel of intricate design, serves as the control centre for our bodies, facilitating myriad interactions and functions. It operates in harmony with the body, typically maintaining a delicate balance that fosters robustness and resilience to environmental insults, ensuring our viability as human beings. But how is this equilibrium sustained? Despite lingering in the background for a while, much credit is owed to glial cells, which outnumber neurons in some brain areas by as much as 1,65:1 (Sherwood et al., 2006). Indeed, these glial cells take centre stage in the process central to our research: (Neuro)inflammation.

Inflammation is a protective mechanism aimed at safeguarding tissues from such insults, identifying and removing causative agents (chemicals, bacteria compounds...), and facilitating overall healing. It is a complex biological phenomenon, and involves various immune system cells depending on the insult (Rocha and Silvia, 1994; Granger and Senchenkova, 2010, National Institutes of Health definition). Neuroinflammation, specifically, refers to inflammation of the nervous system. Similar to general inflammation, it involves the intricate activation of distinct immune cells, but specifically for the nervous system cells such as glia cells as microglia and astrocytes (Rio-Hortega, 1919, Eddleston and Mucke, 1993, Escartin et al., 2021, Paolicelli et al., 2022), peripheral immune system cells and autoantibodies (Roger et al., 2012, Wang et al., 2023), all working in concert to promptly resolve the issue.

However, despite our perceived understanding, the reality is far more unclear, both in terms of cellular implications and functional outcomes, and the role and valence of neuroinflammation is complex and not always positive for the system. Overall, this thesis focuses on the generation of a tool to image microglia and astrocytes *in vivo* and non-invasively, helping to follow the complex reactions and interactions in health and disease from these cell types.

In the following section, I will briefly review the historical and current perspective of these inflammatory processes.

1.1.1. Origin, function and main characters

Historically, the narrative of inflammation is rich and vivid, dating back to the observations of the Greek physician Hippocrates in the 5th century, who described neuroinflammation as an early part of the healing process following tissue injury. Subsequent contributions came from Celsus, a Roman writer, who noted the characteristic signs of inflammation (warmth, redness, swelling, and pain) and it is believed that Galen, a physician in the Roman Empire, added a crucial aspect: the loss of tissue function when inflamed (Rocha and Silvia, 1994;

Granger and Senchenkova, 2010). Reflecting on these observations, a dichotomy already emerged: “healing versus loss of function”. Is inflammation still dichotomous today?

Delving further into history, particularly in the realm of neuroinflammation, great scientific discoveries such as magnification lenses and labelling techniques have propelled the field forward, unveiling new ways of understanding. In the words of Santiago Ramón y Cajal, upon observing labelled cells in his custom-made microscope:

“Ya no es necesario interpretar, si no ver y constatar”
translation: “It is no longer necessary to interpret, but rather to see and verify”
Santiago Ramón y Cajal

The cell substrates of inflamed brain tissue were first observed as early as 1858, and Rudolf Virchow coined the concept of neuroglia, referring to a group of non-neuronal cells interacting with nerve tissue (Virchow, 1858) (Figure I.1.1858). Later, Camillo Golgi, through the development of Golgi staining, produced detailed drawings of glial cells and its ramifications by 1872 (Golgi, 1873) (Figure I.1.1872-3). A few decades later, Lenhossék coined the term “astrocytes”, differentiating them based on their large size and protoplasmic characteristic phenotype (Lenhossék, 1895) (Figure I.1.1895). Subsequently, the term “microglia” was coined by Rio-Hortega in 1919 (Rio-Hortega, 1919), thanks to his descriptions with silver staining (Figure I.1.1919), convinced of its morphologically different aspect from astrocytes.

The immune roles of microglia and astrocytes were soon recognized, primarily driven by observations of their morphological changes in response to chemicals or immune insults, as conducted by Rio-Hortega. He described differences in microglial ramifications in response to varying silver concentrations in the staining (Rio-Hortega, 1919). Moreover, he established that microglia are the principal immune defenders of the brain, using their long and numerous ramifications to sense their environment and become phagocytic against attacks, acting as “voracious macrophages” (Rio-Hortega, 1919), even proliferating in number and changing their morphology significantly. Rio-Hortega's findings were further demonstrated and expanded, showing that microglia were also part of the adaptive immune system, presenting antigens to T lymphocytes after gamma-interferon treatment (Suzumura et al., 1987) and producing cytokines after LPS exposure (Hetier et al., 1988). Additionally, different roles arose in parallel by the 1960s, highlighting, for example, their role in synapse modelling (Blinzinger and Kreutzberg, 1968). Over this time, specific methods have emerged to identify microglia. One of the most renowned markers is Iba-1 (Ionised calcium binding adaptor molecule 1), discovered in 1998, which targets a calcium binding protein (Ito et al., 1998) (Figure I.1.1998). This marker has been consistently employed up to the present day, allowing further definition of morphological reactions (Paolicelli et al., 2022).

Regarding astrocytes, they were early linked to metabolic and nutritive functions in brain tissue by Golgi, thanks again to morphological descriptions, by observing their prolongations around blood brain vessels (Golgi, 1873) (Figure I.1.1872). Later, Ernesto Lugaro pointed to

their role in neurotransmitter homeostasis through their metabolization and uptake (Lugaro et al., 1907), confirmed in 1994 by Mennerick and Zorumski (1994) showing they affect synaptic transmissions using electrophysiological recordings. This role was later extended, demonstrating they can even release neurotransmitters themselves (Szatkowski et al., 1990; Martin., 1992), in a process termed “gliotransmission”, and Araque et al., coined the term "tripartite synapses," with astrocytes as a new synaptic element (Araque et al., 1999). Additionally, like microglia, they react to insults or attacks on the central nervous system, in a process called astrogliosis, leading to significant changes in their morphology and size and the generation of scar tissue that promote nerve healing processes (Eddleston and Mucke, 1993). Finally, it is essential to mention that specific methods for labelling astrocytes did also emerge. In this case, the famous and widely used marker is GFAP, pioneered by Santiago Ramón y Cajal, derived from Glial Fibrillary Acidic Protein, with a chloride-sublimate staining technique (Ramón y Cajal, 1913), (Figure I.1.1913).

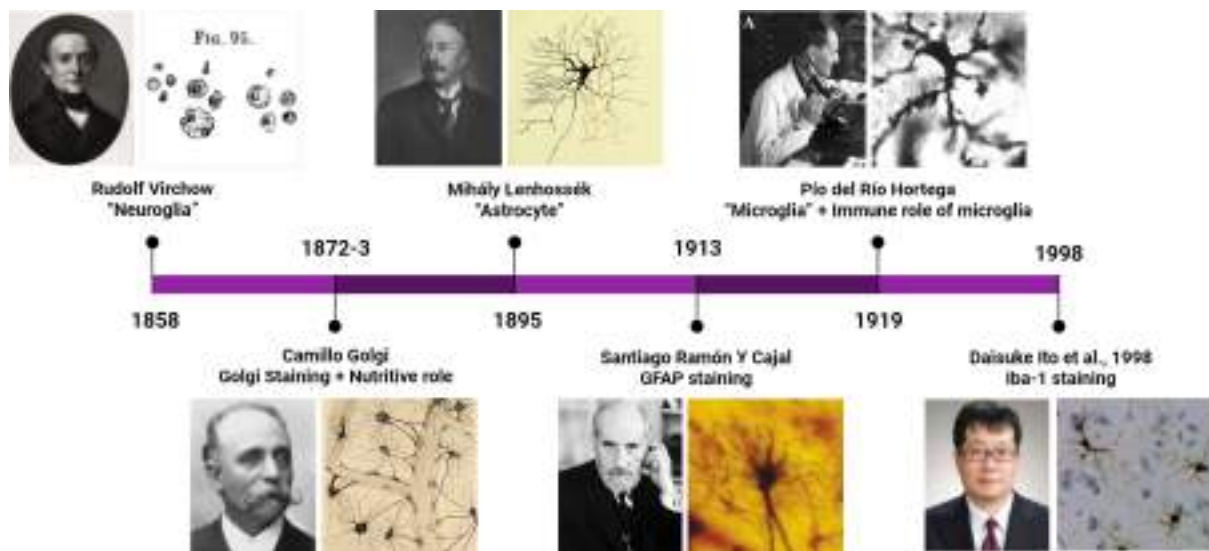


Figure I.1: Historical timeline of neuroinflammation. **1858)** Rudolf Virchow coined the term "Neuroglia" and provided the first drawings of this cell population. Left: Photograph of Rudolf Virchow. Right: His neuroglia drawings (Virchow, 1858). **1872-3)** Camillo Golgi developed Golgi staining, enabling precise visualisation of glia. He also noted their nutritive role by observing their extensions around blood brain vessels. Left: Photograph of Camillo Golgi. Right: His neuroglia drawings (Golgi, 1873). **1895)** Mihály Lenhossék coined the term "Astrocyte" and differentiated them from the glia population based on their characteristic size and shape. Left: Photograph of Mihály Lenhossék. Right: His astrocyte drawings (Lenhossék, 1895). **1913)** Santiago Ramón y Cajal developed GFAP staining for astrocyte-specific labelling. Left: Photograph of Santiago Ramón y Cajal. Right: GFAP staining of astrocytes (Ramón y Cajal, 1913). **1919)** Pío del Río Hortega coined the term "Microglia" and suggested its immune role by observing morphological changes in response to chemicals. Left: Photograph of Pío del Río Hortega. Right: Microglia staining (Río Hortega, 1920). **1998)** Ito et al. developed Iba-1 staining specific for microglia staining. Left: Photograph of Daisuke Ito. Right: Iba-1 staining of microglia in dark and blood vessels in blue (Ito et al., 1998). *Note:* Only historical events mentioned in this thesis introduction are included.

All these remarkable discoveries emphasised the importance of microglia and astrocytes, along with their neuroinflammatory response, for normal brain function in both health and disease. However, ultimately, these cell types were functionally categorised into two general terms: resting or active, with the latter often associated with diseases or attacks. Specific names were even assigned to these states, such as M1 and M2 for microglia representing resting or active states respectively, terms already appearing in the literature by 1970 (Streit et al., 1988). Similarly, for astrocytes, A1-A2 was used to represent resting or active states (Escartin et al., 2021).

Nevertheless, these pioneering discoveries illustrate that neither microglia nor astrocytes are simplistic cells, as they contribute to a multitude of functions. Given their multifaceted nature, is it realistic to categorise them simply as resting or active? In the next section, we will explore how this Linnaeus-like separation, while once useful, is no longer conducive to biology or clinical research. We'll examine how their roles in both health and disease are far more refined than a dichotomous classification suggests.

1.1.2. Current view: dynamism and new (undesired) roles

The last decades have supposed a change in paradigm in our understanding in both the function, physiology and morphology of microglia and astrocytes from what our giants have demonstrated before. And, as we have introduced: their role in health and disease is not always clear.

“Cells are residents of a vast ‘landscape’ of possible states, over which they travel during development and disease”

Conrad H. Waddington

New functions have been assigned to microglia and astrocytes, extending beyond neuroimmune functions. Microglia, for instance, have been implicated in the correct migration of interneurons and morphogenesis during development (Squarzoni et al., 2014, Lawrence et al., 2004). In the adult brain, in remodelling circuits in response to various external visual experiences, even in their supposed "resting" state (Tremblay et al., 2010), as well as regulating neurogenesis in the hippocampus (Sierra et al., 2010). Additionally, microglia have been shown to promote myelination through communication with oligodendrocyte precursors at different states (Giera et al., 2018). Similarly, astrocytes have been observed to respond to external stimuli in a frequency-dependent manner, as evidenced by intracellular calcium recordings in response to whisker stimulation (Wang et al., 2006). Furthermore, they play a role in sleep homeostasis (Halassa et al., 2009), support hippocampal-prefrontal *theta* communication in remote memory (Sardinha et al., 2017), and modulate hippocampal long-term potentiation (Abreu et al., 2023).

These newfound roles and reactions have revealed the multifaceted nature of microglia and astrocytes, blurring the line between active and resting states and adding layers of complexity to their understanding. This issue was recently addressed by over 70 researchers worldwide in

a nomenclature and function compendium for astrocytes (Escartin et al., 2021) (Figure I.2.F) and by over 100 researchers for microglia (Paolicelli et al., 2022) (Figure I.2.C). These compendiums emphasise the need to study microglia, astrocytes, and neuroinflammation in the correct context, considering factors such as age, sex, brain region, external environment, as well as the internal state of each cell: phenomics, metabolomics, proteomics, transcriptomics, and epigenomics. The overarching conclusion is that there are no discrete thresholds for their states, just as there are no discrete implications in neuroinflammation, as we will explore.

To illustrate the complexity of the issue, consider a few seminal experiments that have reshaped our understanding of microglia and astrocytes. One such discovery, published by two laboratories in 2005, visualised microglia *in vivo* using two-photon imaging and revealed that microglia are far from "resting" in healthy conditions; their ramifications are continuously in motion (Davalos et al., 2005; Nimmerjahn et al., 2005) (Figure I.2.A). These movements are now associated with what is known as the *sensome*: the ability to sense the brain parenchyma state through multiple membrane receptors covering their extensions, as "brain sentinels" (Hickman et al., 2013). Similarly, significant differences in astrocyte numbers have been observed just by the passing of time, with considerably higher size and GFAP reactivity occurring during healthy ageing (Jalenques et al., 1997) (Figure I.2.D). Additionally, going beyond phenomics, both microglia and astrocytes exhibit substantial differences in their transcriptomic profiles depending on the brain region being studied in healthy individuals, a topic covered specifically by Tan et al., (2020), grouping several studies.

This new information sheds light on why there is no clear distinction between active and resting microglia or astrocytes; they can be "active," dynamic, and diverse in healthy conditions, depending on numerous factors. Therefore, it has been suggested that perhaps a more appropriate term for them when a specific condition or agent is present could be "reactive" (Escartin et al., 2021).

Moreover, just as there is no clear distinction between active and reactive states, there is not always a clear distinction between pro and anti-inflammatory states. The evolving understanding of microglia and astrocytes biology allow researchers to study them with a new conceptualization, uncovering an extra layer of complexity and key motivation for this investigation: microglia and astrocytes are implicated in the generation and progression of diseases affecting the central nervous system (Figure I.2.B.E).

For instance, abnormal microglial reactions have been linked to Parkinson's disease (Cai et al., 2014; Arena et al., 2022), multiple sclerosis (Sanchez-Guajardo et al., 2015, Distéfano-Gagné et al., 2023), amyotrophic lateral sclerosis (Cooper-Knock et al., 2017, Carke and Patani, 2022) and stroke (Guruswamy and ElAli., 2017, Wang et al., 2022, Planas 2024), where Guruswamy and ElAli demonstrated a change in their morphology. Similarly, astrocytes can deviate from their normal function, acquiring a reactive phenotype characterised by a prolonged overreaction and the generation of toxicity in conditions like

Huntington's disease, amyotrophic lateral sclerosis, and Alzheimer's disease (Simpson et al., 2010; Phatnani et al., 2013, Kim et al., 2024). In the context of pathological ageing, microglial implication has been well observed, linking it to faster neurodegeneration mechanisms with higher number of prolongations (Davies et al., 2017). Moreover, a correlation between ageing and microglial "malfunction" with Alzheimer's Disease in humans has been noted (Davies et al., 2017; Streit et al., 2009, Kim et al., 2024, Rachmian et al., 2024), demonstrating an increase in their ramifications after tau depositions (Arranz and Stropper, 2019). Additionally, microglia has been linked to the progression of other disorders such as alcohol addiction, as it has been suggested that the microglial process retraction could promote addiction (De Santis et al., 2020).

The mechanism underlying these implications remains elusive, potentially involving pathological or sustained neuroinflammation (Walker et al., 2018, Kwon and Koh., 2020), the release of neurotoxic proteins (Perry et al., 2010) or even pathological oligodendrocyte reaction (Psenicka et al., 2021).

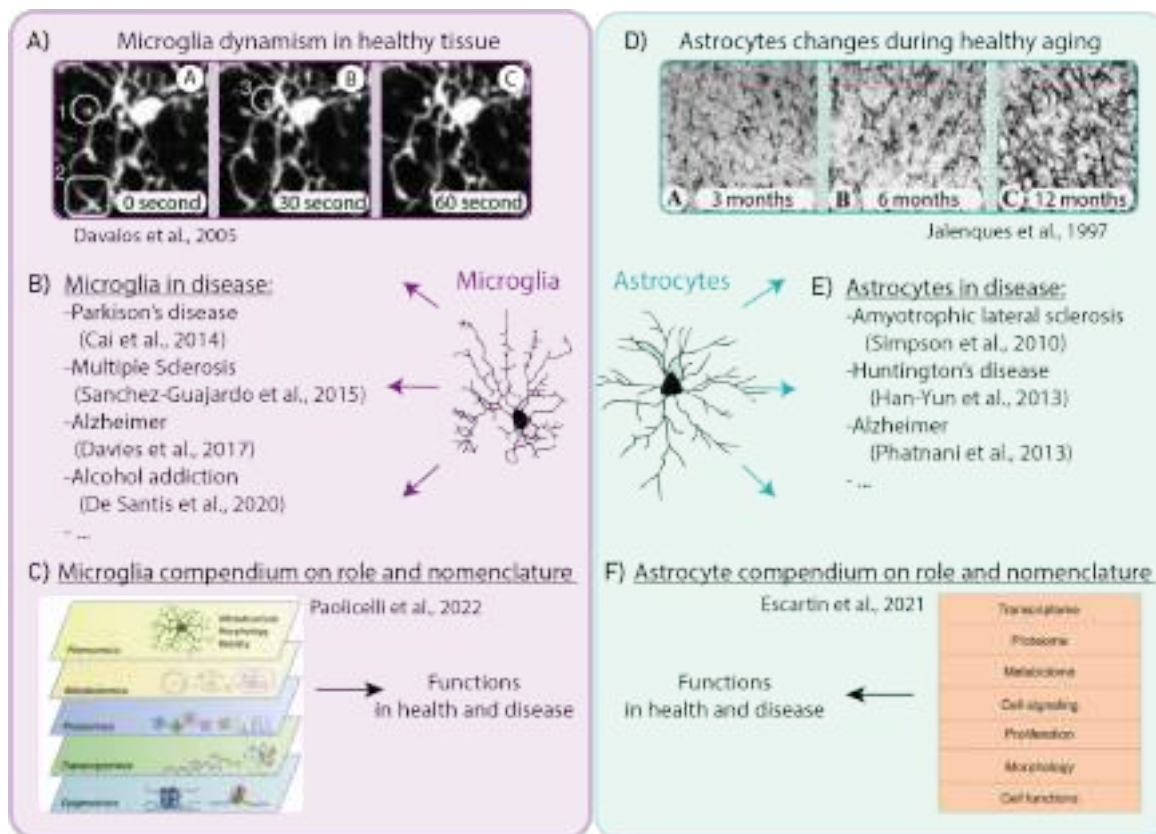


Figure I.2: Microglia and Astrocytes current view; an update. **A)** Example of microglia dynamism in healthy tissue: two-photon imaging of microglia over 60 seconds reveals continuous movement of their ramifications, adapted from Davalos et al., (2005). **B)** Recent implications of microglia in disease. **C)** Multiple layers of complexity defining microglia functions, as defined by the microglia compendium, adapted from Paolicelli et al., (2022). **D)** Example of astrocyte dynamism during ageing, indicating changes in their reactivity, adapted from Jalenques et al., (1999). **E)** Recent implications of astrocytes in disease. **F)** Layers of complexity defining astrocyte functions, as defined by the astrocyte compendium, adapted from Paolicelli et al., (2022). *Note:* Images taken from the articles cited in each panel.

Detecting these changes has become crucial, making tools capable of investigating microglial and astrocyte reactions necessary across all their layers of complexity. For instance, imaging their morphology *in vivo* would allow to observe changes in microglia and astrocyte morphology over the course of disease initiation and progression. Importantly, it has been demonstrated that in many pathological cases, these reactions occur with distinct spatial and/or temporal distributions (Davies et al., 2017, Arranz and Stropper, 2019), validating this idea and opening a new avenue: the discovery of early diagnostic biomarkers.

Given all of the above, the necessity and motivation for current research is clear: to develop a non-invasive tool capable of identifying and tracking microglial and astrocyte reactions *in vivo*, specifically focusing on their phenomics. We hypothesise that these morphological changes observed in different diseases are detectable with imaging techniques, and the development of such a tool would further our understanding of inflammation and its use in clinical research and diagnosis. The question now is: how can we visualise neuroinflammation "from the outside"? In the following section, I will investigate current standards that attempt to visualise neuroinflammation non-invasively.

1.2. Imaging Neuroinflammation

Imaging neuroinflammation has a rich history, evolving from histology to two-photon imaging, transitioning from *post mortem* to *in vivo* studies. However, the advent of minimally or non-invasive methods combined with *in vivo* acquisition has revolutionised both basic and clinical research by enabling assessment of brain morphology and function non-invasively, exemplified by positron emission tomography (PET) and magnetic resonance imaging (MRI).

PET typically employs radioactive tracers to visualise both healthy and pathological conditions. These tracers are often administered via intravenous injection, a minimally invasive method. For instance, the marker ^{11}C -PK11195 is widely used in diseases associated with neuroinflammation, particularly those exhibiting a reactive microglial state, such as amyotrophic lateral sclerosis (Tondo et al., 2020) and Alzheimer's disease (Passamonti et al., 2018). Similarly, the 18 kDa translocator protein, known as another "neuroinflammation marker," binds mainly to reactive microglia (Banati et al., 1997; Guo-Jun et al., 2014), facilitating the study of Alzheimer's disease progression (James et al., 2015). The spectrum of applications is broad; for example, the ^{18}F -florbetapir marker has recently been proposed as a viable method for monitoring myelin loss, particularly in multiple sclerosis (Zhang et al., 2021), and metabolic tracers for detecting stroke as FDG and ^{68}Ga -DOTATATE radioligands (Tawakol et al., 2006; Evans et al., 2017; Tarkin et al., 2017), identifying macrophages and stenosis plaques.

However, PET scanning carries inherent risks, and despite the tracers are approved for its use in humans, its ionising radiations makes it unsuitable for longitudinal studies and poses challenges for assessing treatment efficacy or biomarker evolution (Lee et al., 2013, Guilarte et al., 2019), making it not recommendable for high-risk populations such as pregnant or

breastfeeding women. Additionally, PET scanning can trigger allergic reactions (Codreanu et al., 2013, Lee et al., 2013). Finally, from an imaging perspective, although PET is widely used, it suffers from low spatial resolution which can complicate interpretation (Moses et al., 2011; Rogash et al., 2022) and markers such as 18kDa are not always highly specific in their binding, as they can be expressed in different glial populations (Guilarte et al., 2019) and present different binding genotypes across individuals (Owen et al., 2011) .

In contrast, MRI is a fully non-invasive method capable of imaging brain parenchyma microstructure with higher detail (Basser and Pierpaoli, 1996), holding promise for the study of different aspects of neuroinflammation. For these reasons, we believe that MRI is the most suitable choice for our project. I will elaborate on how MRI works and how we will tailor it to our specific aims in the following sections.

1.2.1. Magnetic resonance imaging and water diffusion

MRI has emerged as a cornerstone technology in the fields of neuroscience, neurology, and psychiatry, revolutionising the approach to both healthy and pathological brain conditions.

This technique, dating back to 1973 (Lauterbur et al., 1989), relies on the behaviour of water molecules within tissue, primarily formed by water within and in the extracellular space, when experiencing a magnetic field. MRI machines operate by applying both static powerful magnetic fields and radiofrequency pulses to interact with the spins of the protons present in water molecules. The spins get aligned thanks to the static magnetic field, generating a macroscopic magnetization, while the radiofrequency pulse is able to rotate such magnetization and generate a resonance phenomenon. When the radiofrequency pulse is discontinued, the water molecules revert to their equilibrium state in a process called "relaxation." The exact characteristics of this relaxation depends on the environment of the water molecules, so that indirect information can be gathered.

Diffusion-weighted MRI (dw-MRI), specifically, uses specialised magnetic field gradients to make the signal sensitive to the random and constant movement of water diffusion, known as Brownian motion. By using a range of b-values (the degree of diffusion weighting applied) and diffusion times, the displacement of water is determined by labelling the protons and measuring this average displacement after a specific diffusion time (Le Bihan et al., 2014). The contrast generated by different diffusion patterns in various environments allows dw-MRI to uncover intricate details of tissue anatomy with higher microscopic precision than conventional MRI (Basser and Pierpaoli, 1996). For example, in an isotropic environment, where there are no barriers, water can travel equally in all directions, similar to a drop of ink diffusing in a glass of water (Figure I.3.A). In contrast, in an axon bundle or tract, due to the cylindrical shape of the axons, diffusion is restricted, and water molecules diffuse more easily along the length of the fibres than across them; this is called anisotropic diffusion (Figure I.3.B). In both cases, we obtain crucial information about the underlying environmental shape where the protons were moving.

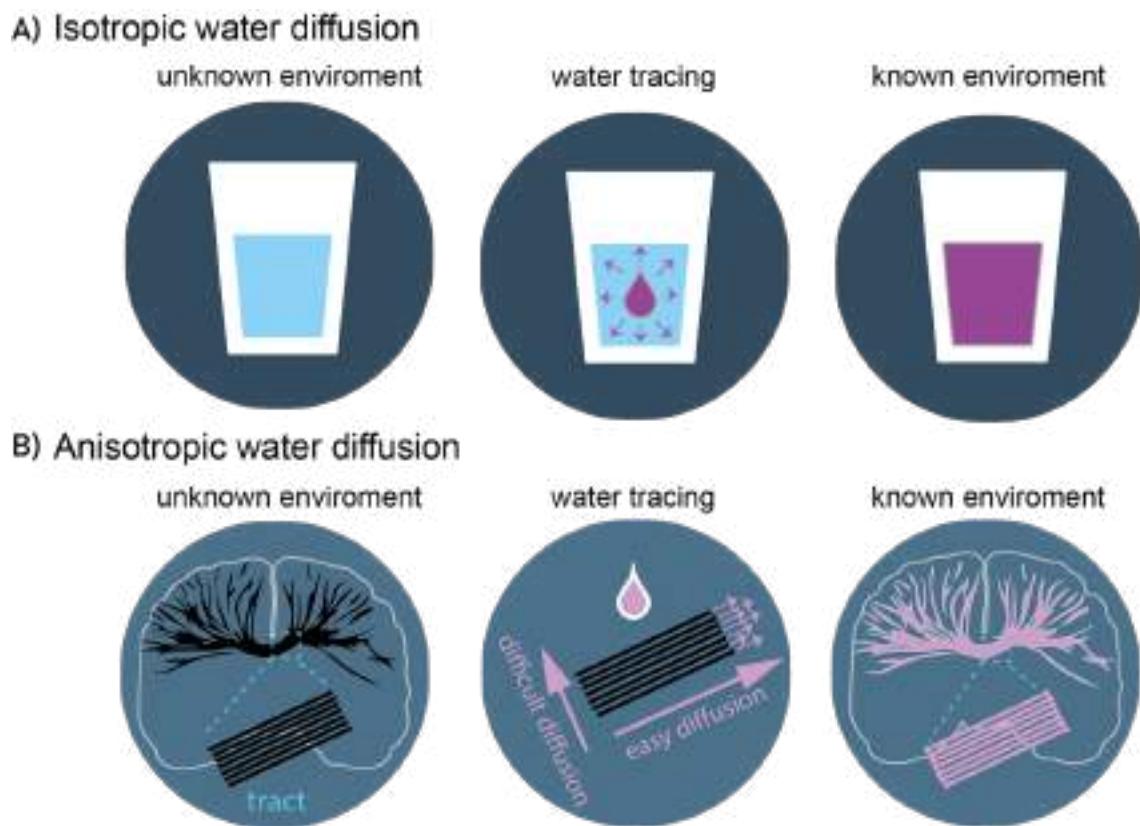


Figure I.3: dw-MRI; conceptual explanation of isotropy vs anisotropy. A) In an isotropic environment, such as a glass of water, a drop of water would diffuse in all directions with equal ease. **B)** Similarly, but in an anisotropic environment like an axon bundle (e.g., the corpus callosum), composed of axons. In this case, the diffusion primarily occurs in one direction, resembling a cylinder. By tracking this directional diffusion, it becomes possible to reconstruct the complete corpus callosum.

The first model introduced to describe anisotropy in dw-MRI images is the so-called diffusion tensor imaging (DTI), dating back to 1994 (Basser et al., 1994). DTI imaging is created by employing different magnetic field gradients to capture diffusion properties in various directions and identifying the one with the highest anisotropy through a diffusion tensor, a mathematical structure capable of accounting for anisotropy in the 3D space in a parsimonious fashion. This allows the generation of images sensitive to a particular direction of water diffusion (O'Donnell and Westing, 2012). Thanks to DTI, it became possible to reconstruct the axon bundles of the entire human brain (Pierpaoli et al., 1996) (Figure I.4.A).

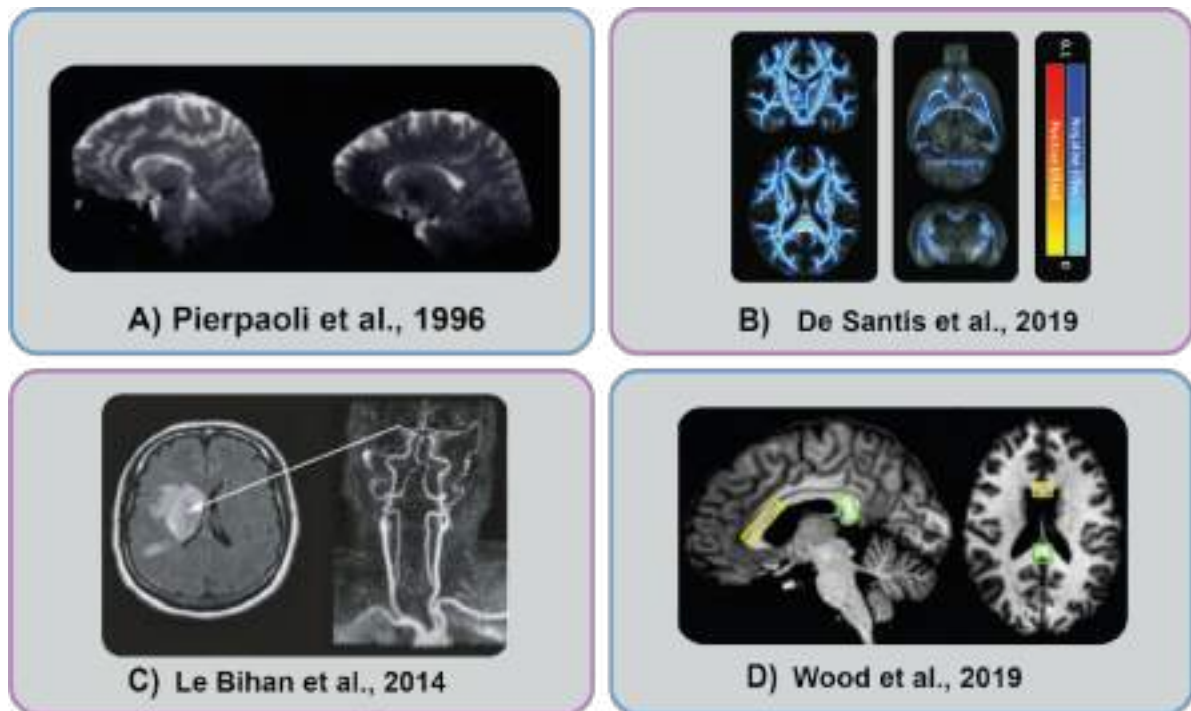


Figure I.4: Examples of diffusion MRI applications. **A)** One of the earliest diffusion-weighted images, from 1996, showing the high anisotropy of the corpus callosum (dark) compared to other areas (white), adapted from Pierpaoli et al., 1996. **B)** White matter DTI results comparing human patients (left) and rats (right) with alcohol use disorders, with darker blue indicating negative effects compared to controls and darker red indicating positive effects, adapted from De Santis et al., (2019). **C)** Utilisation of dw-MRI for stroke diagnosis, presenting the dw-MRI map of a human patient (left) alongside the angiogram (right) confirming the occlusion, adapted from Le Bihan et al., (2014). **D)** dw-MRI map showcasing the corpus callosum (yellow rectangle) and splenium (green) in multiple sclerosis patients for the study of local axonal degeneration, adapted from Wood et al., (2019).

It is crucial for current research to note that these diffusion characteristics within and outside compartments are affected in pathological processes, where changes in diffusion are expected (Baliyan et al., 2016). For example, by calculating the fraction of anisotropic diffusion it was possible to accurately detect white matter alterations in specific tracts in disorders such as alcohol addiction (De Santis et al., 2019) (Figure I.4.B). dw-MRI has also been instrumental in diagnosing stroke (Le Bihan et al., 2014) (Figure I.4.C) and multiple sclerosis by detecting differences in diffusion in injured tracts (Wood et al., 2019) (Figure I.4.D), or by identifying hyperintensities (Tran et al., 2022). Similarly, important metrics like mean diffusivity (MD) and fractional anisotropy can be derived from the tensor, serving as key indicators in assessing the integrity of white matter.

However, despite its widespread popularity, DTI is primarily suited for examining highly organised tissue, such as white matter, which mainly consists of fibre tracts. Although changes in water diffusion are expected in pathological conditions in grey matter as well, the

interpretation of DTI results in these cases is often problematic (Scarpazza et al., 2018; Ligneul et al., 2024).

1.2.1.1. (Lack of) Cell specificity of dw-MRI

Grey matter is the most predominant tissue in the central nervous system, playing a crucial role in facilitating normal brain function (grey et al., 2005; Mercadante and Tadi, 2023). At the cellular level, it comprises neuron somas, their dendrites, portions of their axons, as well as key characters of neuroinflammation: microglia and astrocytes (Barr and Kiernan, 1983; grey et al., 2005; Mercadante and Tadi, 2023) (Figure I.5.B). However, it is also the epicentre of many devastating diseases, making it a prime target for intervention and potential biomarkers.

But, how to image neuroinflammation with dw-MRI? By utilising various b-values and diffusion times, it becomes possible to capture water diffusion in different tissue compartments within the brain parenchyma. However, currently, different configurations of the tissue can give the same results (De Santis et al., 2019), and the interpretation of the morphological changes associated with diseases are difficult and misleading (Scarpazza et al., 2018; Ligneul et al., 2024). In the figure I.5.C we can see an exemplification, with three hypothetical scenarios: a healthy state and two pathological states, one with a microglial reaction resulting in reduced ramifications and the other showing astrocyte density loss. Problematically, both of the pathological conditions would yield a similar output when analysed by dw-MRI methods. For instance, a gold standard variable, MD, which measures total diffusion within a specific space, would yield the same result when measured extracellularly in these two scenarios. However, the cellular origin of this change, whether it be loss of microglial ramifications or astrocyte density, remains ambiguous. Despite this illustrated difficulty, MD is widely used and linked to specific inflammatory processes (Qin et al., 2012).

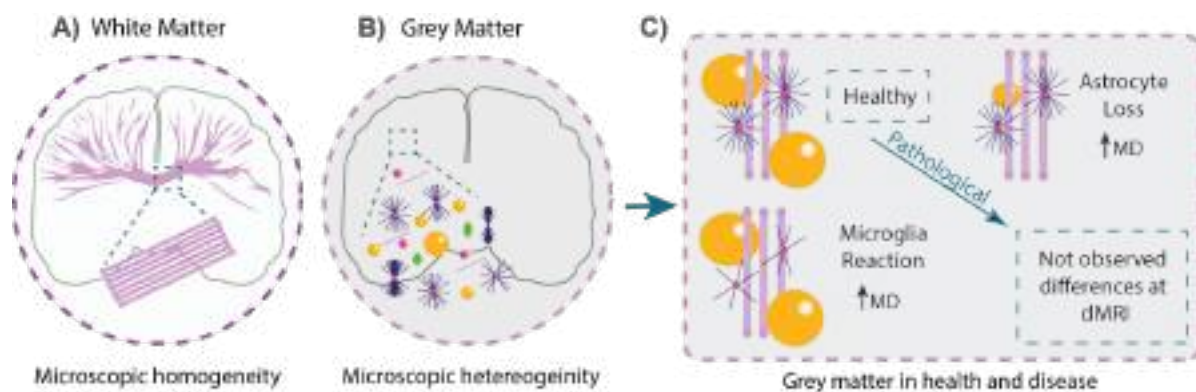
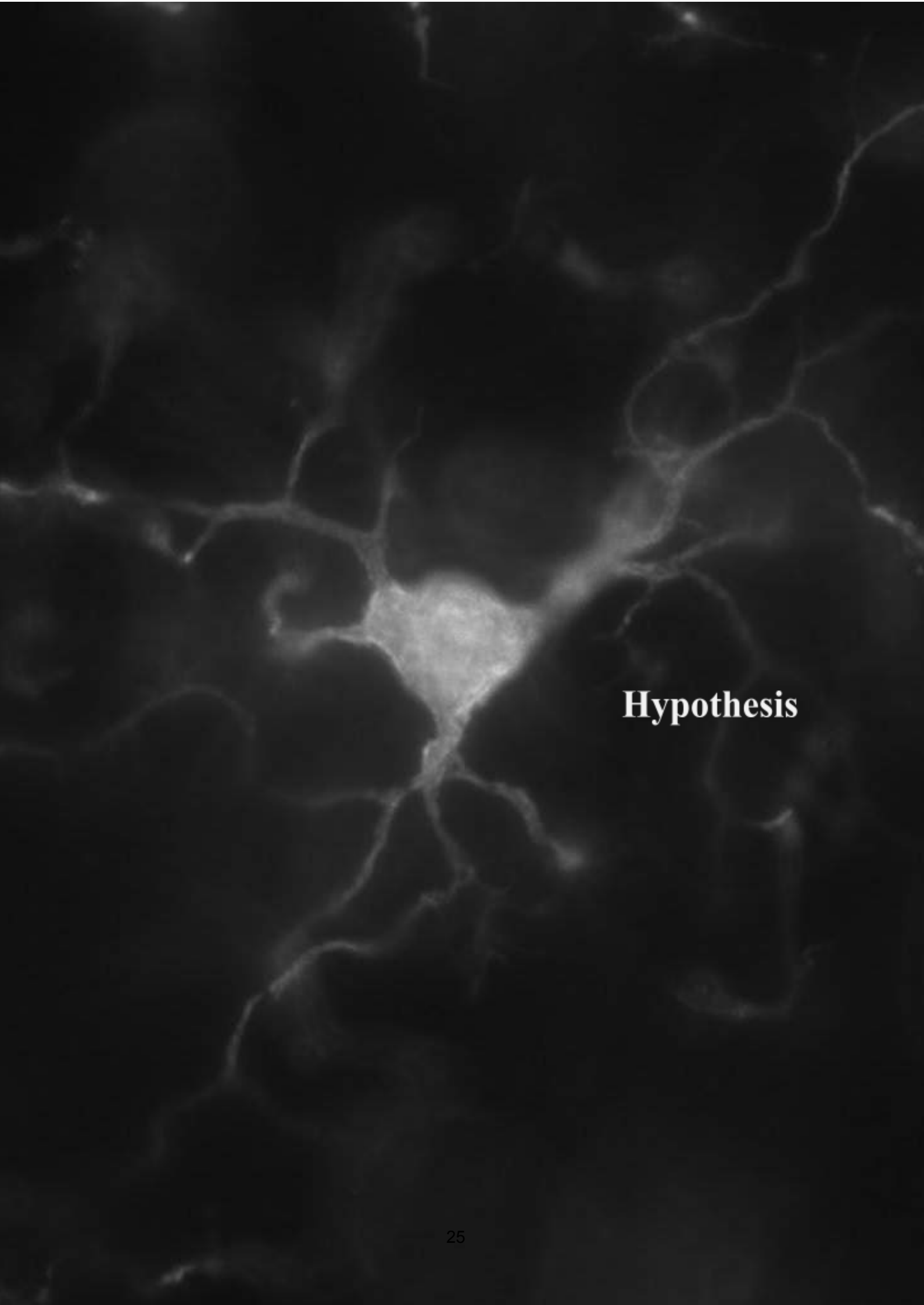


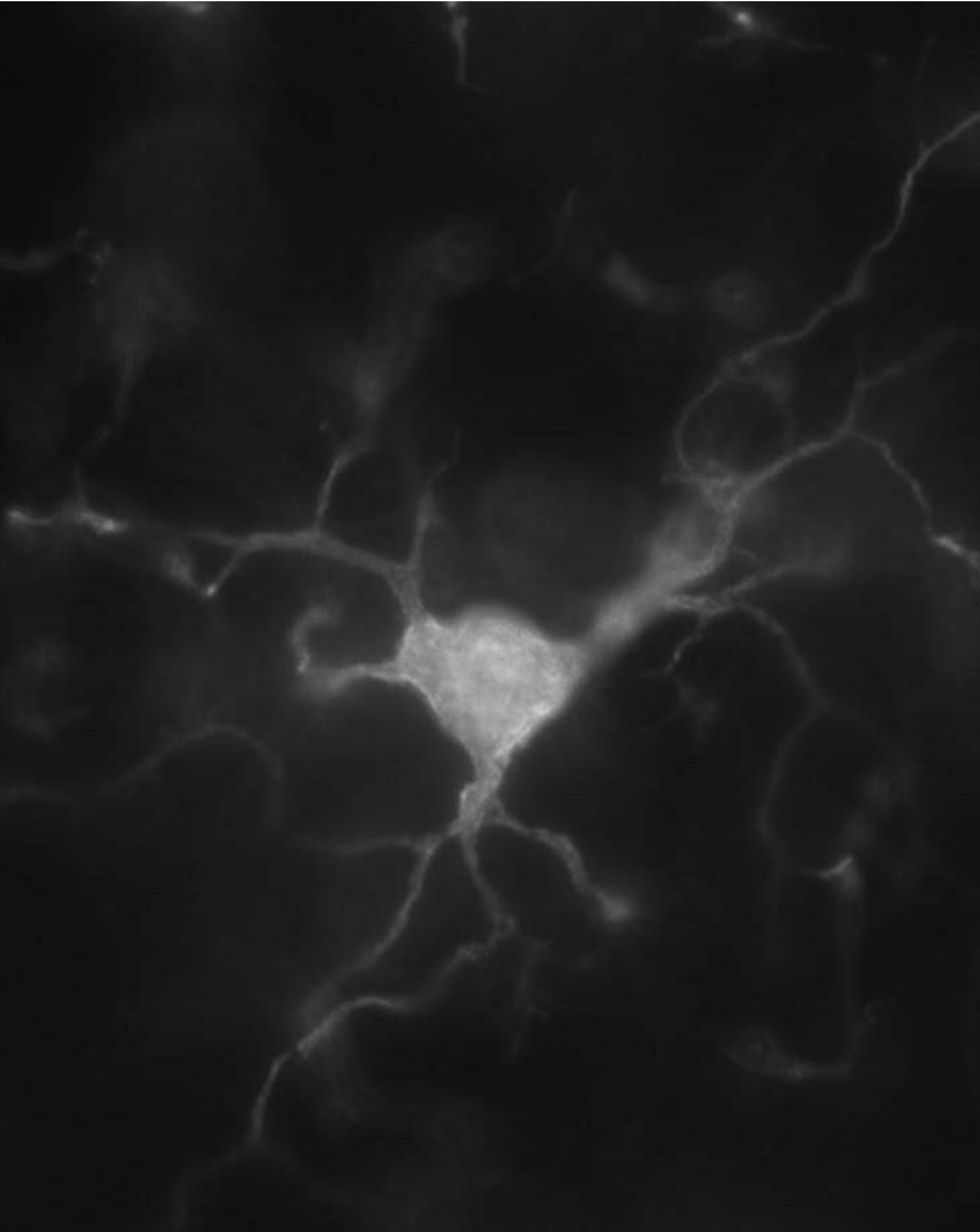
Figure I.5: White versus Grey Matter: cell units presence. A) Schematization of White Matter, illustrating its highly organized tissue with tubular compartments, axons. B) Schematization of Grey Matter, showing neurons (pink spheres), microglia (pink spheres with blue sticks), astrocytes (yellow spheres), and axons (pink sticks). C) Three hypothetical scenarios of grey matter: healthy and two

pathological conditions: microglia reaction or astrocyte loss. Both pathological conditions would exhibit comparable increases in MD, hindering the observation of differences in dw-MRI.

Similarly, other variables used in clinical settings aim to obtain specific and multicellular grey matter information. For example, the T1/T2 ratio is obtained by calculating differences in the relaxation times after the exposure to the magnetic field (Uddin et al., 2019) and is commonly used as a proxy for myelin integrity in both white and grey matter (Glasser et al., 2011; Ganzetti et al., 2014; Niewenhuys and Broere, 2017). Likewise, T2* It is used to detect cellular cavernomas and tumoral haemorrhage (Chavhan et al., 2009). Additionally, extracellular water diffusivity serves as an indicator of neuronal death, utilised in conditions like Parkinson's disease (Planetta et al., 2016).



Hypothesis



Microglia (Iba-1)

Author: Raquel García Hernández

II. Hypothesis

Up to this point, our journey through the colourful history of neuroinflammation has led us to a significant conclusion: microglia and astrocytes are implicated in health and disease, and understanding their complex behaviour, in particular their morphology, open new windows for research and clinical development, highlighting the opportunity for imaging tools. While PET has made strides in biomedical imaging, as mentioned before, its invasive nature and use of radioactive tracers pose risks. In addition, the specificity of PET tracers for glia has been questioned. In this context, we chose advanced dw-MRI as a possible tool to develop specific glia-cell MRI biomarkers.

How can we obtain dw-MRI specificity for microglia and astrocytes? Moreover, can we differentiate microglia and astrocyte reactions from concurrent neurodegeneration or myelin loss if all these alterations are expected to change water diffusivity in the tissue? In this thesis, we aim to develop a non-invasive, *in vivo* imaging tool using dw-MRI to capture microglia and astrocyte morphological dynamics, focusing on their phenomics in various scenarios. Furthermore, we will validate our findings through meticulous histological morphometric quantifications at cell-level population, ensuring the accuracy of our morphological *in vivo* characterization.

Our central hypothesis posits that the distinct morphology of microglia and astrocytes will condition water molecules to diffuse differently in their respective intracellular spaces, producing distinct water diffusion parameters as measured by dw-MRI. We further hypothesise that morphological changes within microglial or astroglial cell types, as those occurring in neuroinflammation, will produce discernible changes in water diffusion parameters, allowing us to identify and quantify specific cellular reactions. This innovative approach shows potential in elucidating the intricate dynamics of neuroinflammation and facilitating more precise diagnostic and therapeutic interventions in neurological disorders.

2.1. Integrating MRI and histology for *in vivo* analysis

To effectively develop our tool utilising dw-MRI for imaging neuroinflammation, our research rests upon three primary pillars: employing specific dw-MRI diffusion models alongside histological validation of observed dw-MRI changes, in conjunction with neuroinflammation animal models.

In the subsequent sections, I will provide a brief overview of each pillar before delving into the method section of the thesis.

2.1.1. dw-MRI multicompartment models: in search of cell specificity

Revolutionary approaches have recently emerged to address the lack of specificity and interpretability inherent in current dw-MRI methods for grey matter. These advancements are characterised by a more detailed conceptualization of brain parenchyma, considering how water diffuses within each cellular compartment while incorporating specific geometry and size, along with extracellular diffusivity, considering each population a different tissue unit or compartment.

This novel perspective involves the design of restricted diffusion models for various geometrical components of brain tissue known *a priori*, and these models are called multi-compartment models of diffusion. They analyse water diffusion within distinct cell compartments, each with unique shapes and sizes trying to mirror specific cell populations' characteristics. For instance, as can be visualised in figure I.6.A.B, water diffusion in a spherical cell would exhibit low anisotropy as a drop of water would diffuse equally in all directions, whereas the diffusion of the drop within a cylindrical cell would be more restricted to a main direction, resulting in higher anisotropy. By combining enough different geometrical shapes in the dw-MRI model, morphological changes in specific tissue units are expected to be detected.

Several years ago, multi-compartments models such as CHARMED (Composite Hindered and Restricted Model of Diffusion) (Assaf et al., 2004; Assaf and Basser, 2005) were starting to be developed, revolutionising white matter analysis by compartmentalising axon bundles. These models introduced hindered water compartments with primary directions of water diffusion within axon bundles, along with intra-axonal compartments representing one or more cylinders. This innovation enhanced the specificity of conventional dw-MRI. Subsequent research led to even more detailed models like AxCaliber, which estimates axon diameter within the nerve (Assaf et al., 2008). Soon later, the protocols were improved and modified for their use in the clinic, reducing the acquisition time of the dw-MRI protocol (De Santis et al., 2014).

Subsequently, researchers turned to compartmentalised models for grey matter, exemplified by NODDI (Neurite Orientation Dispersion and Density Imaging) (Zhang et al., 2012). NODDI, based on a version of CHARMED which incorporates axon density and radius (Alexander et al., 2008), enables its use for both grey and white matter. NODDI, simply, uses a mathematical model of symmetrical axial Watson distribution to estimate neurite direction (neurites aligned versus dispersed) and neurite density, allowing to discern between their signals individually by first time.

Further advancements expanded the sensitivity of these models to other grey matter components, such as microglia density estimation, as done by Yi et al., (2019) based on NODDI, or as done by Taquet et al., (2019) by estimating microscopic anisotropy.

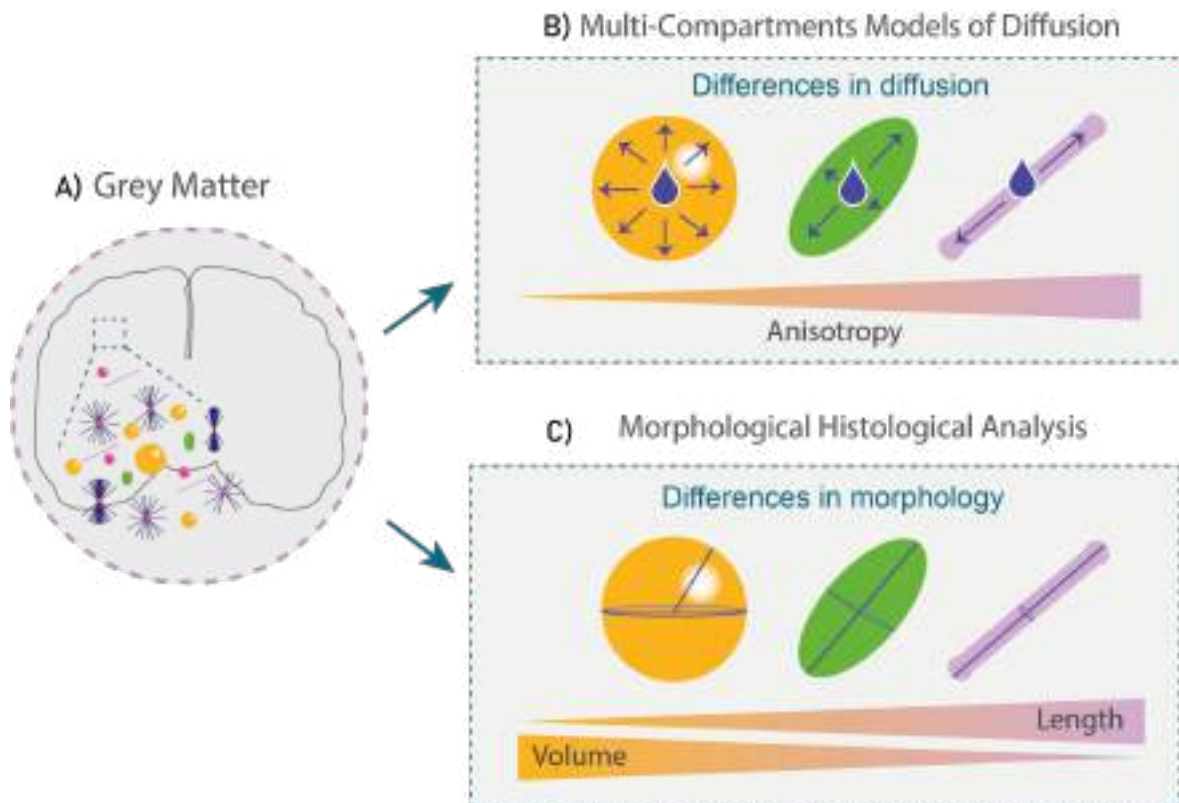


Figure I.6: Grey matter composition and its study; dw-MRI multi-compartments and histology;
A) Schematization of Grey Matter, illustrating neurons (pink spheres), microglia (pink spheres with blue sticks), astrocytes (yellow spheres), and axons (pink sticks). **B)** Multi-compartment model of diffusion detection showing different geometries in the tissue units; a sphere would exhibit low anisotropy as a drop of water would diffuse equally in all directions. Transitioning to a more tubular compartment, the anisotropy would increase. **C)** Morphological histological analysis: similarly, histological parameters would reflect differences in shape. A sphere would have a larger volume than an ellipse and a cylinder, but the length would vary in the opposite direction.

In summary, these advancements have revealed the capabilities of multicompartment models in dw-MRI, extending beyond detecting axon bundles to estimate neurite dispersion and microglia density. While these models still lack specificity for microglia or astrocyte reactivity, they establish the foundation for this study, empowering us with the idea that a microglia and astrocyte *in vivo* dw-MRI model is doable. We specifically postulate that by integrating in a dw-MRI model with the unique geometry and size of microglia and astrocyte population, we will expand the specificity of current imaging tools for grey matter.

2.1.2. Histology of neuroinflammation: characterising glia morphology

We have seen that the history of neuroinflammation revealed diverse layers of complexity in the description of microglia and astrocytes. Within this study, our focus centres on phenomics morphological descriptions as is the corresponding layer to validate and complement the

multi-compartment dw-MRI model results, and specifically we use histological *post mortem* procedures.

Histological procedures, beginning with perfusion and tissue fixation, preserve cellular states at the moment of perfusion fast and uniformly (Gage et al., 2012), facilitating comparisons between MRI acquisitions and subsequent histological observation at the microscope, approximately at the same time point. However, it's important to acknowledge that there can be a total brain volume shrinkage from *in vivo* to post-perfusion conditions (Cerdán et al., 2024). Importantly, staining with specific cellular markers allows us to discern and quantify changes in morphology and cell number, obtaining important information such as ramification number, cell volume and density, etc. allowing specific quantifications into cellular changes associated with neuroinflammation or a stimulus (Escartin et al., 2021, Papollicelli et al., 2022). Significantly, these morphological measurements stay accurate despite brain shrinkage. We argue that this can be directly compared with the diffusion results obtained from the multicompartment model, as it is illustrated in figure I.6: as well as different geometries and sizes giving different results in anisotropy (Figure I.6.A), differences in cell geometry would reflect changes in volume or length at histological level, as shown in Figure I.6.B. This direct comparison would ease the way to validate the dw-MRI model and the *in vivo* results.

For microglia, various markers are employed, despite having some debate around (Paolicelli et al., 2022). CX3CR1, for instance, labels both macrophages and microglia in healthy and pathological states, although downregulated in certain diseases (Jung et al., 2000, Wolf et al., 2013). CD11b/c also labels macrophages and microglia in health and disease, but with higher expression during development (Miligan et al., 1991, McKay et al., 2007). Similarly, F4/80 labels macrophages and microglia but it does allow for detailed reconstruction of the complete microglia morphology (Wadell et al., 2018). Notably, Iba-1, noted for its early introduction in the timeline of neuroinflammation (Ito et al., 1998), provides exceptional and detailed images of microglial cell bodies and ramifications, keeping these characteristics stable in disease conditions (Paolicelli et al., 2022), which makes it a perfect candidate to use it in microglia morphological characterization in response to different stimuli. For a comprehensive overview of current markers, see microglia compendium of Paolicelli et al., (2022).

Regarding astrocytes, several markers are available as well, focusing on cytoskeleton proteins for a morphology assessment. Typical choices include Vimentin (although not astrocyte-specific) (Yamada et al., 1992), Nestin (also labelling progenitor cells) (Moreels et al., 2008), and the ubiquitous and archetypal marker, GFAP (Eng et al., 1971), dating to 1913 (Ramón y Cajal, 1913). Despite controversies surrounding GFAP, such as its differential expression along brain regions (Griemsmann et al., 2015, Haim and Rowitch 2017), it is highly sensitive in reflecting morphological changes at different neuroinflammatory states, highlighting GFAP as an excellent option for this project. For an exhaustive review, consult the astrocyte compendium in the bibliography (Escartin et al., 2021).

Within this framework, we posit that histological *post mortem* characterization of microglia and astrocytes, when coupled with appropriate markers, critically complements and validates dw-MRI findings.

2.1.3. Animal models of neuroinflammation: targeting specific cell populations

To initiate microglia and astrocyte reactions, this project relies on the utilisation of animal models of neuroinflammation, specifically by the use of rat models. These models serve as indispensable tools for investigating the intricate dynamics of neuroinflammatory mechanisms in a controlled and reproducible manner. They offer a means to replicate specific states of inflammatory-related diseases, such as Alzheimer's (Karch et al., 2015) or Multiple Sclerosis (Matsushima and Morrell, 2001, Skripuletz et al., 2011), among others.

In this research, our focus centres on a subset of the possible models, specifically those enabling targeting specific populations: microglia or astrocytes, and generating observable changes in their morphology. Our rationale is straightforward: by activating microglia or astrocytes in isolation, the detection of morphological changes becomes clearer, allowing the validation of the dw-MRI multicompartiment model and minimising the risk of misinterpretation by the reaction of other tissue units.

These animal models can be induced through various methods, including neurotoxin injections such as okadaic acid to induce astrocyte enlargement (Costa et al., 2012), genetic manipulations promoting microglial reactions (Neumann et al., 2009), or immune system challenges using bacterial components like lipopolysaccharide (LPS) to study early microgliosis and late astrogliosis (Jeong et al., 2010).

Taking into account all the aforementioned evidence, we anticipated that employing an array of animal inflammation models with observable morphological changes at different time points would yield a specific signature in water diffusion patterns detectable by dw-MRI, allowing its relative comparison and specific detection. This will provide a platform for dissecting the distinct contributions of microglia and astrocytes to the observed signals *in vivo*, with further confirmation through histological analysis.

“What, then, are the conditions under which we discriminate things differing in a simple way? First, the things must be different, either in time or place, or quality (...) and it is easier to compare successive than simultaneous changes (...)”

William James

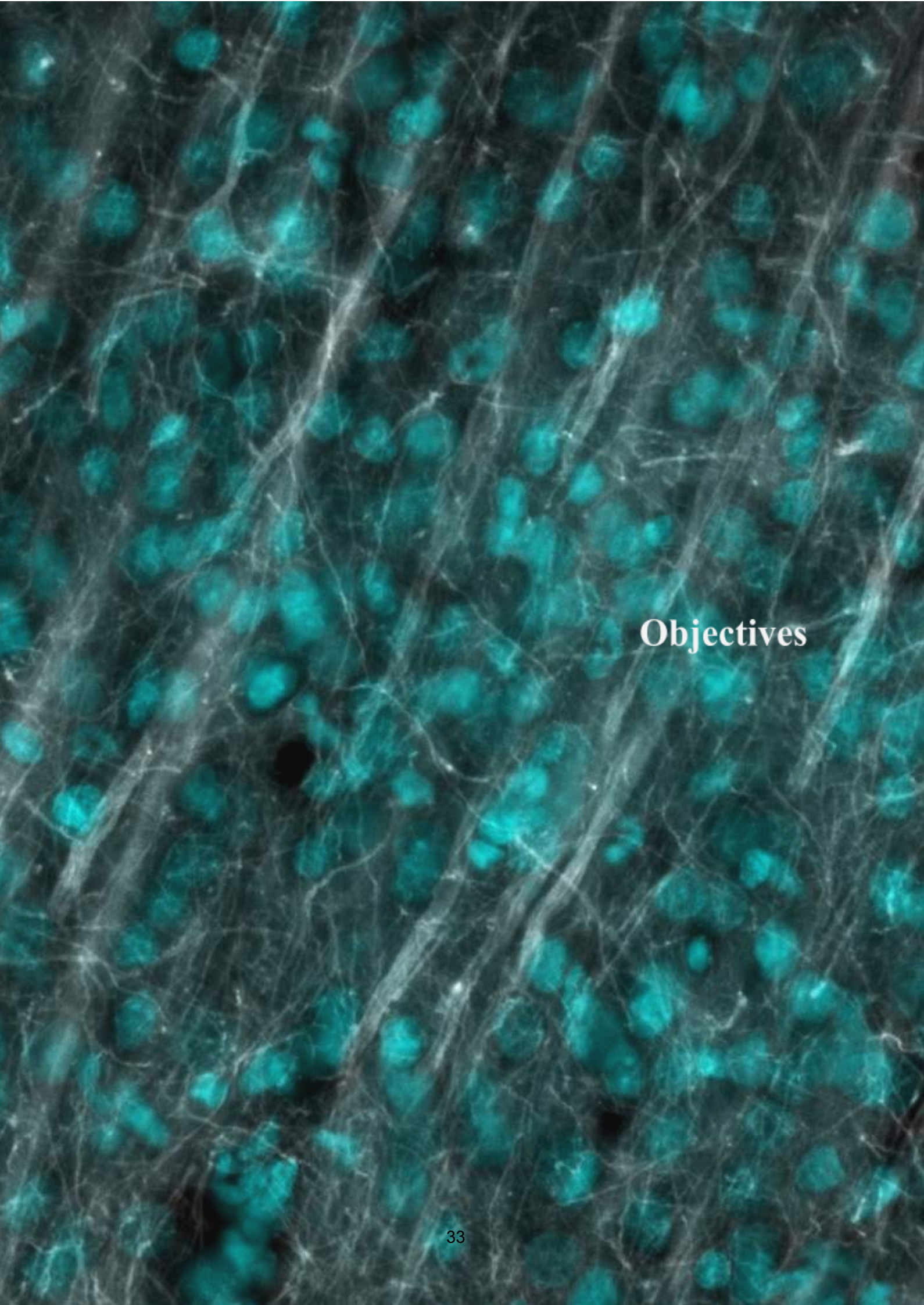
2.2. Translatability of the framework

For the last part of the introduction, I would like to focus on one fundamental characteristic of our framework: its potential to produce results susceptible to translation to the clinic. This key feature is underpinned by two inherent qualities of the project.

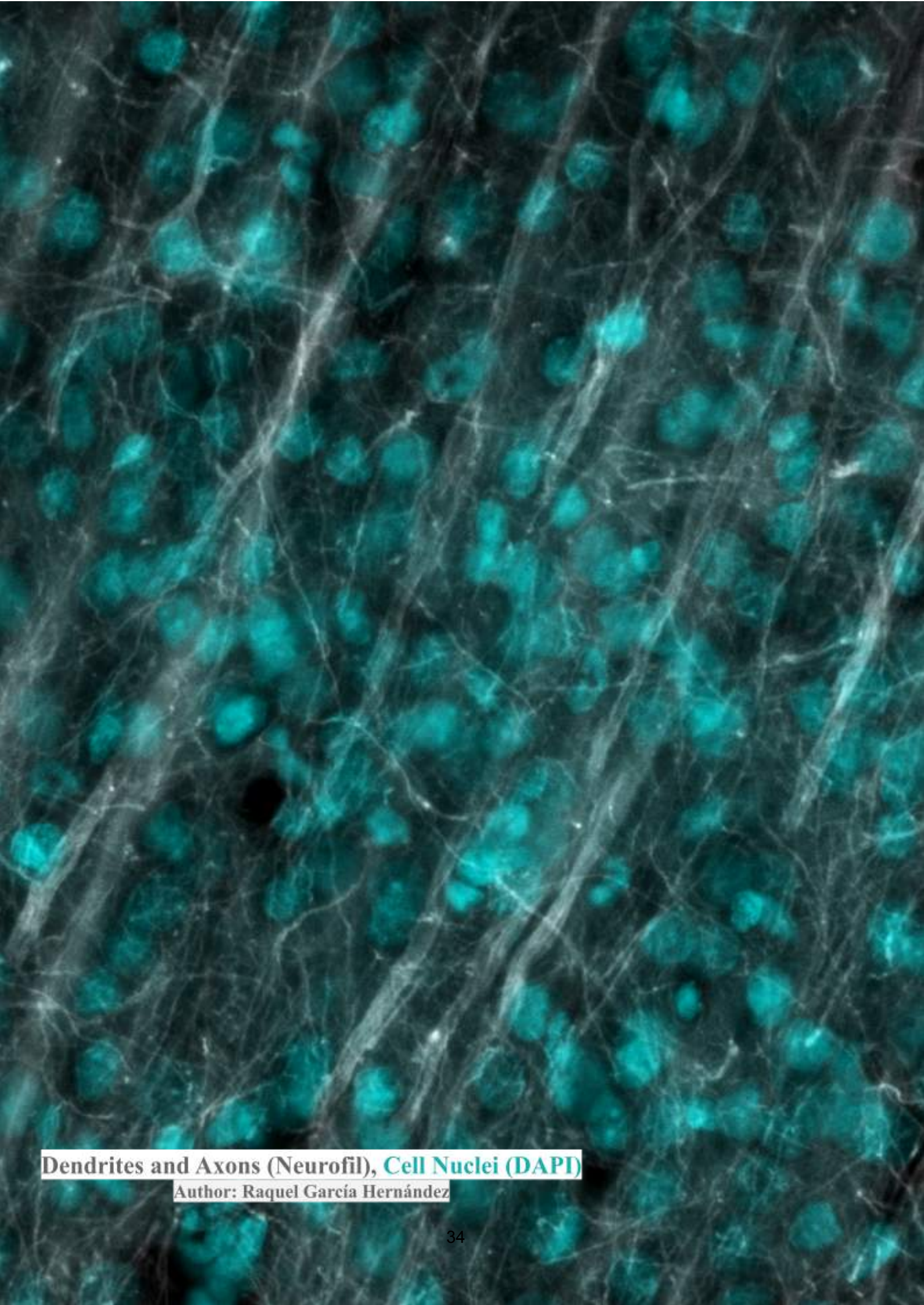
Firstly, MRI holds exceptional translational potential due to its non-invasive nature and ability to provide high-resolution images of soft tissues such as the brain, allowing its use throughout the whole vertebrate evolution (Mandino et al., 2020). This choice of MRI has the extraordinary ability to bridge the gap between mechanistic investigations in animal models and clinical applications, as we show in the example of figure I.4.B for an alcoholism study between rats and human patients as example.

Secondly, the process of neuroinflammation is conserved in the vertebrate lineage on its main features and on its basic morphological reactions for both astrocytes (Andriezen et al., 1983, Sofroniew et al., 2014) and microglia (Savage et al., 2019, Paolicelli et al., 2022). Therefore, although differences are expected in human subjects as their complexity it is unique in the human brain as there are distinctions (Oberheim et al., 2006, Geirsdottir et al., 2019), the ability of the dw-MRI multicompartmental model approach to discern morphological changes should be preserved across species. Furthermore, in relation to histology, the changes are also comparable because even the markers we have chosen for this project are used in humans for microglia and astrocytes morphological characterization, ultimately facilitating the translation and validation of the framework.

To demonstrate the clinical feasibility and applicability of our approach, we will expand our dw-MRI model to conduct a pilot study involving healthy human subjects. In this study, we will estimate the abundance of microglia across various brain regions and compare it with bibliographic *post mortem* quantifications using Iba-1 (Mittelbronn et al., 2001). By extending the versatility of our model, we aim to unlock immense potential for clinical translation. This will facilitate the testing of treatments and the discovery and validation of early disease biomarkers.



Objectives



Dendrites and Axons (Neurofil), Cell Nuclei (DAPI)

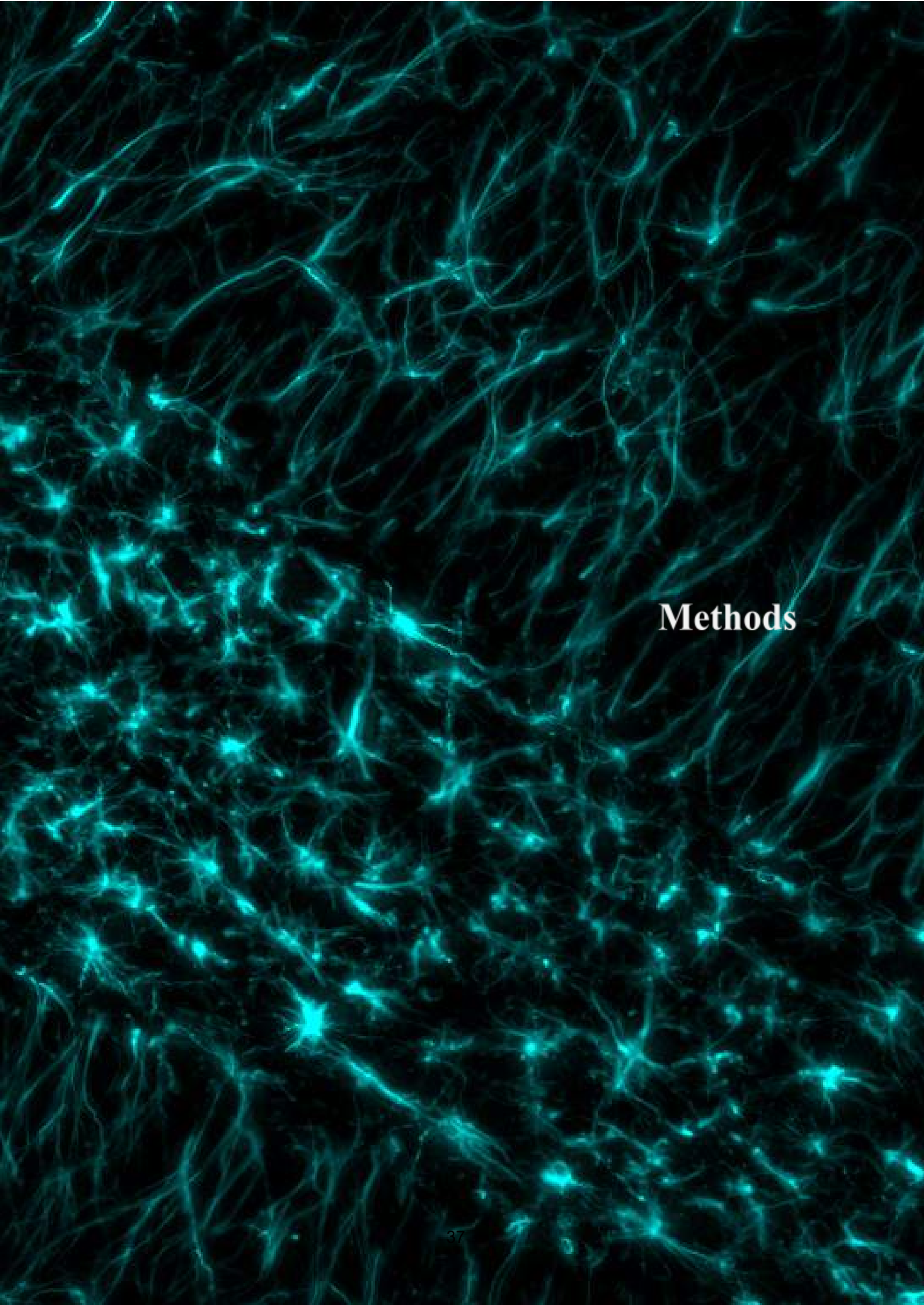
Author: Raquel García Hernández

III. Objectives

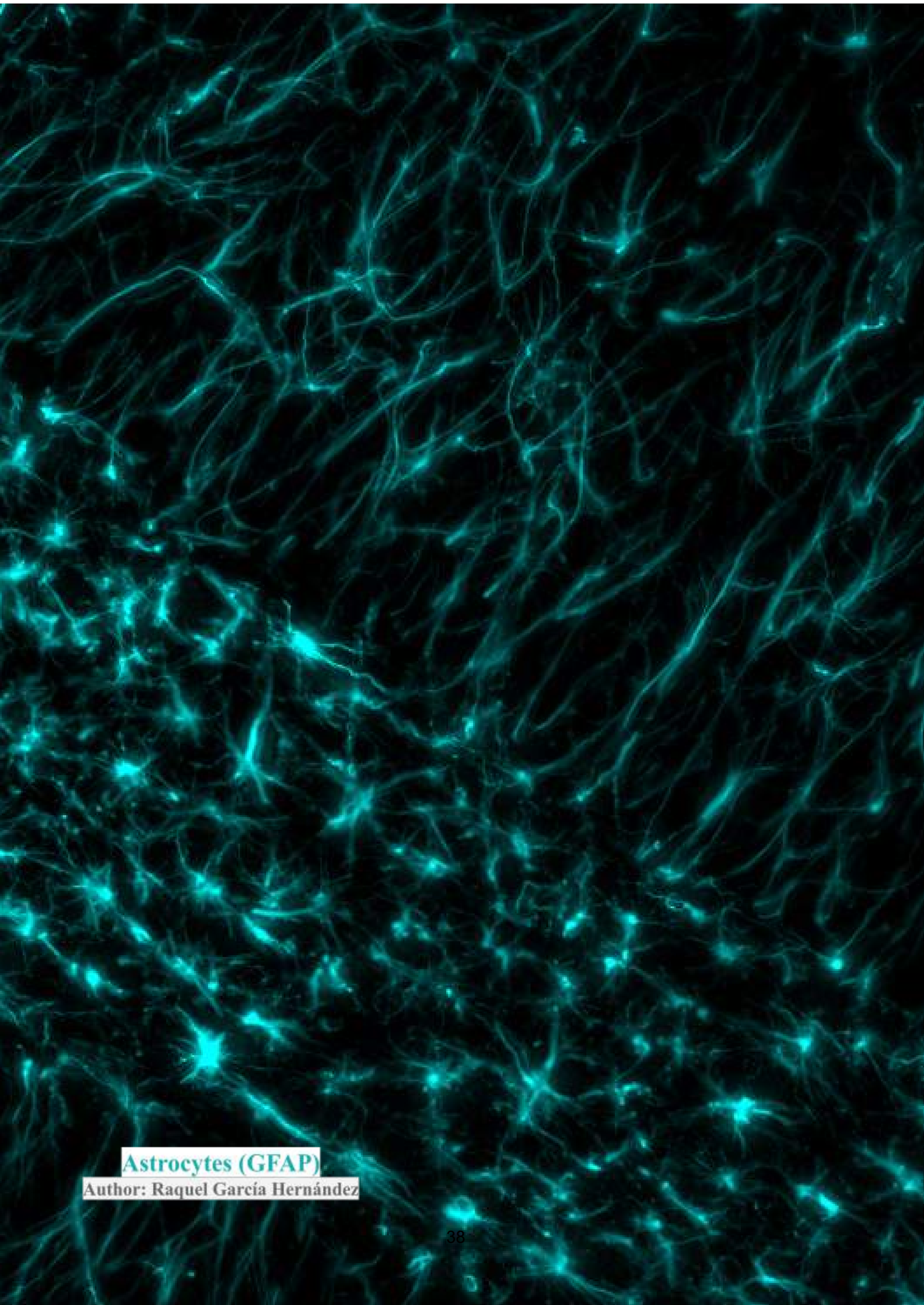
The primary aim of this research is to develop a dw-MRI model capable of imaging microglia and astrocytes *in vivo* and non-invasively, specifically designed to capture their distinct geometry and size. To validate the model, we will use animal models of neuroinflammation and *post mortem* histological quantification of these glial populations. Finally, we will test the model's translatability in a proof-of-concept study with human patients. We hypothesise that this model will accurately capture morphological changes in these cells, opening new avenues for both basic and clinical investigation.

The specific objectives of this study are:

1. To implement and validate experimental models of neuroinflammation that may allow us to differentiate between microglial and astroglial responses.
2. To evaluate the ability of dw-MRI to measure microglial and astrocyte changes *in vivo* and non-invasively.
3. To correlate *in vivo* dw-MRI measures and *post mortem* histological quantifications to validate the model.
4. To demonstrate the robustness of the dw-MRI model in detecting microglial and astrocyte responses in demyelination and neuronal loss scenarios.
5. To test the translatability of the framework in a proof of concept study with healthy human participants.



Methods



Astrocytes (GFAP)

Author: Raquel García Hernández

IV. Methods

4.1. Animal inflammation models: experimental design

Male Long-Evans rats, weighing between 250-300g, were employed for the current research experiments. All the experiments received ethical approval from the Instituto de Neurociencias (Alicante, Spain) and its Animal Care and Use Committee, in compliance with Spanish law 32/2007 and European regulations (EU directive 86/609, EU decree 2001-486, and EU recommendation 2007/526/EC). Rats were housed in groups of 3-4, with 12-hour/12-hour light/dark cycle, lights on at 8:00, at room temperature ($23 \pm 2^\circ\text{C}$) and food and water at *ad libitum*. The sample size was determined based on a power calculation conducted using the expected effect size, which was derived from mean diffusivity changes reported in rat grey matter in a previous study investigating inflammation (De Santis et al., 2020).

The experimental methodology for generating distinct inflammation models relied on intracerebral drug injections of different proinflammatory agents, following established protocols from the literature for each case. These injections were tailored to induce cell-specific and time-specific reactions, forming a pivotal aspect of the project.

The intracerebral injections were conducted stereotaxically, targeting the dorsal hippocampus across all drug models. Stereotaxic surgery adhered to standard procedures outlined in the literature (Geiger et al., 2008; Espinosa-Oliva et al., 2013) and protocols established by the laboratory (Caramés et al., 2020), ensuring precise and accurate injections. The specific coordinates for the injections at dorsal dentate gyrus of rats, relative to the *bregma-lambda* axis, were as follows: anterior-posterior -3.8mm, latero-medial 2mm, dorso-ventral 3mm. Details regarding drug volumes and concentrations are provided in subsequent paragraphs for each inflammation model.

The choice of the dorsal hippocampus was guided by three primary considerations. Firstly, this region is anatomically isolated from adjacent structures due to distinct axonal tracts and myelination patterns. As a result, drug injections in this area tend to remain localised, primarily diffusing along the dorso-ventral axis without impacting surrounding regions. This localised effect has been previously validated by the host laboratory through radioactive marking of injections (Rossato et al., 2018). This precise and confined injection enhances the accuracy of both imaging and analysis, minimising confusion with neighbouring areas and facilitating the detection of subtle changes. Secondly, the hippocampus exhibits bilateral symmetry (Amaral et al., 2007), providing a significant advantage: one hemisphere can be treated with the drug while the other serves as a control, injected with the same volume of saline. This allows each rat to serve as its own within-animal sham control. By leveraging this bilateral symmetry, we can effectively compare changes in the injected hemisphere with those in the contralateral control hemisphere, thereby enhancing the robustness and interpretability of our findings. Unless otherwise stated, the right hemisphere will be the

treated one in all rat models. Thirdly, there is a high density of microglia and astrocytes compared to other brain regions, such as the cerebellum, and it has great homogeneity in its distribution (Jinno et al., 2007).

Specifically, the different animal groups of neuroinflammation to target microglia, astrocytes neurons and myelin were established as follows, and can be schematically visualised at figure M.1 using the same nomenclature:

- Group 1: Microglia reaction

To induce microglial reaction, we injected intracerebrally 2µl of LPS from *Escherichia coli* (Sigma-Aldrich ref.L2880, Madrid, Spain) in the dorsal hippocampus, as described in Espinosa-Oliva et al. (2013), at a concentration of 2.5 µg/µl. In the contralateral hemisphere, the same amount of saline. LPS is a compound of the gram- bacteria cell wall (Herrera et al., 2000), and it has been shown to generate inflammation by releasing cytokines and nitric oxide, between others (Chao et al., 1992, Giulian 1993). This method preserves neuronal viability and morphology while triggering only microglial reaction within a short time frame of about 7-9 hours post injection (Jeong et al., 2010). This temporal dissociation allows for the investigation of reactive microglia independently of any concurrent astrogliosis.

For group 1, which focused solely on microglia reaction, we utilised 6 rats.

- Group 2: Microglia and astrocyte reaction

Astrocyte and microglia reaction was achieved with the same strategy as group 1, with an intracerebral injection of (LPS), however with a longer timing: 24h post injection. This timeframe generates both a microglia and astrocytes response (Jeong et al., 2010).

For group 2, which involved microglia and astrocyte reaction, we had a total of 11 rats, combining the 7 rats from this group 2 with the 4 rats from group 3.1 (sham-treated).

- Group 3: Isolated astrocyte reaction

To discern the distinct imaging characteristics of astrocyte and microglia reaction, we employed the same approach as in groups 1 and 2. However, in this case, rats were treated with the CSF1R (Colony-Stimulating Factor 1 Receptor) inhibitor PLX5622 (Plexxikon Inc.California, USA). This inhibitor is known for its ability to transiently deplete approximately 90% of microglia (Han et al., 2017), thereby facilitating the isolation of imaging characteristics specifically associated with astrocytic reaction.

The inhibitor was introduced in two parallel manners. Firstly, as a dietary supplement integrated into standard food at a concentration of 1200 ppm (Research Diets). Secondly, the inhibitor was administered via intraperitoneal injection at a dose of 50 mg/kg dissolved in the vehicle, with a dose volume of 10 ml/kg, administered daily for 7 consecutive days. On the last day, all rats underwent LPS intracerebral injection, and we

waited 24 hours for the consecutive steps, thus activating only astrocytes after microglia systematic depletion.

For group 3, focusing on isolated astrocyte reactions, we utilised a total of 7 rats.

- Group 3.1 = Group 2

We included a sham group for the CSF1R inhibitor treatment, which received control food and vehicle injections, totaling 4 animals. Since this group activates both microglia and astrocytes, akin to group 2, we combined the rats used in this batch with group 2.

Group 3.1, consisting of rats with microglia and astrocyte reaction, CSF1R sham-treated, comprised a total of 4 rats.

- Group 4: Microglia and astrocyte reaction returned to baseline

Group 4 also received intracerebral injection of LPS. However, in this case, we waited for at least 15 days before proceeding with subsequent procedures. This extended time frame was intended to allow both microglia and astrocytes to return to their control state (Jeong et al., 2010).

For group 4, where microglia and astrocyte reaction returned to baseline, we employed 5 rats.

- Group 5: Inflammation with neuronal death

To induce neuronal damage, we utilised a well-established model of intracerebral ibotenic acid administration (Drouin-Ouellet et al., 2011) (Cayman Chemical Company ref. 14584, Michigan, USA), for which we injected 1µl of the compound at 2.5 µg/µl in the dorsal hippocampus and wait 14 days. As before, the contralateral one was injected with the same amount of saline. This compound is derived from *Amanita* mushrooms and it is known for its action as an agonist of the NMDA (N-methyl-D-aspartate) glutamate receptor (Zinkand et al., 1992) and its effects inducing neuro excitotoxicity, accompanied by neuroinflammation in areas expressing these receptors, such as the dentate gyrus (Abe et al., 1992). Consequently, this model allowed us to demonstrate the versatility of our approach in studying both neurodegeneration with concomitant neuroinflammation, a known common phenomenon in neurodegenerative diseases as in Parkinson and Alzheimer disease (McGeer et al., 1993, Dickson et al., 1993, Stephenson et al., 2018, Mayne et al., 2020)

For group 5, focused on neuronal death, we utilised 6 rats.

- Group 5.1: Isolated neuronal death

In order to disentangle neurodegeneration from surrounding neuroinflammation and expand the specificity of the detection, we had an independent batch of animals injected as well with ibotenic acid but treated with the anti inflammatory drug

minocycline hydrochloride (Sigma-Aldrich ref.M9511, Madrid, Spain), a broad-spectrum tetracycline antibiotic with recognized effect reducing microglia and astrocyte reaction levels (Cheng et al., 2015), thus affecting only the neuronal cells compartment. Additionally, this would allow us to verify if dw-MRI can quantitatively follow neuronal death. The treatment regimen involved intraperitoneal injections administered over five consecutive days, commencing the day before ibotenic acid stereotaxic injection. The injections were administered at a concentration of 45 mg/kg.

For group 5.1, isolated neuronal death, we had 3 rats.

- Group 6: Demyelination

To induce a demyelination phenotype we employed a lysolecithin-based model through intracerebral injection (Woodruff & Franklin, 1999). Lysolecithin, known as a solubilizing agent, exhibits particular toxicity toward myelinated cells, disrupting the myelin sheath (Tiarhou and Herndon 1986, Ou et al., 2016).

Demyelination processes are key factors in various degenerative diseases and often present with surrounding neuroinflammation, such as in multiple sclerosis (Tallantyre et al., 2009; Karussis, 2014), neuromyelitis optica (Wingerchuk et al., 2015), and encephalomyelitis and related disorders (Young et al., 2010). Being able to not confuse a microglia or astrocyte reaction with demyelination is crucial for the correct development of our tool. To induce it in our model, we injected 1 μ l of L- α -lysolecithin from bovine brain (Sigma-Aldrich ref.L1381, Madrid, Spain) diluted to 1% in saline into the left hemisphere, with the contralateral hemisphere receiving an equal volume of saline. In this case, the waiting period ranged from 14 to 21 days, as indicated by Woodruff and Franklin (1999), which generates minimal effects on other cell units and with low variability within that time frame.

After various post-injection delays, the rats underwent MRI scanning followed by immediate perfusion for *post mortem* immunohistological analysis.

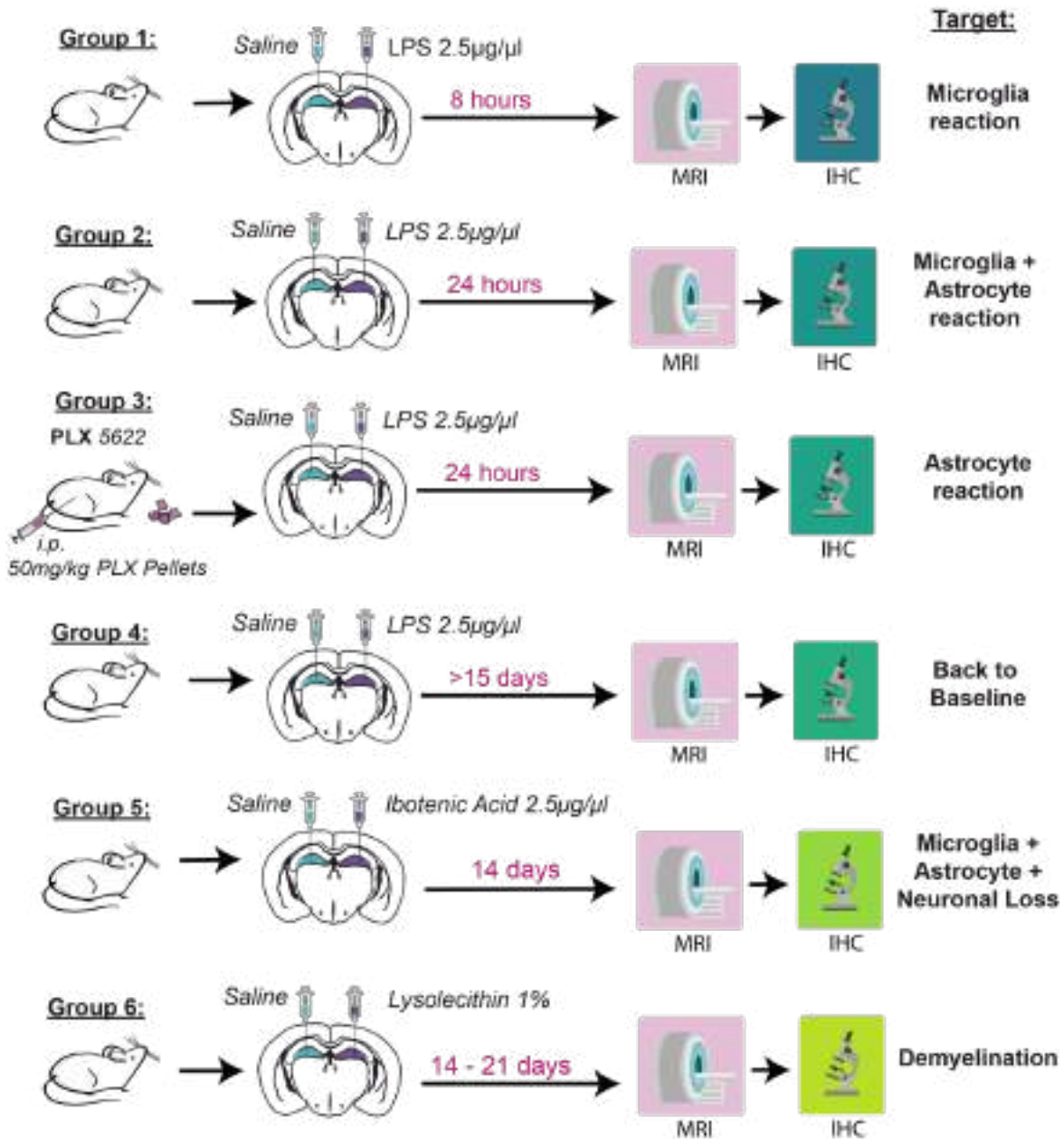


Figure. M1: Animal inflammation models. Experimental scheme showing bilateral stereotaxic injection of the different compounds. **A)** Group 1: LPS injection in the left hemisphere plus 8 hours of waiting time. **B)** Group 2: LPS injection in the left hemisphere plus 24 hours of waiting time. **C)** Group 3: Same as group 2 but treated with PLX5622. **D)** Group 4: LPS injection in the left hemisphere plus >15 days of waiting time. **E)** Group 5: Ibotenic acid injection in the left hemisphere plus 14 days of waiting time. Some of the animals (n=6) were treated with minocycline **F)** group 6: Lysolecithin injection in the left hemisphere plus 14-21 days of waiting time. In all cases, saline was injected in the left hemisphere.

4.2. Magnetic Resonance Imaging

4.2.1. Rats Acquisition

MRI experiments on rats were conducted using a 7-Tesla scanner (Bruker, BioSpect 70/30, Ettlingen, Germany) equipped with a receive-only phase array coil featuring an integrated combiner and preamplifier, in conjunction with an actively detuned transmit-only resonator. dw-MRI data was acquired using an Echo Planar Imaging diffusion sequence. We employed 30 uniformly distributed gradient directions, with b-values of 2000 and 4000 s/mm². Diffusion times were set at 15, 25, 40, and 60 ms, with four images obtained without diffusion weighting (b = 0, referred to as B0). The repetition time (TR) was set to 7000 ms, and the echo time (TE) was set to 25 ms. By utilising these combinations alongside higher b-values, our objective is to integrate diverse imaging contrast strategies, thus enhancing the segmentation in the analysis and obtaining information about more restricted compartments (Yovel and Assaf, 2007), allowing the generation of our dw-MRI multi-compartment model.

Regarding the ROIs (Regions of Interest), fourteen horizontal slices were positioned centred on the hippocampus, with a field of view (FOV) of 25 mm × 25 mm, matrix size of 110 × 110, in-plane resolution of 0.225 mm × 0.225 mm, and slice thickness of 0.6 mm. Additionally, three relaxometry sequences were acquired with the same geometry as the dw-MRI scan: a gradient echo sequence with TR = 1500 ms, 30 equally spaced echo times (TE) ranging from 3.3 to 83.4 ms, and 3 averages; a T1-weighted sequence with TR = 300 ms, TE = 12.6 ms, and 2 averages; and another T1-weighted sequence with TR = 3000 ms, TE = 7.7 ms, and 4 averages. Finally, a high-resolution anatomical scan covering the entire brain was obtained with TR = 8000 ms, TE = 14 ms, 4 averages, FOV = 25 mm × 25 mm, matrix size = 200 × 200, in-plane resolution of 0.125 mm × 0.125 mm, and 56 slices with a thickness of 0.5 mm.

The total scan time, including animal positioning, was approximately 2 hours.

4.2.2. Humans Acquisition

For the human experiments, we collaborated with the CUBRIC Institute at Cardiff University, leveraging their expertise in human neuroimaging. Their facility accommodated our study as they possess a machine compatible and with the necessary specifications to seamlessly transfer the MRI acquisition protocols developed in rats to human patients (Jones et al., 2018). Specifically, by employing gradient intensities comparable to those available in animal scanners, it allows to achieve longer diffusion times without extreme signal loss. The study received approval from the local Institutional Review Board at Cardiff University.

Six healthy subjects underwent scanning sessions 5 times each using a 3T Siemens Connectom scanner, resulting in a total of 30 acquisitions. dw-MRI data was obtained utilising an Echo Planar Imaging diffusion sequence with the following parameters: TE = 80 ms; TR = 3.9 s; diffusion times of 17.3, 30, 42, and 55 ms; b-values of 2000 and 4000 s/mm²,

with 30 and 60 uniformly oriented gradient directions, respectively. Each diffusion time included six B0 images, yielding a total of 384 images. Additional acquisition parameters were as follows: flip angle of 90°; slice thickness of 2 mm; in-plane voxel size of 2 mm; FOV of 220 mm × 220 mm; and matrix size of 110 × 110.

The total scan time per subject was approximately 40 minutes.

4.2.3. Analysis and statistics

Initial observations on rat MRI data confirmed the location of the injection and the symmetrical procedures between both hemispheres. Next, ROIs were manually outlined within the dentate gyrus of the dorsal hippocampus. The injection trail aided in identifying the central slice of the injection, from which ROIs were delineated two slices before and up to two slices after the injection, spanning a total length of 3 mm. Subsequent visual inspection confirmed that the injection scar was minimal and limited to the central slice, while excluding heavily damaged brains or those with enlarged ventricles, resulting in the exclusion of one animal from each of groups 1, 2, 5.1, and 6 (animals already discounted from the expressed sample size in section 4.1).

The raw dw-MRI data underwent nonlinear registration to the T2-weighted scan for correction of Echo-planar Imaging distortions. Subsequently, motion and eddy current distortions were corrected using affine registration.

4.2.3.1. Diffusion Weighted Multi-compartment model (dw-MRI model)

The processed data were then inputted into a custom MATLAB pipeline (R2018a, the MathWorks), which implemented our novel dw-MRI multi-compartment model. This model is inspired by the AxCaliber model for white matter (Assaf et al., 2008), but we have tailored it to grey matter morphology, comprising more cell compartments than white matter (Figure M.2.A). Importantly, it takes into account the differences in geometry and size of each cell unit to obtain distinct multicellular and specific water diffusion fingerprints, with the final objective of differentiating them.

Consequently, the signal is expressed by a complex mathematical expression encompassing these various compartments:

$$S = f_{IC} \times S_{IC}(\kappa) + f_{SS} \times S_{SS}(R_{SS}) + f_{LS} \times S_{LS}(R_{LS}) + f_{EC} \times S_{EC} + (1 - f_T) \times S_{FW}$$

In the provided model, the specific parameters for the diffusion signal within different tissue compartments are as follows, and can be schematically visualised figure M2:

- f_{IC} : Fraction of water undergoing restricted diffusion in cylinders, referred to as the stick fraction, and representing microglia's ramifications and myelin.

- S_{IC} : Signal in Watson-dispersed cylinders, representing a main orientation dispersion, critical for capturing the slight degree of anisotropy present in grey matter due to axons.
- K : Watson dispersion parameter, referred to as the stick dispersion parameter. This parameter accounts for the orientation of the microglia cell ramifications.
- f_{SS} : Fractions of water undergoing restricted diffusion in small spherical (ss) compartments, representing microglia cell bodies.
- f_{LS} : Fractions of water undergoing restricted diffusion in large spherical (Ls) compartments, representing whole astrocytes as a sphere. This is due to the fact that, despite astrocytes labelled with GFAP appear similar to microglia in their ramified structure, they are covered by a membrane of actin (Haseleu et al., 2013), which makes them resemble a sphere more closely than a sphere-and-sticks model used for intracellular water diffusion.
- S_{SS} : Signals of water undergoing restricted diffusion in small spheres, accounting for microglia.
- S_{LS} : Signals of water undergoing restricted diffusion in large spheres, accounting for astrocytes.
- f_{EC} : Fraction of water hindered in the extracellular space, referring to neurons.
- S_{IC} : Signal in the extracellular space modelled as a tensor with radial symmetry.
- $1 - f_T$: Fraction of free water.
- S_{FW} : Free water signal.

The fitting parameters for this model are f_{IC} , f_{SS} , f_{LS} , K , R_{SS} , R_{LS} , the extracellular tensor diffusivity, and f_T . Water diffusivity inside the restriction is assumed to be 1×10^{-9} mm²/s as indicated by Zhang et al., (2012), and two different sphere radii are initialised to ensure convergence of microglia and astrocytes (S_{SS} , S_{LS}). The fitting algorithm utilised an average speed of 5.9 seconds per voxel, a common speed for MATLAB scripts used for these types of analyses.

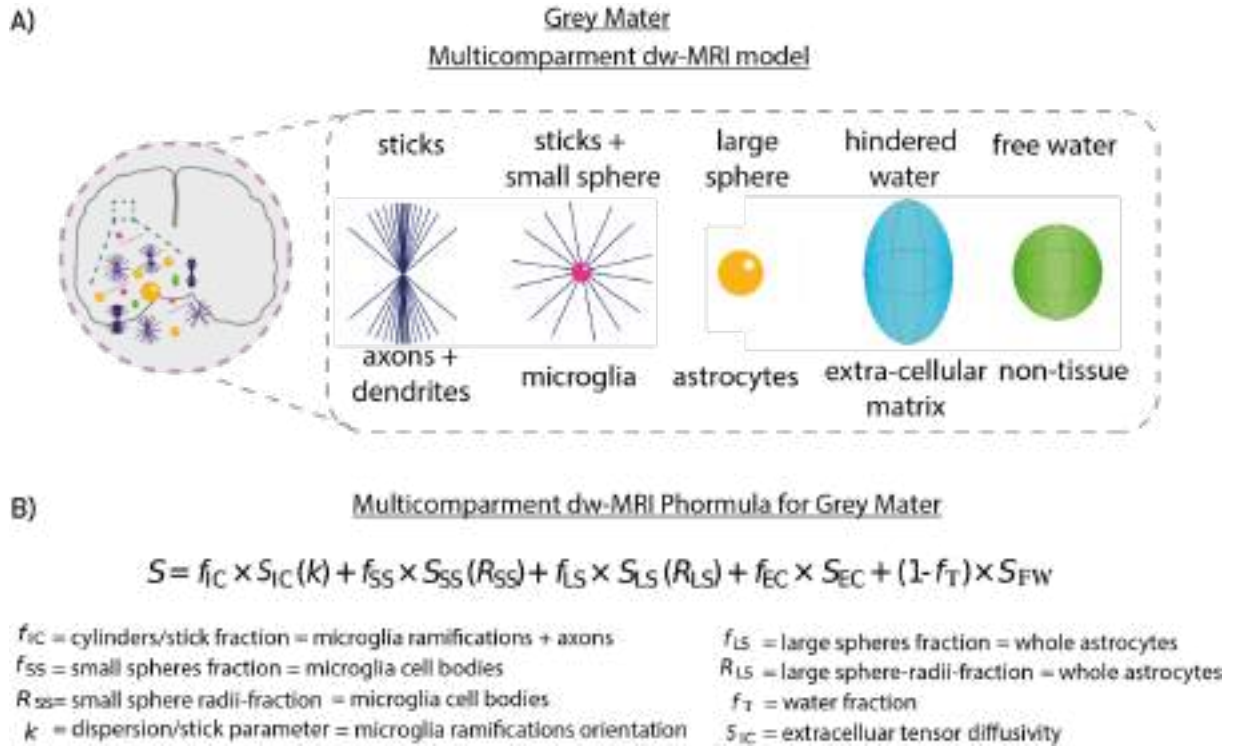


Figure. M2: Multi-compartment tissue model. **A)** Grey matter visual representation constituting the parenchyma in our model: microglia, astrocytes, neurons, extracellular space: sticks (axons + dendrites), sticks and small spheres (microglia), large spheres (astrocytes), hindered water (extracellular matrix), and free water (non-tissue, accounting for neurons). **B)** Multi-compartment tissue model formula, explaining specifically the fitting parameters and what they represent in the biological tissue.

4.2.3.2. Conventional MRI data

Finally, we also acquired conventional MRI sequences in rats experiments to further compare our new dw-MRI model tissue model with the current standard. To do so, we used a low b-value to fit the conventional tensor model and generate MD maps. We acquired T1- and T2-weighted maps to compute the T1/T2 ratio. Additionally, T2* maps were also obtained, derived from T2*-weighted images by fitting an exponential decay. Finally, high-resolution anatomical scans were registered nonlinearly to a rat brain template using an advanced normalisation approach.

4.2.3.3. Human patient data

In relation to the processing of human patient data, the workflow was very similar to the rat one, increasing the translatability of the research: Motion, eddy current, and EPI distortions were corrected using FSL TOPUP and EDDY tools (FSL from FMRIB, Oxford, United Kingdom). Correction for gradient nonlinearities, signal drift, and Gibbs ringing artefacts was also carried out. Later on, all diffusion data was registered to a skull-stripped structural T1-weighted image using EPIREG. B0 scans were then nonlinearly registered to a high-resolution human brain template, and the inverse transformation was applied to align the

Desikan grey matter parcellation to the single subject space (Desikan et al., 2006). Subsequently, all masks were eroded by one voxel using the FSL command `fslmaths` manually to reduce potential contamination from adjacent white matter.

Additionally, brain parcellation into grey and white matter was performed for each subject using the B0 scan, retaining only voxels with minimal white matter contamination (<5%) for analysis. Intra- and intersubject coefficients of variation were computed for each MRI measure, and the Desikan parcellation (Desikan et al., 2006) was utilised to determine the mean and SD of the stick fraction and dispersion parameter in eight ROIs (hippocampus, cerebellum, substantia nigra, basal ganglia, thalamus, motor, frontal, and occipital cortices). These metrics were then correlated with *pos mortem* histological staining for microglia, as described in (Mittelbronn et al., 2001).

4.3. Histological Analysis of Inflammation

4.3.1. Tissue processing and immunohistochemistry (IHC)

Immediately after the MRI scanning protocols, rats were euthanized by administering a lethal dose of sodium pentobarbital (46 mg/kg) via intraperitoneal injection (Dolethal, E.V.S.A. laboratories, Madrid, Spain). Following euthanasia, rats underwent intracardiac perfusion with 100 ml of 0.9% warm PBS (Phosphate Buffered Saline) followed by 100 ml of ice-cold 4% PFA (Paraformaldehyde) (BDH, Prolabo, VWR International, Lovaina, Belgium). The brains were promptly extracted from the skull and fixed in 4% PFA for 1 hour at room temperature while gently shaking. Subsequently, the brains were embedded in 3% agarose/PBS (Sigma-Aldrich ref.x, Madrid, Spain) and sliced into 50µm thick serial coronal sections using a vibratome (VT 1000S, Leica, Wetzlar, Germany).

The coronal sections were then rinsed and permeabilized three times in 1× PBS with Triton X-100 at 0.5% (Sigma-Aldrich ref.X100, Madrid, Spain) for 10 minutes each. Following permeabilization, the sections were on blocking solution containing 4% bovine serum albumin (Sigma-Aldrich ref.A9418, Madrid, Spain) and 2% goat serum donor herd (Sigma-Aldrich ref.G6767, Madrid, Spain) in 1xPBS with Triton X-100 at 0.5% for 2 hours at room temperature. Later on, the slices were incubated overnight at 4°C with primary antibodies against our different cell compartments in 1xPBS with Triton X-100 at 0.5%. For microglia; Iba-1 (1:1000; Wako Chemicals ref.019-19741, Osaka, Japan); for astrocytes GFAP (1:1000; Sigma-Aldrich ref.G3893, Madrid, Spain); for myelin basic protein (1:250; Merck Millipore ref.MAB384, Massachusetts, USA); for dendrites and axon neurofilament 160Kd medium (1:250; Abcam ref.ab134458, Cambridge, United Kingdom); for neuron population NeuN (1:250; Merck Millipore ref.MAB377, Madrid, Spain)

After primary antibody incubation, the sections were incubated with specific secondary antibodies conjugated to fluorescent probes, each at 1:500 (Thermo Fisher Scientific, Waltham, USA) for 2 hours at room temperature in 1xPBS with Triton X-100 at 0.5%.

Subsequently, the sections were treated with 4',6-Diamidino-2'-phenylindole dihydrochloride (DAPI) at 15 mM (Sigma-Aldrich ref.D9542, Madrid, Spain) for 15 minutes at room temperature in PBS. Finally, the sections were mounted on slides and covered with a custom-made anti-fading medium using a mixture solution of 1:10 propyl-gallate:Mowiol (Sigma-Aldrich ref.P3130, Madrid, Spain; Merck Millipore ref. 475904, Massachusetts, USA), crafted to minimise autofluorescence and prolong the longevity of fluorophores.

For myelin basic protein, an additional step was needed: antigen retrieval for protein unmasking as myelin sheets are tightly joined. It was performed in 1% citrate buffer on PBS (Sigma-Aldrich ref.C9999, Madrid, Spain) and 0.05% Tween-20 (Sigma-Aldrich ref.P7949, Madrid, Spain) at pH=6, warmed to 80°C in shaking for 15 minutes. Then, the sections followed the aforementioned steps.

4.3.2. Imaging and data extraction

The tissue sections underwent examination using a computer-assisted morphometry system comprising a Leica DM4000 fluorescence microscope (Leica, Wetzlar, Germany) equipped with a QICAM Qimaging camera 22577 (Biocompare, San Francisco, USA) and NeuroLucida morphometric software (MBF, Biosciences, VT, USA). Microglia was visualised and reconstructed using a Leica HC PLC APO objective 20×/0.5 (Figure. M.3.A), while astrocytes were visualised with a Leica HC PLC APO objective 40×/0.75 (Figure. M.4.A). A total of 820 cells (410 microglia, 410 astrocytes) from five cells per dentate gyrus per hemisphere were randomly selected for analysis. Only cells exhibiting intact and clear processes were included. Cells were meticulously traced manually throughout the entire section thickness in an “online” method: manually adjusting the micrometric focus of the microscope as needed to visualise them totally. Trace information was saved as 2D diagrams plus the three-dimensional model reconstructions (Figures. M3.A and M4.A).

The metric analysis of the complete morphology was extracted using NeuroLucida Explorer software (MBF, Biosciences, VT, USA). From all the possible parameters, we focused our attention on the ones with higher similarity with the dw-MRI model and thus could explain better the water diffusion within these cell compartments embedded in the brain parenchyma. As shown in figure M.3.B, for microglia we extracted cell body volume quantifying the volume occupied by the cell body of microglia (as a small sphere for dw-MCM), process density (stick fraction) and process dispersion (stick dispersion). To obtain process dispersion, polar plots were constructed and analysed, where lower values indicate a more uniform distribution of fibres around the cell body.

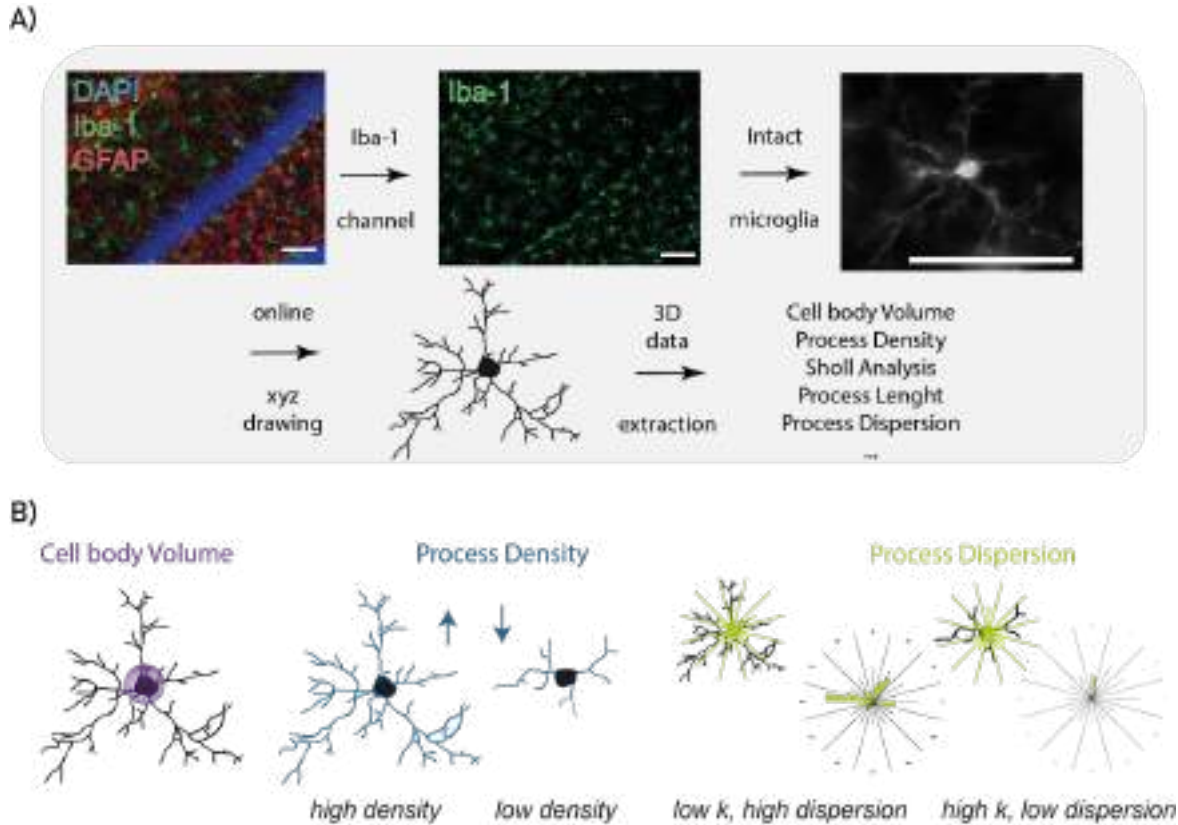


Figure. M3: Microglia analysis workflow. A) Microglia reconstruction pipeline for a representative histological section showing microglia (labelled in green with Iba-1), astrocytes (labelled in red with GFAP), and cell nuclei (stained in blue with DAPI). 3D reconstruction of microglial cells is performed under magnification (20x). B) Main parameters extracted from microglia's reconstruction: cell body volume, process density and process dispersion. Scale bars = 100 μm .

In the case of the astrocyte population, we performed 3D convex analysis to estimate their volume (Figure M.4.B) as a big sphere, just as modelled in the dw-MRI model. This is because our antibody for labelling astrocytes is GFAP, which has been shown to underrepresent the morphology of astrocytes. As explained, all the ramifications of GFAP-positive astrocytes are covered by a membrane of actin, as demonstrated in the microphotograph from Haseleu et al., 2013, included in Figure M.4.B (GFAP depicted in red, actin membrane in green). To address this challenge and accurately quantify astrocytic volume we employed convex analysis. Specifically, this method entails estimating the volume from lines connecting all the extreme points of the astrocytes' ramifications, forming a polygon (Rodieck 1973, SheikhBahaei et al., 2018). Thus, detailed reconstruction of each GFAP-positive process in 3D was still necessary to execute this analysis accurately (Figure M.4.A).

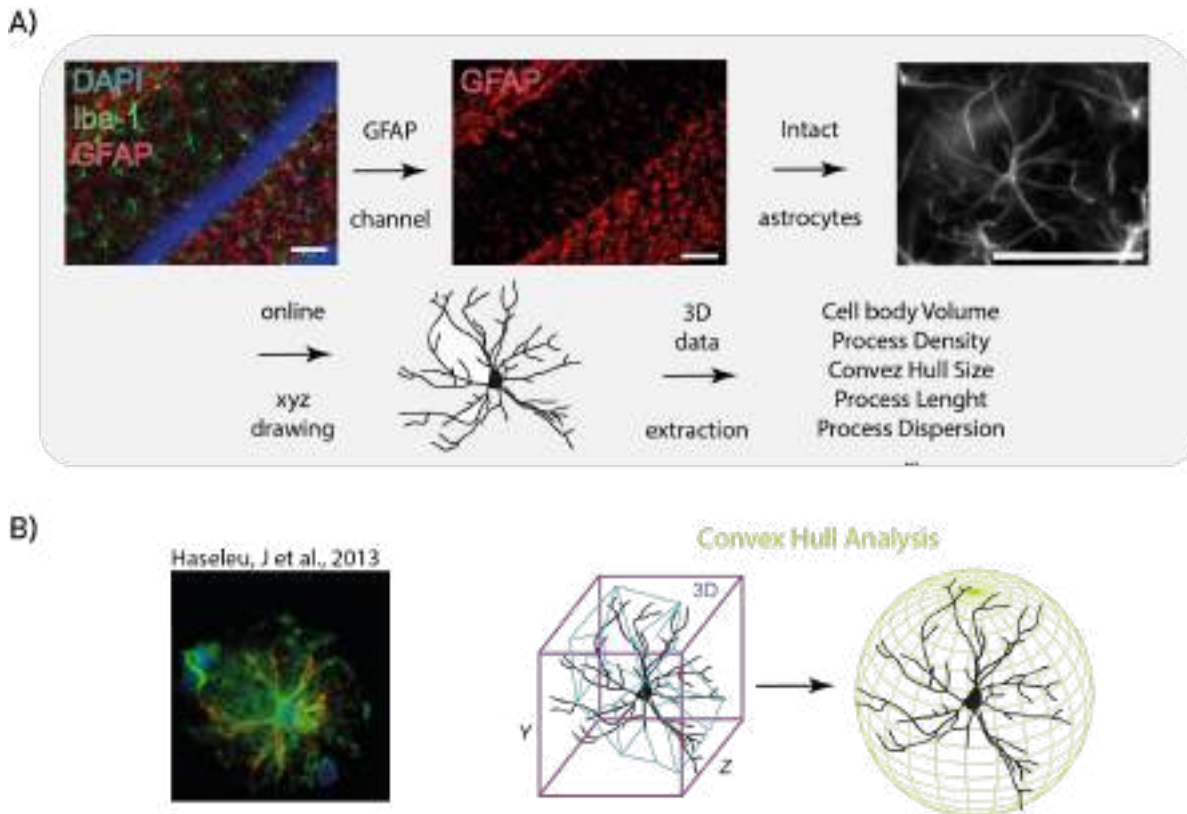


Figure. M4: Astrocyte analysis workflow. **A)** Astrocyte reconstruction pipeline for a representative histological section showing microglia (labelled in green with Iba-1), astrocytes (labelled in red with GFAP), and cell nuclei (stained in blue with DAPI). 3D reconstruction of astrocyte cells is performed under magnification (40x). **B)** Left: microphotography from Haseleu et al., (2013) highlights the challenge with using GFAP labelling for astrocyte morphology (GFAP for astrocytes in red, Phalloidin for actin membrane in green, DAPI for cell nuclei in blue), as it underrepresents its volume. Right: Main parameter extracted from astrocyte's reconstruction to overcome this limitation: convex hull. Scale bars = 100 μm .

Microglia and astrocyte cell density analysis was conducted as follows: Images were captured in 12-bit greyscale using the specified microscope, and the dentate gyrus was manually delineated following the Franklin and Paxinos rat brain atlas (Franklin and Paxinos, 2019). Quantification was semi-automated using Icy software and the spot detector tool (Icy Software, Paris, France). The threshold for detecting positive nuclei was established for each condition based on the average nuclei size (converted to pixel size) and a signal-to-noise ratio greater than 23% of the cell body intensity value in relation to the background level, following the Rayleigh criterion for resolution and the ability to distinguish two closely spaced points (Rayleigh, 1896). The signal-to-noise ratio was computed by placing a line that intersects both the cell body and the background, from which the fluorescence intensity was extracted along the entire profile. This process was repeated for several microglia and astrocytes to assess the overall staining quality for each batch of histology. Data were collected from both control and treated hemispheres in at least five slices per rat. The analysis pipeline can be visualised in Figure M.5.

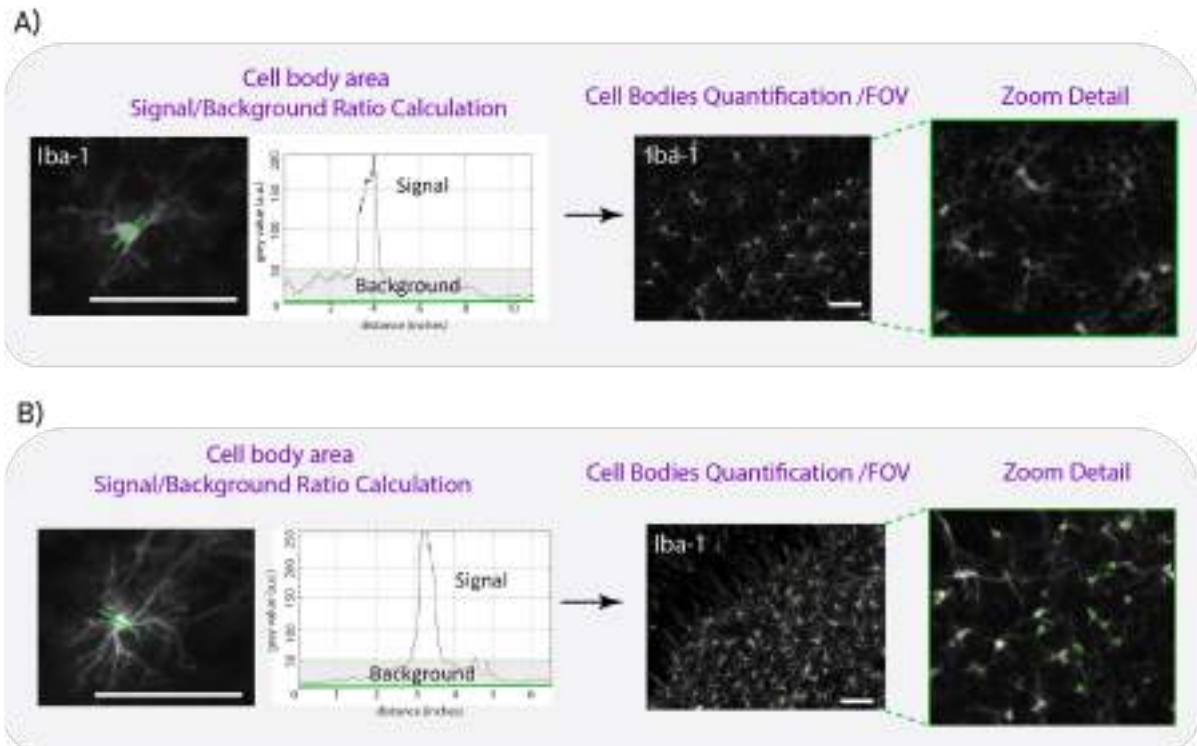


Figure. M5: Density analysis pipeline **A)** Example for microglia density quantification: a green line is placed intersecting both the cell body and the background, from which the fluorescence intensity is extracted along the entire profile allowing calculation of the signal over background ratio. Subsequently, the software can accurately identify all microglia in the microphotographs. **B)** Same for astrocytes. Scale bars = 100 μm .

For analysing the state of myelin sheets, ramifications of neurons (including both axons and dendrites), and neuronal loss, we quantified the labelling intensity for each corresponding marker: MBP, Neurofilament, and NeuN, respectively (Figure M.6). To achieve this, we acquired images in 12-bit greyscale. The analysis was performed using Icy software. In this case, we placed two ROIs measuring $100 \mu\text{m}^2$ in the dentate gyrus and used the ROIs-statistics tool to obtain the intensity value of each ROI. For MBP and neurofilament analysis, the ROIs were positioned on the hilus, as previously described in the literature (Long et al., 2021) (Figure M6.A-B). For NeuN analysis, the ROIs were placed in the granule cell layer, where neuronal cell bodies are predominantly located (Amaral et al., 2007) (Figure M.6.C). The data was obtained from both hemispheres and in at least five slices per animal.

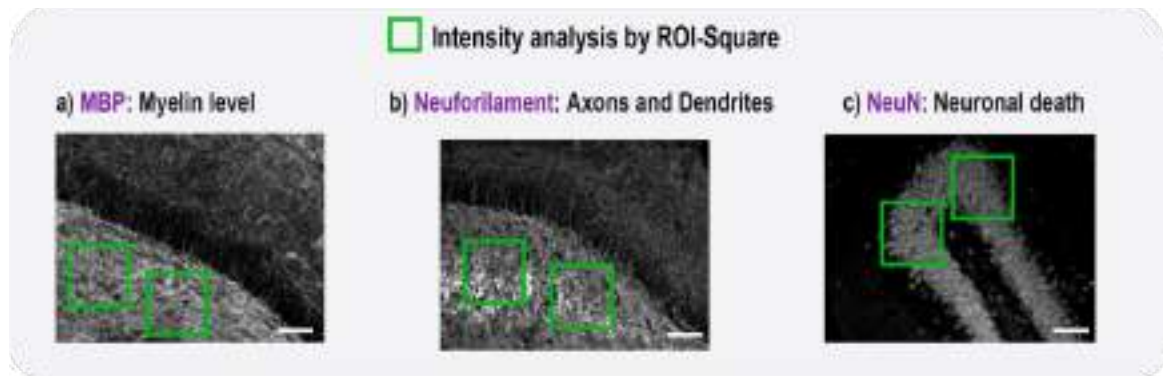


Figure. M6: Intensity analysis pipeline. Green squares represent the $100\mu\text{m}^2$ ROIs used for the intensity analysis. **A)** Example for MBP analysis, placing the ROIs in the hilus layer. **B)** Similar for neurofilament. **C)** Same approach for NeuN analysis, with ROIs positioned in the granule cell layer. Scale bars = $100\ \mu\text{m}$.

Finally, in table 1, we present a summary of the correspondences between the measurements obtained from the dw-MRI model and the measurements obtained from the histological analysis.

Table. M.1: Table summary comparing dw-MRI model measurements and histological measurements.

<i>MRI/Histo comparison</i>	Microglia	Astrocytes	Myelin	Neurons cell bodies
dw-MRI model measurement	Small Spheres + Stick fraction + Stick dispersion	Big Spheres	Stick fraction	Tissue Fraction
Histological markers	IBA-1	GFAP	MBP	NeuN and Neurofilament
Histological measurement	Ramifications + dispersion + cell body volume	Volume as a sphere	Myelin density	Neuronal death quantification

4.4. Statistics and graphical representation

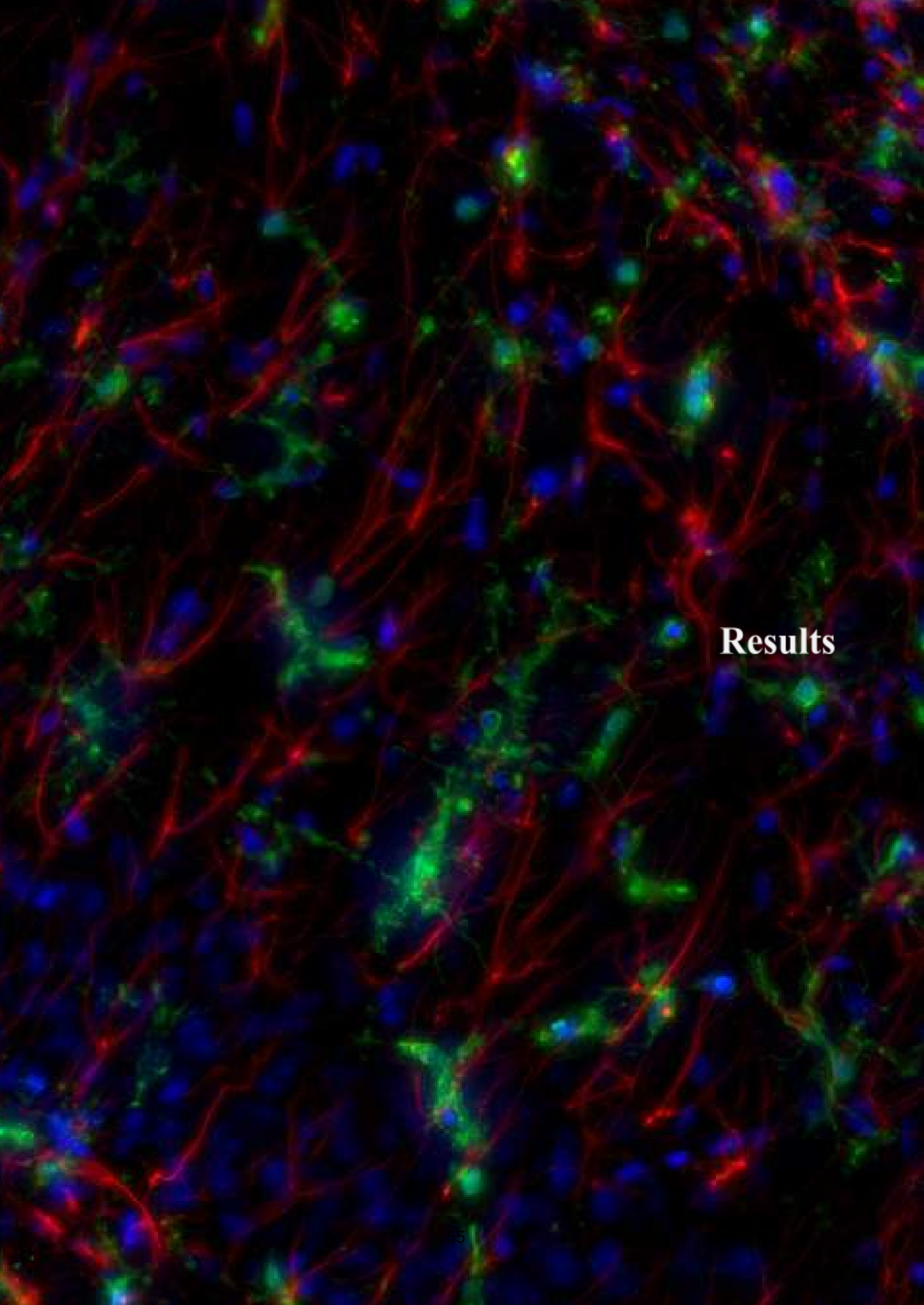
For statistical analysis and representation of the main results, we utilised Rstudio (RStudio 2015 Inc., Boston, MA) and GraphPad Prism 7 software (GraphPad Software Inc., La Jolla, CA, USA). Following the assessment of data normality distribution, we conducted paired t-tests between the control and injected hemispheres for each time point for both dw-MRI and histological results. For linear regressions, we employed Pearson correlation, and significance

was determined using Fisher’s (1925) test. For conventional MRI data, repeated-measures analysis of variance (ANOVA) was employed to assess significant effects of the injection and group, followed by post hoc t-tests to compare injected versus control hemisphere, with corrections for multiple comparisons.

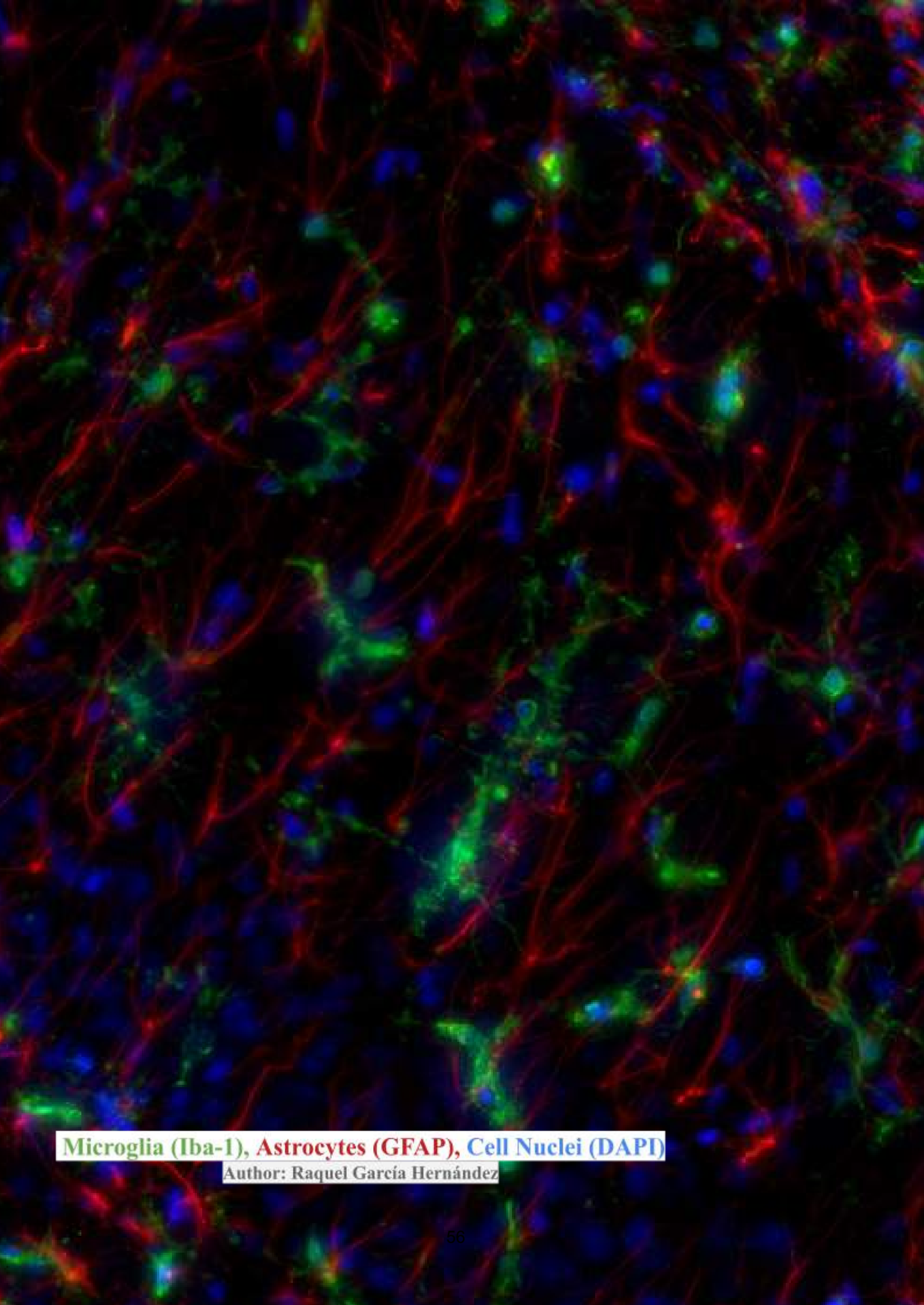
For representation, we focused on changes rather than absolute magnitudes. Consequently, all data presented in the following results section (both imaging and histology) are calculated as ratios of change, as indicated by the following formula:

$$change = \frac{treated - control}{control}$$

Each animal in our study serves as its own control, with one hemisphere treated and the other serving as the control. This provides the opportunity to detect relative changes within a controlled setting and offers several benefits. First, it adheres to the “reduction” principle of the 3Rs rule in animal research (replacement, reduction, and refinement). By utilising each animal as its own control, we have significantly minimised the number of animals required for this research. Secondly, it enables us to effectively account for variability between animals, thereby mitigating discrepancies in cellular states and across subjects. Thirdly, it facilitates the transferability of the model to other brain regions, compensating for variability between areas by targeting specific compartments for both microglia and astrocytes (Olah et al., 2011, Bayraktar et al., 2014, Bernardinelli et al., 2014, Khak and Sofroniew, 2015, Escartin et al., 2021). This versatility allows for the detection of changes in specific populations and enables comparison with control areas within the same region. Lastly, given the similarity between inflammatory responses in humans and rats and the comparable size of the cells (Andriezen et al., 1983, Sofroniew et al., 2014, Savage et al., 2019, Paolicelli et al., 2022), this approach holds promise for fast and direct translatability to human patients. This potential for clinical application enhances its future utility as an imaging tool in hospitals, a capability further supported by our testing within this research.



Results



Microglia (Iba-1), Astrocytes (GFAP), Cell Nuclei (DAPI)

Author: Raquel García Hernández

V. Results

5.1. Characterising glia reaction with histology and MRI

While various attempts have been made to quantify microglia density using dw-MRI (Yi et al., 2019; Taquet et al., 2019), there are currently no tools capable of specifically quantifying microglial or astrocytic reactions *in vivo* and non-invasively. In this section, we elaborate on our results obtained from the LPS intracerebral injection model, focusing on glial population dynamics. This model, which induces an early microglial reaction followed by a late astrocytic reaction (Jeong et al., 2019), enables us to distinguish and examine their separate contributions to both dw-MRI and histological signals (Figure R.1.A).

5.1.1. Histological glial response to LPS immunological challenge

Our initial approach aimed to effectively demonstrate the glia dynamics as shown in the original publication of the LPS model (Jeong et al., 2019) while simultaneously validating the histological procedures outlined in the methods section. Firstly, we examined the staining of Iba-1 and GFAP for microglia and astrocytes, respectively, at different reaction states for groups 1, 2, and 4 from the animal models of neuroinflammation explained in methods. Secondly, we sought to validate the initial choice of histological measures to correspond with the dw-MRI model.

As depicted in Figure R.1.B, upon initial observation, it is evident that in the control group, microglia exhibit a uniform distribution along the layers of the dentate gyrus, consistent with previously published observations (Jinno et al., 2007). Conversely, astrocytes demonstrate a higher density of cell bodies in the molecular layer of the dentate gyrus, with their processes extending throughout the granular layer and hilus. Based on these distributions, we selected the hilar region for quantitative measures and comparisons across models and time points.

Focusing specifically on the first time point, 8 hours post the intracerebral injection of LPS (Figure R.1.B), it is apparent that microglia has been significantly affected; there is a noticeable loss of processes throughout most of the dentate gyrus compared to the saline-injected hemisphere. Conversely, no visual differences were observed in astrocytes at this time point. At 24 hours post-injection (Figure R.1.B), there is a further increase in the microglial ramification phenotype, accompanied by an apparent enlargement of their cell body size. Regarding astrocytes, an expansion of their volume is indeed observed. Lastly, it was observed that the hippocampus returns to its normal state after 15 days from the injection, both at the microglial and astrocytic levels (Figure R.1.B). Importantly, in both Iba-1 and GFAP staining, we observed high-quality labelling, even of the most distal and thin processes, consistent across all conditions. These results, in summary, demonstrate the effectiveness of characterising microglia and astrocyte reactions with Iba-1 and GFAP.

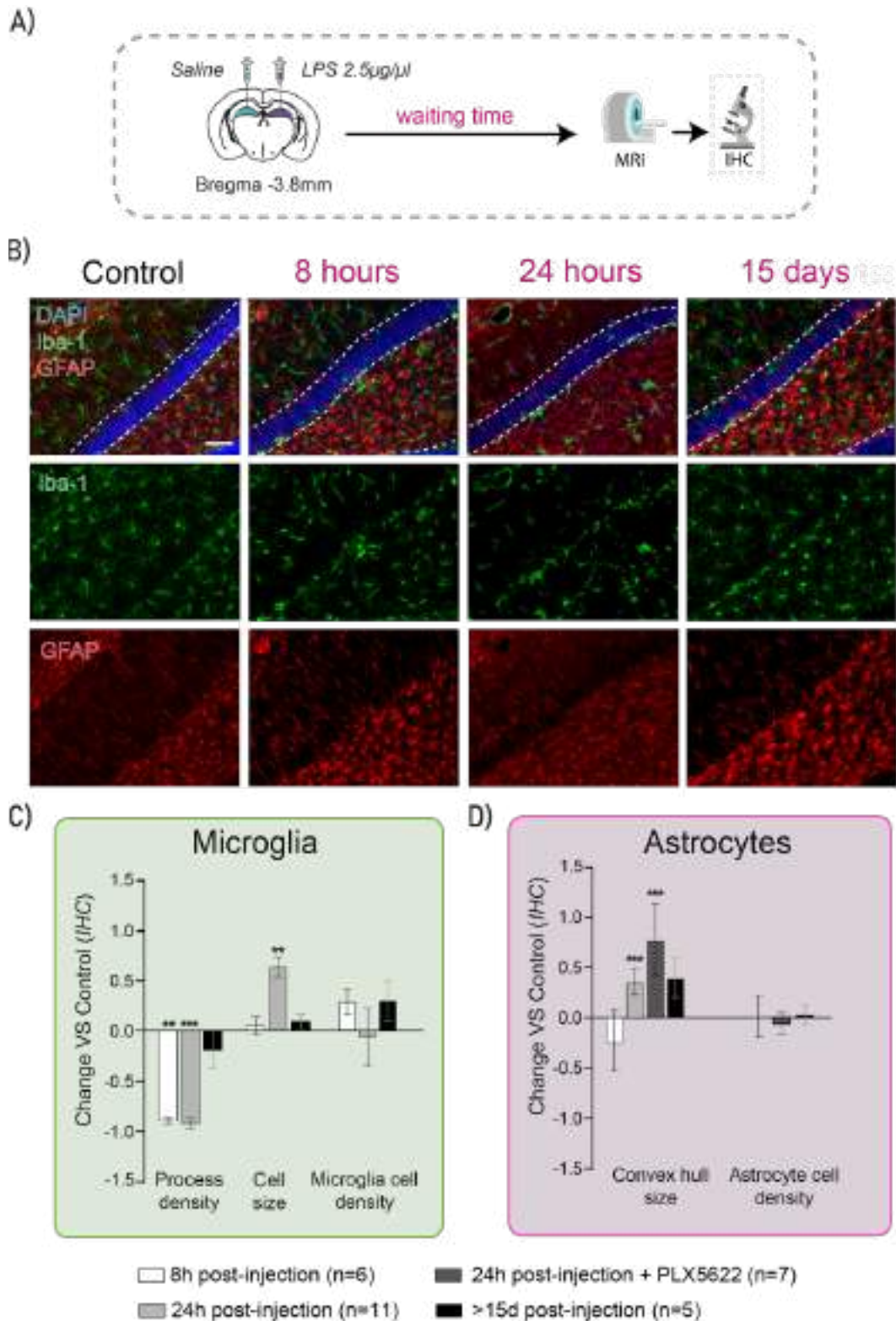


Figure R.1: Microglia and astrocytes main results. **A)** Experimental Schema of LPS experiments. **B)** Representative microphotographs of the dentate gyrus showing microglia (green), astrocytes (red) and their co-localization with cell nuclei (merge) for the control group and 8h, 24h and 15 days post LPS injection. Dashed line surrounds the granular layer of the dentate gyrus. **C)** Histological results for microglia, expressed as change vs control for process density, cell size and microglia cell density. **D)** Same for astrocytes. Asterisks represent significant paired t-test difference between injected and control (** $p < 0.01$ and *** $p < 0.001$). Error bars represent SD. Scale bar = 100 μm .

Quantitatively, we assessed microglia and astrocyte reactions as described in the methods. For microglia (Figure R.1.C), we focused on process density, cell size, and their cell density. As expected from the observations, a rapid microglial reaction was detected, and a paired t-test comparison with the control hemisphere revealed the significance of these results and the low variance between subjects. By 24 hours post-LPS, this effect was maintained, with an additional increase in microglial cell body volume. Additionally, we did not find differences in microglia cell density at any time point.

Regarding astrocytes (Figure R.1.D), there was not a consistent change in convex hull size at 8 hours post-injection, nor in astrocyte cell density, validating the expected solely microgliosis at this time point (Jeong et al., 2019). At 24 hours post-injection, we found the predicted reaction in the astrocyte population: there was a substantial increase in convex hull size at the histological level for all subjects in the study. Finally, after 15 days of recovery, astrocytes returned toward baseline, albeit with high variability between subjects. In relation to astrocyte cell density, we did not find differences for 24 hours or 15 days post-injection either.

These results effectively demonstrate that the model of Jeong et al. (2019) works as expected in our hands, resulting in early microgliosis with no concomitant astrogliosis at 8 hours post-injection, microglia and astrocyte reaction at 24 hours, and a return to baseline at 15 days. These findings are crucial as they pave the way for the next step in our research: developing the specific dw-MRI model capable of mirroring these changes.

5.1.2. Microglia reaction characterised using Iba-1 staining and MRI

After validating the animal model of inflammation, we proceeded to validate our dw-MRI model, designed to capture the microglia population as a model of small spheres and sticks with a Watson dispersion. To achieve this, we calculated the stick fraction to infer microglia ramification, small sphere radius for cell size, and additionally, the stick dispersion to understand how the ramifications are distributed around the cell body of microglia.

The results are presented in Figure R.2, where we display the dw-MRI model outcomes (Figure R.2.B) alongside the already shown microglia histological results (Figure R.2.B) for a comprehensive comparison, but now adding the process dispersion values of microglia ramifications quantified in histology.

As depicted in the figure, a significant reduction in stick dispersion was observed at both 8h and 24h post-injection, as evidenced in the histological micrometric results, indicating that the stick fraction variable effectively mirrors microglial processes. Furthermore, regarding the process dispersion of the current ramifications, we found no significant differences for either the dw-MRI model or the histological results at 8h post-injection. However, at 24h, an

increase in the dispersion K value was observed, indicating less dispersion of the current ramifications of microglia. This outcome is attributed to the topological distribution of these ramifications around the microglia cell body, as the few that remain are found to be at the poles of the cell.

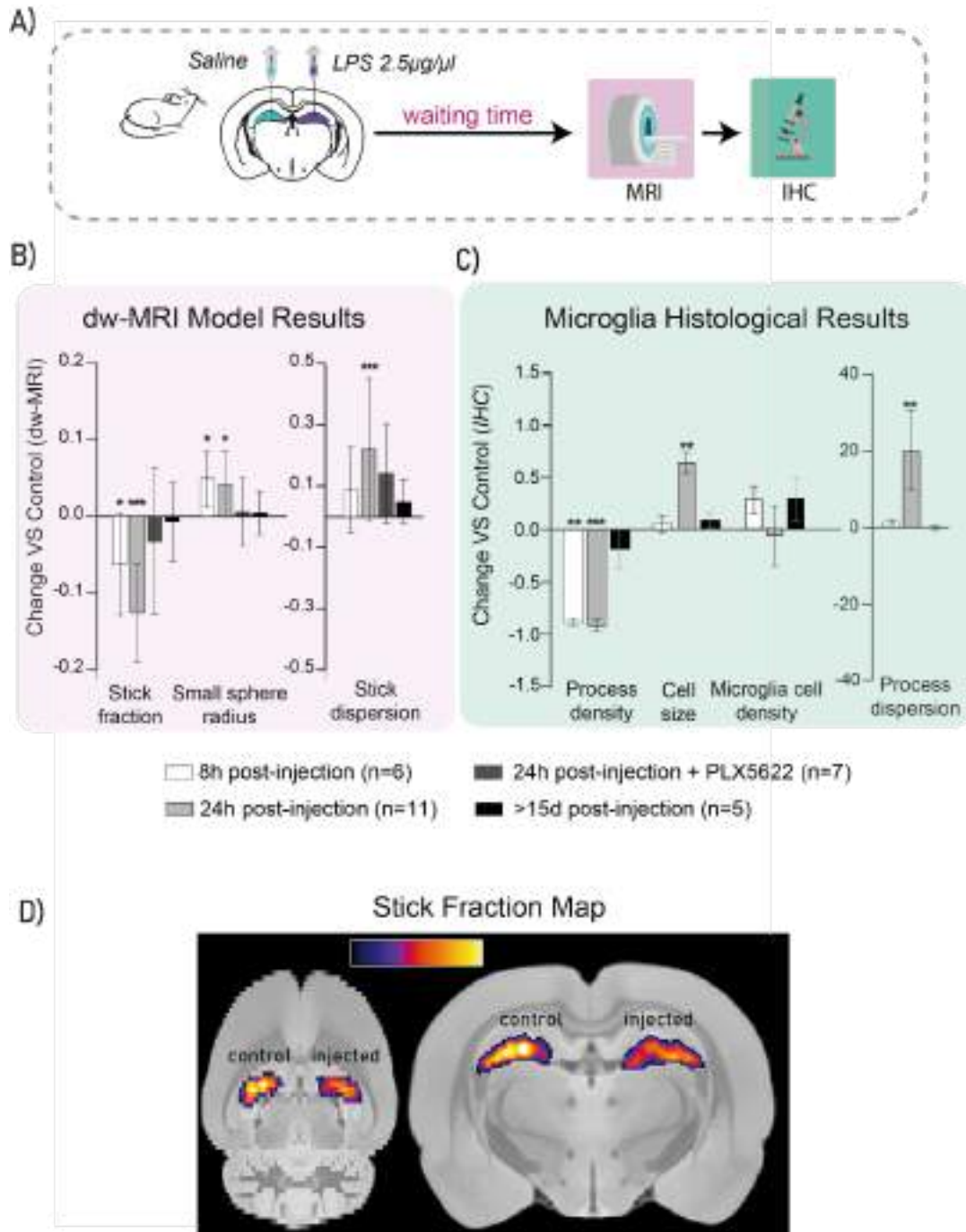


Figure R.2: Microglia reaction characterization with dw-MRI and histology. A) Experimental Schema of LPS experiments. B) Microglial results for the dw-MRI model, expressed as change vs control for stick fraction, small sphere radius and stick dispersion. C) Histological results for microglia, expressed as change vs control for: process density, cell size and microglia cell density (same as Figure R.1) and process dispersion. D) Mean stick fraction maps at 24 hours after injection, normalised to a rat brain template and averaged over all rats. Asterisks represent significant paired t-test difference between injected and control (* $p < 0.1$, ** $p < 0.01$ and *** $p < 0.001$). Error bars represent SD.

The corresponding dw-MRI variable, stick dispersion, follows the same trend with the same directional result: no significant effects were observed at 8h, but there were at 24h post-injection. However, regarding the cell size of the microglia cell body, an increase in small sphere size was detected at both 8h post-injection and 24 hours, while it was only observed in histology at 8h post-injection. At 15 days post-injection, no significant results were observed for any of the dw-MRI models, mirroring the histological results.

Overall, these findings demonstrate the potential to recover a microglia-specific signal from the dw-MRI model, capable of revealing a microglial reaction *in vivo* and non-invasively (Figure R2.D), following the establishment of a strong correlation between imaging and histological parameters.

5.1.2.1. Microglia reaction on PLX-LPS animals

Next, to further confirm the microglial origin and continue validating our model, we depleted microglia from the system using the PLX animal model (group 3 from animal models of neuroinflammation), which was also injected with LPS (Figure R.3.A)

The initial step was to validate the effect on microglia depletion of the PLX treatment (Figure R.3), for which we have focused on 24 hours post-injection of the LPS to later isolate astrocyte reaction. As illustrated in the microphotographs (Figure R.3.B), microglial disappearance is nearly complete, consistent with the results reported by Hang et al. (2017). To further validate the effect, we quantified the number of ramifications in the residual microglia compared to PLX sham rats not injected with LPS, and the results indicated a sixfold reduction in ramifications compared to control microglia.

Subsequently, we quantified the microglia-related dw-MRI features in these animals. As can be seen by the stripped bars at Figure 2.B, we found that the microglia related parameters indeed disappeared when animals were pretreated with PLX, being true for stick fraction, small sphere radius and stick dispersion.

These results conclusively demonstrate that the microglia results captured previously by dw-MRI were, in fact, microglial-specific.

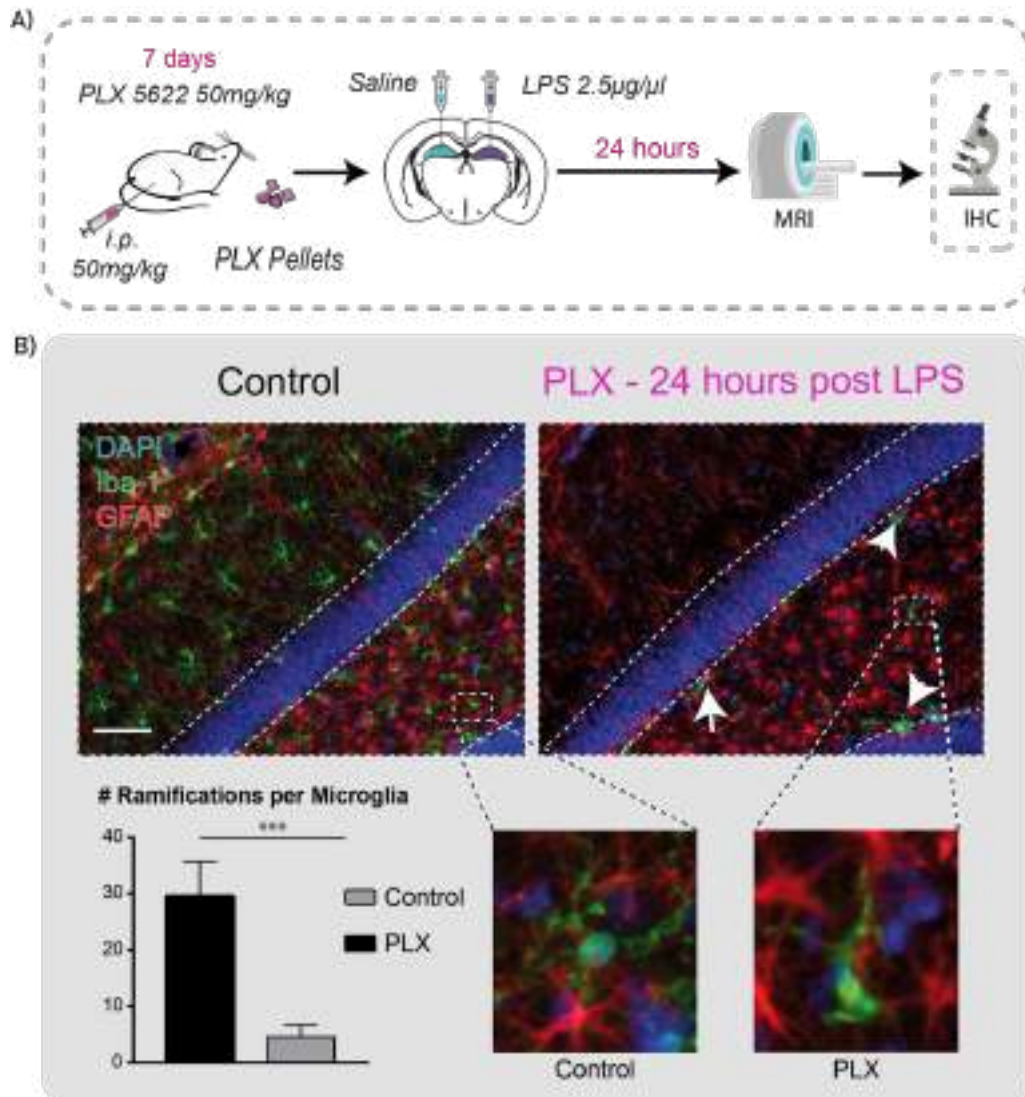


Figure R.3: Microglia in PLX animals. Experimental Schema of LPS experiment for Group 3 of animals (PLX animals). **B)** Representative microphotographs of the dentate gyrus showing microglia (green), astrocytes (red) and cell nuclei (blue) for sham-control animals and PLX - 24 hours post LPS animals. In the detail, a zoom-in of a microglia cell for both conditions. Dashed line surrounds the granular layer of the dentate gyrus. **C)** Ramification per microglia quantifications for both groups. Asterisks represent significant paired t-test difference between injected and control ($***p < 0.001$). Error bars represent SD. Scale bar = 100 µm.

5.1.3. Astrocyte reaction characterised using GFAP staining and MRI

In the previous section, we demonstrated that our dw-MRI model is capable of imaging specific microglial reactions. Our subsequent objective was to further assess the capability of the dw-MRI model with the other glial population of interest: astrocytes. To accomplish this, we calculated the big sphere radius to estimate astrocyte volume and examined it alongside its histological counterpart, convex hull size.

Similar to microglia, we present the results of the dw-MRI model (Figure R.4.B) and place again the histological ones for a more robust comparison (Figure R.4.C). As we can notice in the quantifications, at 8 hours post-injection, there was no discernible astrocyte reaction measured with the big-sphere radius, consistent with the histological findings where no differences were found for convex hull size at this time point. These results further validate the previous findings regarding microglial specificity, as no astrocyte reaction was detected by the dw-MRI model at this time point. Transitioning to the 24-hour post-injection period, importantly, we observed a significant and notable increase in the big sphere radius, aligning with the reported results of convex hull size from histology. Finally, at 15 days post-injection, dw-MRI indicated no significant changes in astrocyte populations, once again matching the histological counterparts.

5.1.3.1. Astrocyte reaction on PLX-LPS animals

Although the dw-MRI model mirrors the histological results characterising astrocytic reaction, elucidating its specificity in a microglia free reaction environment remained essential. To address this, we investigated the results of the model on the PLX-LPS animals (group 3 from animal models of neuroinflammation) without microglia in the system (Figure R.3), resulting in a unique astrocyte reaction.

As depicted in Figure R.4, represented by the striped bars, we observed a substantial increase in convex hull size for astrocytes, surpassing even the levels seen in animals 24 hours post-injection. These findings align with observations previously reported by others, suggesting that in the absence of microglia, the astrocytic reaction can be more pronounced (Van Zeller et al., 2022). Regarding the big sphere radius, as determined by the dw-MRI model, it closely corresponds to the histological results: the big sphere radius exhibited a significant increase in these animals, with the magnitude of change paralleling the histological findings.

Consequently, the results obtained for the astrocytic compartment demonstrate the potential to quantify an astrocyte-specific signal from dw-MRI, distinctly from a microglia signal, opening avenues to map astrocytic reactions *in vivo* (Figure R.4.D).

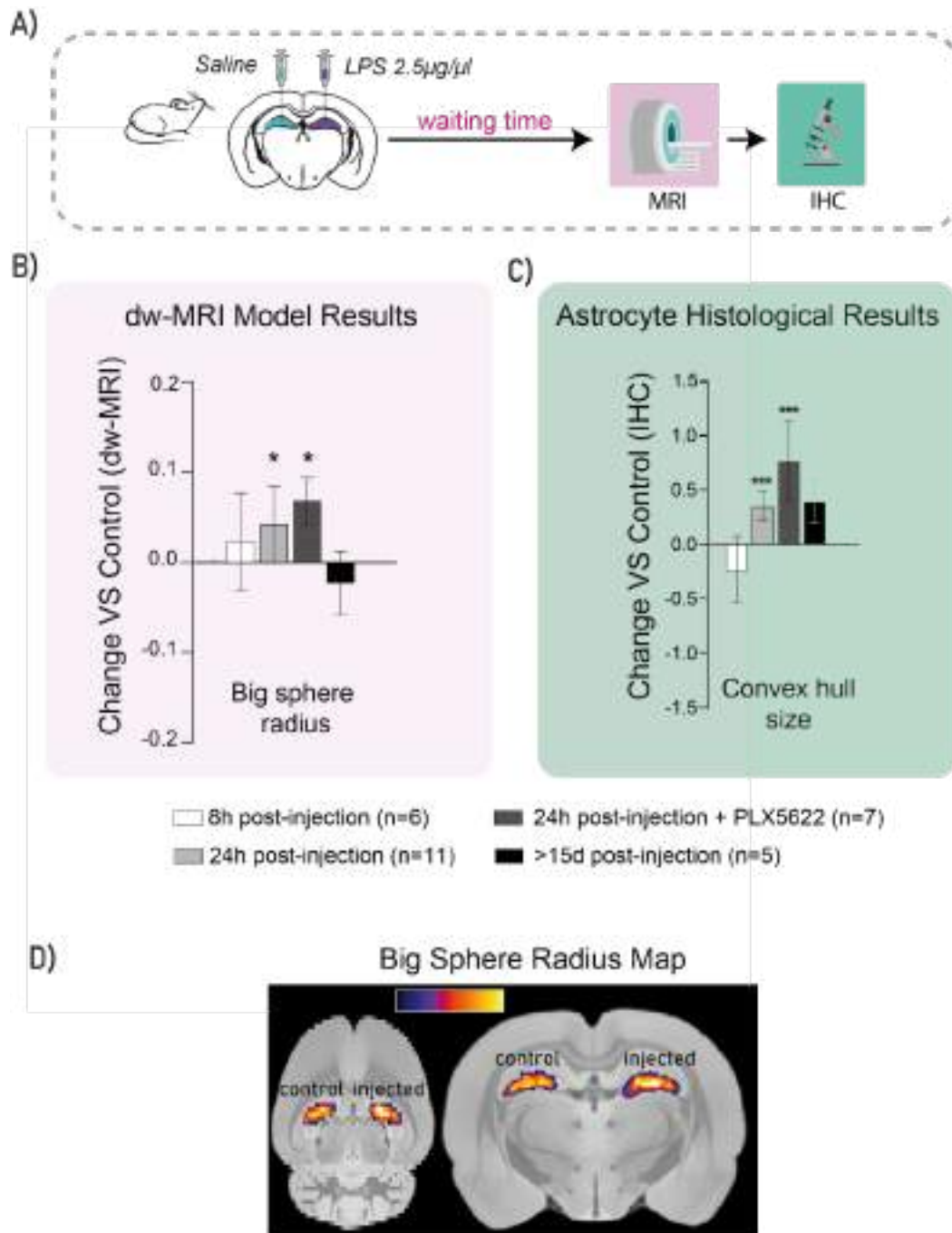


Figure R.4: Astrocyte reaction characterization with dw-MRI and histology. **A)** Experimental Schema of LPS experiments. **B)** Astrocyte results for the dw-MRI model, expressed as change vs control for the big sphere radius. **C)** Histological results for astrocytes, expressed as change vs control of convex hull size (same as Figure R.1) **D)** Large sphere radius maps at 24 hours after injection, averaged over all rats. Asterisks represent significant paired t-test difference between injected and control ($*p < 0.1$ and $***p < 0.001$). Error bars represent SD.

5.1.4. LPS protocol preserves neuronal and myelin integrity

Finally, we aimed to determine if there was any neurodegeneration or demyelination following the injection of LPS at different time points. This is crucial because, as highlighted in the introduction, different tissue configurations can yield similar results with dw-MRI analysis (Scarpazza et al., 2018; Ligneul et al., 2024), emphasising the necessity of ensuring the specificity of our model and the glial origin of the presented results.

To achieve this, we conducted intensity analysis on MBP and Neurofil staining to infer myelin and axon/dendrite states, respectively. The results are depicted in Figure R.5.

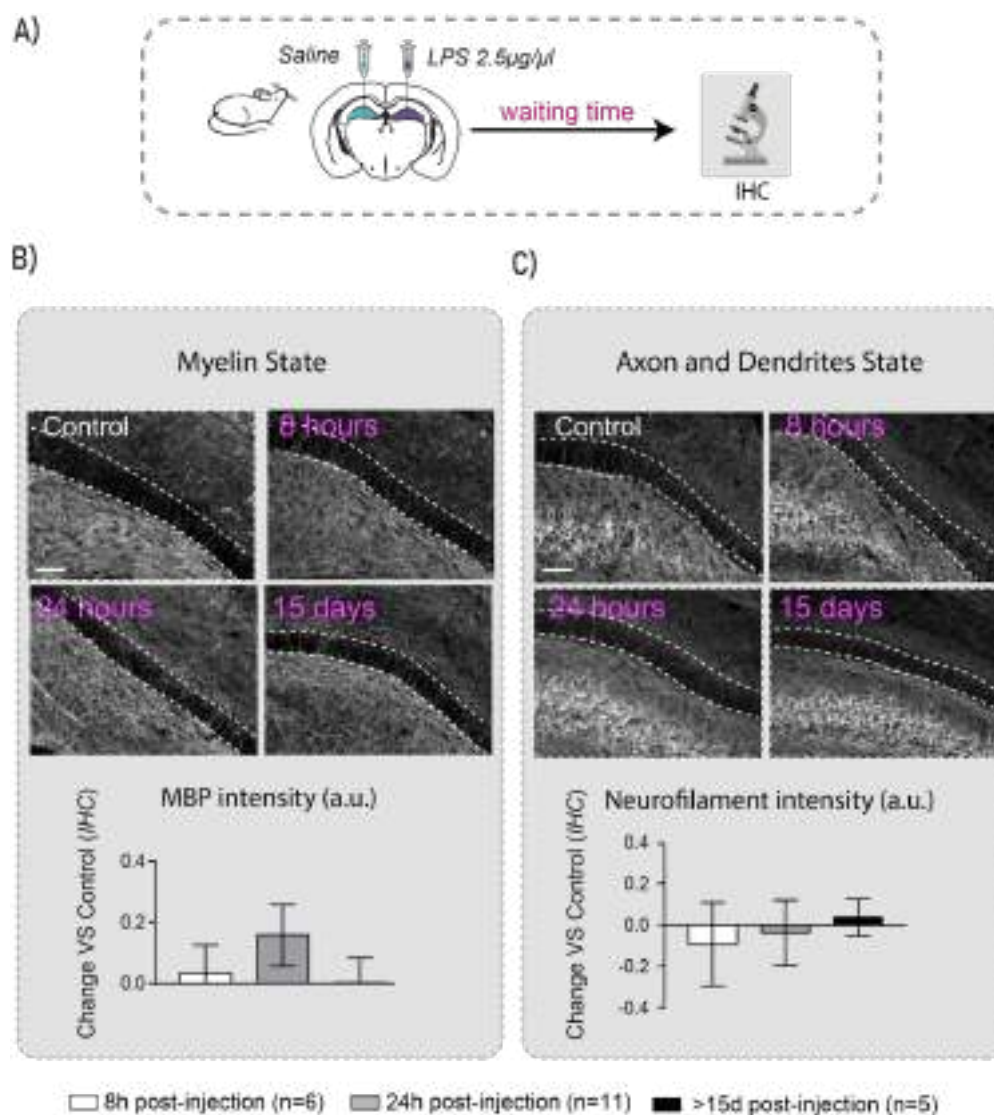


Figure R.5: LPS protocol preserves neuronal and myelin integrity. A) Experimental Schema of LPS experiments B) Myelin state results by labelling MBP protein: Representative microphotographs of the dentate gyrus showing MBP staining for control 8 hours, 24 hours and 15 days post-LPS injection. Below: Intensity value of MBP in arbitrary units (a.u.), expressed as change vs control. Dashed line surrounds the granular layer of the dentate gyrus. C) Same for axon and dendrites state with neurofilament staining. Error bars represent SD. Scale bar = 100 µm.

The intensity analysis revealed no significant differences in MBP staining at any of the time points, including 8 hours, 24 hours, and the recovery phase beyond 15 days (Figure R.5.B). Similarly, the analysis of neurofilament showed no differences in staining intensity across these different time points (Figure R.5.C).

These results further validate the experimental model of LPS, demonstrating that the LPS rat model is capable of inducing specific neuroinflammation without concomitantly causing neuronal death or demyelination (Jeong et al., 2019). Importantly, they also underscore the specificity of our dw-MRI multicompartment model for the current results on reflecting glia reaction detection.

5.2. Distinguishing glia reaction with concomitant neurodegeneration

In addition to microglia and astrocyte dynamics on health and disease, other phenomena as neurodegeneration often coexist with neuroinflammation (Ward et al., 2015, McGeer et al., 1993, Dickson et al., 1993, Stephenson et al., 2018, Mayne et al., 2020). This highlights the necessity of a tool capable of distinguishing between these two signals, both for research and clinical purposes. Furthermore, considering the reported challenge of misinterpreting dw-MRI results due to different tissue configurations (Scarpazza et al., 2018; Ligneul et al., 2024), there's a pressing need to expand our research to test and validate the dw-MRI model in additional scenarios.

Specifically, we utilised a known scenario of neurodegeneration with concomitant microglia reaction by ibotenic acid injection and 14 days of waiting (Drouin-Ouellet et al., 2011) (Figure R.6.A). To quantify the reaction, we quantify NeuN intensity and conduct morphometric reconstructions of microglia and astrocytes.

5.2.1 Neuronal death with microglia reaction characterised using NeuN staining and MRI

First, we investigated the histological reactions of glial and neuronal populations in this model. As illustrated in Figure R.6.C.D, microglia exhibited a significant loss of their ramification, consistent with the published results of the model (Drouin-Ouellet et al., 2011) and similarly as observed in the LPS model (Figure R.1.C and 2.C). This outcome was accompanied by an increase in process dispersion (indicating reduction), mirroring again the trend observed in the LPS model (Figure R.1.C and 2.C). Concerning the cell size of microglial cell bodies, we did not discriminate any significant changes. However, we did observe a notable increase in the number of microglia in the system, as evidenced by the density results (Figure R.6.C). In relation to astrocytes, as expected, we did not observe any observable differences in the size of the astrocyte population (Figure R.6.C).

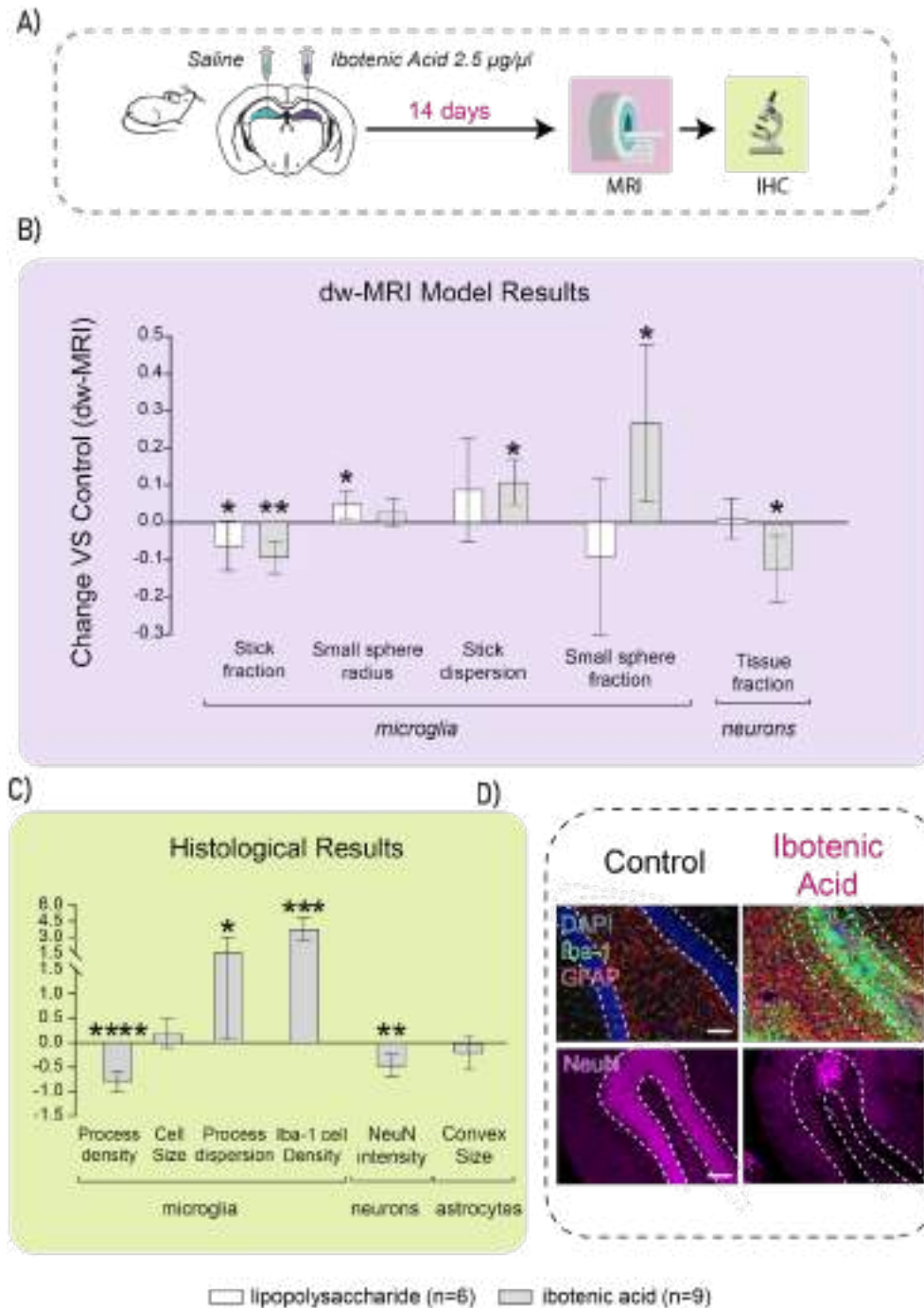


Figure R.6: Neuronal death characterization with dw-MRI and histology. **A)** Experimental Schema of ibotenic acid experiments. **B)** Microglia (stick fraction, small sphere radius, stick dispersion and small sphere fraction) and neuron (tissue fractions= results for the dw-MRI model, expressed as change vs control. **C)** Histological results for microglia (process density, cell size, process dispersion, Iba-1 cell density), neurons (NeuN intensity) and astrocytes (convex size) expressed as change vs control **D)** Representative microphotographs of the dentate gyrus showing microglia (green), astrocytes (red) and cell nuclei (blue) for a control and an ibotenic acid animal. Below: similarly for neurons (pink). Dashed line surrounds the granular layer of the dentate gyrus. Asterisks represent significant paired t-test difference between injected and control ($*p < 0.1$, $**p < 0.01$ $***p < 0.001$ and $****p < 0.0001$). Error bars represent SD. Scale bars = 100 μm .

Next, we investigated whether these changes were mirrored by the dw-MRI model. The results are presented in Figure R.6.B, which also displays the LPS results for better comparison due to the similarity of the histological outcomes. We observed a significant decrease in the stick fraction parameter accompanied by an increase in dispersion, closely mirroring the results of microglia histology. Importantly, regarding neuronal death, measured by tissue fraction as explained in the methods, we observed a significant decrease, matching the NeuN results. Notably when comparing this with the LPS model results, we observed striking similarities in microglial diffusion outcomes, except for the tissue fraction, which was absent in the LPS model. Finally, we even observed that the parameter of microglial proliferation was tightly mirrored as well: the number of small sphere fractions indicated, similar to histology, a substantial increase in microglia in the analysed area.

These results underscore two crucial findings. Firstly, the parameter of the dw-MRI model quantifying microglial cell density demonstrated promising outcomes: the density of small spheres, corresponding to microglial cell density in histological analysis, closely mimicked the histology. Secondly, this model reaffirmed the effectiveness of our model in detecting microgliosis independent of concomitant neurodegeneration, demonstrating its specificity and robustness, without being confounded by other cell unit reactions in the model.

5.2.2. Isolated neuronal death characterisation

To further demonstrate our ability to distinguish and quantify between neuroinflammation and neurodegeneration, as well as the impact of microglia reaction on the measured tissue fraction from the previous section, we conducted an additional experiment using an additional group of animals injected with ibotenic acid but treated with minocycline (group 5.1) (Figure 7.A). Minocycline is an anti-inflammatory drug known for its ability to reduce microglial and astrocytic reaction (Cheng et al., 2015).

The results of these animals are shown in Figure R.7, where NeuN intensity is plotted against tissue fraction within the same plot. We observed a significant decrease in NeuN intensity upon injection, although less pronounced than in animals without minocycline treatment. Nevertheless, importantly, we note that this result correlates directionally and in magnitude with the diffusion dw-MRI results.

From these experiments, we can conclude that our dw-MRI units are specific to their intended purpose, reaffirming not only its robustness and specificity but also the quantitative value of our dw-MRI model

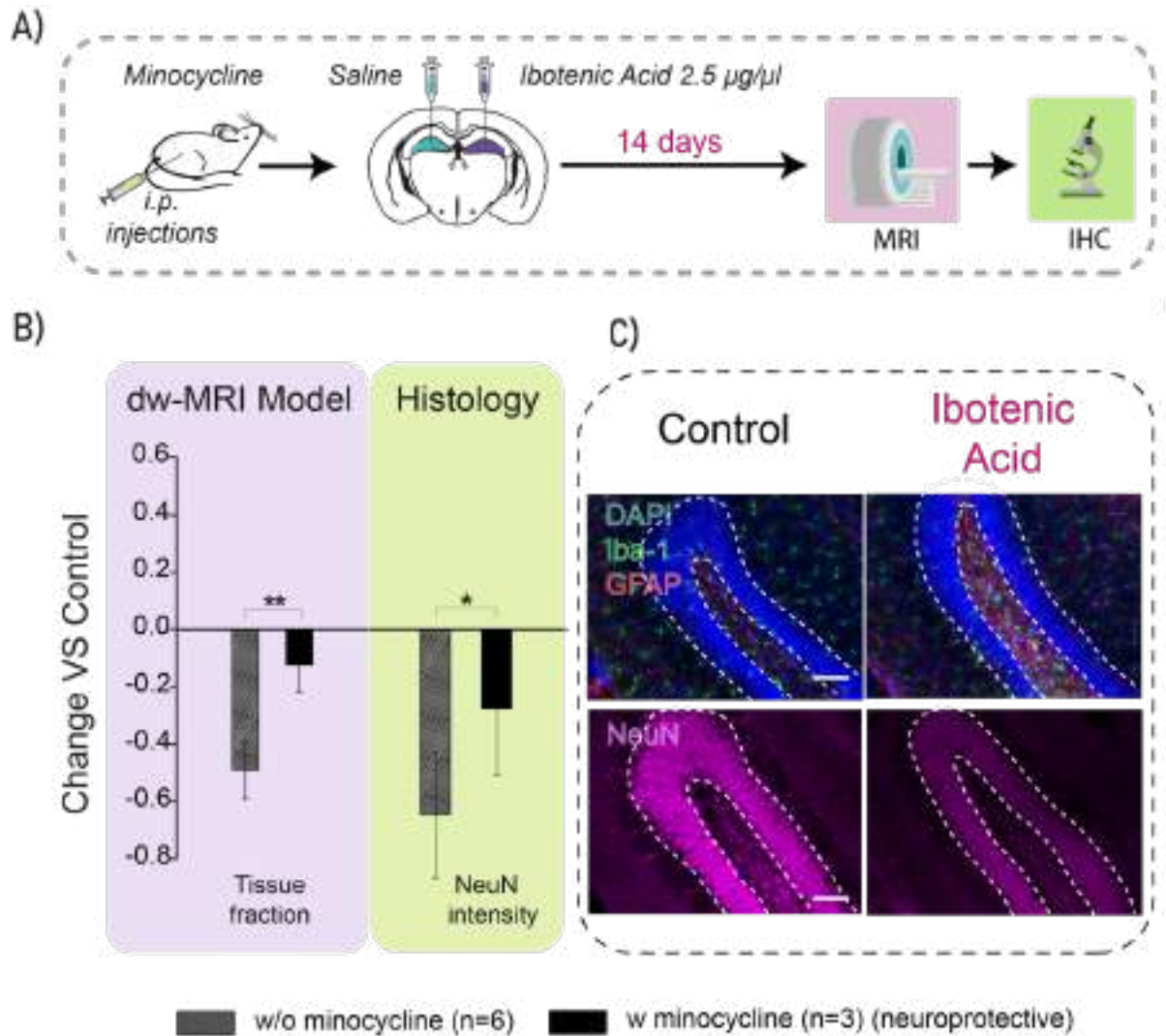


Figure R.7: Isolated neuronal death characterisation. **A)** Experimental Schema of ibotenic acid experiments with minocycline treatment. **B)** dw-MRI model (tissue fraction) and histological results (NeuN intensity) for neurons, expressed as change vs control. **C)** Representative microphotographs of the dentate gyrus showing microglia (green), astrocytes (red) and cell nuclei (blue) for control and ibotenic acid treated with minocycline. Below: similarly for neurons (pink). Dashed line surrounds the granular layer of the dentate gyrus. Asterisks represent significant paired t-test difference between injected and control (* $p < 0.1$ and ** $p < 0.01$). Error bars represent SD. Scale bars = 100 µm.

5.3. Specificity of the model in the presence of demyelination

In the preceding sections, we have demonstrated the capability of our model to differentiate between microglia and astrocyte reaction, while also avoiding confusion in the presence of concomitant neuronal loss. However, to further enhance the specificity of the model, we incorporated another tissue unit: myelin. This is important because myelin dysregulation often accompanies neuroinflammation (Tallantyre et al., 2009; Karussis, Young et al., 2010, 2014; Wingerchuk et al., 2015).

To address this, we employed another well-established model of immune attack: lysolecithin intracerebral injection (Woodruff & Franklin, 1999), a microgliotoxin known to induce considerable demyelination without axonal damage within 14-24 days post-injection (Woodruff and Franklin, 1999) (group 6 of animals) (Figure R.8.A). For the analysis of these results, microglia and astrocytes were reconstructed as usual. For assessing demyelination, we measured MBP labelling as previously indicated.

5.3.1. Myelin reaction characterised using MBP staining and MRI

At the histological level (Figure R.8.C-D), concerning the microglia and astrocyte populations, we observed no discernible reaction to the lysolecithin, consistent with previously reported results (Woodruff & Franklin, 1999). Regarding the myelin unit, the primary target of lysolecithin, we indeed observed a significant reduction in the intensity of MBP labelling in the treated hemisphere compared to the control. Although the reduction varied among animals, it was significant (Figure R.8.C).

Next, we characterised the results for the dw-MRI model (Figure R.8.B). As explained in the method, for myelin, we utilised a stick fraction similar to that used for microglia but in a non-overlapping manner. This is because we can differentiate microglia from myelin units thanks to the combination of other parameters related to microglia: stick dispersion and small sphere radius. The results, as seen in Figure R.8.B, follow our prediction: we find a significant decrease in the stick fraction signal, but not in stick dispersion or small sphere radius. As observed in the LPS model (Figure R.2) and Ibotenic model (Figure R.6), a reduction of microglia stick fraction was accompanied by a change in stick dispersion.

To corroborate our predictions and further characterise the results, we computed four simulated dw-MRI environments with different phenotypic characteristics of each cell unit (Figure R.9.A-D). Neuron ramifications were defined by the size and dispersion of their processes measured in the bibliography (Papageorgiu et al., 2015; Maisonnave and Garcia-Cairasco, 2007).

The synthetic environments modelled represent the following scenarios: a control brain with microglia, astrocytes, neurons, and the myelin compartment (Figure R.9.A), followed by microglia reaction represented by a 50% reduction of its ramifications and a 10% increase in cell size (Figure R.9.B), reflecting what we observed in the 24-hour post-LPS injection results (Figure R.1). The third environment consists of neuronal loss by a 50% reduction in dendrites (Figure R.9.C), similar to the ibotenic acid injection results (Figure R.6). Finally, the last synthetic environment (Figure R.8.D) corresponds to the current model of lysolecithin-induced demyelination (Figure R.8).

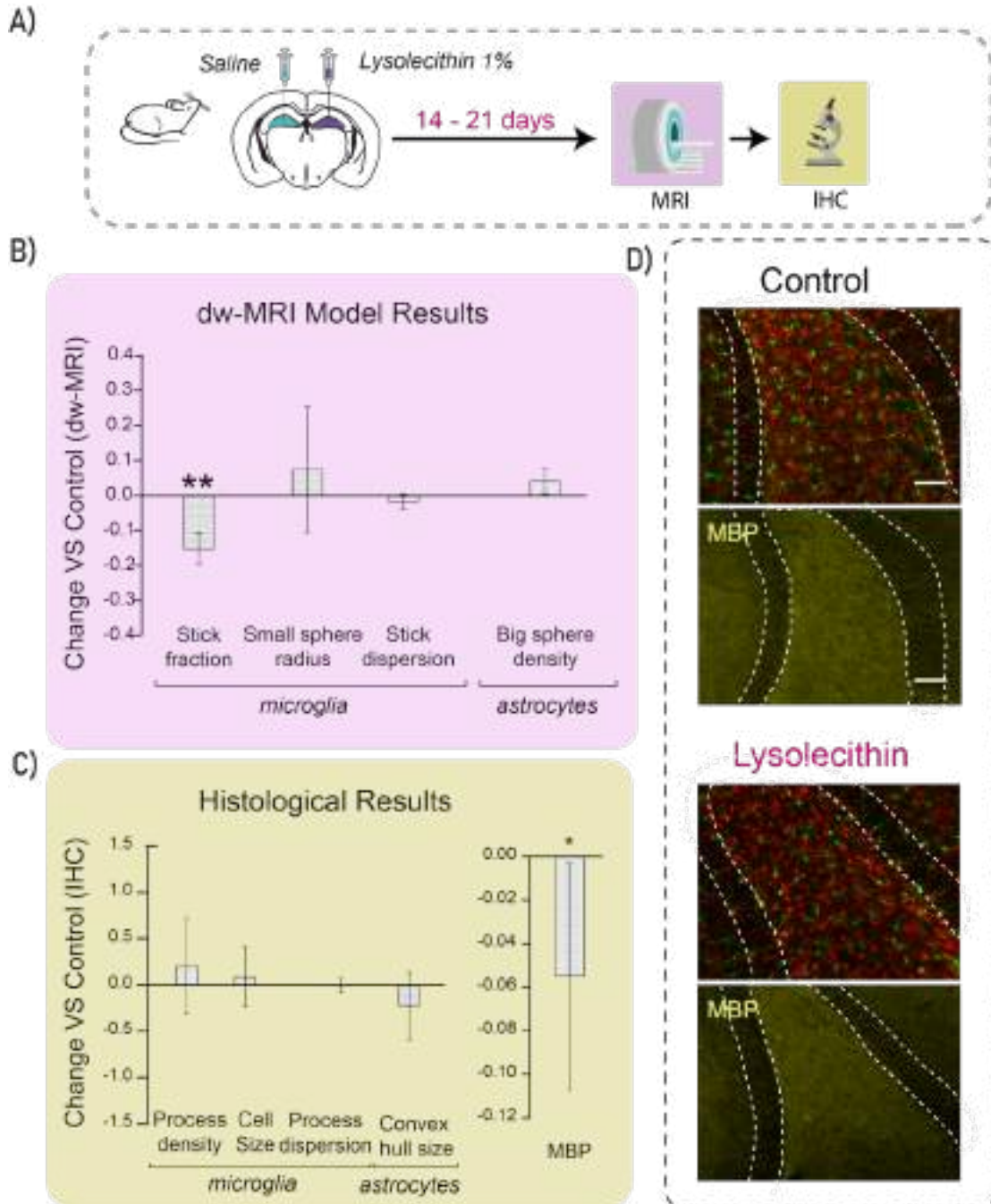


Figure R.8: Myelin reaction characterised using MBP staining and MRI. **A)** Experimental Schema of lysolecithin experiments. **B)** dw-MRI model results for microglia (stick fraction, small sphere radius and stick dispersion) and astrocytes (big sphere density), expressed as change vs control. **C)** Histological results for microglia (process density, cell size and process dispersion) and astrocytes (Convex Size) expressed as change vs control. **D)** Representative microphotographs of the dentate gyrus showing microglia (green) and astrocytes (red), and below for myelin (yellow) for both control and a lysolecithin treated animal. Dashed line surrounds the granular layer of the dentate gyrus. Asterisks represent significant paired t-test difference between injected and control ($*p < 0.1$ and $**p < 0.01$). Error bars represent SD. Scale bars = 100 μm .

For each of the environments, we calculated the K dispersion parameter for estimating the ramification dispersion. As seen in the results (Figure R.9.C), we notice a significant increase in K (meaning reduction), which aligns with previously reported findings for LPS data (Figure R.1). This result is markedly different from the paradigm of neuronal loss, both in magnitude and direction, and closely mirrors the results for the ibotenic acid group (Figure R.6). Importantly, demyelination has no discernible effect on the K parameter, consistent with the lysolecithin results (Figure R.8) and our predictions.

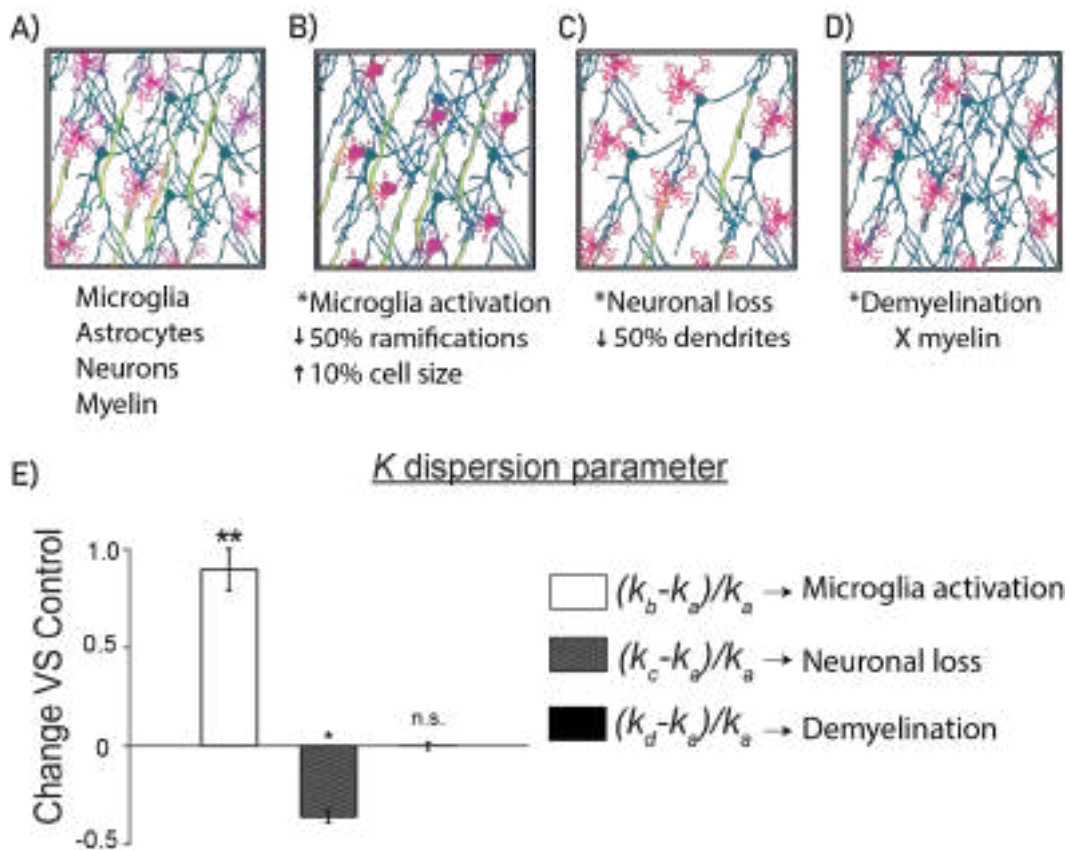


Figure R.9: Dispersion parameter at different *in silico* scenarios. Different synthetic scenarios of brain parenchyma modelled by a different combination of microglia, astrocytes, neurons and myelin. **A)** Control brain with all the compartment mentioned. **B)** Microglia reaction paradigm, with a reduction of 50% of the ramifications and an increase of cell size of 10%. **C)** Neuronal loss paradigm, with a reduction of 50% of the dendrites. **D)** Demyelination paradigm, with no myelin in the system. **E)** Results for K dispersion parameter for each condition, expressed as change vs control. Asterisks represent a significant paired t-test difference between injected and control ($*p < 0.1$ and $**p < 0.01$). Error bars represent SD.

These findings underscore that microglia reaction and demyelination are effectively discriminated against by incorporating other microglia parameters into the equation, especially stick dispersion. Overall, this unequivocally validates our diffusion model's ability to distinguish microglia ramifications from myelin state and adds a promising possibility of detecting myelin degeneration.

5.4. Translation to human patients

Until now, our model's predictions have been validated through successful differentiation between microglia and astrocyte reactions, even in scenarios involving neuronal or myelin loss, in animal inflammation models.

However, as our ultimate goal is to develop a tool capable of detecting these tissue situations in human patients, non-invasively and *in vivo*, the next essential step was to evaluate our tool in human patients. We anticipated a high translatability from the tool, as the main characteristics of neuroinflammation are shared across species (Andriezen et al., 1983; Sofroniew et al., 2014; Savage et al., 2019; Paolicelli et al., 2022).

In the following section, I will outline the main results of the clinical trial conducted for this purpose.

5.4.1. Quantifying human microglia density at whole brain *in vivo*

We collaborated with the CUBRIC Institute, holders of a 3T Siemens Connectome MRI machine compatible with the necessary specifications to translate our scanning protocols to human patients (Jones et al., 2018). Our focus was particularly on calculating the density of microglia across different brain regions, taking advantage of its naturally heterogeneous distribution across its anatomy (Mittelbronn et al., 2001), in six healthy human participants (Figure R.10.A).

Firstly, we computed the stick fraction for the average of all the patients and represented it as a stick fraction heat map, showing both sagittal and coronal slices in Figure R.10.B. In the figure, differences in microglia density in certain brain areas are already evident, such as the cerebellum exhibiting lower density than the hippocampus.

Secondly, we numerically computed microglia density by combining both stick fraction and stick dispersion to ensure the specificity of microglia, as explained in the previous section. This was done for eight brain regions: cerebellum, motor cortex, frontal lobe, occipital lobe, basal ganglia, substantia nigra, hippocampus, and thalamus. To demonstrate the feasibility of our calculations, we compared this *in vivo* characterization with *post mortem* quantifications of microglia with Iba-1 from the bibliography (Mittelbronn et al., (2001). The results, presented in Figure R.10.C, revealed a high correlation between the patterns of microglia cell density obtained from our results and those published on human tissue) A multiple linear regression demonstrated that this correlation is indeed statistically significant.

These findings demonstrate the high potential utility of our tool for human patients. While further validation is required, our tool has shown promising capabilities in calculating microglia cell density *in vivo* and non-invasively in human patients.

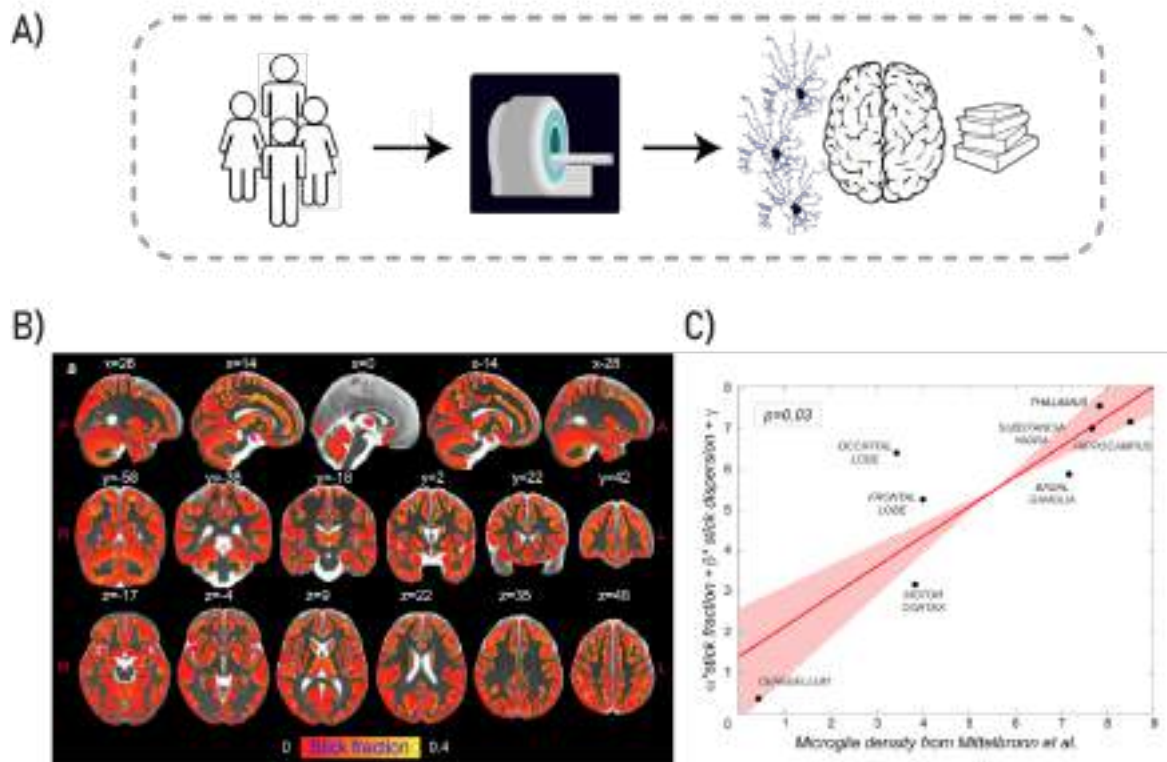


Figure R.10: Quantifying human microglia density at whole brain *in vivo*. **A)** Workflow of the proof-of-concept experiment. **B)** Stick fraction maps according to the dw-MRI model, normalised to the brain template (Desikan et al., 2006), averaged across subjects **C)** Multiple linear regression, conducted using stick fraction and dispersion to explain microglia density measured using histological staining of *post mortem* human tissue in eight grey matter regions (hippocampus, cerebellum, substantia nigra, basal ganglia, thalamus, motor, frontal, and occipital cortices) as reported in (Mittelbronn et al., 2001). Regression confidence intervals were calculated using bootstrap.

5.5. Comparison with conventional MRI techniques

Previous methods for modelling diffusion MRI in the brain parenchyma have indeed led to remarkable discoveries, thanks to their ability to assess brain structure non-invasively. However, as we've discussed in our research, applying these methods to grey matter remains challenging due to the potential for different tissue configurations to yield the same results (Scarpazza et al., 2018; Ligneul et al., 2024).

In the last part of our research, to highlight the importance of the developed framework, we present the conventional MRI measures typically used in both research and clinical settings: MD, T1/T2 ratio, T2*, and extracellular diffusivity. We calculated these values for all rat models utilised in our research (Figure R.11.A), taking advantage of the fact that we have characterised meticulously their tissue reactions.

Regarding MD, we did not observe significant differences at 8 hours post-LPS injection, despite the histological results evidenced a significant decrease in the ramifications of

microglia compared to the saline-injected hemisphere (Figure R.3). In relation to the other animal models, we observed a significant increase in MD. However, this increase was similar across all models despite the quantified histological differences in their tissues, highlighting the lack of cell unit specificity of this variable.

Concerning the T1/T2 ratio, typically linked to myelin content in both white and grey matter (Glasser et al., 2011; Ganzetti et al., 2014, Niewenhuis and Broere., 2017) we noted a reduction in all three LPS conditions, while the histology demonstrated no change (Figure R.5). About T2*, we did not detect significant changes for almost any condition, except for ibotenic acid injection (Figure R.6), which, in fact, had very similar results histologically as the LPS model (Figure R.1).

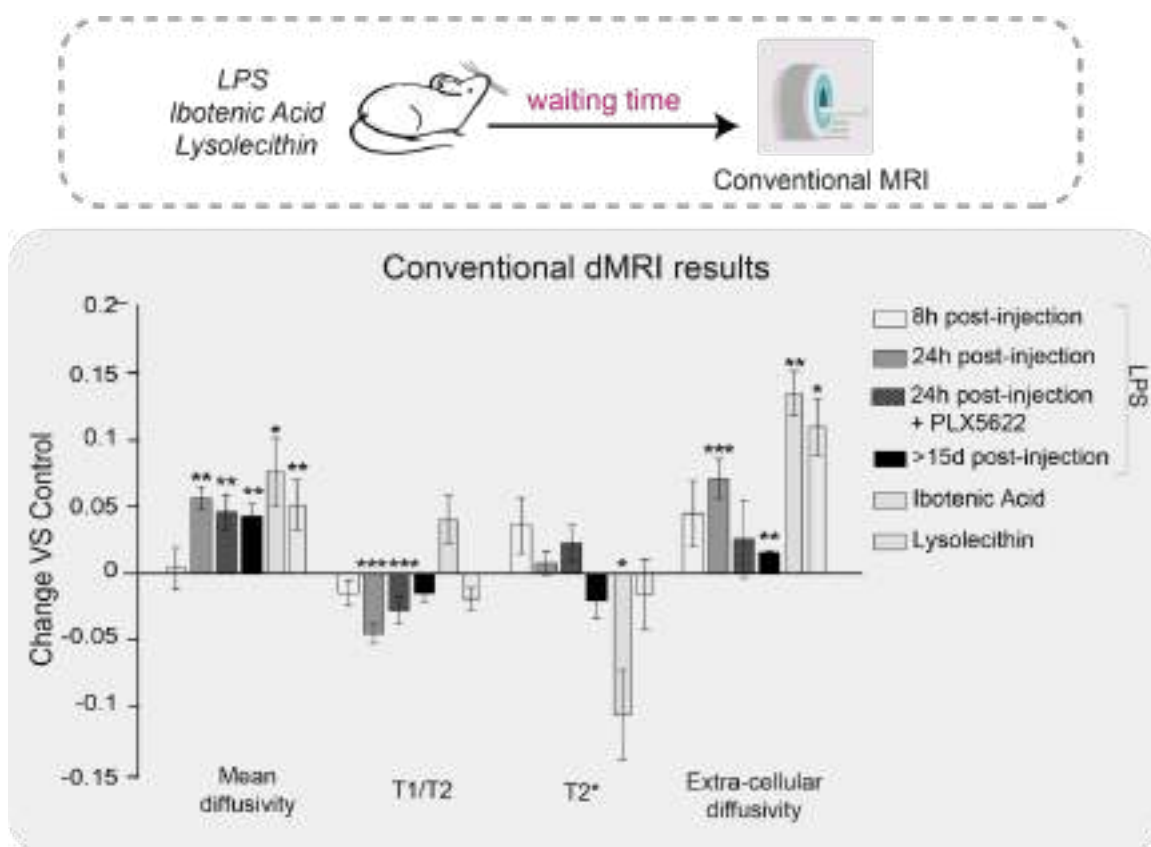


Figure R.11: Comparison with conventional MRI techniques. A) Experimental workflow for all the animal models in the research. B) Results for conventional MRI parameters: mean diffusivity, T1/Tw ratio, T2* star and extra-cellular diffusivity, expressed as change vs control. Asterisks represent a significant paired difference between injected and control. (* $p < 0.1$, ** $p < 0.01$ and *** $p < 0.001$). Error bars represent SD.

At last, extracellular diffusivity followed a similar trend as MD, suggesting an increase in the treated hemisphere across all rat models, even for the LPS 15 day post-injection model, where no significant changes were demonstrated at the histological level for microglia or astrocytes (Figure R.1).

Overall, these findings underscore the importance of handling conventional MRI data with care when dealing with complex cerebral grey matter tissue. We have demonstrated that different tissue scenarios can produce similar results and may even suggest an effect where there may be none. These results emphasise the significance of our approach and model, highlighting the necessity of further advancements in the field of imaging multi-tissue compartments.

Discussion



Cell Nuclei (DAPI)

Author: Raquel García Hernández

VI. Discussion

In recent years, our understanding of neuroinflammation has undergone a significant shift, recognizing it as an intricate phenomenon involving multiple layers of complexity. While traditionally viewed as protective, emerging research suggests that dysregulated or prolonged reaction of these cells may contribute to the progression and even the onset of some diseases as Alzheimer's Disease (Davies et al., 2017; Streit et al., 2009, Kim et al., 2024, Rachmian et al., 2024), Parkinson's disease (Cai et al., 2014; Arena et al., 2022), multiple sclerosis (Sanchez-Guajardo et al., 2015, Distéfano-Gagné et al., 2023), amyotrophic lateral sclerosis (Cooper-Knock et al., 2017, Carke and Patani, 2022) and stroke (Guruswamy and ElAli., 2017, Wang et al., 2022, Planas 2024). Similarly, astrocytes have been implicated in Huntington's disease, amyotrophic lateral sclerosis, and Alzheimer's disease (Simpson et al., 2010; Phatnani et al., 2013; Kim et al., 2024). Furthermore, it is now recognized that these cell populations exhibit dynamic responses even in their "resting state," influenced by factors such as age, sex, brain area, and environmental cues, as we mentioned in the introduction. These influences regulate genetic transcription, epigenetics, and phenomics, among other factors, ultimately dictating their roles and behaviours in health and disease (Escartin et al., 2021; Paolicelli et al., 2022). Furthermore, it have been found morphological shifts across a wide spectrum of this conditions (Simpson et al., 2010; Phatnani et al., 2013; Guruswamy and ElAli, 2017; Davies et al., 2017; Arranz and Stropper et al., 2019; De Santis et al., 2020, Kim et al., 2024, De Santis et al., 2020) and other diseases like HIV infection (Kong et al., 2024).

These studies underscore the critical need for tools capable of investigating these complex reactions. The ability to non-invasively image and track these morphological changes *in vivo* could revolutionise our comprehension of these cells, their implications in disease, and ease the way for the identification of early diagnostic biomarkers and the design and monitoring of new treatments targeting microglia or astrocytes. However, to date, there is no imaging tool specially designed to discern the cellular signature of microglia and astrocyte reaction.

In our research, we have developed a multi-compartment diffusion model for grey matter tissue with dw-MRI, designed to image the unique geometrical and size characteristics of microglia and astrocyte populations. We have validated this model against their histological counterparts in animal models of neuroinflammation, employing precise morphometric *post mortem* quantifications. Our findings unveiled three distinct dw-MRI parameters specific to microglia and one for astrocytes. Furthermore, we have tested these parameters across scenarios involving solely microgliosis or astrogliosis, alongside concurrent neurodegeneration or demyelination, with a successful outcome. Additionally, we've showcased its translational potential by applying it to healthy human subjects in a proof-of-concept study. We firmly believe that this tool will have a profound impact on both research and clinical domains, providing a novel and validated framework for *in vivo*, non-invasive imaging of microglia and astrocyte morphology with multicellular specificity.

6.1. Animal models of inflammation

One of the primary pillars in achieving our objective was the utilisation of animal inflammation models. These models allowed us the opportunity to discern microglial or astrocytic reactions at various time points with specificity. By integrating data from these animal models with their corresponding histological analyses, we were able to groundwork for the development of our effective *in vivo* strategy. In this section, I will discuss the results in relation to the animal models employed in our research and elucidate how the used histological variables successfully measured their respective changes.

Initially, we employed an LPS-driven inflammatory challenge, with the hypothesis of eliciting a primarily microglial reaction within 8 hours, followed by concurrent microglial and astrocytic reactions at 24 hours, and eventual return to baseline by 15 days (Jeong et al., 2010). Our findings aligned well with these predictions, as we observed a pronounced microglial reaction at 8 hours, with no concurrent astrocytic response (Figure R.1.C). This microglial reaction was characterised by a reduced ramification density, consistent with similar observations in studies such as Hung et al. (2023), which also reported a less ramified microglial morphology in an analogous paradigm. However, our results diverged from studies where LPS was administered via intraperitoneal injection, inducing peripheral inflammation rather than a localised microglial response, thereby prompting different phenotypic reactions in microglia cells with an increase number of ramifications (Chen et al., 2012, Huang et al., 2020). This discrepancy in response has been documented by others (Sheppard et al., 2019), demonstrating that direct exposure to LPS in cell culture diminishes microglial arborization, possibly explaining these divergences.

At 24 hours (Figure R.1.C), we continued to observe a notable reduction in microglial processes alongside a significant increase in cell size, corroborating findings from Jeong et al. (2019) and later supported by Hung et al. (2023). Additionally, we made a novel observation of a clear decrease in the dispersion of microglial processes, with a predominant directionality evident. In the PLX group, as anticipated, we effectively depleted microglia from the system (Figure R.3), consistent with previous findings (Han et al., 2017).

Regarding astrocytic responses, we identified a delayed reaction characterised by an increase in GFAP size (Figure R.1.D), affirming the expected outcomes from our model and similar methodologies (Jeong et al., 2019, Ambrosini et al., 2005, Campbell et al., 2012). We assessed this astrocytic reaction by measuring changes in convex hull volume, with our results indicating the effectiveness of this volume estimate in tracking astrocytic reactions, aligning with previous studies (Ambrosini et al., 2005, Wilhelmsomm et al., 2006, Carvalho-Paul et al., 2018). However, it is crucial to acknowledge that the accuracy of this analysis relies on the quality of staining, as it relies on the creation of a polygon by connecting all reconstructed ramifications. Thus, the choice of a robust labelling strategy remains crucial for precise measurements, such as GFAP, which labels thin processes in both healthy and diseased states (Griemsmann et al., 2015, Haim and Rowitch 2017).

Regarding the density of both cell populations, we did not observe quantifiable differences. This contrasts with previous findings indicating elevated numbers of both astrocytes and microglia following LPS administration. However, we cannot draw any conclusion as they do not indicate the concentration, and the waiting time post-injection is different, from 4 hours (Bharani et al. 2017). Finally, regarding neuronal loss in the LPS model, we did not reach concentrations known to induce neuronal loss, from 5ug (Li et al., 2004) to 20ug (Pugh et al., 2007). However, a limitation of our study is that we did not verify neuronal loss in our histological analyses. Although the granule cell layer appeared qualitatively intact with DAPI staining (Fig. R.1) and the analysis of MBP and Neurofil revealed no differences versus the control hemisphere, a quantitative analysis of NeuN would have been necessary to corroborate these observations.

Using the ibotenic acid model, a well-established approach for inducing neuronal loss (Drouin-Ouellet et al., 2011), we observed pronounced microglial reactions (Figure R.4.C), as reported as well by others (Thomsen et al., 2015). These reactions were similar to those induced by LPS (Figure R.1.C), characterised by reduced ramification density and dispersion, along with reduced cell dispersion. However, we also found a novel result: it increases the microglia cell density. To the best of our knowledge, this was only demonstrated with injections in neonatal rats followed by a two-month waiting period (Wai Huy et al., 2019). Regarding the neuronal loss, we did observe a significant decrease of NeuN intensity in the granule cell layer of the dentate gyrus, consistent with findings by Pak et al. (2022) and supporting the expected mechanism of action of ibotenic acid (Drouin-Ouellet et al., 2011). Ibotenic is known to damage neurons expressing NMDA receptors, such as those found in the dentate gyrus granule cell layer (Zinkand et al., 1992; Abe et al., 1992, Drouin-Ouellet et al., 2011), as evidenced by our quantified results.

Next, we treated another group with minocycline to attenuate microglial reaction and isolate the neurodegeneration signature (Drouin-Ouellet et al., 2011; Cheng et al., 2015). As hypothesised, we still observed neuronal loss, although with a smaller effect (Figure R.7). These results align with previous research directly pointing to neuroinflammation as a catalyst of neurodegeneration (Drouin-Ouellet et al., 2011; Gómez-Nicola et al., 2013; Thomsen et al., 2015).

The final model we utilised in our research involved inducing demyelination using a well-established method of lysolecithin intracerebral injection, known to produce demyelination within 14-24 days (Woodruff & Franklin, 1999). The results, shown in Fig.R.8, reveal a significant decrease in myelin fraction as measured by labelling MBP protein intensity, a method used by others (Tilborg et al. 2017, Long et al. 2021). These results align with the original lysolecithin model proposed by Woodruff & Franklin (1999) and have been supported over the years by subsequent studies (Azin et al., 2013; Yang et al., 2022). However, the findings of Yang et al. (2022), showed a microglia reaction, in contrast to our measurements (Fig. R.8). These results may be influenced by their shorter waiting time post-injection (7 days). However, empirical data would be necessary to confirm this hypothesis.

In summary, our analysis has validated the effectiveness of the models chosen for developing our tool, including the LPS, Ibotenic acid, and lysolecithin models. Our findings align with the majority of existing literature that employs similar methodologies and histological measurements, as demonstrated for each of them.

Furthermore, these results possess another significant attribute: reproducibility. Despite assertions of heterogeneity, such as those regarding LPS models (Da Silva et al., 2024), we have demonstrated that the majority of our findings exhibit low variability and align closely with the existing literature employing similar methodology. This serves to further validate the suitability of these models for the subsequent stages or improvements of this and other investigations.

6.2. Imaging Neuroinflammation non invasively *in vivo*

After confirming our ability to target specific and single populations, microglia or astrocytes, and track their morphological changes with histology, we entered into validating whether our dw-MRI multicompartiment model could accurately reflect these phenomical changes. Here, we demonstrate, through the integration of different animal models and verified outputs, that we have successfully identified specific parameters to track microglia and astrocyte reactions. For microglia, we have identified three parameters, stick fraction, stick dispersion, and small sphere radius, that effectively capture microglial dynamics over time when used in combination. These parameters closely mirror histological results for both the LPS model (Figure R.2) and the Ibotenic model (Figure R.4). Importantly, these parameters were absent in the PLX groups (Figure R.2) and remained unaffected by astrocyte reaction, maintaining specificity for both solely microgliosis or microgliosis with astrogliosis (Figure R.2 and Figure R.4). Moreover, their specificity persisted in scenarios of neurodegeneration, distinguishing between glia reaction and proliferation independent of neuronal loss (Figure R.7). Additionally, our results showed that even in demyelination scenarios, typical in diseases like multiple sclerosis (Tallantyre et al., 2009; Karussis, 2014), the specifics of the microglia variables remained consistent (Figure R.8). These findings are parallel to a previous published model, SANDI (Palombo et al., 2020), which also modelled ramified cells, neurons, using sticks and spheres. They demonstrated, as we did here, that restricted diffusion with predefined geometry and size can aid in separating multicellularity sources of the dw-MRI signal. However, our results provide a clearer understanding as the validation is supported by quantitative morphometric analysis at the cellular level in the same brain regions using a combination of animal models.

For astrocytes, we propose modelling them using a large sphere. This is because, despite their ramified appearance, they are surrounded by an actin membrane (Haseleu et al., 2013), giving them more of a spherical cell structure. Our results have shown its sensitivity in tracking astrocyte reactions for the LPS model (Figure R.4), while no detection was observed in the ibotenic acid and lysolecithin models, accurately reflecting histological dynamics. To our knowledge, this approach represents the first modelling of astrocytes in the literature until a

recent preprint (Barsoum et al., 2024). Furthermore, we have identified a dw-MRI parameter to track neurodegeneration: tissue fraction (Figure R.6), although further experiments are necessary to validate with the same level of detail as microglia and astrocytes. This parameter has promising implications in both basic and clinical research, as it commonly accompanies neuroinflammation (McGeer et al., 1993, Dickson et al., 1993, Stephenson et al., 2018, Mayne et al., 2020).

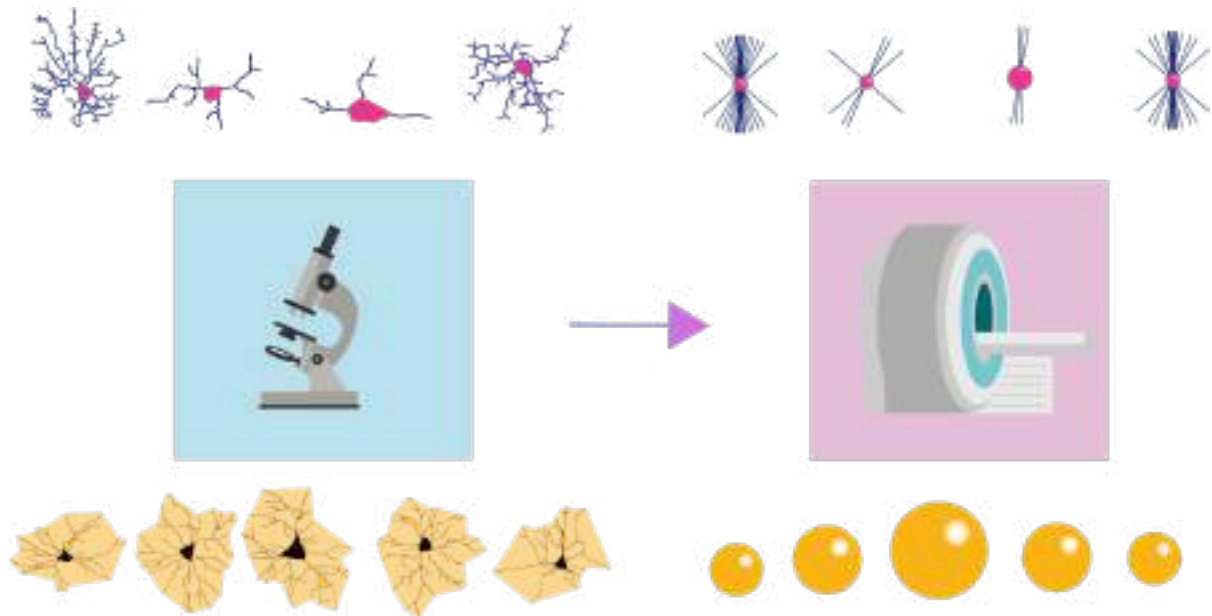


Figure D.1: Imaging Neuroinflammation non invasively and *in vivo*, an MRI-histology approach. Graphical abstract illustrating the main strategy and results of the project. On the left, microscopic reconstructions of microglia (top) and astrocytes (bottom) are shown, from LPS experiments. On the right, the corresponding representations using the dw-MRI model, highlighting the accuracy of our dw-MRI multicompartiment model in mirroring the morphological changes detected at histological level.

Importantly, we attribute part of our success to the measurement of relative changes in morphology rather than absolute quantities, considering the considerable heterogeneity within both astrocyte and microglia populations. Microglia, for instance, exhibit diverse morphologies depending on factors such as brain region (Grabert et al., 2016, Tan et al., 2022), age (Villa et al., 2016, Tay et al., 2017), and sex (Lenz and McCarthy, 2015, McCarthy and Nugent 2017), which have been extensively reviewed recently (Vidal-Itriago et al., 2022, Paolicelli et al., 2022). Similarly, astrocytes display variations with age and brain region (Bernardinelli et al., 2014, Khak and Sofroniew, 2015, Escartin et al., 2021). Therefore, basing our project on a single brain area, rat strain, or age group would limit its applicability in both animal models and humans patients. We believe these limitations were effectively mitigated by measuring changes on the treated hemisphere versus the control one, demonstrating a high correlation for both histology and dw-MRI between both hemispheres.

These conclusions also underscore the importance of selecting appropriate histological variables to correlate with biophysical models of diffusion. We conducted an exhaustive literature review before choosing the variables to analyse with histology. The literature documents a wide range of variables for both microglia (Fernández-Arjona et al., 2017; Heindl et al., 2018; Vendonk et al., 2016) and astrocytes (SheikhBahaei et al., 2018; Carvalho-Paulo et al., 2018). For instance, Sholl analysis is commonly used for microglia (Kongsui et al., 2014, Fernández-Arjona et al., 2017, Heindl et al., 2018, Athammer et al., 2020), while total ramification length is often considered for astrocytes (Cerbai et al., 2012, Carvalho-Paulo et al., 2018, Zhang et al., 2020), among many others. However, these variables focus into very detailed characteristics of glial populations, so we found more "general variables" encapsulating cell geometry and size with minimal complexity, aligning better with counterparts of the dw-MRI model. Convex hull analysis emerged as a promising tool for morphological assessment of astrocytes, having been used previously by others (Ambrosini et al., 2005, Wilhelmsomm et al., 2006, Carvalho-Paulo et al., 2018). In our analysis it showed a high correlation with corresponding dw-MRI measures. Regarding microglia, ramification dispersion and branching density, showed a high correlation between histology and imaging.

In conclusion, these results demonstrate our ability to distinguish microglia and astrocyte reactions (Figure D.1), both between themselves and regardless of a background of neurodegeneration or myelin loss. These findings open new ways of looking at brain tissue with MRI tools, as there were previously no models for astrocytes, and very limited for microglia, only for density estimation.

6.2.1. The value of our model and the emergence of new ones

Since its publication in May 2022, our paper has significantly impacted the MRI field. With over 18,000 downloads and more than 50 citations on Google Scholar, and a field-weighted citation impact of 2.93 in Scopus, placing it in the top 8% worldwide, its influence is evident. Furthermore, our dissemination article has garnered over 1200 reads, enhancing its impact and understanding across various fields and populations (Garcia-Hernandez et al., 2023).

The value of our work has been highlighted in several publications. For instance, Merenstein et al. (2023) utilised similar ramification orientation calculations to measure microstructural changes in restricted compartments after a learning task. Likewise, another model was developed using sticks and spheres to quantify neuron density, comparing the results with the histological data reported in Allen Brain Atlas. Kor et al. (2022) advocated for more studies like ours that compare histology with dw-MRI, emphasising the necessity of advanced and validated multicompartiment models. Reviews by DiPiero et al. (2022) and Xia et al. (2023) highlighted the power of our model for discerning microglia contributions to the image in brain development studies and expanding immunotherapies.

Meanwhile, other researchers have been working to fill existing gaps in the field. Reveley et al. (2024) verified the use of another dw-MRI variable for measuring myelin content *in vivo* in monkey grey matter, validating it as well with histology: diffusion kurtosis. Barsoum et al. (2024) developed an MRI marker for astrogliosis validating with GFAP histological quantifications. Additionally, alternative MRI modalities, such as functional MRI, are also being explored, as seen in Beliard et al. (2024), where they aim to detect demyelination through changes in the hemodynamic response in grey matter tissue.

To sum up, since its release in May 2022, our model has been a groundbreaking innovation. Its adoption by other researchers underscores its utility in measuring microstructural changes and advancing in multicompartment models. As well as the parallel efforts to address current gaps, underscoring the need for this kind of tools: the field is moving toward a unified objective of multicellular imaging with dw-MRI.

6.3. Implications and perspectives from our evidences: from research to clinical purposes

We have shown that our parameters for microglia and astrocyte have demonstrated high fidelity with the histological counterparts in tracking morphological changes in a specific manner in different conditions. Very importantly, we have shown as well that its translation is possible in a proof-of-concept experiment. Our framework was adapted to a human MRI scanner with 6 healthy patients, and we successfully tested that our dw-MRI model it is able to capture the differential microglia density across brain regions (Figure R.10), following the *post mortem* quantifications from Mittelbronn et al., (2001), resulting in, for example, higher microglia concentration in the hippocampus than the cerebellum, as expected (Lawson et al., 1990, Tan et al., 2020) (Figure D.2). Specifically, this was calculated by the combination of stick fraction and stick dispersion, a combination with high fidelity to microglia as demonstrated by the animals models, but as well with our *in silico* computations in different hypothetical brain scenarios (Figure R.9). These results are in accordance with previous work demonstrating that quantifying microglia density with multi compartment MRI is possible (Yi et al., 2019, Taquet et al., 2019). However, our approach was the first in the literature, to the best of our knowledge, that has demonstrated its direct utility with human patients without further modifications, now also achieved by Barakovic et al., 2024 by modelling microglia in a similar manner in multiple sclerosis patients (Barakovic et al., 2024).

But how multicellular models of dw-MRI can help the understanding of microglia and astrocyte contributions to health and disease?

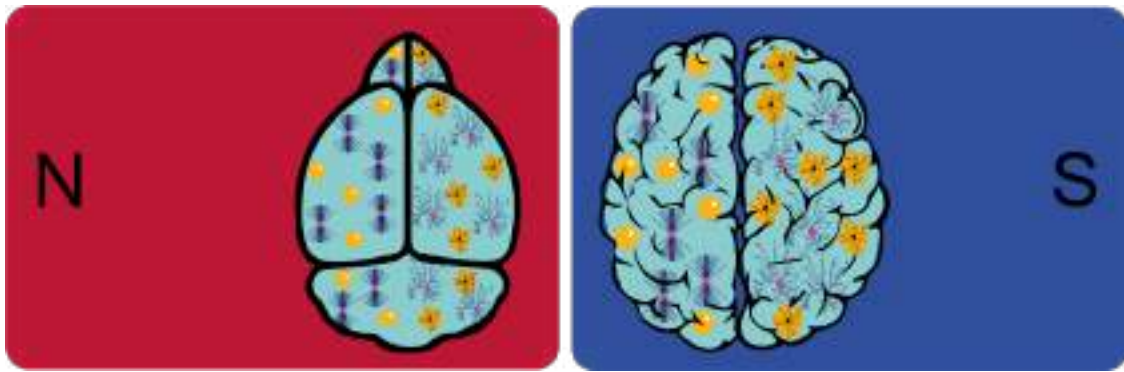


Figure D.2 Imaging microglia and astrocyte *in vivo*, from research to clinical purposes. Artistic schematization illustrating implications of our model, showing the visualisation of microglia and astrocytes using a magnet, with red representing the North pole and blue representing the South pole. Importantly, this technique applies to both rodent and human brains with several perspectives and benefits for the neuroscience field.

Our findings underscore the effectiveness of conventional clinical parameters in detecting tissue changes following microglia or astrocyte reactions (Figure R.11). However, these changes exhibit similar directions and magnitudes across diverse tissue units, thereby constraining their interpretative and applicative scope in both basic research and clinical contexts. Nonetheless, ongoing investigations, exemplified by Goebel et al., (2024), are trying to create tools to re-analyze already acquired data with a focus on cellular specificity, particularly in conditions such as multiple sclerosis. Additionally, our previous work in De Santis et al., (2020), evidenced that the observed increase in MD could be attributed to a reduction in the volume of microglial filaments in alcohol use disorders. This finding served as a cornerstone, suggesting a direct influence of microglia on MD alterations. Going further, our present results have demonstrated the potential to detect the multicellular source of a signal, and for example, by comparing a affected area with the healthy contralateral one or by comparing it with bibliography data, we hypothesise that we are able to monitor the mentioned morphological changes associated to diseases as multiple sclerosis or Alzheimer (Simpson et al., 2010; Phatnani et al., 2013; Guruswamy and ElAli, 2017; Davies et al., 2017; Arranz and Stropper et al., 2019; De Santis et al., 2020; Shahidehpour et al., 2021; Kim et al., 2024). Supporting our idea, Rios-Carrillos et al. (2023) have suggested using our model to overcome limitations in machine learning automatic classification of histopathologies in white matter. Additionally, Mills et al. (2022) highlighted our model as a promising alternative to mitigate limitations of PET imaging in clinical settings, shedding light on microglia status in different diseases. The practical application of sticks and spheres to track microglia in multiple sclerosis patients by Barakovic et al. (2024) further supports our hypothesis and perspectives.

Our dw-MRI model tool also opens new avenues for tracking the novel therapies targeting microglia and astrocyte reactions in pathological scenarios, such as the ones generated specifically for Alzheimer's disease and multiple sclerosis in the latest years (Wilbanks et al.,

2019, Janus et al., 2020, Geladaris et al., 2024, Wasén et al., 2024, Guadalupi et al., 2024). We believe our DW-MRI model can capture the associated reactions when the drugs generate observable changes in the morphology of microglia and/or astrocytes, as evidenced by the histological changes shown in Geladaris et al. (2024). Specifically, by scanning animals before, during, and after treatment, alterations in the specific contribution of the target population to the dw-MRI signal could be detected.

However, and at this point of the discussion, an important question arises: What if the disease does not generate morphological changes typically considered ‘reactive’ in microglia or astrocytes but rather induces a specific disease-associated profile? As emphasised in compendiums for microglia and astrocytes (Escartin et al., 2021, Paolicelli et al., 2022), characterising glia requires consideration of their various layers of complexity, as they exhibit a continuum of behaviour from genetic to morphological levels. Is it possible to merge multiple layers of complexity in one single tool for a comprehensive characterization of glial roles in a given scenario? Recent research, such as that by Androvic et al. (2023), suggests promising avenues for integrating structural, molecular, and morphological profiles of microglia. By combining spatial transcriptomics with electron microscopy, Androvic et al. were able to identify heterogeneous microglia populations responding to interferon. By correlating transcriptomic profiles with histological morphological data, they successfully clustered different microglia populations, ultimately linking these features with gene expression. This integration enables a deeper understanding of microglial dynamics, bridging the gap between morphology, genetic expression and transcriptomics. We believe that augmenting our model with an additional layer would be possible and would enhance the interpretability of MRI results. For instance, by incorporating variables related to microglial reaction in health and disease, such as transcriptomic profiles (Chiu et al., 2013, Wes et al., 2016, Pavlou et al., 2019, Maurya et al., 2023, Matusova et al., 2023, Rachmian et al., 2024) or epigenomics signatures (Cho et al., 2015, Datta et al., 2018, Pavlou et al., 2019, Welle et al., 2021, Petralla et al., 2021). Supporting this idea, some variables are already being obtained in clinical settings to improve the interpretation of MRI signals. For instance, blood sample collection, as demonstrated by Barakovic et al. (2024), can provide additional insights to complement sphere and stick characterization of microglia, by measuring serum neurofilament, a proxy of axonal damage. Incorporating these multidimensional approaches would not only enrich our understanding of glial dynamics but also prepare the ground for more targeted and effective interventions in neurological disorders.

6.4. Limitations

Despite the aforementioned results and implications, this study presents some limitations. Our methodological decisions in constructing the model are limited by one biophysical variable we did not consider: the exchange of water between the glial compartments and the extracellular space. While we assumed this water interchange to be minimal based on previous studies (Pasternak et al., 2009), it has been demonstrated that both microglia and astrocytes possess active aquaporins in their membrane (Gao et al., 2006, Roberta and

Rosella, 2010), specialised channels for water extrusion, such as aquaporin 1 (Gao et al., 2006) and aquaporin 4, the most common one in astrocytes (Xiao and Hu, 2014). Additionally, and as example, aquaporin 1 has been implicated in pathological scenarios like multiple sclerosis (Sato et al., 2007) and haemorrhage (Amiry-Moghaddam and Ottersen, 2003). So, despite our findings suggesting minimal influence of water exchange, a future comprehensive study could aim to enhance the model's complexity by incorporating these variables (Nilsson et al., 2013) and testing it against the MRI data we have already acquired, offering additional new avenues for diagnosing diseases like multiple sclerosis.

Besides, a possible limitation of our model is that we have not incorporated another very glial cell type: oligodendrocytes. They are the principal myelinators of the central nervous system (Penfeld 1924, Bauman and Pham-Dinh, 2001, Simons and Nave, 2015, Franklin et al., 2021) and they are also linked to the progression of certain diseases and chronic inflammation (Ozawa et al., 2004, Kragh et al., 2013, Chen et al., 2022, Gim et al., 2022). The exclusion of this specific glial type may have impacted the accuracy of our results in mapping microglia and astrocytes. However, after calculating the dimensions of oligodendrocytes, we find that their ramifications can double in number and triplicate in length compared to microglia (Chan et al., 2013), and they have at least double the size of our astrocytes when considering the convex hull. Additionally, supporting this conclusion, we did not observe any alteration in the signal of astrocytes or microglia in the lysolecithin model (Figure R.8). After demyelination, the morphology of oligodendrocytes would certainly have been affected.

Finally, while we have demonstrated that our model is directly translatable to human patients by the use of research MRI scanners, its translation to routinary hospital machines is limited without further modifications. The major constraint is that the protocol needs adaptations since the magnetic gradients power requirements exceed what typical hospital MRI machines can provide. Additionally, these machines usually have software constraints that prevent the modification of parameters such as b-value or diffusion time for research purposes. Lately, another significant constraint is the time required for each patient acquisition, which can last up to 40 minutes per session as we have indicated. When combined with the conventional variables typically acquired (MD, T1/T2, T2*, and extracellular diffusivity), this can extend the total acquisition time to 1 hour and 30 minutes for a single patient. Practically, this presents a significant time burden. This limitation is currently an investigation line (see Futures lines).

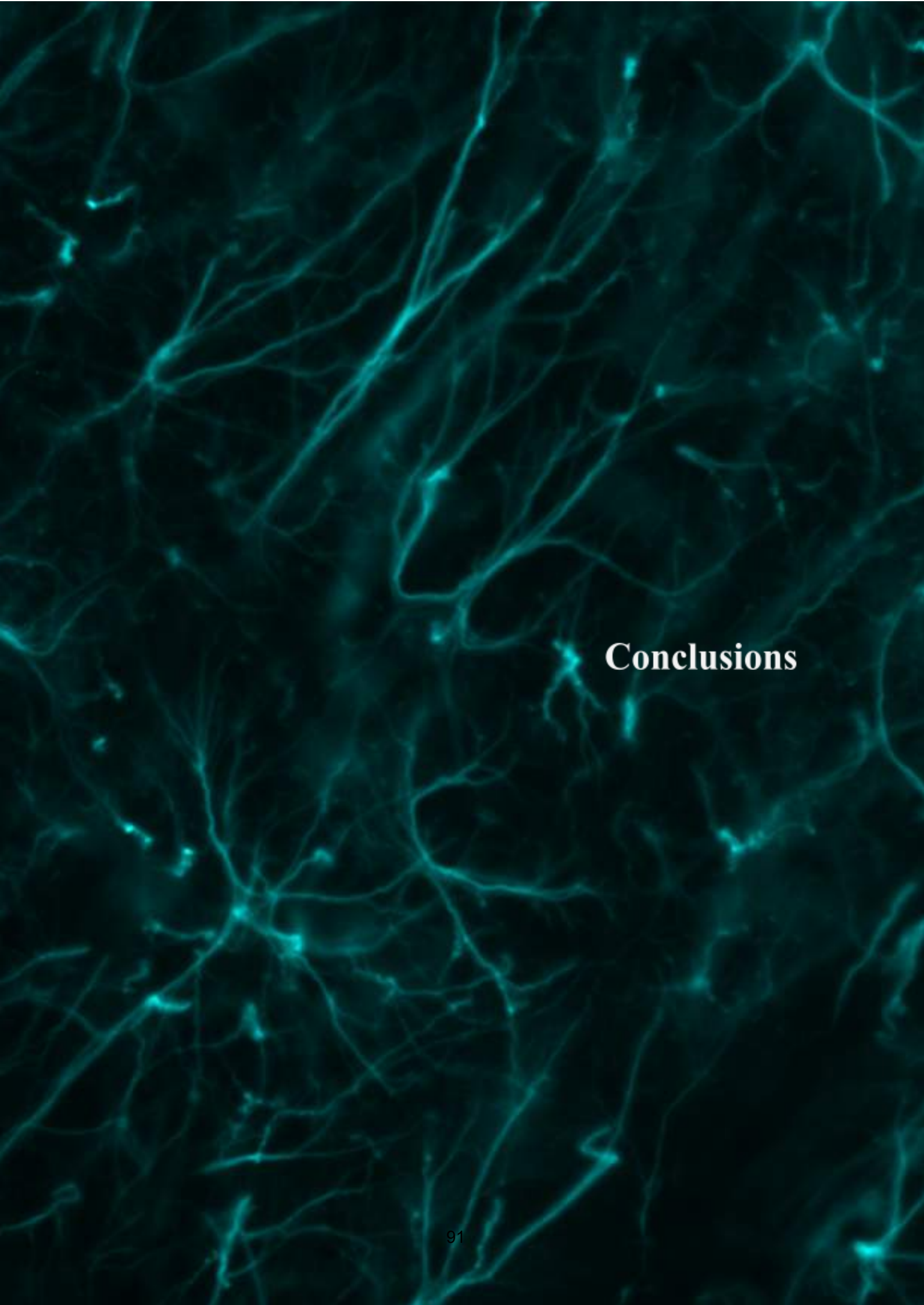
6.5. Future lines

In summary, our progress with dw-MRI is groundbreaking, enabling non-invasive imaging of neuroinflammation dynamics in living subjects for the first time in the literature. We've also highlighted the value of multicellular models for understanding grey matter, which has implications for both basic and clinical research, interrogating microglia and astrocyte morphological dynamics in health and disease. Despite its current limitations, these

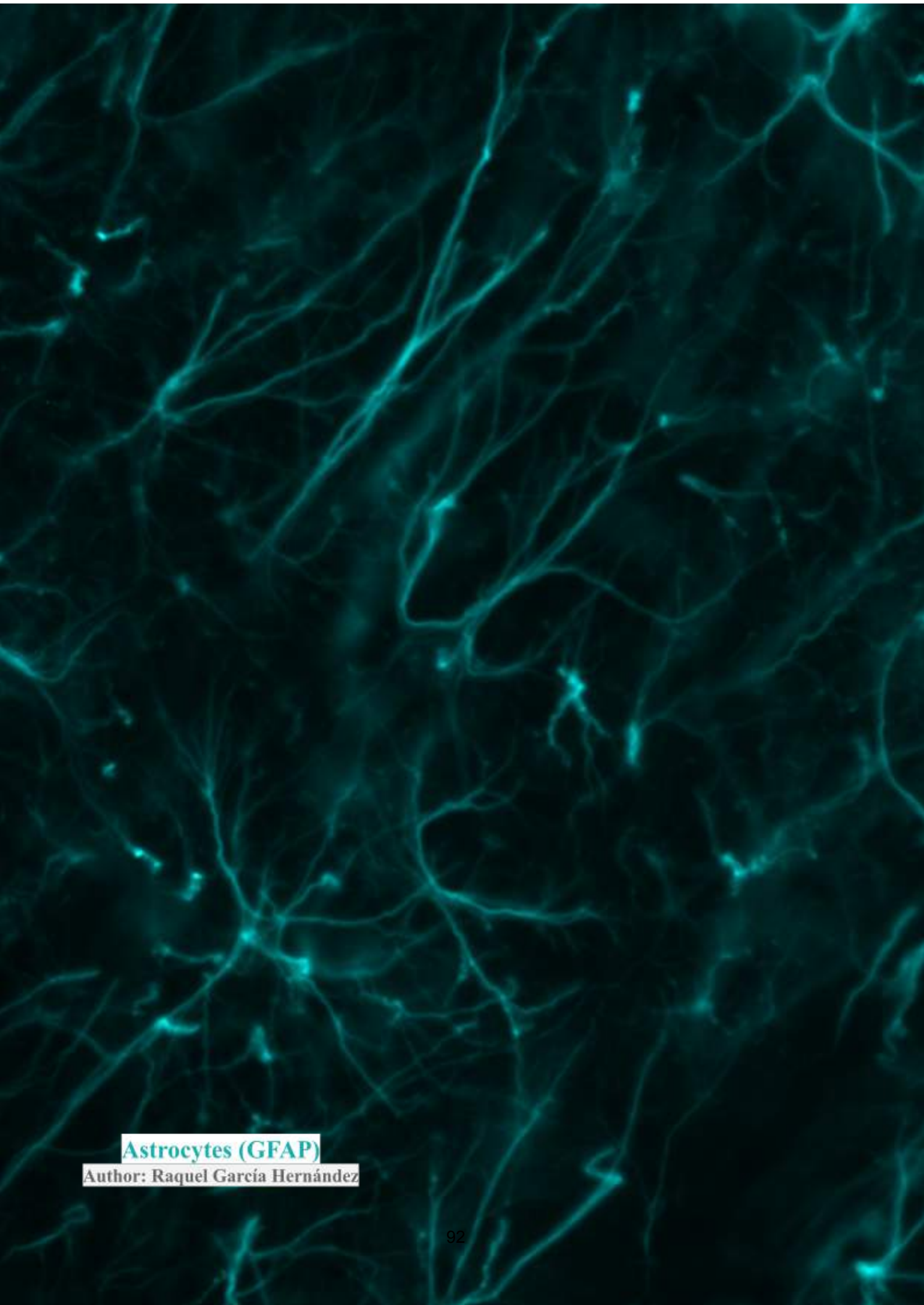
advancements mark a major step forward in studying brain phenomena related to glial responses.

However, although significant progress has been achieved, there are still unanswered questions and opportunities for improvement, prompting further research in three primary directions:

- Improving tissue characterisation and sensitivity: In the future, to further characterise the tissue, we will include specific variables for oligodendrocytes in the dw-MRI model, with the specific use of animal models targeting oligodendrocytes (Abraham et al., 2023). We will also refine the compartments of the model already developed to increase sensitivity, by testing in animals models of diseases such as Alzheimer's or multiple sclerosis with milder morphological glial phenotypes than those presented in this research. Furthermore, we will also investigate the incorporation of a water exchange variable for each of the compartments in the dw-MRI model.
- Adapting for hospital MRI machines. To achieve this integration, we need to make adjustments to reduce acquisition time and adapt acquisition and power parameters. This might mean simplifying the acquisition protocols or reducing the required variables for the dw-MRI analysis. Implementing the first solution would require redoing experiments with animal models of neuroinflammation. However, the second option would only involve re-analyzing the existing data to validate its feasibility with a lower number of variables, especially given the completed histological validation. It's important to note that Silvia De Santis and her laboratory are actively working on these research aspects. They are using artificial intelligence methods to minimise the number of variables needed for analysis without compromising result accuracy.
- Exploring glial dynamics beyond pathology: Our model also opens new avenues for understanding how microglia and astrocytes respond to various brain phenomena. For instance, it would allow to further understand the role of glia in learning (Sardinha et al., 2017; Kol et al., 2020; Abreu et al., 2023) by examining the source of the observable differences in conventional MRI parameters after learning paradigms in rodents (Blumenfeld-Katzir et al., 2011; Merenstein et al., 2023). Alternatively, and as another example, our model can be utilised to investigate the involvement of microglia in the maternal brain during birth, delivery, and postpartum, as directly suggested by the authors (Paternina-Die et al., 2024).



Conclusions



Astrocytes (GFAP)

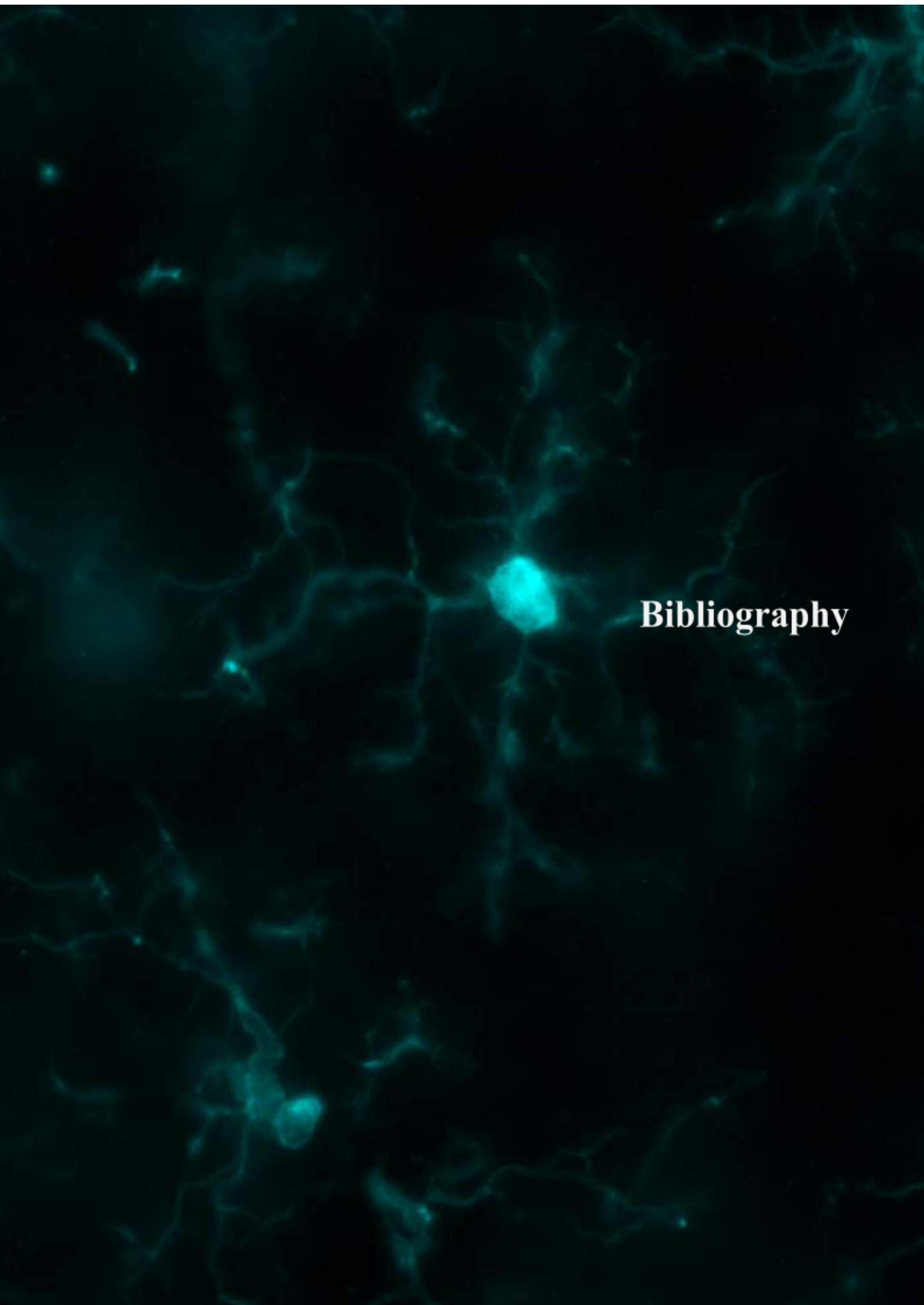
Author: Raquel García Hernández

VII. Conclusions

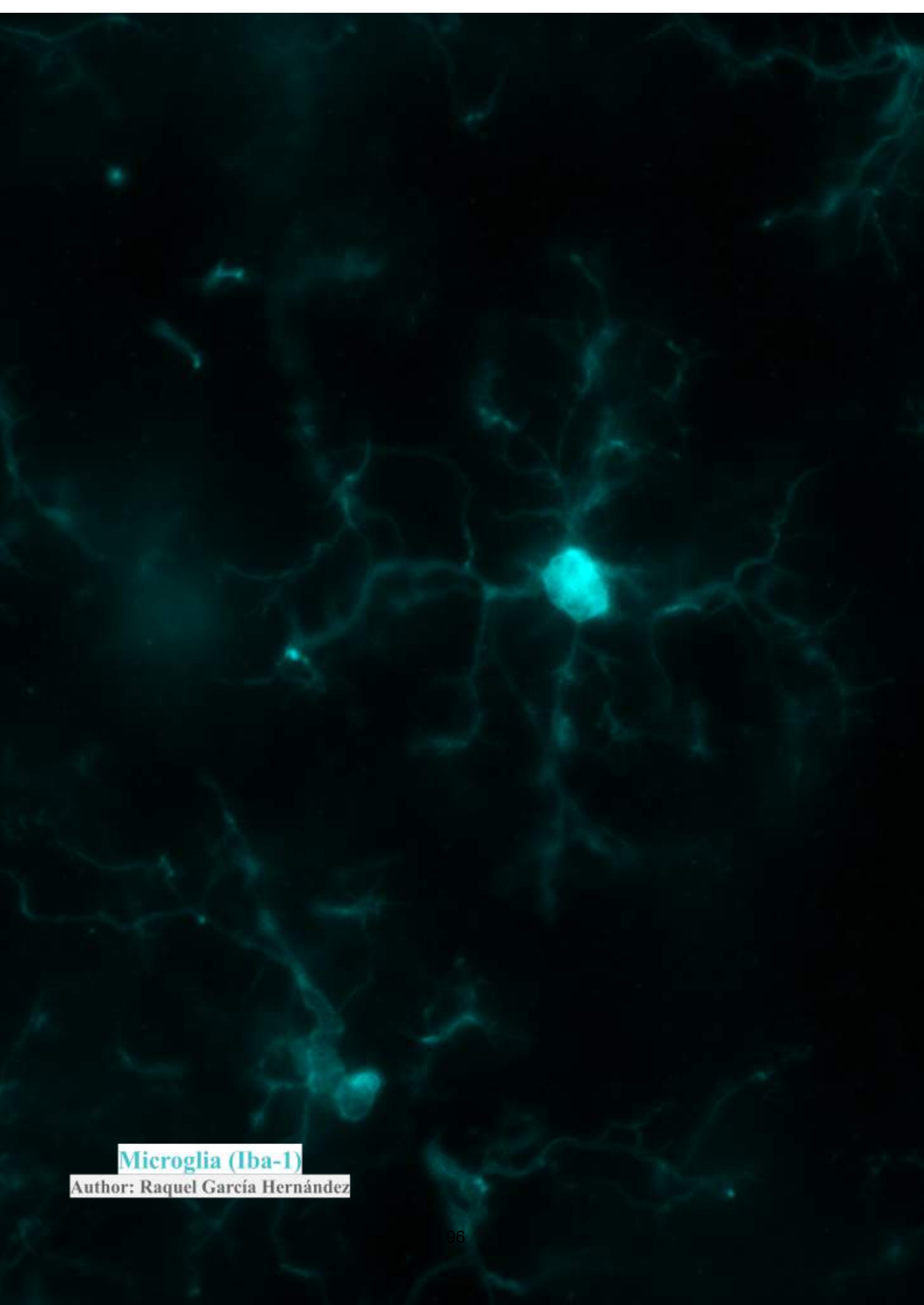
1. We have identified three dw-MRI model parameters that specifically characterise microglia reaction: small sphere radius, stick fraction, and stick dispersion. These parameters show a high correlation with their histological counterparts, validating their specificity.
2. We have discovered one diffusion parameter that specifically characterises astrocytes reaction: big sphere radius. This parameter also shows a high correlation with its histological counterpart, validating its specificity.
3. The model has demonstrated great robustness in differentiating microglia and astrocyte reactions, even in scenarios such as neurodegeneration and demyelination.
4. We have identified a promising variable for measuring neurodegeneration: tissue fraction, which shows a strong correlation between histology and dw-MRI model results.
5. The proof of concept study in healthy patients has been satisfactory, accurately estimating microglia density in different brain areas, demonstrating the high translational potential of the presented model.

VII. Conclusiones

1. Hemos identificado tres parámetros del modelo de IRMd que caracterizan específicamente la reacción de la microglía: radio de esfera pequeña, fracción de barra y dispersión de barra. Estos parámetros muestran una alta correlación con sus contrapartes histológicas, validando su especificidad.
2. Hemos descubierto un parámetro de difusión que caracteriza específicamente la reacción de los astrocitos: radio de esfera grande. Este parámetro también muestra una alta correlación con su contraparte histológica, validando su especificidad.
3. El modelo ha demostrado una gran robustez en la diferenciación de las reacciones de microglía y astrocitos, incluso en escenarios como la neurodegeneración y la desmielinización.
4. Hemos identificado una variable prometedora para medir la neurodegeneración: fracción de tejido, que muestra una fuerte correlación entre los resultados de histología y del modelo de IRMd.
5. El estudio de prueba de concepto en pacientes sanos ha sido satisfactorio, estimando con precisión la densidad de la microglía en diferentes áreas del cerebro, demostrando el alto potencial de traducción del modelo presentado.



Bibliography



Microglia (Iba-1)

Author: Raquel García Hernández

VIII. Bibliography

Andersson, P. B., Perry, V. H., & Gordon, S. (1992). The acute inflammatory response to lipopolysaccharide in CNS parenchyma differs from that in other body tissues. *Neuroscience*, *48*(1), 169–186. [https://doi.org/10.1016/0306-4522\(92\)90347-5](https://doi.org/10.1016/0306-4522(92)90347-5)

Abe, T., Sugihara, H., Nawa, H., Shigemoto, R., Mizuno, N., & Nakanishi, S. (1992). Molecular characterization of a novel metabotropic glutamate receptor mGluR5 coupled to inositol phosphate/Ca²⁺ signal transduction. *The Journal of biological chemistry*, *267*(19), 13361–13368.

Abraham, M., Peterburs, J., & Mundorf, A. (2023). Oligodendrocytes matter: a review of animal studies on early adversity. *Journal of neural transmission (Vienna, Austria : 1996)*, *130*(9), 1177–1185. <https://doi.org/10.1007/s00702-023-02643-4>

Abreu, D. S., Gomes, J. I., Ribeiro, F. F., Diógenes, M. J., Sebastião, A. M., & Vaz, S. H. (2023). Astrocytes control hippocampal synaptic plasticity through the vesicular-dependent release of D-serine. *Frontiers in cellular neuroscience*, *17*, 1282841. <https://doi.org/10.3389/fncel.2023.1282841>

Albertini, R., & Bianchi, R. (2010). Aquaporins and glia. *Current neuropharmacology*, *8*(2), 84–91. <https://doi.org/10.2174/157015910791233178>

Alexander D. C. (2008). A general framework for experiment design in diffusion MRI and its application in measuring direct tissue-microstructure features. *Magnetic resonance in medicine*, *60*(2), 439–448. <https://doi.org/10.1002/mrm.21646>

Alexander, A. L., Lee, J. E., Lazar, M., & Field, A. S. (2007). Diffusion tensor imaging of the brain. *Neurotherapeutics : the journal of the American Society for Experimental NeuroTherapeutics*, *4*(3), 316–329. <https://doi.org/10.1016/j.nurt.2007.05.011>

Althammer, F., Ferreira-Neto, H. C., Rubaharan, M., Roy, R. K., Patel, A. A., Murphy, A., Cox, D. N., & Stern, J. E. (2020). Three-dimensional morphometric analysis reveals time-dependent structural changes in microglia and astrocytes in the central amygdala and hypothalamic paraventricular nucleus of heart failure rats. *Journal of neuroinflammation*, *17*(1), 221. <https://doi.org/10.1186/s12974-020-01892-4>

Althammer, F., Ferreira-Neto, H. C., Rubaharan, M., Roy, R. K., Patel, A. A., Murphy, A., Cox, D. N., & Stern, J. E. (2020). Three-dimensional morphometric analysis reveals time-dependent structural changes in microglia and astrocytes in the central amygdala and hypothalamic paraventricular nucleus of heart failure rats. *Journal of neuroinflammation*, *17*(1), 221. <https://doi.org/10.1186/s12974-020-01892-4>

Amaral, D. G., Scharfman, H. E., & Lavenex, P. (2007). The dentate gyrus: fundamental neuroanatomical organization (dentate gyrus for dummies). *Progress in brain research*, *163*, 3–22. [https://doi.org/10.1016/S0079-6123\(07\)63001-5](https://doi.org/10.1016/S0079-6123(07)63001-5)

Amaral, D., Lavenex, P., Andersen, P., Morris, R., Bliss, T., & O'Keefe, J. (2007). The hippocampus book. *The hippocampus book*, 37-45.

Ambrosini, A., Louin, G., Croci, N., Plotkine, M., & Jafarian-Tehrani, M. (2005). Characterization of a rat model to study acute neuroinflammation on histopathological, biochemical and functional outcomes. *Journal of neuroscience methods*, *144*(2), 183–191. <https://doi.org/10.1016/j.jneumeth.2004.11.002>

Amiry-Moghaddam, M., & Ottersen, O. P. (2003). The molecular basis of water transport in the brain. *Nature reviews. Neuroscience*, *4*(12), 991–1001. <https://doi.org/10.1038/nrn1252>

Andriezen W. L. (1893). The Neuroglia Elements in the Human Brain. *British medical journal*, *2*(1700), 227–230. <https://doi.org/10.1136/bmj.2.1700.227>

Androvic, P., Schifferer, M., Perez Anderson, K., Cantuti-Castelvetri, L., Jiang, H., Ji, H., Liu, L., Gouna, G., Berghoff, S. A., Besson-Girard, S., Knoferle, J., Simons, M., & Gokce, O. (2023). Spatial Transcriptomics-correlated Electron Microscopy maps transcriptional and ultrastructural responses to brain injury. *Nature communications*, *14*(1), 4115. <https://doi.org/10.1038/s41467-023-39447-9>

Araque, A., Parpura, V., Sanzgiri, R. P., & Haydon, P. G. (1999). Tripartite synapses: glia, the unacknowledged partner. *Trends in neurosciences*, *22*(5), 208–215. [https://doi.org/10.1016/s0166-2236\(98\)01349-6](https://doi.org/10.1016/s0166-2236(98)01349-6)

Arena, G., Sharma, K., Agyeah, G., Krüger, R., Grünewald, A., & Fitzgerald, J. C. (2022). Neurodegeneration and Neuroinflammation in Parkinson's Disease: a Self-Sustained Loop. *Current neurology and neuroscience reports*, *22*(8), 427–440. <https://doi.org/10.1007/s11910-022-01207-5>

Arisi, G. M., & Garcia-Cairasco, N. (2007). Doublecortin-positive newly born granule cells of hippocampus have abnormal apical dendritic morphology in the pilocarpine model of temporal lobe epilepsy. *Brain research*, *1165*, 126–134. <https://doi.org/10.1016/j.brainres.2007.06.037>

Arranz, A. M., & De Strooper, B. (2019). The role of astroglia in Alzheimer's disease: pathophysiology and clinical implications. *The Lancet. Neurology*, *18*(4), 406–414. [https://doi.org/10.1016/S1474-4422\(18\)30490-3](https://doi.org/10.1016/S1474-4422(18)30490-3)

Assaf, Y., & Basser, P. J. (2005). Composite hindered and restricted model of diffusion (CHARMED) MR imaging of the human brain. *NeuroImage*, *27*(1), 48–58. <https://doi.org/10.1016/j.neuroimage.2005.03.042>

Assaf, Y., Ben-Bashat, D., Chapman, J., Peled, S., Biton, I. E., Kafri, M., Segev, Y., Hendler, T., Korczyn, A. D., Graif, M., & Cohen, Y. (2002). High b-value q-space analyzed diffusion-weighted MRI: application to multiple sclerosis. *Magnetic resonance in medicine*, *47*(1), 115–126. <https://doi.org/10.1002/mrm.10040>

Assaf, Y., Blumenfeld-Katzir, T., Yovel, Y., & Basser, P. J. (2008). AxCaliber: a method for measuring axon diameter distribution from diffusion MRI. *Magnetic resonance in medicine*, *59*(6), 1347–1354. <https://doi.org/10.1002/mrm.21577>

Assaf, Y., Freidlin, R. Z., Rohde, G. K., & Basser, P. J. (2004). New modeling and experimental framework to characterize hindered and restricted water diffusion in brain white matter. *Magnetic resonance in medicine*, 52(5), 965–978. <https://doi.org/10.1002/mrm.20274>

Azin, M., Goudarzvand, M., Mirnajafi-Zadeh, J., & Javan, M. (2013). Field potential recording from rat hippocampus provides a functional evaluation method for assessing demyelination and myelin repair. *Neurological research*, 35(8), 837–843. <https://doi.org/10.1179/1743132813Y.0000000221>

Baliyan, V., Das, C. J., Sharma, R., & Gupta, A. K. (2016). Diffusion weighted imaging: Technique and applications. *World journal of radiology*, 8(9), 785–798. <https://doi.org/10.4329/wjr.v8.i9.785>

Banati, R. B., Myers, R., & Kreutzberg, G. W. (1997). PK ('peripheral benzodiazepine')--binding sites in the CNS indicate early and discrete brain lesions: microautoradiographic detection of [3H]PK11195 binding to activated microglia. *Journal of neurocytology*, 26(2), 77–82. <https://doi.org/10.1023/a:1018567510105>

Barakovic, M., Weigel, M., Cagol, A., Schaedelin, S., Galbusera, R., Lu, P. J., Chen, X., Melie-Garcia, L., Ocampo-Pineda, M., Bahn, E., Stadelmann, C., Palombo, M., Kappos, L., Kuhle, J., Magon, S., & Granziera, C. (2024). A novel imaging marker of cortical "cellularity" in multiple sclerosis patients. *Scientific reports*, 14(1), 9848. <https://doi.org/10.1038/s41598-024-60497-6>

Barr, M. L. (1974). *The human nervous system: An anatomical viewpoint*. Harper & Row.

Barsoum, S., Latimer, C. S., Nolan, A. L., Barrett, A., Chang, K., Troncoso, J., Keene, C. D., & Benjamini, D. (2024). Resiliency to Alzheimer's disease neuropathology can be distinguished from dementia using cortical astrogliosis imaging. *BioRxiv*, 2024.05.06.592719. <https://doi.org/10.1101/2024.05.06.592719>

Basser, P. J., & Pierpaoli, C. (1996). Microstructural and physiological features of tissues elucidated by quantitative-diffusion-tensor MRI. *Journal of magnetic resonance. Series B*, 111(3), 209–219. <https://doi.org/10.1006/jmrb.1996.0086>

Basser, P. J., & Pierpaoli, C. (1996). Microstructural and physiological features of tissues elucidated by quantitative-diffusion-tensor MRI. *Journal of magnetic resonance. Series B*, 111(3), 209–219. <https://doi.org/10.1006/jmrb.1996.0086>

Basser, P. J., Mattiello, J., & LeBihan, D. (1994). MR diffusion tensor spectroscopy and imaging. *Biophysical journal*, 66(1), 259–267. [https://doi.org/10.1016/S0006-3495\(94\)80775-1](https://doi.org/10.1016/S0006-3495(94)80775-1)

Baumann, N., & Pham-Dinh, D. (2001). Biology of oligodendrocyte and myelin in the mammalian central nervous system. *Physiological reviews*, 81(2), 871–927. <https://doi.org/10.1152/physrev.2001.81.2.871>

Bayraktar, O. A., Fuentealba, L. C., Alvarez-Buylla, A., & Rowitch, D. H. (2014). Astrocyte development and heterogeneity. *Cold Spring Harbor perspectives in biology*, 7(1), a020362. <https://doi.org/10.1101/cshperspect.a020362>

- Becher, B., Spath, S., & Goverman, J. (2017). Cytokine networks in neuroinflammation. *Nature reviews. Immunology*, *17*(1), 49–59. <https://doi.org/10.1038/nri.2016.123>
- Beliard, B., Delay, L., Rivals, I., Travert-Jounnaeu, Y., Ialy-Radio, N., Réaux-Le Goazigo, A., Deffieux, T., Bradley, D., Tanter, M. & Pezet, S. (2024). Development of a novel, non-invasive and whole brain biomarker of demyelination in a mouse model of multiple sclerosis. 2024.03.18.585596 bioRxiv <https://doi.org/10.1101/2024.03.18.585596>
- Ben Haim, L., & Rowitch, D. H. (2017). Functional diversity of astrocytes in neural circuit regulation. *Nature reviews. Neuroscience*, *18*(1), 31–41. <https://doi.org/10.1038/nrn.2016.159>
- Bernardinelli, Y., Muller, D., & Nikonenko, I. (2014). Astrocyte-synapse structural plasticity. *Neural plasticity, 2014*, 232105. <https://doi.org/10.1155/2014/232105>
- Bharani, K. L., Derex, R., Granholm, A. C., & Ledreux, A. (2017). A noradrenergic lesion aggravates the effects of systemic inflammation on the hippocampus of aged rats. *PloS one*, *12*(12), e0189821. <https://doi.org/10.1371/journal.pone.0189821>
- Blinzinger, K., & Kreutzberg, G. (1968). Displacement of synaptic terminals from regenerating motoneurons by microglial cells. *Zeitschrift fur Zellforschung und mikroskopische Anatomie (Vienna, Austria : 1948)*, *85*(2), 145–157. <https://doi.org/10.1007/BF00325030>
- Blumenfeld-Katzir, T., Pasternak, O., Dagan, M., & Assaf, Y. (2011). Diffusion MRI of structural brain plasticity induced by a learning and memory task. *PloS one*, *6*(6), e20678. <https://doi.org/10.1371/journal.pone.0020678>
- Cai, Z., Hussain, M. D., & Yan, L. J. (2014). Microglia, neuroinflammation, and beta-amyloid protein in Alzheimer's disease. *The International journal of neuroscience*, *124*(5), 307–321. <https://doi.org/10.3109/00207454.2013.833510>
- Campbell, L. R., Pang, Y., Ojeda, N. B., Zheng, B., Rhodes, P. G., & Alexander, B. T. (2012). Intracerebral lipopolysaccharide induces neuroinflammatory change and augmented brain injury in growth-restricted neonatal rats. *Pediatric research*, *71*(6), 645–652. <https://doi.org/10.1038/pr.2012.26>
- Caramés JM, Pérez-Montoyo E, Garcia-Hernandez R & Canals S. (2020). Hippocampal dentate gyrus coordinates brain-wide communication and memory updating through an inhibitory gating. bioRxiv 2020.07.14.202218 . <https://doi.org/10.1101/2020.07.14.202218>
- Carvalho-Paulo, D., de Moraes Magalhães, N. G., de Almeida Miranda, D., Diniz, D. G., Henrique, E. P., Moraes, I. A. M., Pereira, P. D. C., de Melo, M. A. D., de Lima, C. M., de Oliveira, M. A., Guerreiro-Diniz, C., Sherry, D. F., & Diniz, C. W. P. (2018). Hippocampal Astrocytes in Migrating and Wintering Semipalmated Sandpiper *Calidris pusilla*. *Frontiers in neuroanatomy*, *11*, 126. <https://doi.org/10.3389/fnana.2017.00126>
- Cerdán Cerdá, A., Toschi, N., Treaba, C. A., Barletta, V., Herranz, E., Mehndiratta, A., Gomez-Sanchez, J. A., Mainero, C., & De Santis, S. (2024). A translational MRI approach to validate acute axonal damage detection as an early event in multiple sclerosis. *eLife*, *13*, e79169. <https://doi.org/10.7554/eLife.79169>

Chan, C. F., Kuo, T. W., Weng, J. Y., Lin, Y. C., Chen, T. Y., Cheng, J. K., & Lien, C. C. (2013). Ba²⁺- and bupivacaine-sensitive background K⁺ conductances mediate rapid EPSP attenuation in oligodendrocyte precursor cells. *The Journal of physiology*, *591*(19), 4843–4858. <https://doi.org/10.1113/jphysiol.2013.257113>

Chao, C. C., Hu, S., Molitor, T. W., Shaskan, E. G., & Peterson, P. K. (1992). Activated microglia mediate neuronal cell injury via a nitric oxide mechanism. *Journal of immunology (Baltimore, Md. : 1950)*, *149*(8), 2736–2741.

Chavhan, G. B., Babyn, P. S., Thomas, B., Shroff, M. M., & Haacke, E. M. (2009). Principles, techniques, and applications of T2*-based MR imaging and its special applications. *Radiographics : a review publication of the Radiological Society of North America, Inc*, *29*(5), 1433–1449. <https://doi.org/10.1148/rg.295095034>

Chen, W. T., Lu, A., Craessaerts, K., Pavie, B., Sala Frigerio, C., Corthout, N., Qian, X., Laláková, J., Kühnemund, M., Voytyuk, I., Wolfs, L., Mancuso, R., Salta, E., Balusu, S., Snellinx, A., Munck, S., Jurek, A., Fernandez Navarro, J., Saido, T. C., Huitinga, I., ... De Strooper, B. (2020). Spatial Transcriptomics and In Situ Sequencing to Study Alzheimer's Disease. *Cell*, *182*(4), 976–991.e19. <https://doi.org/10.1016/j.cell.2020.06.038>

Chen, Z., Jalabi, W., Shpargel, K. B., Farabaugh, K. T., Dutta, R., Yin, X., Kidd, G. J., Bergmann, C. C., Stohman, S. A., & Trapp, B. D. (2012). lipopolysaccharide-induced microglial activation and neuroprotection against experimental brain injury is independent of hematogenous TLR4. *The Journal of neuroscience : the official journal of the Society for Neuroscience*, *32*(34), 11706–11715. <https://doi.org/10.1523/JNEUROSCI.0730-12.2012>

Cheng, S., Hou, J., Zhang, C., Xu, C., Wang, L., Zou, X., Yu, H., Shi, Y., Yin, Z., & Chen, G. (2015). Minocycline reduces neuroinflammation but does not ameliorate neuron loss in a mouse model of neurodegeneration. *Scientific reports*, *5*, 10535. <https://doi.org/10.1038/srep10535>

Chiu, I. M., Morimoto, E. T., Goodarzi, H., Liao, J. T., O'Keeffe, S., Phatnani, H. P., Muratet, M., Carroll, M. C., Levy, S., Tavazoie, S., Myers, R. M., & Maniatis, T. (2013). A neurodegeneration-specific gene-expression signature of acutely isolated microglia from an amyotrophic lateral sclerosis mouse model. *Cell reports*, *4*(2), 385–401. <https://doi.org/10.1016/j.celrep.2013.06.018>

Cho, S. H., Chen, J. A., Sayed, F., Ward, M. E., Gao, F., Nguyen, T. A., Krabbe, G., Sohn, P. D., Lo, I., Minami, S., Devidze, N., Zhou, Y., Coppola, G., & Gan, L. (2015). SIRT1 deficiency in microglia contributes to cognitive decline in aging and neurodegeneration via epigenetic regulation of IL-1 β . *The Journal of neuroscience : the official journal of the Society for Neuroscience*, *35*(2), 807–818. <https://doi.org/10.1523/JNEUROSCI.2939-14.2015>

Clarke, B. E., & Patani, R. (2020). The microglial component of amyotrophic lateral sclerosis. *Brain : a journal of neurology*, *143*(12), 3526–3539. <https://doi.org/10.1093/brain/awaa309>

Codreanu, I., Dasanu, C. A., Weinstein, G. S., & Divgi, C. (2013). Fluorodeoxyglucose-induced allergic reaction: a case report. *Journal of oncology pharmacy practice : official publication of the*

International Society of Oncology Pharmacy Practitioners, 19(1), 86–88.
<https://doi.org/10.1177/1078155211436023>

Cooper-Knock, J., Green, C., Altschuler, G., Wei, W., Bury, J. J., Heath, P. R., Wyles, M., Gelsthorpe, C., Highley, J. R., Lorente-Pons, A., Beck, T., Doyle, K., Otero, K., Traynor, B., Kirby, J., Shaw, P. J., & Hide, W. (2017). A data-driven approach links microglia to pathology and prognosis in amyotrophic lateral sclerosis. *Acta neuropathologica communications*, 5(1), 23.
<https://doi.org/10.1186/s40478-017-0424-x>

Costa, A. P., Tramontina, A. C., Biasibetti, R., Batassini, C., Lopes, M. W., Wartchow, K. M., Bernardi, C., Tortorelli, L. S., Leal, R. B., & Gonçalves, C. A. (2012). Neuroglial alterations in rats submitted to the okadaic acid-induced model of dementia. *Behavioural brain research*, 226(2), 420–427. <https://doi.org/10.1016/j.bbr.2011.09.035>

da Silva, A. A. F., Fiadeiro, M. B., Bernardino, L. I., Fonseca, C. S. P., Baltazar, G. M. F., & Cristóvão, A. C. B. (2024). "lipopolysaccharide-induced animal models for neuroinflammation - An overview." *Journal of neuroimmunology*, 387, 578273.
<https://doi.org/10.1016/j.jneuroim.2023.578273>

Datta, M., Staszewski, O., Raschi, E., Frosch, M., Hagemeyer, N., Tay, T. L., Blank, T., Kreutzfeldt, M., Merkler, D., Ziegler-Waldkirch, S., Matthias, P., Meyer-Luehmann, M., & Prinz, M. (2018). Histone Deacetylases 1 and 2 Regulate Microglia Function during Development, Homeostasis, and Neurodegeneration in a Context-Dependent Manner. *Immunity*, 48(3), 514–529.e6.
<https://doi.org/10.1016/j.immuni.2018.02.016>

Davalos, D., Grutzendler, J., Yang, G., Kim, J. V., Zuo, Y., Jung, S., Littman, D. R., Dustin, M. L., & Gan, W. B. (2005). ATP mediates rapid microglial response to local brain injury in vivo. *Nature neuroscience*, 8(6), 752–758. <https://doi.org/10.1038/nn1472>

Davies, D. S., Ma, J., Jegathees, T., & Goldsbury, C. (2017). Microglia show altered morphology and reduced arborization in human brain during aging and Alzheimer's disease. *Brain pathology (Zurich, Switzerland)*, 27(6), 795–808. <https://doi.org/10.1111/bpa.12456>

De Santis, S., & Canals, S. (2019). Non-invasive MRI windows to neuroinflammation. *Neuroscience*, 403, 1–3. <https://doi.org/10.1016/j.neuroscience.2019.01.051>

De Santis, S., Bach, P., Pérez-Cervera, L., Cosa-Linan, A., Weil, G., Vollstädt-Klein, S., Hermann, D., Kiefer, F., Kirsch, P., Ciccocioppo, R., Sommer, W. H., & Canals, S. (2019). Microstructural White Matter Alterations in Men With Alcohol Use Disorder and Rats With Excessive Alcohol Consumption During Early Abstinence. *JAMA psychiatry*, 76(7), 749–758.
<https://doi.org/10.1001/jamapsychiatry.2019.0318>

De Santis, S., Cosa-Linan, A., Garcia-Hernandez, R., Dmytrenko, L., Vargova, L., Vorisek, I., Stopponi, S., Bach, P., Kirsch, P., Kiefer, F., Ciccocioppo, R., Sykova, E., Moratal, D., Sommer, W. H., & Canals, S. (2020). Chronic alcohol consumption alters extracellular space geometry and transmitter diffusion in the brain. *Science advances*, 6(26), eaba0154.
<https://doi.org/10.1126/sciadv.aba0154>

- De Santis, S., Sommer, W. H., & Canals, S. (2019). Detecting Alcohol-Induced Brain Damage Noninvasively Using Diffusion Tensor Imaging. *ACS chemical neuroscience*, *10*(10), 4187–4189. <https://doi.org/10.1021/acscchemneuro.9b00481>
- Desikan, R. S., Ségonne, F., Fischl, B., Quinn, B. T., Dickerson, B. C., Blacker, D., Buckner, R. L., Dale, A. M., Maguire, R. P., Hyman, B. T., Albert, M. S., & Killiany, R. J. (2006). An automated labeling system for subdividing the human cerebral cortex on MRI scans into gyral based regions of interest. *NeuroImage*, *31*(3), 968–980. <https://doi.org/10.1016/j.neuroimage.2006.01.021>
- Dickson, D. W., Lee, S. C., Mattiace, L. A., Yen, S. H., & Brosnan, C. (1993). Microglia and cytokines in neurological disease, with special reference to AIDS and Alzheimer's disease. *Glia*, *7*(1), 75–83. <https://doi.org/10.1002/glia.440070113>
- Diniz, P. H. B., Valente, T. L. A., Diniz, J. O. B., Silva, A. C., Gattass, M., Ventura, N., Muniz, B. C., & Gasparetto, E. L. (2018). Detection of white matter lesion regions in MRI using SLIC0 and convolutional neural network. *Computer methods and programs in biomedicine*, *167*, 49–63. <https://doi.org/10.1016/j.cmpb.2018.04.011>
- DiPiero, M., Rodrigues, P. G., Gromala, A., & Dean, D. C., 3rd (2023). Applications of advanced diffusion MRI in early brain development: a comprehensive review. *Brain structure & function*, *228*(2), 367–392. <https://doi.org/10.1007/s00429-022-02605-8>
- Distéfano-Gagné, F., Bitarafan, S., Lacroix, S., & Gosselin, D. (2023). Roles and regulation of microglia activity in multiple sclerosis: insights from animal models. *Nature reviews. Neuroscience*, *24*(7), 397–415. <https://doi.org/10.1038/s41583-023-00709-6>
- Drouin-Ouellet, J., Brownell, A. L., Saint-Pierre, M., Fasano, C., Emond, V., Trudeau, L. E., Lévesque, D., & Cicchetti, F. (2011). Neuroinflammation is associated with changes in glial mGluR5 expression and the development of neonatal excitotoxic lesions. *Glia*, *59*(2), 188–199. <https://doi.org/10.1002/glia.21086>
- Eddleston, M., & Mucke, L. (1993). Molecular profile of reactive astrocytes--implications for their role in neurologic disease. *Neuroscience*, *54*(1), 15–36. [https://doi.org/10.1016/0306-4522\(93\)90380-x](https://doi.org/10.1016/0306-4522(93)90380-x)
- Eng, L. F., Vanderhaeghen, J. J., Bignami, A., & Gerstl, B. (1971). An acidic protein isolated from fibrous astrocytes. *Brain research*, *28*(2), 351–354. [https://doi.org/10.1016/0006-8993\(71\)90668-8](https://doi.org/10.1016/0006-8993(71)90668-8)
- Escartin, C., Galea, E., Lakatos, A., O'Callaghan, J. P., Petzold, G. C., Serrano-Pozo, A., Steinhäuser, C., Volterra, A., Carmignoto, G., Agarwal, A., Allen, N. J., Araque, A., Barbeito, L., Barzilai, A., Bergles, D. E., Bonvento, G., Butt, A. M., Chen, W. T., Cohen-Salmon, M., Cunningham, C., ... Verkhratsky, A. (2021). Reactive astrocyte nomenclature, definitions, and future directions. *Nature neuroscience*, *24*(3), 312–325. <https://doi.org/10.1038/s41593-020-00783-4>
- Espinosa-Oliva, A. M., de Pablos, R. M., & Herrera, A. J. (2013). Intracranial injection of LPS in rat as animal model of neuroinflammation. *Methods in molecular biology (Clifton, N.J.)*, *1041*, 295–305. https://doi.org/10.1007/978-1-62703-520-0_26

- Evans, N. R., Tarkin, J. M., Buscombe, J. R., Markus, H. S., Rudd, J. H. F., & Warburton, E. A. (2018). PET imaging of the neurovascular interface in cerebrovascular disease. *Nature reviews. Neurology*, *14*(5), 313. <https://doi.org/10.1038/nrneurol.2018.42>
- Fernández-Arjona, M. D. M., Grondona, J. M., Granados-Durán, P., Fernández-Llebrez, P., & López-Ávalos, M. D. (2017). Microglia Morphological Categorization in a Rat Model of Neuroinflammation by Hierarchical Cluster and Principal Components Analysis. *Frontiers in cellular neuroscience*, *11*, 235. <https://doi.org/10.3389/fncel.2017.00235>
- Franklin, R. J. M., Frisén, J., & Lyons, D. A. (2021). Revisiting remyelination: Towards a consensus on the regeneration of CNS myelin. *Seminars in cell & developmental biology*, *116*, 3–9. <https://doi.org/10.1016/j.semcd.2020.09.009>
- Frischer, J. M., Bramow, S., Dal-Bianco, A., Lucchinetti, C. F., Rauschka, H., Schmidbauer, M., Laursen, H., Sorensen, P. S., & Lassmann, H. (2009). The relation between inflammation and neurodegeneration in multiple sclerosis brains. *Brain : a journal of neurology*, *132*(Pt 5), 1175–1189. <https://doi.org/10.1093/brain/awp070>
- Gage, G. J., Kipke, D. R., & Shain, W. (2012). Whole animal perfusion fixation for rodents. *Journal of visualized experiments : JoVE*, (65), 3564. <https://doi.org/10.3791/3564>
- Ganzetti, M., Wenderoth, N., & Mantini, D. (2014). Whole brain myelin mapping using T1- and T2-weighted MR imaging data. *Frontiers in human neuroscience*, *8*, 671. <https://doi.org/10.3389/fnhum.2014.00671>
- Gao, H., He, C., Fang, X., Hou, X., Feng, X., Yang, H., Zhao, X., & Ma, T. (2006). Localization of aquaporin-1 water channel in glial cells of the human peripheral nervous system. *Glia*, *53*(7), 783–787. <https://doi.org/10.1002/glia.20336>
- Garcia-Hernandez, R., Canals, S., & De Santis, S. (2023). Can we use a magnet to see brain inflammation?. *The Science Breaker*, thescbr.brk747. <https://doi.org/10.25250/thescbr.brk747>
- Geiger, B. M., Frank, L. E., Caldera-Siu, A. D., & Pothos, E. N. (2008). Survivable stereotaxic surgery in rodents. *Journal of visualized experiments : JoVE*, (20), 880. <https://doi.org/10.3791/880>
- Geirsdottir, L., David, E., Keren-Shaul, H., Weiner, A., Bohlen, S. C., Neuber, J., Balic, A., Giladi, A., Sheban, F., Dutertre, C. A., Pfeifle, C., Peri, F., Raffo-Romero, A., Vizioli, J., Matiassek, K., Scheiwe, C., Meckel, S., Mätz-Rensing, K., van der Meer, F., Thormodsson, F. R., ... Prinz, M. (2019). Cross-Species Single-Cell Analysis Reveals Divergence of the Primate Microglia Program. *Cell*, *179*(7), 1609–1622.e16. <https://doi.org/10.1016/j.cell.2019.11.010>
- Geladaris, A., Torke, S., Saberi, D., Alankus, Y. B., Streit, F., Zechel, S., Stadelmann-Nessler, C., Fischer, A., Boschert, U., Häusler, D., & Weber, M. S. (2024). BTK inhibition limits microglia-perpetuated CNS inflammation and promotes myelin repair. *Acta neuropathologica*, *147*(1), 75. <https://doi.org/10.1007/s00401-024-02730-0>
- Giera, S., Luo, R., Ying, Y., Ackerman, S. D., Jeong, S. J., Stoveken, H. M., Folts, C. J., Welsh, C. A., Tall, G. G., Stevens, B., Monk, K. R., & Piao, X. (2018). Microglial transglutaminase-2 drives

myelination and myelin repair via GPR56/ADGRG1 in oligodendrocyte precursor cells. *eLife*, 7, e33385. <https://doi.org/10.7554/eLife.33385>

Giulian D. (1993). Reactive glia as rivals in regulating neuronal survival. *Glia*, 7(1), 102–110. <https://doi.org/10.1002/glia.440070116>

Glasser, M. F., & Van Essen, D. C. (2011). Mapping human cortical areas in vivo based on myelin content as revealed by T1- and T2-weighted MRI. *The Journal of neuroscience : the official journal of the Society for Neuroscience*, 31(32), 11597–11616. <https://doi.org/10.1523/JNEUROSCI.2180-11.2011>

Goebel, P., Wingrove, J., Abdelmannan, O., Vega, B. B., Stutters, J., Graca Ramos, S. da, Kenway, O., Rosoor, T., Wassmer, E., Chataway, J., Arnold, D., Collins, L., Hemmingway, C., Narayanan, S., Chard, D., Iglesias, J. E., Barkhof, F., Hacothen, Y., Thompson, A., ... Eshaghi, A. (2024). Repurposing Clinical MRI Archives for Multiple Sclerosis Research with a Flexible, Single-Modality Approach: New Insights from Old Scans. *MedRxiv*, 2024.03.29.24305083. <https://doi.org/10.1101/2024.03.29.24305083>

Golgi, C. (1873). On structure of the grey matter of the brain. *Gazzetta Medica Italiana Lombardia* 3:244–6

Gómez-Nicola, D., Fransen, N. L., Suzzi, S., & Perry, V. H. (2013). Regulation of microglial proliferation during chronic neurodegeneration. *The Journal of neuroscience : the official journal of the Society for Neuroscience*, 33(6), 2481–2493. <https://doi.org/10.1523/JNEUROSCI.4440-12.2013>

Grabert, K., Michoel, T., Karavolos, M. H., Clohisey, S., Baillie, J. K., Stevens, M. P., Freeman, T. C., Summers, K. M., & McColl, B. W. (2016). Microglial brain region-dependent diversity and selective regional sensitivities to aging. *Nature neuroscience*, 19(3), 504–516. <https://doi.org/10.1038/nn.4222>

Granger, D. N., & Senchenkov, E. (2010). *Inflammation and Microcirculation*. Morgan & Claypool Life Sciences.

grey, H., Standring, S., Ellis, H., & Berkovitz, B. K. B. (2005). *grey's anatomy: the anatomical basis of clinical practice*. 39th ed. / Edinburgh ; New York, Elsevier Churchill Livingstone.

Griemsmann, S., Höft, S. P., Bedner, P., Zhang, J., von Staden, E., Beinhauer, A., Degen, J., Dublin, P., Cope, D. W., Richter, N., Crunelli, V., Jabs, R., Willecke, K., Theis, M., Seifert, G., Kettenmann, H., & Steinhäuser, C. (2015). Characterization of Panglial Gap Junction Networks in the Thalamus, Neocortex, and Hippocampus Reveals a Unique Population of Glial Cells. *Cerebral cortex (New York, N.Y. : 1991)*, 25(10), 3420–3433. <https://doi.org/10.1093/cercor/bhu157>

Guadalupi, L., Vanni, V., Balletta, S., Caioli, S., De Vito, F., Fresegna, D., Sanna, K., Nencini, M., Donninelli, G., Volpe, E., Mariani, F., Battistini, L., Stampanoni Bassi, M., Gilio, L., Bruno, A., Dolcetti, E., Buttari, F., Mandolesi, G., Centonze, D., & Musella, A. (2024). Interleukin-9 protects from microglia- and TNF-mediated synaptotoxicity in experimental multiple sclerosis. *Journal of neuroinflammation*, 21(1), 128. <https://doi.org/10.1186/s12974-024-03120-9>

- Guilarte T. R. (2019). TSPO in diverse CNS pathologies and psychiatric disease: A critical review and a way forward. *Pharmacology & therapeutics*, *194*, 44–58. <https://doi.org/10.1016/j.pharmthera.2018.09.003>
- Guruswamy, R., & ElAli, A. (2017). Complex Roles of Microglial Cells in Ischemic Stroke Pathobiology: New Insights and Future Directions. *International journal of molecular sciences*, *18*(3), 496. <https://doi.org/10.3390/ijms18030496>
- Halassa, M. M., Florian, C., Fellin, T., Munoz, J. R., Lee, S. Y., Abel, T., Haydon, P. G., & Frank, M. G. (2009). Astrocytic modulation of sleep homeostasis and cognitive consequences of sleep loss. *Neuron*, *61*(2), 213–219. <https://doi.org/10.1016/j.neuron.2008.11.024>
- Han, J., Harris, R. A., & Zhang, X. M. (2017). An updated assessment of microglia depletion: current concepts and future directions. *Molecular brain*, *10*(1), 25. <https://doi.org/10.1186/s13041-017-0307-x>
- Han, S., Gim, Y., Jang, E. H., & Hur, E. M. (2022). Functions and dysfunctions of oligodendrocytes in neurodegenerative diseases. *Frontiers in cellular neuroscience*, *16*, 1083159. <https://doi.org/10.3389/fncel.2022.1083159>
- Haseleu, J., Anlauf, E., Blaess, S., Endl, E., & Derouiche, A. (2013). Studying subcellular detail in fixed astrocytes: dissociation of morphologically intact glial cells (DIMIGs). *Frontiers in cellular neuroscience*, *7*, 54. <https://doi.org/10.3389/fncel.2013.00054>
- Heindl, S., Gesierich, B., Benakis, C., Llovera, G., Duering, M., & Liesz, A. (2018). Automated Morphological Analysis of Microglia After Stroke. *Frontiers in cellular neuroscience*, *12*, 106. <https://doi.org/10.3389/fncel.2018.00106>
- Heindl, S., Gesierich, B., Benakis, C., Llovera, G., Duering, M., & Liesz, A. (2018). Automated Morphological Analysis of Microglia After Stroke. *Frontiers in cellular neuroscience*, *12*, 106. <https://doi.org/10.3389/fncel.2018.00106>
- Herrera, A. J., Castaño, A., Venero, J. L., Cano, J., & Machado, A. (2000). The single intranigral injection of LPS as a new model for studying the selective effects of inflammatory reactions on dopaminergic system. *Neurobiology of disease*, *7*(4), 429–447. <https://doi.org/10.1006/nbdi.2000.0289>
- Hetier, E., Ayala, J., Denèfle, P., Bousseau, A., Rouget, P., Mallat, M., & Prochiantz, A. (1988). Brain macrophages synthesize interleukin-1 and interleukin-1 mRNAs in vitro. *Journal of neuroscience research*, *21*(2-4), 391–397. <https://doi.org/10.1002/jnr.490210230>
- Hickman, S. E., Kingery, N. D., Ohsumi, T. K., Borowsky, M. L., Wang, L. C., Means, T. K., & El Khoury, J. (2013). The microglial sensome revealed by direct RNA sequencing. *Nature neuroscience*, *16*(12), 1896–1905. <https://doi.org/10.1038/nn.3554>
- Hsiao, H. Y., Chen, Y. C., Chen, H. M., Tu, P. H., & Chern, Y. (2013). A critical role of astrocyte-mediated nuclear factor- κ B-dependent inflammation in Huntington's disease. *Human molecular genetics*, *22*(9), 1826–1842. <https://doi.org/10.1093/hmg/ddt036>

Huang, H. T., Chen, P. S., Kuo, Y. M., & Tzeng, S. F. (2020). Intermittent peripheral exposure to lipopolysaccharide induces exploratory behavior in mice and regulates brain glial activity in obese mice. *Journal of neuroinflammation*, *17*(1), 163. <https://doi.org/10.1186/s12974-020-01837-x>

Hui, C. W., Bhardwaj, S. K., Sharma, K., Joseph, A. T., Bisht, K., Picard, K., Tremblay, M. È., & Srivastava, L. K. (2019). Microglia in the developing prefrontal cortex of rats show dynamic changes following neonatal disconnection of the ventral hippocampus. *Neuropharmacology*, *146*, 264–275. <https://doi.org/10.1016/j.neuropharm.2018.12.007>

Ianuș, A., Carvalho, J., Fernandes, F. F., Cruz, R., Chavarrias, C., Palombo, M., & Shemesh, N. (2022). Soma and Neurite Density MRI (SANDI) of the in-vivo mouse brain and comparison with the Allen Brain Atlas. *NeuroImage*, *254*, 119135. <https://doi.org/10.1016/j.neuroimage.2022.119135>

Ito, D., Imai, Y., Ohsawa, K., Nakajima, K., Fukuuchi, Y., & Kohsaka, S. (1998). Microglia-specific localisation of a novel calcium binding protein, Iba-1. *Brain research. Molecular brain research*, *57*(1), 1–9. [https://doi.org/10.1016/s0169-328x\(98\)00040-0](https://doi.org/10.1016/s0169-328x(98)00040-0)

Jalenques, I., Burette, A., Albuissou, E., & Romand, R. (1997). Age-related changes in GFAP-immunoreactive astrocytes in the rat ventral cochlear nucleus. *Hearing research*, *107*(1-2), 113–124. [https://doi.org/10.1016/s0378-5955\(97\)00026-9](https://doi.org/10.1016/s0378-5955(97)00026-9)

James, M. L., Belichenko, N. P., Nguyen, T. V., Andrews, L. E., Ding, Z., Liu, H., Bodapati, D., Arksey, N., Shen, B., Cheng, Z., Wyss-Coray, T., Gambhir, S. S., Longo, F. M., & Chin, F. T. (2015). PET imaging of translocator protein (18 kDa) in a mouse model of Alzheimer's disease using N-(2,5-dimethoxybenzyl)-2-18F-fluoro-N-(2-phenoxyphenyl)acetamide. *Journal of nuclear medicine : official publication, Society of Nuclear Medicine*, *56*(2), 311–316. <https://doi.org/10.2967/jnumed.114.141648>

Janus, C., Pearson, J., McLaurin, J., Mathews, P. M., Jiang, Y., Schmidt, S. D., Chishti, M. A., Horne, P., Heslin, D., French, J., Mount, H. T., Nixon, R. A., Mercken, M., Bergeron, C., Fraser, P. E., St George-Hyslop, P., & Westaway, D. (2000). A beta peptide immunization reduces behavioural impairment and plaques in a model of Alzheimer's disease. *Nature*, *408*(6815), 979–982. <https://doi.org/10.1038/35050110>

Jeong, H. K., Jou, I., & Joe, E. H. (2010). Systemic LPS administration induces brain inflammation but not dopaminergic neuronal death in the substantia nigra. *Experimental & molecular medicine*, *42*(12), 823–832. <https://doi.org/10.3858/emm.2010.42.12.085>

Jiang, J., Tang, B., Wang, L., Huo, Q., Tan, S., Misrani, A., Han, Y., Li, H., Hu, H., Wang, J., Cheng, T., Tabassum, S., Chen, M., Xie, W., Long, C., & Yang, L. (2022). Systemic LPS-induced microglial activation results in increased GABAergic tone: A mechanism of protection against neuroinflammation in the medial prefrontal cortex in mice. *Brain, behavior, and immunity*, *99*, 53–69. <https://doi.org/10.1016/j.bbi.2021.09.017>

Jinno, S., Fleischer, F., Eckel, S., Schmidt, V., & Kosaka, T. (2007). Spatial arrangement of microglia in the mouse hippocampus: a stereological study in comparison with astrocytes. *Glia*, *55*(13), 1334–1347. <https://doi.org/10.1002/glia.20552>

Jones, D. K., Alexander, D. C., Bowtell, R., Cercignani, M., Dell'Acqua, F., McHugh, D. J., Miller, K. L., Palombo, M., Parker, G. J. M., Rudrapatna, U. S., & Tax, C. M. W. (2018). Microstructural imaging of the human brain with a 'super-scanner': 10 key advantages of ultra-strong gradients for diffusion MRI. *NeuroImage*, *182*, 8–38. <https://doi.org/10.1016/j.neuroimage.2018.05.047>

Jung, H., Lee, D., You, H., Lee, M., Kim, H., Cheong, E., & Um, J. W. (2023). LPS induces microglial activation and GABAergic synaptic deficits in the hippocampus accompanied by prolonged cognitive impairment. *Scientific reports*, *13*(1), 6547. <https://doi.org/10.1038/s41598-023-32798-9>

Jung, S., Aliberti, J., Graemmel, P., Sunshine, M. J., Kreutzberg, G. W., Sher, A., & Littman, D. R. (2000). Analysis of fractalkine receptor CX(3)CR1 function by targeted deletion and green fluorescent protein reporter gene insertion. *Molecular and cellular biology*, *20*(11), 4106–4114. <https://doi.org/10.1128/MCB.20.11.4106-4114.2000>

Karch, C. M., & Goate, A. M. (2015). Alzheimer's disease risk genes and mechanisms of disease pathogenesis. *Biological psychiatry*, *77*(1), 43–51. <https://doi.org/10.1016/j.biopsych.2014.05.006>

Karussis D. (2014). The diagnosis of multiple sclerosis and the various related demyelinating syndromes: a critical review. *Journal of autoimmunity*, *48-49*, 134–142. <https://doi.org/10.1016/j.jaut.2014.01.022>

Khakh, B. S., & Sofroniew, M. V. (2015). Diversity of astrocyte functions and phenotypes in neural circuits. *Nature neuroscience*, *18*(7), 942–952. <https://doi.org/10.1038/nn.4043>

Kim, J., Yoo, I. D., Lim, J., & Moon, J. S. (2024). Pathological phenotypes of astrocytes in Alzheimer's disease. *Experimental & molecular medicine*, *56*(1), 95–99. <https://doi.org/10.1038/s12276-023-01148-0>

Kim, S. U., & de Vellis, J. (2005). Microglia in health and disease. *Journal of neuroscience research*, *81*(3), 302–313. <https://doi.org/10.1002/jnr.20562>

Kol, A., Adamsky, A., Groysman, M., Kreisel, T., London, M., & Goshen, I. (2020). Astrocytes contribute to remote memory formation by modulating hippocampal-cortical communication during learning. *Nature neuroscience*, *23*(10), 1229–1239. <https://doi.org/10.1038/s41593-020-0679-6>

Kong, W., Frouard, J., Xie, G., Corley, M. J., Helmy, E., Zhang, G., Schwarzer, R., Montano, M., Sohn, P., Roan, N. R., Ndhlovu, L. C., Gan, L., & Greene, W. C. (2024). Neuroinflammation generated by HIV-infected microglia promotes dysfunction and death of neurons in human brain organoids. *PNAS nexus*, *3*(5), pgae179. <https://doi.org/10.1093/pnasnexus/pgae179>

Kongsui, R., Beynon, S. B., Johnson, S. J., & Walker, F. R. (2014). Quantitative assessment of microglial morphology and density reveals remarkable consistency in the distribution and morphology of cells within the healthy prefrontal cortex of the rat. *Journal of neuroinflammation*, *11*, 182. <https://doi.org/10.1186/s12974-014-0182-7>

Kor, D. Z. L., Jbabdi, S., Huszar, I. N., Mollink, J., Tendler, B. C., Foxley, S., Wang, C., Scott, C., Smart, A., Ansorge, O., Pallebage-Gamarallage, M., Miller, K. L., & Howard, A. F. D. (2022). An automated pipeline for extracting histological stain area fraction for voxelwise quantitative

MRI-histology comparisons. *NeuroImage*, 264, 119726.
<https://doi.org/10.1016/j.neuroimage.2022.119726>

Kragh, C. L., Fillon, G., Gysbers, A., Hansen, H. D., Neumann, M., Richter-Landsberg, C., Haass, C., Zalc, B., Lubetzki, C., Gai, W. P., Halliday, G. M., Kahle, P. J., & Jensen, P. H. (2013). FAS-dependent cell death in α -synuclein transgenic oligodendrocyte models of multiple system atrophy. *PLoS one*, 8(1), e55243. <https://doi.org/10.1371/journal.pone.0055243>

Kwon, H. S., & Koh, S. H. (2020). Neuroinflammation in neurodegenerative disorders: the roles of microglia and astrocytes. *Translational neurodegeneration*, 9(1), 42. <https://doi.org/10.1186/s40035-020-00221-2>

Lauterbur P. C. (1989). Image formation by induced local interactions. Examples employing nuclear magnetic resonance. 1973. *Clinical orthopaedics and related research*, (244), 3–6.

Lawrence, A. R., Canzi, A., Bridlance, C., Oliivié, N., Lansonneur, C., Catale, C., Pizzamiglio, L., Kloeckner, B., Silvin, A., Munro, D. A. D., Fortoul, A., Boido, D., Zehani, F., Cartonnet, H., Viguier, S., Oller, G., Squarzone, P., Candat, A., Helft, J., Allet, C., ... Garel, S. (2024). Microglia maintain structural integrity during fetal brain morphogenesis. *Cell*, 187(4), 962–980.e19. <https://doi.org/10.1016/j.cell.2024.01.012>

Lawson, L. J., Perry, V. H., Dri, P., & Gordon, S. (1990). Heterogeneity in the distribution and morphology of microglia in the normal adult mouse brain. *Neuroscience*, 39(1), 151–170. [https://doi.org/10.1016/0306-4522\(90\)90229-w](https://doi.org/10.1016/0306-4522(90)90229-w)

Le Bihan D. (2014). Diffusion MRI: what water tells us about the brain. *EMBO molecular medicine*, 6(5), 569–573. <https://doi.org/10.1002/emmm.201404055>

Le Bihan, D., Mangin, J. F., Poupon, C., Clark, C. A., Pappata, S., Molko, N., & Chabriat, H. (2001). Diffusion tensor imaging: concepts and applications. *Journal of magnetic resonance imaging : JMRI*, 13(4), 534–546. <https://doi.org/10.1002/jmri.1076>

Lee, D. Y., Lee, J. J., Kwon, H. S., Moon, W. Y., Jin, S. Y., Lee, S. J., Oh, S. J., & Ryu, J. S. (2013). An unusual case of anaphylaxis after fluorine-18-labeled fluorodeoxyglucose injection. *Nuclear medicine and molecular imaging*, 47(3), 201–204. <https://doi.org/10.1007/s13139-013-0202-z>

Lenhossék, M. (1895). *Der Feinere Bau des Nervensystems im Lichte Neuester Forschung*, 2nd ed.; Fischer's Medicinische Buchhandlung H. Kornfeld

Lenz, K. M., & McCarthy, M. M. (2015). A starring role for microglia in brain sex differences. *The Neuroscientist : a review journal bringing neurobiology, neurology and psychiatry*, 21(3), 306–321. <https://doi.org/10.1177/1073858414536468>

Li, G., Sun, S., Cao, X., Zhong, J., & Tong, E. (2004). LPS-induced degeneration of dopaminergic neurons of substantia nigra in rats. *Journal of Huazhong University of Science and Technology. Medical sciences = Hua zhong ke ji da xue xue bao. Yi xue Ying De wen ban = Huazhong keji daxue xuebao. Yixue Yingdewen ban*, 24(1), 83–86. <https://doi.org/10.1007/BF02830714>

Ligneul, C., Najac, C., Döring, A., Beaulieu, C., Branzoli, F., Clarke, W. T., Cudalbu, C., Genovese, G., Jbabdi, S., Jelescu, I., Karampinos, D., Kreis, R., Lundell, H., Marjańska, M., Möller, H. E., Mosso, J., Mougél, E., Posse, S., Ruschke, S., Simsek, K., ... Valette, J. (2024). Diffusion-weighted MR spectroscopy: Consensus, recommendations, and resources from acquisition to modeling. *Magnetic resonance in medicine*, *91*(3), 860–885. <https://doi.org/10.1002/mrm.29877>

Liu, G. J., Middleton, R. J., Hatty, C. R., Kam, W. W., Chan, R., Pham, T., Harrison-Brown, M., Dodson, E., Veale, K., & Banati, R. B. (2014). The 18 kDa translocator protein, microglia and neuroinflammation. *Brain pathology* (Zurich, Switzerland), *24*(6), 631–653. <https://doi.org/10.1111/bpa.12196>

Long, K. L. P., Chao, L. L., Kazama, Y., An, A., Hu, K. Y., Peretz, L., Muller, D. C. Y., Roan, V. D., Misra, R., Toth, C. E., Breton, J. M., Casazza, W., Mostafavi, S., Huber, B. R., Woodward, S. H., Neylan, T. C., & Kaufer, D. (2021). Regional grey matter oligodendrocyte- and myelin-related measures are associated with differential susceptibility to stress-induced behavior in rats and humans. *Translational psychiatry*, *11*(1), 631. <https://doi.org/10.1038/s41398-021-01745-5>

Lugaro, E. (1907). On the functions of the neuroglia. *Riv Patol Nerv Ment*, *12*, 225-33.

Mandino, F., Cerri, D. H., Garin, C. M., Straathof, M., van Tilborg, G. A. F., Chakravarty, M. M., Dhenain, M., Dijkhuizen, R. M., Gozzi, A., Hess, A., Keilholz, S. D., Lerch, J. P., Shih, Y. I., & Grandjean, J. (2020). Animal Functional Magnetic Resonance Imaging: Trends and Path Toward Standardization. *Frontiers in neuroinformatics*, *13*, 78. <https://doi.org/10.3389/fninf.2019.00078>

Mansour, H., Chamberlain, C. G., Weible, M. W., 2nd, Hughes, S., Chu, Y., & Chan-Ling, T. (2008). Aging-related changes in astrocytes in the rat retina: imbalance between cell proliferation and cell death reduces astrocyte availability. *Aging cell*, *7*(4), 526–540. <https://doi.org/10.1111/j.1474-9726.2008.00402.x>

Martin D. L. (1992). Synthesis and release of neuroactive substances by glial cells. *Glia*, *5*(2), 81–94. <https://doi.org/10.1002/glia.440050202>

Matsushima, G. K., & Morell, P. (2001). The neurotoxicant, cuprizone, as a model to study demyelination and remyelination in the central nervous system. *Brain pathology*, *11*(1), 107–116. <https://doi.org/10.1111/j.1750-3639.2001.tb00385.x>

Matusova, Z., Hol, E. M., Pekny, M., Kubista, M., & Valihrach, L. (2023). Reactive astrogliosis in the era of single-cell transcriptomics. *Frontiers in cellular neuroscience*, *17*, 1173200. <https://doi.org/10.3389/fncel.2023.1173200>

Maurya, S. K., Gupta, S., & Mishra, R. (2023). Transcriptional and epigenetic regulation of microglia in maintenance of brain homeostasis and neurodegeneration. *Frontiers in molecular neuroscience*, *15*, 1072046. <https://doi.org/10.3389/fnmol.2022.1072046>

Mayne, K., White, J. A., McMurrin, C. E., Rivera, F. J., & de la Fuente, A. G. (2020). Aging and Neurodegenerative Disease: Is the Adaptive Immune System a Friend or Foe?. *Frontiers in aging neuroscience*, *12*, 572090. <https://doi.org/10.3389/fnagi.2020.572090>

- McCarthy, M. M., Nugent, B. M., & Lenz, K. M. (2017). Neuroimmunology and neuroepigenetics in the establishment of sex differences in the brain. *Nature reviews. Neuroscience*, *18*(8), 471–484. <https://doi.org/10.1038/nrn.2017.61>
- McGeer, P. L., Kawamata, T., Walker, D. G., Akiyama, H., Tooyama, I., & McGeer, E. G. (1993). Microglia in degenerative neurological disease. *Glia*, *7*(1), 84–92. <https://doi.org/10.1002/glia.440070114>
- McKay, S. M., Brooks, D. J., Hu, P., & McLachlan, E. M. (2007). Distinct types of microglial activation in white and grey matter of rat lumbosacral cord after mid-thoracic spinal transection. *Journal of neuropathology and experimental neurology*, *66*(8), 698–710. <https://doi.org/10.1097/nen.0b013e3181256b32>
- Mennerick, S., & Zorumski, C. F. (1994). Glial contributions to excitatory neurotransmission in cultured hippocampal cells. *Nature*, *368*(6466), 59–62. <https://doi.org/10.1038/368059a0>
- Mercadante, A. A., & Tadi, P. (2023). Neuroanatomy, grey Matter. In *StatPearls*. StatPearls Publishing.
- Merenstein, J. L., Corrada, M. M., Kawas, C. H., & Bennett, I. J. (2023). White matter microstructural correlates of associative learning in the oldest-old. *Cognitive, affective & behavioral neuroscience*, *23*(1), 114–124. <https://doi.org/10.3758/s13415-022-01035-7>
- Milligan, C. E., Cunningham, T. J., & Levitt, P. (1991). Differential immunochemical markers reveal the normal distribution of brain macrophages and microglia in the developing rat brain. *The Journal of comparative neurology*, *314*(1), 125–135. <https://doi.org/10.1002/cne.903140112>
- Mills, J., Ladner, L., Soliman, E., Leonard, J., Morton, P. D., & Theus, M. H. (2022). Cross-Talk and Subset Control of Microglia and Associated Myeloid Cells in Neurological Disorders. *Cells*, *11*(21), 3364. <https://doi.org/10.3390/cells11213364>
- Mittelbronn, M., Dietz, K., Schluesener, H. J., & Meyermann, R. (2001). Local distribution of microglia in the normal adult human central nervous system differs by up to one order of magnitude. *Acta*
- Moreels, M., Vandenabeele, F., Dumont, D., Robben, J., & Lambrichts, I. (2008). Alpha-smooth muscle actin (alpha-SMA) and nestin expression in reactive astrocytes in multiple sclerosis lesions: potential regulatory role of transforming growth factor-beta 1 (TGF-beta1). *Neuropathology and applied neurobiology*, *34*(5), 532–546. <https://doi.org/10.1111/j.1365-2990.2007.00910.x>
- Moses W. W. (2011). Fundamental Limits of Spatial Resolution in PET. *Nuclear instruments & methods in physics research. Section A, Accelerators, spectrometers, detectors and associated equipment*, *648 Supplement 1*, S236–S240. <https://doi.org/10.1016/j.nima.2010.11.092>
- Nebeling, F. C., Poll, S., Justus, L. C., Steffen, J., Keppler, K., Mittag, M., & Fuhrmann, M. (2023). Microglial motility is modulated by neuronal activity and correlates with dendritic spine plasticity in the hippocampus of awake mice. *eLife*, *12*, e83176. <https://doi.org/10.7554/eLife.83176>

- Neumann, H., Kotter, M. R., & Franklin, R. J. (2009). Debris clearance by microglia: an essential link between degeneration and regeneration. *Brain: a journal of neurology*, *132*(Pt 2), 288–295. <https://doi.org/10.1093/brain/awn109>
- Nieuwenhuys, R., & Broere, C. A. (2017). A map of the human neocortex showing the estimated overall myelin content of the individual architectonic areas based on the studies of Adolf Hopf. *Brain structure & function*, *222*(1), 465–480. <https://doi.org/10.1007/s00429-016-1228-7>
- Nilsson, M., Lätt, J., van Westen, D., Brockstedt, S., Lasič, S., Ståhlberg, F., & Topgaard, D. (2013). Noninvasive mapping of water diffusional exchange in the human brain using filter-exchange imaging. *Magnetic resonance in medicine*, *69*(6), 1573–1581. <https://doi.org/10.1002/mrm.24395>
- Nimmerjahn, A., Kirchhoff, F., & Helmchen, F. (2005). Resting microglial cells are highly dynamic surveillants of brain parenchyma in vivo. *Science (New York, N.Y.)*, *308*(5726), 1314–1318. <https://doi.org/10.1126/science.1110647>
- Olah, M., Biber, K., Vinet, J., & Boddeke, H. W. (2011). Microglia phenotype diversity. *CNS & neurological disorders drug targets*, *10*(1), 108–118. <https://doi.org/10.2174/187152711794488575>
- Ou, Z., Sun, Y., Lin, L., You, N., Liu, X., Li, H., Ma, Y., Cao, L., Han, Y., Liu, M., Deng, Y., Yao, L., Lu, Q. R., & Chen, Y. (2016). Olig2-Targeted G-Protein-Coupled Receptor Gpr17 Regulates Oligodendrocyte Survival in Response to Lysolecithin-Induced Demyelination. *The Journal of neuroscience : the official journal of the Society for Neuroscience*, *36*(41), 10560–10573. <https://doi.org/10.1523/JNEUROSCI.0898-16.2016>
- Owen, D. R., Gunn, R. N., Rabiner, E. A., Bennacef, I., Fujita, M., Kreisl, W. C., Innis, R. B., Pike, V. W., Reynolds, R., Matthews, P. M., & Parker, C. A. (2011). Mixed-affinity binding in humans with 18-kDa translocator protein ligands. *Journal of nuclear medicine : official publication, Society of Nuclear Medicine*, *52*(1), 24–32. <https://doi.org/10.2967/jnumed.110.079459>
- Ozawa, T., Paviour, D., Quinn, N. P., Josephs, K. A., Sangha, H., Kilford, L., Healy, D. G., Wood, N. W., Lees, A. J., Holton, J. L., & Revesz, T. (2004). The spectrum of pathological involvement of the striatonigral and olivopontocerebellar systems in multiple system atrophy: clinicopathological correlations. *Brain : a journal of neurology*, *127*(Pt 12), 2657–2671. <https://doi.org/10.1093/brain/awh303>
- Pak, S., Choi, G., Roy, J., Poon, C. H., Lee, J., Cho, D., Lee, M., Lim, L. W., Bao, S., Yang, S., & Yang, S. (2022). Altered synaptic plasticity of the longitudinal dentate gyrus network in noise-induced anxiety. *iScience*, *25*(6), 104364. <https://doi.org/10.1016/j.isci.2022.104364>
- Palombo, M., Alexander, D. C., & Zhang, H. (2019). A generative model of realistic brain cells with application to numerical simulation of the diffusion-weighted MR signal. *NeuroImage*, *188*, 391–402. <https://doi.org/10.1016/j.neuroimage.2018.12.025>
- Palombo, M., Ianus, A., Guerreri, M., Nunes, D., Alexander, D. C., Shemesh, N., & Zhang, H. (2020). SANDI: A compartment-based model for non-invasive apparent soma and neurite imaging by diffusion MRI. *NeuroImage*, *215*, 116835. <https://doi.org/10.1016/j.neuroimage.2020.116835>

Paolicelli, R. C., Sierra, A., Stevens, B., Tremblay, M. E., Aguzzi, A., Ajami, B., Amit, I., Audinat, E., Bechmann, I., Bennett, M., Bennett, F., Bessis, A., Biber, K., Bilbo, S., Blurton-Jones, M., Boddeke, E., Brites, D., Brône, B., Brown, G. C., Butovsky, O., ... Wyss-Coray, T. (2022). Microglia states and nomenclature: A field at its crossroads. *Neuron*, *110*(21), 3458–3483. <https://doi.org/10.1016/j.neuron.2022.10.020>

Papageorgiou, I. E., Fetani, A. F., Lewen, A., Heinemann, U., & Kann, O. (2015). Widespread activation of microglial cells in the hippocampus of chronic epileptic rats correlates only partially with neurodegeneration. *Brain structure & function*, *220*(4), 2423–2439. <https://doi.org/10.1007/s00429-014-0802-0>

Passamonti, L., Rodríguez, P. V., Hong, Y. T., Allinson, K. S. J., Bevan-Jones, W. R., Williamson, D., Jones, P. S., Arnold, R., Borchert, R. J., Surendranathan, A., Mak, E., Su, L., Fryer, T. D., Aigbirhio, F. I., O'Brien, J. T., & Rowe, J. B. (2018). [11C]PK11195 binding in Alzheimer disease and progressive supranuclear palsy. *Neurology*, *90*(22), e1989–e1996. <https://doi.org/10.1212/WNL.0000000000005610>

Pasternak, O., Sochen, N., Gur, Y., Intrator, N., & Assaf, Y. (2009). Free water elimination and mapping from diffusion MRI. *Magnetic resonance in medicine*, *62*(3), 717–730. <https://doi.org/10.1002/mrm.22055>

Paternina-Die, M., Martínez-García, M., Martín de Blas, D., Noguero, I., Servin-Barthet, C., Pretus, C., Soler, A., López-Montoya, G., Desco, M., & Carmona, S. (2024). Women's neuroplasticity during gestation, childbirth and postpartum. *Nature neuroscience*, *27*(2), 319–327. <https://doi.org/10.1038/s41593-023-01513-2>

Pavlou, M. A. S., Grandbarbe, L., Buckley, N. J., Niclou, S. P., & Michelucci, A. (2019). Transcriptional and epigenetic mechanisms underlying astrocyte identity. *Progress in neurobiology*, *174*, 36–52. <https://doi.org/10.1016/j.pneurobio.2018.12.007>

Paxinos, G., & Franklin, K. (2019). Paxinos and Franklin's the Mouse Brain in stereotaxic coordinates (5th ed.). Academic Press.

Penfield W. (1924). Oligodendroglia and its relation to classical neuroglia. *Brain* 47: 430–452.

Petralla, S., De Chirico, F., Miti, A., Tartagni, O., Massenzio, F., Poeta, E., Virgili, M., Zuccheri, G., & Monti, B. (2021). Epigenetics and Communication Mechanisms in Microglia Activation with a View on Technological Approaches. *Biomolecules*, *11*(2), 306. <https://doi.org/10.3390/biom11020306>

Phatnani, H. P., Guarnieri, P., Friedman, B. A., Carrasco, M. A., Muratet, M., O'Keefe, S., Nwakeze, C., Pauli-Behn, F., Newberry, K. M., Meadows, S. K., Tapia, J. C., Myers, R. M., & Maniatis, T. (2013). Intricate interplay between astrocytes and motor neurons in ALS. *Proceedings of the National Academy of Sciences of the United States of America*, *110*(8), E756–E765. <https://doi.org/10.1073/pnas.1222361110>

Pierpaoli, C., & Basser, P. J. (1996). Toward a quantitative assessment of diffusion anisotropy. *Magnetic resonance in medicine*, *36*(6), 893–906. <https://doi.org/10.1002/mrm.1910360612>

Pierpaoli, C., Jezzard, P., Basser, P. J., Barnett, A., & Di Chiro, G. (1996). Diffusion tensor MR imaging of the human brain. *Radiology*, 201(3), 637–648. <https://doi.org/10.1148/radiology.201.3.8939209>

Planetta, P. J., Ofori, E., Pasternak, O., Burciu, R. G., Shukla, P., DeSimone, J. C., Okun, M. S., McFarland, N. R., & Vaillancourt, D. E. (2016). Free-water imaging in Parkinson's disease and atypical Parkinsonism. *Brain : a journal of neurology*, 139(Pt 2), 495–508. <https://doi.org/10.1093/brain/awv361>

Psenicka, M. W., Smith, B. C., Tinkey, R. A., & Williams, J. L. (2021). Connecting Neuroinflammation and Neurodegeneration in Multiple Sclerosis: Are Oligodendrocyte Precursor Cells a Nexus of Disease?. *Frontiers in cellular neuroscience*, 15, 654284. <https://doi.org/10.3389/fncel.2021.654284>

Pugh, P. L. (2007). Development of Rodent in Vivo Models: Neuroinflammation and Neurodegeneration Relevant to Alzheimer's Disease. Thesis Dissertation, Cardiff University. URL: <https://orca.cardiff.ac.uk/id/eprint/56148>

Qin, W., Zhang, M., Piao, Y., Guo, D., Zhu, Z., Tian, X., Li, K., & Yu, C. (2012). Wallerian degeneration in central nervous system: dynamic associations between diffusion indices and their underlying pathology. *PloS one*, 7(7), e41441. <https://doi.org/10.1371/journal.pone.0041441>

Rachmian, N., Medina, S., Cherqui, U., Akiva, H., Deitch, D., Edilbi, D., Croese, T., Salame, T. M., Ramos, J. M. P., Cahalon, L., Krizhanovsky, V., & Schwartz, M. (2024). Identification of senescent, TREM2-expressing microglia in aging and Alzheimer's disease model mouse brain. *Nature neuroscience*, 10.1038/s41593-024-01620-8. Advance online publication. <https://doi.org/10.1038/s41593-024-01620-8>

Rachmian, N., Medina, S., Cherqui, U., Akiva, H., Deitch, D., Edilbi, D., Croese, T., Salame, T. M., Ramos, J. M. P., Cahalon, L., Krizhanovsky, V., & Schwartz, M. (2024). Identification of senescent, TREM2-expressing microglia in aging and Alzheimer's disease model mouse brain. *Nature neuroscience*, 10.1038/s41593-024-01620-8. Advance online publication. <https://doi.org/10.1038/s41593-024-01620-8>

Ramón y Cajal, S. (1913) Sobre un nuevo proceder de impregnación de la neuroglia y sus resultados en el cerebro del hombre y animales. *Trab. Lab. Inv. Biol.*; 11: 219-37.

Rayleigh, L. (1896) On the theory of optical images, with special reference to the microscope. London, Edinburgh, and Dublin Philosophical Magazine and Journal of Science, 42, Part XV, 167–195.

Reveley, C., Ye, F. Q., & Leopold, D. A. (2024). Diffusion kurtosis MRI tracks grey matter myelin content in the primate cerebral cortex. *bioRxiv : the preprint server for biology*, 2024.03.08.584058. <https://doi.org/10.1101/2024.03.08.584058>

Río-Hortega, P. (1919). El “Tercer Elemento“ de los Centros Nerviosos. I. La Microglía en Estado Normal.

Rio-Hortega, P. (1920) El tercer elemento de los centros nerviosos. Poder fagocitario y movilidad de la microglía. *Bol. Soc. Esp. Biol.* 154-66

Rios-Carrillo, R., Ramírez-Manzanares, A., Luna-Munguía, H., Regalado, M., & Concha, L. (2023). Differentiation of white matter histopathology using b-tensor encoding and machine learning. *PLoS one*, 18(6), e0282549. <https://doi.org/10.1371/journal.pone.0282549>

Rocha e Silva M. (1994). A brief survey of the history of inflammation. 1978. *Agents and actions*, 43(3-4), 86–90. <https://doi.org/10.1007/BF01986675>

Rodieck, R. W. (1973). The vertebrate retina: Principles of structure and function. W. H. Freeman.
Rogasch, J. M. M., Hofheinz, F., van Heek, L., Voltin, C. A., Boellaard, R., & Kobe, C. (2022). Influences on PET Quantification and Interpretation. *Diagnostics (Basel, Switzerland)*, 12(2), 451. <https://doi.org/10.3390/diagnostics12020451>

Roger, V. L., Go, A. S., Lloyd-Jones, D. M., Benjamin, E. J., Berry, J. D., Borden, W. B., Bravata, D. M., Dai, S., Ford, E. S., Fox, C. S., Fullerton, H. J., Gillespie, C., Hailpern, S. M., Heit, J. A., Howard, V. J., Kissela, B. M., Kittner, S. J., Lackland, D. T., Lichtman, J. H., Lisabeth, L. D., ... American Heart Association Statistics Committee and Stroke Statistics Subcommittee (2012). Heart disease and stroke statistics--2012 update: a report from the American Heart Association. *Circulation*, 125(1), e2–e220. <https://doi.org/10.1161/CIR.0b013e31823ac046>

Rossato, J. I., Moreno, A., Genzel, L., Yamasaki, M., Takeuchi, T., Canals, S., & Morris, R. G. M. (2018). Silent Learning. *Current biology : CB*, 28(21), 3508–3515.e5. <https://doi.org/10.1016/j.cub.2018.09.012>

Sanchez-Guajardo, V., Tentillier, N., & Romero-Ramos, M. (2015). The relation between α -synuclein and microglia in Parkinson's disease: Recent developments. *Neuroscience*, 302, 47–58. <https://doi.org/10.1016/j.neuroscience.2015.02.008>

Santis, S., Assaf, Y., Evans, C. J., & Jones, D. K. (2014). Improved precision in CHARMED assessment of white matter through sampling scheme optimization and model parsimony testing. *Magnetic resonance in medicine*, 71(2), 661–671. <https://doi.org/10.1002/mrm.24717>

Satoh, J., Tabunoki, H., Yamamura, T., Arima, K., & Konno, H. (2007). Human astrocytes express aquaporin-1 and aquaporin-4 in vitro and in vivo. *Neuropathology : official journal of the Japanese Society of Neuropathology*, 27(3), 245–256. <https://doi.org/10.1111/j.1440-1789.2007.00774.x>

Savage, J. C., Carrier, M., & Tremblay, M. È. (2019). Morphology of Microglia Across Contexts of Health and Disease. *Methods in molecular biology (Clifton, N.J.)*, 2034, 13–26. https://doi.org/10.1007/978-1-4939-9658-2_2

Scarpazza, C., Ferracuti, S., Miolla, A., & Sartori, G. (2018). The charm of structural neuroimaging in insanity evaluations: guidelines to avoid misinterpretation of the findings. *Translational psychiatry*, 8(1), 227. <https://doi.org/10.1038/s41398-018-0274-8>

Shahidehpour, R. K., Higdon, R. E., Crawford, N. G., Neltner, J. H., Ighodaro, E. T., Patel, E., Price, D., Nelson, P. T., & Bachstetter, A. D. (2021). Dystrophic microglia are associated with

neurodegenerative disease and not healthy aging in the human brain. *Neurobiology of aging*, 99, 19–27. <https://doi.org/10.1016/j.neurobiolaging.2020.12.003>

SheikhBahaei, S., Morris, B., Collina, J., Anjum, S., Znati, S., Gamarra, J., Zhang, R., Gourine, A. V., & Smith, J. C. (2018). Morphometric analysis of astrocytes in brainstem respiratory regions. *The Journal of comparative neurology*, 526(13), 2032–2047. <https://doi.org/10.1002/cne.24472>

SheikhBahaei, S., Morris, B., Collina, J., Anjum, S., Znati, S., Gamarra, J., Zhang, R., Gourine, A. V., & Smith, J. C. (2018). Morphometric analysis of astrocytes in brainstem respiratory regions. *The Journal of comparative neurology*, 526(13), 2032–2047. <https://doi.org/10.1002/cne.24472>

Sheppard, O., Coleman, M. P., & Durrant, C. S. (2019). lipopolysaccharide-induced neuroinflammation induces presynaptic disruption through a direct action on brain tissue involving microglia-derived interleukin 1 beta. *Journal of neuroinflammation*, 16(1), 106. <https://doi.org/10.1186/s12974-019-1490-8>

Sherwood, C. C., Stimpson, C. D., Raghanti, M. A., Wildman, D. E., Uddin, M., Grossman, L. I., Goodman, M., Redmond, J. C., Bonar, C. J., Erwin, J. M., & Hof, P. R. (2006). Evolution of increased glia-neuron ratios in the human frontal cortex. *Proceedings of the National Academy of Sciences of the United States of America*, 103(37), 13606–13611. <https://doi.org/10.1073/pnas.0605843103>

Sierra, A., Encinas, J. M., Deudero, J. J., Chancey, J. H., Enikolopov, G., Overstreet-Wadiche, L. S., Tsirka, S. E., & Maletic-Savatic, M. (2010). Microglia shape adult hippocampal neurogenesis through apoptosis-coupled phagocytosis. *Cell stem cell*, 7(4), 483–495. <https://doi.org/10.1016/j.stem.2010.08.014>

Simons, M., & Nave, K. A. (2015). Oligodendrocytes: Myelination and Axonal Support. *Cold Spring Harbor perspectives in biology*, 8(1), a020479. <https://doi.org/10.1101/cshperspect.a020479>

Simpson, J. E., Ince, P. G., Lace, G., Forster, G., Shaw, P. J., Matthews, F., Savva, G., Brayne, C., Wharton, S. B., & MRC Cognitive Function and Ageing Neuropathology Study Group (2010). Astrocyte phenotype in relation to Alzheimer-type pathology in the ageing brain. *Neurobiology of aging*, 31(4), 578–590. <https://doi.org/10.1016/j.neurobiolaging.2008.05.015>

Skipuletz, T., Gudi, V., Hackstette, D., & Stangel, M. (2011). De- and remyelination in the CNS white and grey matter induced by cuprizone: the old, the new, and the unexpected. *Histology and histopathology*, 26(12), 1585–1597. <https://doi.org/10.14670/HH-26.1585>

Sofroniew M. V. (2005). Reactive astrocytes in neural repair and protection. *The Neuroscientist : a review journal bringing neurobiology, neurology and psychiatry*, 11(5), 400–407. <https://doi.org/10.1177/1073858405278321>

Sofroniew, M. V., & Vinters, H. V. (2010). Astrocytes: biology and pathology. *Acta neuropathologica*, 119(1), 7–35. <https://doi.org/10.1007/s00401-009-0619-8>

Squarzoni, P., Oller, G., Hoeffel, G., Pont-Lezica, L., Rostaing, P., Low, D., Bessis, A., Ginhoux, F., & Garel, S. (2014). Microglia modulate wiring of the embryonic forebrain. *Cell reports*, 8(5), 1271–1279. <https://doi.org/10.1016/j.celrep.2014.07.042>

- Stephenson, J., Nutma, E., van der Valk, P., & Amor, S. (2018). Inflammation in CNS neurodegenerative diseases. *Immunology*, *154*(2), 204–219. <https://doi.org/10.1111/imm.12922>
- Streit, W. J., Braak, H., Xue, Q. S., & Bechmann, I. (2009). Dystrophic (senescent) rather than activated microglial cells are associated with tau pathology and likely precede neurodegeneration in Alzheimer's disease. *Acta neuropathologica*, *118*(4), 475–485. <https://doi.org/10.1007/s00401-009-0556-6>
- Streit, W. J., Graeber, M. B., & Kreutzberg, G. W. (1988). Functional plasticity of microglia: a review. *Glia*, *1*(5), 301–307. <https://doi.org/10.1002/glia.440010502>
- Surala, M., Soso-Zdravkovic, L., Munro, D., Rifat, A., Ouk, K., Vida, I., Priller, J., & Madry, C. (2024). Lifelong absence of microglia alters hippocampal glutamatergic networks but not synapse and spine density. *EMBO reports*, 10.1038/s44319-024-00130-9. Advance online publication. <https://doi.org/10.1038/s44319-024-00130-9>
- Suzumura, A., Mezitis, S. G., Gonatas, N. K., & Silberberg, D. H. (1987). MHC antigen expression on bulk isolated macrophage-microglia from newborn mouse brain: induction of Ia antigen expression by gamma-interferon. *Journal of neuroimmunology*, *15*(3), 263–278. [https://doi.org/10.1016/0165-5728\(87\)90121-4](https://doi.org/10.1016/0165-5728(87)90121-4)
- Szatkowski, M., Barbour, B., & Attwell, D. (1990). Non-vesicular release of glutamate from glial cells by reversed electrogenic glutamate uptake. *Nature*, *348*(6300), 443–446. <https://doi.org/10.1038/348443a0>
- Szczepanik, A. M., Fishkin, R. J., Rush, D. K., & Wilmot, C. A. (1996). Effects of chronic intrahippocampal infusion of lipopolysaccharide in the rat. *Neuroscience*, *70*(1), 57–65. [https://doi.org/10.1016/0306-4522\(95\)00296-u](https://doi.org/10.1016/0306-4522(95)00296-u)
- Tan, Y. L., Yuan, Y., & Tian, L. (2020). Microglial regional heterogeneity and its role in the brain. *Molecular psychiatry*, *25*(2), 351–367. <https://doi.org/10.1038/s41380-019-0609-8>
- Tan, Y. L., Yuan, Y., & Tian, L. (2020). Microglial regional heterogeneity and its role in the brain. *Molecular psychiatry*, *25*(2), 351–367. <https://doi.org/10.1038/s41380-019-0609-8>
- Taquet, M., Jankovski, A., Rensonnet, G., Jacobs, D., des Rieux, A., Macq, B., Warfield, S. K., & Scherrer, B. (2019). Extra-axonal restricted diffusion as an in-vivo marker of reactive microglia. *Scientific reports*, *9*(1), 13874. <https://doi.org/10.1038/s41598-019-50432-5>
- Tarkin, J. M., Joshi, F. R., Evans, N. R., Chowdhury, M. M., Figg, N. L., Shah, A. V., Starks, L. T., Martin-Garrido, A., Manavaki, R., Yu, E., Kuc, R. E., Grassi, L., Kreuzhuber, R., Kostadima, M. A., Frontini, M., Kirkpatrick, P. J., Coughlin, P. A., Gopalan, D., Fryer, T. D., Buscombe, J. R., ... Rudd, J. H. (2017). Detection of Atherosclerotic Inflammation by 68Ga-DOTATATE PET Compared to [18F]FDG PET Imaging. *Journal of the American College of Cardiology*, *69*(14), 1774–1791. <https://doi.org/10.1016/j.jacc.2017.01.060>
- Tawakol, A., Migrino, R. Q., Bashian, G. G., Bedri, S., Vermylen, D., Cury, R. C., Yates, D., LaMuraglia, G. M., Furie, K., Houser, S., Gewirtz, H., Muller, J. E., Brady, T. J., & Fischman, A. J.

(2006). In vivo 18F-fluorodeoxyglucose positron emission tomography imaging provides a noninvasive measure of carotid plaque inflammation in patients. *Journal of the American College of Cardiology*, 48(9), 1818–1824. <https://doi.org/10.1016/j.jacc.2006.05.076>

Tay, T. L., Savage, J. C., Hui, C. W., Bisht, K., & Tremblay, M. È. (2017). Microglia across the lifespan: from origin to function in brain development, plasticity and cognition. *The Journal of physiology*, 595(6), 1929–1945. <https://doi.org/10.1113/JP272134>

Thomsen, M. S., Andersen, M. V., Christoffersen, P. R., Jensen, M. D., Lichota, J., & Moos, T. (2015). Neurodegeneration with inflammation is accompanied by accumulation of iron and ferritin in microglia and neurons. *Neurobiology of disease*, 81, 108–118. <https://doi.org/10.1016/j.nbd.2015.03.013>

Tondo, G., Iaccarino, L., Cerami, C., Vanoli, G. E., Presotto, L., Masiello, V., Coliva, A., Salvi, F., Bartolomei, I., Mosca, L., Lunetta, C., & Perani, D. (2020). 11 C-PK11195 PET-based molecular study of microglia activation in SOD1 amyotrophic lateral sclerosis. *Annals of clinical and translational neurology*, 7(9), 1513–1523. <https://doi.org/10.1002/acn3.51112>

Tran, P., Thoprakarn, U., Gourieux, E., Dos Santos, C. L., Cavedo, E., Guizard, N., Cotton, F., Krolak-Salmon, P., Delmaire, C., Heidelberg, D., Pyatigorskaya, N., Ströer, S., Dormont, D., Martini, J. B., Chupin, M., & Alzheimer's Disease Neuroimaging Initiatives, for the Frontotemporal Lobar Degeneration Neuroimaging Initiative (2022). Automatic segmentation of white matter hyperintensities: validation and comparison with state-of-the-art methods on both Multiple Sclerosis and elderly subjects. *NeuroImage. Clinical*, 33, 102940. <https://doi.org/10.1016/j.nicl.2022.102940>

Tran, P., Thoprakarn, U., Gourieux, E., Dos Santos, C. L., Cavedo, E., Guizard, N., Cotton, F., Krolak-Salmon, P., Delmaire, C., Heidelberg, D., Pyatigorskaya, N., Ströer, S., Dormont, D., Martini, J. B., Chupin, M., & Alzheimer's Disease Neuroimaging Initiatives, for the Frontotemporal Lobar Degeneration Neuroimaging Initiative (2022). Automatic segmentation of white matter hyperintensities: validation and comparison with state-of-the-art methods on both Multiple Sclerosis and elderly subjects. *NeuroImage. Clinical*, 33, 102940. <https://doi.org/10.1016/j.nicl.2022.102940>

Tremblay, M. È., Lowery, R. L., & Majewska, A. K. (2010). Microglial interactions with synapses are modulated by visual experience. *PLoS biology*, 8(11), e1000527. <https://doi.org/10.1371/journal.pbio.1000527>

Triarhou, L. C., & Herndon, R. M. (1986). The effect of dexamethasone on L-alpha-lysophosphatidyl choline (lysolecithin)-induced demyelination of the rat spinal cord. *Archives of neurology*, 43(2), 121–125. <https://doi.org/10.1001/archneur.1986.00520020015008>

Uddin, M. N., Figley, T. D., Solar, K. G., Shatil, A. S., & Figley, C. R. (2019). Comparisons between multi-component myelin water fraction, T1w/T2w ratio, and diffusion tensor imaging measures in healthy human brain structures. *Scientific reports*, 9(1), 2500. <https://doi.org/10.1038/s41598-019-39199-x>

van Tilborg, E., van Kammen, C. M., de Theije, C. G. M., van Meer, M. P. A., Dijkhuizen, R. M., & Nijboer, C. H. (2017). A quantitative method for microstructural analysis of myelinated axons in the injured rodent brain. *Scientific reports*, 7(1), 16492. <https://doi.org/10.1038/s41598-017-16797-1>

Van Zeller, M., Sebastião, A. M., & Valente, C. A. (2022). Microglia Depletion from Primary Glial Cultures Enables to Accurately Address the Immune Response of Astrocytes. *Biomolecules*, *12*(5), 666. <https://doi.org/10.3390/biom12050666>

Verdonk, F., Roux, P., Flamant, P., Fiette, L., Bozza, F. A., Simard, S., Lemaire, M., Plaud, B., Shorte, S. L., Sharshar, T., Chrétien, F., & Danckaert, A. (2016). Phenotypic clustering: a novel method for microglial morphology analysis. *Journal of neuroinflammation*, *13*(1), 153. <https://doi.org/10.1186/s12974-016-0614-7>

Virchow, R. (1858). Cellular pathology: as based upon physiological and pathological histology. Pathological institute of Berlin lectures.

Waddell, L. A., Lefevre, L., Bush, S. J., Raper, A., Young, R., Lisowski, Z. M., McCulloch, M. E. B., Muriuki, C., Sauter, K. A., Clark, E. L., Irvine, K. M., Pridans, C., Hope, J. C., & Hume, D. A. (2018). ADGRE1 (EMR1, F4/80) Is a Rapidly-Evolving Gene Expressed in Mammalian Monocyte-Macrophages. *Frontiers in immunology*, *9*, 2246. <https://doi.org/10.3389/fimmu.2018.02246>

Walker K. A. (2018). Inflammation and neurodegeneration: chronicity matters. *Aging*, *11*(1), 3–4. <https://doi.org/10.18632/aging.101704>

Wang, H., Zhang, S., Xie, L., Zhong, Z., & Yan, F. (2023). Neuroinflammation and peripheral immunity: Focus on ischemic stroke. *International immunopharmacology*, *120*, 110332. <https://doi.org/10.1016/j.intimp.2023.110332>

Wang, X., Lou, N., Xu, Q., Tian, G. F., Peng, W. G., Han, X., Kang, J., Takano, T., & Nedergaard, M. (2006). Astrocytic Ca²⁺ signaling evoked by sensory stimulation in vivo. *Nature neuroscience*, *9*(6), 816–823. <https://doi.org/10.1038/nn1703>

Wang, Y., Leak, R. K., & Cao, G. (2022). Microglia-mediated neuroinflammation and neuroplasticity after stroke. *Frontiers in cellular neuroscience*, *16*, 980722. <https://doi.org/10.3389/fncel.2022.980722>

Ward, R. J., Dexter, D. T., & Crichton, R. R. (2015). Ageing, neuroinflammation and neurodegeneration. *Frontiers in bioscience (Scholar edition)*, *7*(1), 189–204. <https://doi.org/10.2741/S433>

Wasén, C., Beauchamp, L. C., Vincentini, J., Li, S., LeServe, D. S., Gauthier, C., Lopes, J. R., Moreira, T. G., Ekwudo, M. N., Yin, Z., da Silva, P., Krishnan, R. K., Butovsky, O., Cox, L. M., & Weiner, H. L. (2024). Bacteroidota inhibit microglia clearance of amyloid-beta and promote plaque deposition in Alzheimer's disease mouse models. *Nature communications*, *15*(1), 3872. <https://doi.org/10.1038/s41467-024-47683-w>

Wattjes, M. P., Rovira, À., Miller, D., Yousry, T. A., Sormani, M. P., de Stefano, M. P., Tintoré, M., Auger, C., Tur, C., Filippi, M., Rocca, M. A., Fazekas, F., Kappos, L., Polman, C., Frederik Barkhof, Xavier Montalban, & MAGNIMS study group (2015). Evidence-based guidelines: MAGNIMS consensus guidelines on the use of MRI in multiple sclerosis--establishing disease prognosis and

monitoring patients. *Nature reviews. Neurology*, 11(10), 597–606. <https://doi.org/10.1038/nrneurol.2015.157>

Welle, A., Kasakow, C. V., Jungmann, A. M., Gobbo, D., Stopper, L., Nordström, K., Salhab, A., Gasparoni, G., Scheller, A., Kirchhoff, F., & Walter, J. (2021). Epigenetic control of region-specific transcriptional programs in mouse cerebellar and cortical astrocytes. *Glia*, 69(9), 2160–2177. <https://doi.org/10.1002/glia.24016>

Wes, P. D., Holtman, I. R., Boddeke, E. W., Möller, T., & Eggen, B. J. (2016). Next generation transcriptomics and genomics elucidate biological complexity of microglia in health and disease. *Glia*, 64(2), 197–213. <https://doi.org/10.1002/glia.22866>

Wilbanks, B., Maher, L. J., 3rd, & Rodriguez, M. (2019). Glial cells as therapeutic targets in progressive multiple sclerosis. *Expert review of neurotherapeutics*, 19(6), 481–494. <https://doi.org/10.1080/14737175.2019.1614443>

Wilhelmsson, U., Bushong, E. A., Price, D. L., Smarr, B. L., Phung, V., Terada, M., Ellisman, M. H., & Pekny, M. (2006). Redefining the concept of reactive astrocytes as cells that remain within their unique domains upon reaction to injury. *Proceedings of the National Academy of Sciences of the United States of America*, 103(46), 17513–17518. <https://doi.org/10.1073/pnas.0602841103>

Wingerchuk, D. M., Banwell, B., Bennett, J. L., Cabre, P., Carroll, W., Chitnis, T., de Seze, J., Fujihara, K., Greenberg, B., Jacob, A., Jarius, S., Lana-Peixoto, M., Levy, M., Simon, J. H., Tenenbaum, S., Traboulsee, A. L., Waters, P., Wellik, K. E., Weinshenker, B. G., & International Panel for NMO Diagnosis (2015). International consensus diagnostic criteria for neuromyelitis optica spectrum disorders. *Neurology*, 85(2), 177–189. <https://doi.org/10.1212/WNL.0000000000001729>

Wolf, Y., Yona, S., Kim, K. W., & Jung, S. (2013). Microglia, seen from the CX3CR1 angle. *Frontiers in cellular neuroscience*, 7, 26. <https://doi.org/10.3389/fncel.2013.00026>

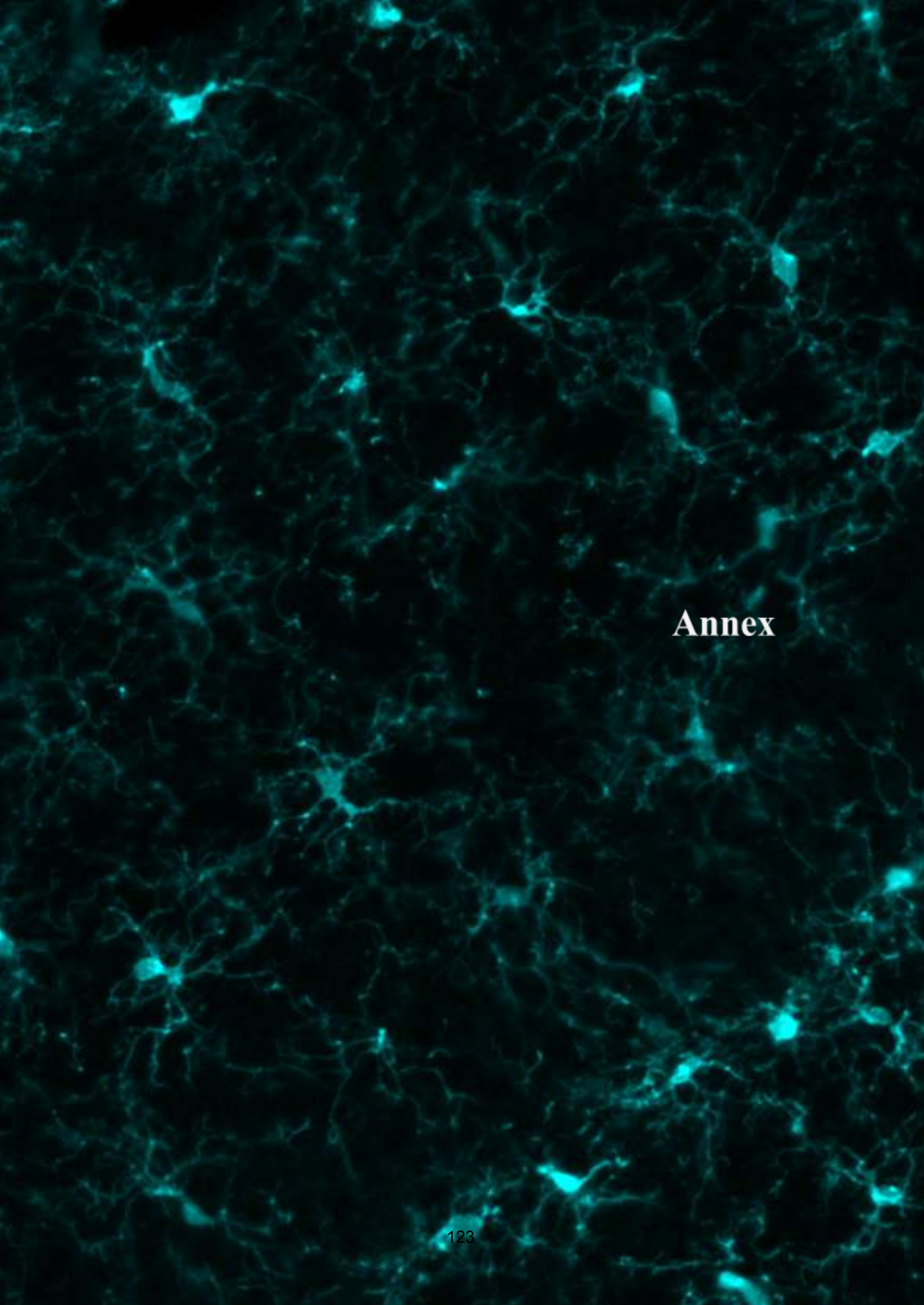
Wood, E. T., Ercan, E., Sati, P., Cortese, I. C. M., Ronen, I., & Reich, D. S. (2017). Longitudinal MR spectroscopy of neurodegeneration in multiple sclerosis with diffusion of the intra-axonal constituent *N*-acetylaspartate. *NeuroImage. Clinical*, 15, 780–788. <https://doi.org/10.1016/j.nicl.2017.06.028>

Woodruff, R. H., & Franklin, R. J. (1999). Demyelination and remyelination of the caudal cerebellar peduncle of adult rats following stereotaxic injections of lysolecithin, ethidium bromide, and complement/anti-galactocerebroside: a comparative study. *Glia*, 25(3), 216–228. [https://doi.org/10.1002/\(sici\)1098-1136\(19990201\)25:3](https://doi.org/10.1002/(sici)1098-1136(19990201)25:3)

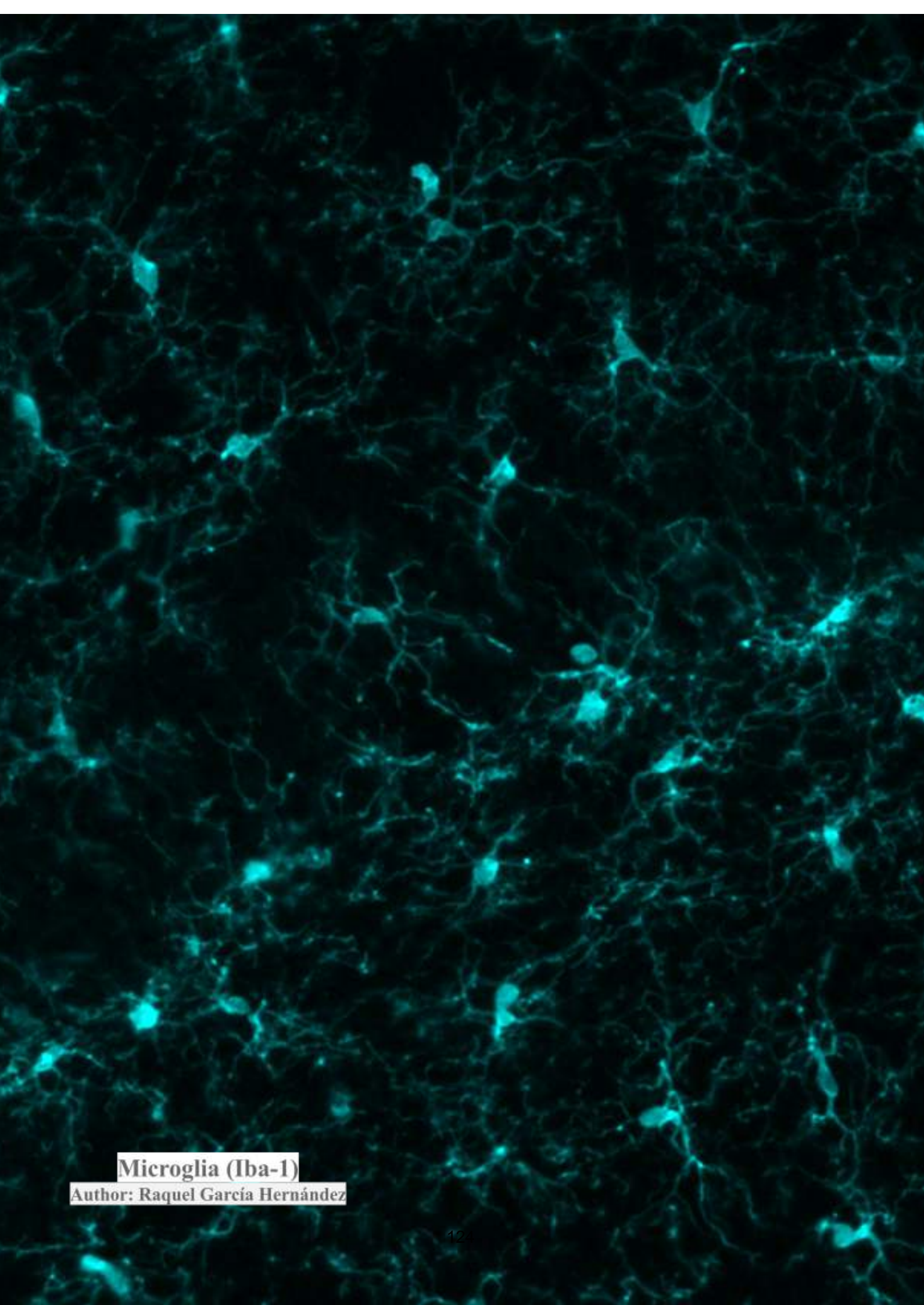
Wu, W., He, Y., Chen, Y., Fu, Y., He, S., Liu, K., & Qu, J. Y. (2024). Microglial-Mediated Prevention of Axonal Degeneration in the Injured Spinal Cord: Insights from an In Vivo Imaging Study. *BioRxiv*, 2024.04.13.589343. <https://doi.org/10.1101/2024.04.13.589343>

Xia, W., Singh, N., Goel, S., & Shi, S. (2023). Molecular imaging of innate immunity and immunotherapy. *Advanced drug delivery reviews*, 198, 114865. <https://doi.org/10.1016/j.addr.2023.114865>

- Xiao, M., & Hu, G. (2014). Involvement of aquaporin 4 in astrocyte function and neuropsychiatric disorders. *CNS neuroscience & therapeutics*, 20(5), 385–390. <https://doi.org/10.1111/cns.12267>
- Yamada, T., Kawamata, T., Walker, D. G., & McGeer, P. L. (1992). Vimentin immunoreactivity in normal and pathological human brain tissue. *Acta neuropathologica*, 84(2), 157–162. <https://doi.org/10.1007/BF00311389>
- Yang, F. Y., Huang, L. H., Wu, M. T., & Pan, Z. Y. (2022). Ultrasound Neuromodulation Reduces Demyelination in a Rat Model of Multiple Sclerosis. *International journal of molecular sciences*, 23(17), 10034. <https://doi.org/10.3390/ijms231710034>
- Yi, S. Y., Barnett, B. R., Torres-Velázquez, M., Zhang, Y., Hurley, S. A., Rowley, P. A., Hernando, D., & Yu, J. J. (2019). Detecting Microglial Density With Quantitative Multi-Compartment Diffusion MRI. *Frontiers in neuroscience*, 13, 81. <https://doi.org/10.3389/fnins.2019.00081>
- Young, N. P., Weinshenker, B. G., Parisi, J. E., Scheithauer, B., Giannini, C., Roemer, S. F., Thomsen, K. M., Mandrekar, J. N., Erickson, B. J., & Lucchinetti, C. F. (2010). Perivenous demyelination: association with clinically defined acute disseminated encephalomyelitis and comparison with pathologically confirmed multiple sclerosis. *Brain : a journal of neurology*, 133(Pt 2), 333–348. <https://doi.org/10.1093/brain/awp321>
- Yovel, Y., & Assaf, Y. (2007). Virtual definition of neuronal tissue by cluster analysis of multi-parametric imaging (virtual-dot-com imaging). *NeuroImage*, 35(1), 58–69. <https://doi.org/10.1016/j.neuroimage.2006.08.055>
- Zhang, H., Schneider, T., Wheeler-Kingshott, C. A., & Alexander, D. C. (2012). NODDI: practical in vivo neurite orientation dispersion and density imaging of the human brain. *NeuroImage*, 61(4), 1000–1016. <https://doi.org/10.1016/j.neuroimage.2012.03.072>
- Zhang, J., Zhang, L., Yi, S., Jiang, X., Qiao, Y., Zhang, Y., Xiao, C., & Zhou, T. (2020). Mouse Astrocytes Promote Microglial Ramification by Releasing TGF- β and Forming Glial Fibers. *Frontiers in cellular neuroscience*, 14, 195. <https://doi.org/10.3389/fncel.2020.00195>
- Zhang, M., Ni, Y., Zhou, Q., He, L., Meng, H., Gao, Y., Huang, X., Meng, H., Li, P., Chen, M., Wang, D., Hu, J., Huang, Q., Li, Y., Chauveau, F., Li, B., & Chen, S. (2021). 18F-florbetapir PET/MRI for quantitatively monitoring myelin loss and recovery in patients with multiple sclerosis: A longitudinal study. *EClinicalMedicine*, 37, 100982. <https://doi.org/10.1016/j.eclinm.2021.100982>
- Zinkand, W. C., Moore, W. C., Thompson, C., Salama, A. I., & Patel, J. (1992). Ibotenic acid mediates neurotoxicity and phosphoinositide hydrolysis by independent receptor mechanisms. *Molecular and chemical neuropathology*, 16(1-2), 1–10. <https://doi.org/10.1007/BF03159956>



Annex



Microglia (Iba-1)

Author: Raquel García Hernández

Mapping microglia and astrocyte activation in vivo using diffusion MRI

Raquel Garcia-Hernandez¹, Antonio Cerdán Cerdá¹, Alejandro Trouve Carpena¹, Mark Drakesmith²†, Kristin Koller², Derek K. Jones², Santiago Canals^{1*}, Silvia De Santis^{1,2*}

While glia are increasingly implicated in the pathophysiology of psychiatric and neurodegenerative disorders, available methods for imaging these cells in vivo involve either invasive procedures or positron emission tomography radiotracers, which afford low resolution and specificity. Here, we present a noninvasive diffusion-weighted magnetic resonance imaging (MRI) method to image changes in glia morphology. Using rat models of neuroinflammation, degeneration, and demyelination, we demonstrate that diffusion-weighted MRI carries a fingerprint of microglia and astrocyte activation and that specific signatures from each population can be quantified noninvasively. The method is sensitive to changes in glia morphology and proliferation, providing a quantitative account of neuroinflammation, regardless of the existence of a concomitant neuronal loss or demyelinating injury. We prove the translational value of the approach showing significant associations between MRI and histological microglia markers in humans. This framework holds the potential to transform basic and clinical research by clarifying the role of inflammation in health and disease.

INTRODUCTION

Brain diseases with a degenerative component such as Alzheimer's, Parkinson's, multiple sclerosis, and dementia are a pressing problem for developed societies with aging populations (1–3). Accumulating evidence suggests chronic neuroinflammation, the sustained activation of microglia and astrocytes, to strongly influence neurodegeneration and contribute to its progression. A major question is whether inhibition of the inflammatory response has the ability to reverse or slow down its symptoms (4). In addition, abnormal immune activation during puberty and adolescence has been associated with increased vulnerability to brain disorders later in life (5), making the characterization of the inflammatory profile along the life span a hot topic. Therapies targeting glial cells are currently being proposed as disease-altering treatments to improve the outcome of neurological disorders, with extremely promising results (4, 6, 7). Furthermore, for many brain diseases, neuroinflammation is emerging as a cause, rather than a consequence, of the pathogenesis (8); thus, characterizing the tissue inflammatory state could provide valuable early disease biomarkers. In this context, desired properties of such biomarkers would be the capacity to detect both changes in morphology and proliferation/depletion (both hallmarks of glia activation), and to discriminate inflammation with and without neurodegeneration. In addition, the set of biomarkers should show a response specific to glia, which can be teased apart from the response to other tissue insults relevant in some neurodegenerative diseases, e.g., demyelination.

While imaging techniques are widely adopted to monitor neurological conditions, noninvasive approaches able to specifically characterize brain inflammation in vivo are lacking. The current gold standard is positron emission tomography (PET)–based targeting of the 18-kDa translocator protein. While difficult to generalize due

to different binding genotypes across individuals (9), PET is associated with ionizing radiation exposure, which limits its use in vulnerable populations and longitudinal studies, and also has low spatial resolution, making it unsuitable to image small structures. In addition, while PET's main advantage relates to molecular specificity of tracer binding, inflammation-specific radiotracers express across multiple cell types (microglia, astrocytes, and endothelium). Last, a significant tracer uptake in the periphery makes it hard to separate central from peripheral inflammation (10). Diffusion-weighted magnetic resonance imaging (dw-MRI), on the other hand, has the unique ability to image brain microstructure in vivo, noninvasively, and with high resolution by capturing the random motion of water molecules in brain parenchyma (11).

While the dw-MRI signal is potentially sensitive to all extracellular and intracellular spaces that restrict water displacement in the tissue, current formulations are mostly designed for white matter and axons. A few recent studies, establishing the groundwork for this work, showed that conventional MRI signal can be sensitive to various alterations in microglia (12–14), but none so far showed specificity to microglia and astrocyte activation, or inflammation in the presence of neurodegeneration. Achieving specificity is of key importance as neurodegenerative diseases manifest through different mechanisms, involving specific cell populations, all playing potentially different roles in disease causation and progression. By combining advanced dw-MRI sequences with mathematical models based on neurobiological knowledge of brain parenchyma morphology, the diffusion characteristics within specific tissue compartments, and even cell types, could be measured (15).

With this idea in mind, we developed an innovative strategy to image microglia and astrocyte activation in gray matter using dw-MRI, by building a microstructural multicompartment tissue model informed by knowledge of microglia and astrocyte morphology. To validate the model, we first used an established rat paradigm of inflammation based on intracerebral lipopolysaccharide (LPS) administration (16). In this paradigm, neuronal viability and morphology are preserved, while inducing microglial activation within a few hours, and a delayed astrocytic response that is detectable only

¹Instituto de Neurociencias, CSIC/UMH, San Juan de Alicante, Alicante, Spain.

²CUBRIC, School of Psychology, Cardiff University, Cardiff, UK.

*Corresponding author. Email: dsilvia@umh.es (S.D.S.); scanals@umh.es (S.C.)

†Present address: Communicable Disease Surveillance Centre, Public Health Wales, 2 Capital Quarter, Tyndall Street, Cardiff, CF10 4BZ, Wales, UK.

24 hours after injection (17). Therefore, glial responses can be transiently dissociated from neuronal degeneration, and the signature of reactive microglia investigated independently of any astrogliosis. Then, to isolate the imaging fingerprint of astrocyte activation, we repeated the LPS experiment but pretreating the animals with the CSF1R inhibitor PLX5622 (Plexxikon Inc.), which is known to temporally deplete around 90% of the microglia (18). Then, we used an established paradigm of neuronal damage, based on ibotenic acid administration (19), to test whether the model was able to disentangle neuroinflammatory signatures with and without a concomitant neurodegeneration. This is pivotal for demonstrating the utility of the framework as a biomarker discovery platform for the inflammatory status in neurodegenerative diseases, where both glia activation and neuronal damage are key players. Last, we used an established paradigm of demyelination, based on focal administration of lysolecithin (20), to demonstrate that the developed biomarkers are not confounded by tissue alterations frequently found in brain disorders and with a strong impact on water diffusivity.

We demonstrate that the dw-MRI signal carries the fingerprint of microglial and astrocyte activation, with signatures specific to each glia population, reflecting the morphological changes as validated postmortem by quantitative immunohistochemistry. We demonstrate that the framework is both sensitive and specific to inflammation with and without neurodegeneration so that the two conditions can be teased apart. In addition, we demonstrate that the biomarker set can discriminate between inflammation and demyelination, supporting the possibility to interrogate and characterize brain parenchyma with compartment-specific biomarkers. We demonstrate the translational value of the approach in a cohort of healthy humans at high resolution, in which we performed a reproducibility analysis. Statistically significant association with known microglia density patterns in the human brain supports the utility of the method to generate reliable glia biomarkers. A framework able to characterize relevant aspects of tissue microstructure during inflammation, *in vivo* and noninvasively, is expected to have a tremendous impact on our understanding of the pathophysiology of many brain conditions and transform current diagnostic practice and treatment monitoring strategies.

RESULTS

Microstructural model of diffusion and immunological challenge in rats

We built a model of gray matter diffusivity, as detailed in Materials and Methods. Briefly, the model accounts for water diffusion in the microglial compartment corresponding to small cell somas, modeled as small spheres, with thin cellular processes, modeled as sticks, growing radially with a dispersion captured by a dispersion parameter (according to a Watson distribution of orientations), and an astrocytic compartment consisting of large globular cells, modeled as large spheres (21). Note that while glial fibrillary acidic protein (GFAP) stains the cytoskeleton of the cell, astrocytes have a globular shape (22). Both compartments are embedded in an extracellular space compartment, composed of a tensor-like subcompartment (hindered water in contact with structures and cells) and a free water compartment of water undergoing unrestricted diffusion. All MRI markers analyzed (stick fraction, stick dispersion, small and big sphere radius, and tissue fraction) are defined in Materials and Methods. Changes in the tissue fraction (the reciprocal of the free

water signal) are interpreted as a surrogate measure of tissue loss, *i.e.*, of degeneration (23). We then tested the mathematical model with three experimental paradigms. In the first one, neuroinflammation without neurodegeneration is induced by an injection of LPS; in the second, neuroinflammation with degeneration is induced by an injection of ibotenic acid; in the third one, we induced demyelination using injections of lysolecithin, which causes a transient, rapidly resolving inflammation and a long-lasting demyelination (at least 3 weeks) without remyelination. All injections were performed in one hemisphere targeting the dentate gyrus of the hippocampus, with the contralateral side as within-subjects control (vehicle injected; see Materials and Methods for details).

Microglia activation characterized using Iba-1 staining and MRI

Morphological analysis of Iba-1⁺ cells by histology in the tissue at different time points after LPS injection demonstrated a fast microglial reaction with retraction of cellular processes at 8 hours, which progressed at 24 hours with an additional increase in the microglial cell body size and an increase in the process dispersion parameter (indicating less dispersion), as shown in Fig. 1 (B and C). No changes in cell density are found (fig. S6). The distinct and time-dependent changes in microglial cell morphology were tightly mirrored by the imaging parameters specifically related to the microglia compartment, *i.e.*, sticks (cellular processes) and the small spheres (cell soma), as shown in Fig. 1E. Accordingly, the stick fraction was significantly reduced at 8 hours in the injected versus control hippocampus and further reduced at 24 hours. The stick dispersion parameter was increased at 24 hours, and the radius of the small sphere component was significantly increased at 8 and 24 hours. These LPS-induced changes disappeared when the animals were depleted of microglia by pretreatment with PLX5622 (fig. S7), demonstrating the specificity of these MRI signatures to microglia. Moreover, when looking at interindividual variability, a strong association was found between MRI-derived microglial marker change and their histological counterparts at all measured time points (Fig. 1, F and G). Last, 2 weeks after the injection, when complete recovery was expected, all parameters measured from both histology and MRI converged, showing no statistically significant difference between injected and control hemispheres. Overall, these results demonstrated the possibility to recover a microglia-specific signal from dw-MRI with capacity to unmask a microglial reaction *in vivo* (Fig. 1H). Whole grey matter average map of the stick fraction is reported in fig. S8.

Astrocyte activation characterized using GFAP staining and MRI

We next performed a comparable analysis with astrocytes (labeled as GFAP⁺ cells), taking advantage of the distinct time course of their response to LPS injection. This cell population, unlike microglia, showed no significant alterations in either density or morphology at 8 hours after LPS injection, as shown in Fig. 2 (A and C). However, at 24 hours, astrocytes grow in volume as measured by the mean radius of the convex hull (Fig. 2C; see Materials and Methods for details). The associated MRI compartment for astrocytes, *i.e.*, the large spheres, followed the same pattern of changes across conditions (Fig. 2D). Volume of GFAP⁺ cells and the mean radius of the large spheres measured by dw-MRI grew in parallel at 24 hours after LPS injection, were insensitive to microglia depletion with PLX5622, and recovered toward baseline levels at 15 days after injection.

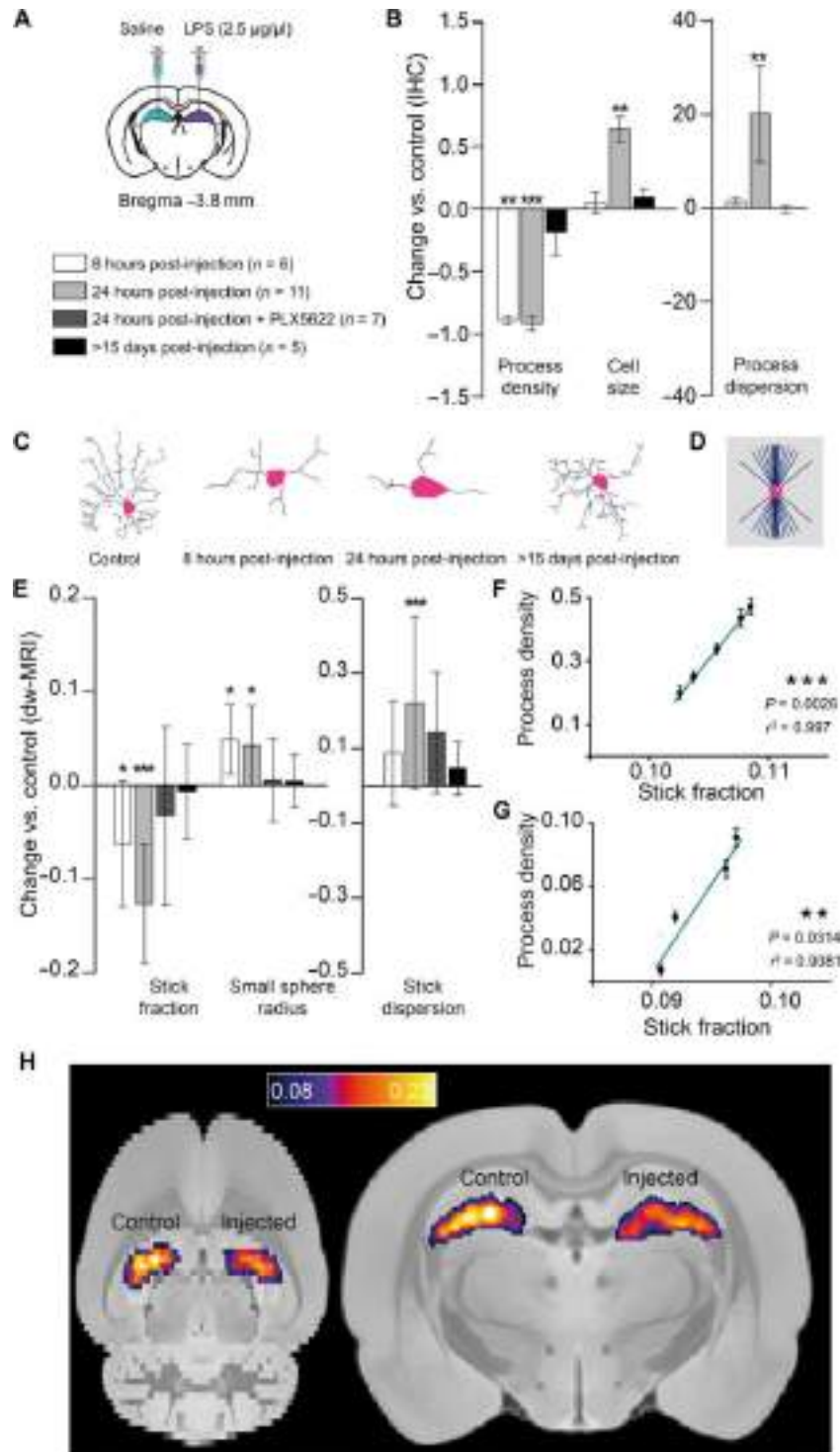


Fig. 1. Histological characterization of microglia reaction and its associated MRI signature. (A) Experimental scheme showing bilateral stereotaxic injection of LPS (left hemisphere)/saline (right hemisphere) and the composition of the four groups: Six animals were scanned 8 hours after injection, 11 animals were scanned 24 hours after injection, 7 animals were treated with PLX5622 for 7 days before the injection and then scanned 24 hours after injection, and 5 animals were scanned 15 days or more after injection. (B) Normalized change $(P_{\text{injected}} - P_{\text{control}})/P_{\text{control}}$ in process density, cell size, and process dispersion parameter for the injected versus control hippocampus, measured in Iba-1⁺-stained microglia for the different groups. Asterisks represent significant paired difference between injected and control (** $P < 0.01$ and *** $P < 0.001$). Error bars represent SD. IHC, immunohistochemistry. (C) Morphology reconstruction of representative microglia at the different times. (D) Geometrical model used for microglia. (E) Normalized change $(P_{\text{injected}} - P_{\text{control}})/P_{\text{control}}$ between MRI parameter calculated in the injected versus control hemisphere for the microglia compartment. Asterisks represent significant paired difference between injected and control (* $P < 0.05$ and *** $P < 0.001$). (F and G) Correlations between stick fraction from MRI and process density from Iba-1 at 8 (F) and 24 hours after injection (G). (H) Mean stick fraction maps at 24 hours after injection, normalized to a rat brain template and averaged over all rats.

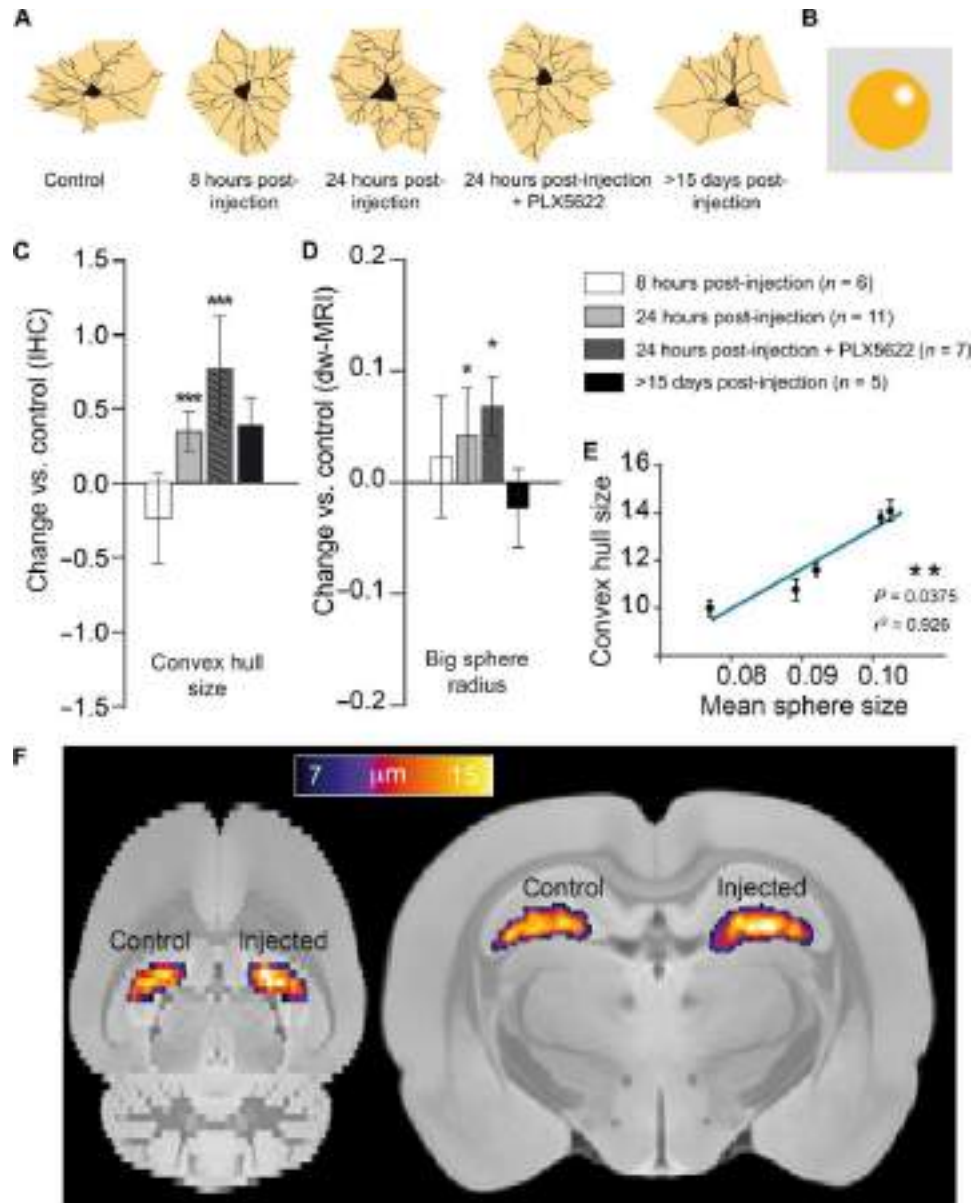


Fig. 2. Histological characterization of astrocyte reaction and its associated MRI signature. (A) Morphology reconstruction of representative astrocytes at the different times in black and two-dimensional (2D) convex hull in orange. (B) Geometrical model used for astrocytes. (C) Normalized change $(P_{\text{injected}} - P_{\text{control}})/P_{\text{control}}$ in convex hull mean radius for the injected versus control hippocampus, measured in GFAP⁺-stained astrocytes for the different groups. Asterisks represent significant paired difference between injected and control ($***P < 0.001$). Error bars represent SD. (D) Normalized change $(P_{\text{injected}} - P_{\text{control}})/P_{\text{control}}$ between MRI-derived large sphere radius calculated in the injected versus control hemisphere for the astrocyte compartment (shown in the inset). Asterisks represent significant paired difference between injected and control ($*P < 0.05$). (E) Correlation between mean sphere radius from MRI and convex hull mean radius from GFAP. (F) Large sphere radius maps at 24 hours after injection, normalized to a rat brain template and averaged over all rats.

Accordingly, their interindividual variability showed a strong correlation (Fig. 2E). Therefore, the results obtained for the astrocytic component also demonstrate the possibility of recovering an astrocyte-specific signal from dw-MRI and the capacity to map astrocyte reactions in vivo (Fig. 2F).

Concomitant microglia activation and neuronal death characterized using NeuN staining and MRI

To challenge the capability of the developed model to distinguish between pure inflammation and inflammation with concomitant

neurodegeneration, a cohort of animals was injected as before, but with ibotenic acid, using the contralateral (right) hemisphere as control (saline injected). Histological staining demonstrated that ibotenic acid at the chosen concentration induced a microglial reaction characterized by retraction of the cellular processes with increased dispersion parameter and a significant increase in cell density (Fig. 3, A and B). No alterations in astrocytes were observed, as shown in the Supplementary Materials (fig. S9). Neuronal staining with NeuN unveiled a large decrease in staining intensity in the injected hemisphere, demonstrating the severe neuronal loss induced

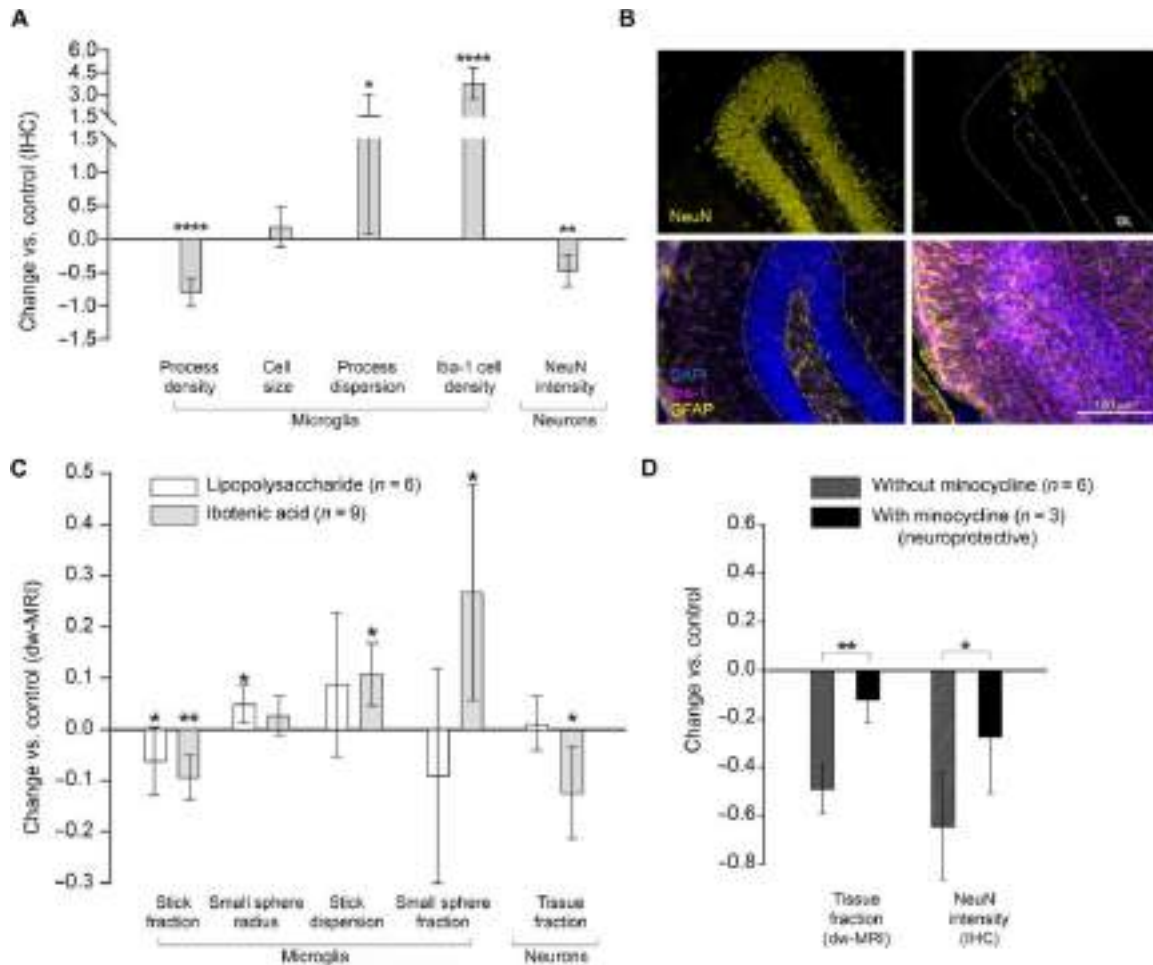


Fig. 3. Characterization of inflammation in the presence of neuronal death. (A) Normalized change ($P_{\text{injected}} - P_{\text{control}}/P_{\text{control}}$) in histological measures for the injected versus control hippocampus. Asterisks represent significant paired difference between injected and control (* $P < 0.05$, ** $P < 0.01$, and **** $P < 0.0001$). (B) NeuN and GFAP-Iba-1 staining of a representative animal (left, control; right, injected). GL, granular layer. (C) Normalized change ($P_{\text{injected}} - P_{\text{control}}/P_{\text{control}}$) in MRI parameter calculated in the ibotenic-injected versus control hemisphere for microglia and neuron compartments (light gray). For comparison, the same parameters obtained in group 2 of the LPS-injected animals are reported in white. Asterisks represent significant paired difference between injected and control (* $P < 0.05$ and ** $P < 0.01$). (D) Normalized change ($P_{\text{injected}} - P_{\text{control}}/P_{\text{control}}$) for MRI and histological markers of neuronal death calculated separately in the untreated animals and in those treated with minocycline. Asterisks represent significant unpaired difference between the two groups (* $P < 0.05$ and ** $P < 0.01$).

by ibotenic acid (19). These histological findings were tightly mirrored by the MRI parameters (Fig. 3C), with a significant decrease of stick fraction, increase in the stick dispersion parameter, and, notably, increase in the small sphere fraction. In Fig. 3C, the MRI parameters measured in the LPS cohort at 8 hours after injection, where we detected microglia activation but no neuronal damage (Fig. 1), are shown here in white to facilitate the comparison of hallmarks of a glia reaction with and without neuronal damage. Furthermore, a distinct signature for microglia proliferation, captured by the small sphere fraction, differentiating LPS from ibotenic lesions, could be extracted from the dw-MRI data (Fig. 3C).

The tissue fraction component was significantly decreased in the injected hemisphere, compared to control, and only for the ibotenic acid injection not for LPS, suggesting an association with neuronal degeneration. To test this hypothesis, we pretreated the animals with minocycline, an anti-inflammatory drug (24), and repeated the ibotenic acid injections as before. NeuN staining demonstrated the protective effect of minocycline on ibotenic-induced neuronal

death, and the MRI parameter tissue fraction captured this effect, showing a significant reduction of the ibotenic-induced decrease in this parameter. These results demonstrated the utility of the tissue fraction component to monitor neuronal degeneration.

Specificity of the model in the presence of demyelination

A reduction in the myelin content can occur in some brain disorders, which could challenge the specificity of the model. To investigate this possibility, we demyelinated the hippocampus in one hemisphere with an injection of lysolecithin and waited until the induced inflammation was resolved. Demyelination was confirmed as a decrease in the myelin basic protein content in the injected hemisphere (Fig. 4A) and resolved inflammation with glia staining showing no morphological changes (Fig. 4C). In agreement with our model (see below), the only parameter from the MRI biomarker that showed some sensitivity to demyelination was the microglia-associated stick fraction (Fig. 4D). However, demyelination and microglia activation were efficiently discriminated by considering

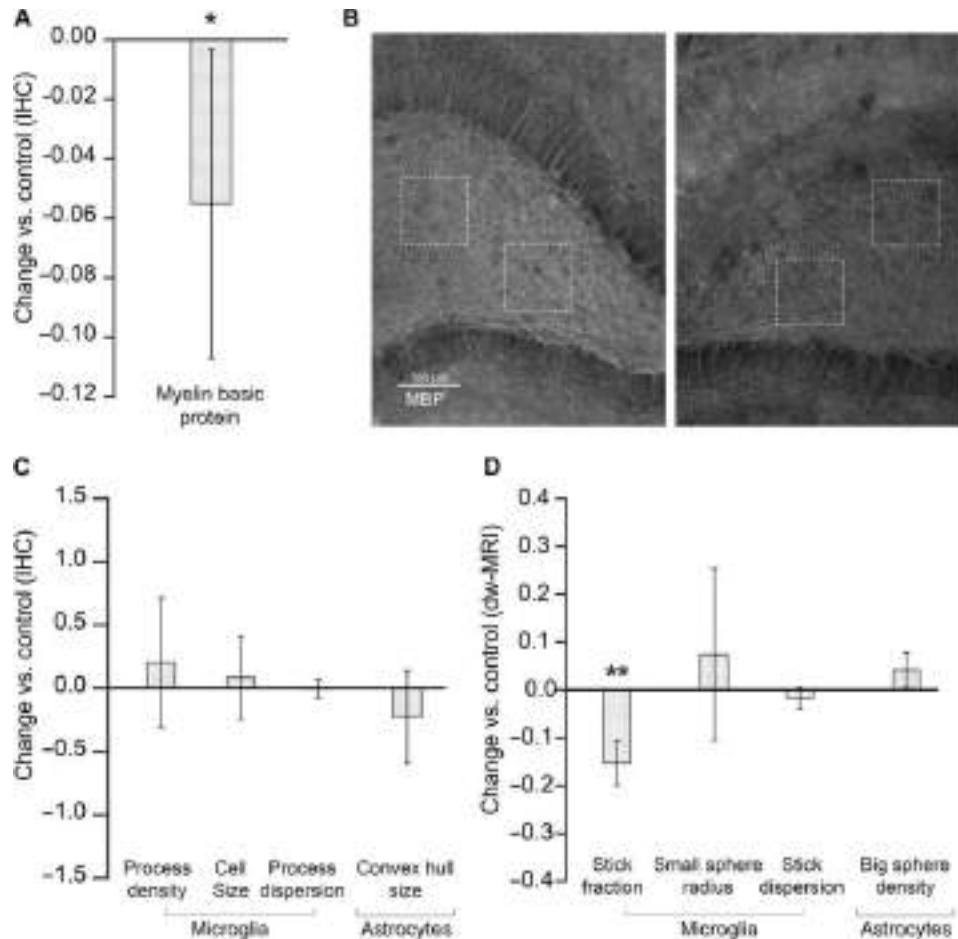


Fig. 4. Specificity of glia biomarkers in demyelinated tissue. (A) Normalized change $(P_{\text{injected}} - P_{\text{control}})/P_{\text{control}}$ in histological Myelin basic protein measures for the injected versus control hippocampus. (B) MBP staining of a representative animal (left, control; right, injected). (C) Normalized change $(P_{\text{injected}} - P_{\text{control}})/P_{\text{control}}$ in histological staining calculated in the lysolecithin-injected versus control hemisphere for microglia and astrocyte compartments. (D) Same as (C) but for MRI parameters.

the other microglia compartment parameters, namely, the stick dispersion parameter and the small sphere radius. This finding was further supported by the simulation in fig. S10.

Comparison with conventional MRI techniques

To highlight the importance of the developed framework, it is important to show that conventional MRI is sensitive to morphological changes due to inflammation, but cannot disentangle the different populations involved across different conditions, as shown in fig. S4. Glia activation, neuronal loss, and demyelination all caused an increase in mean diffusivity, but different conditions could not be differentiated. A clear reduction of T_1/T_2 is observed in all three conditions, while histology demonstrates no myelin change (fig. S3). T_2^* does not have enough sensitivity to reflect glia morphological changes at any stages, but a significant reduction is observed in the presence of neuronal loss.

Translation to human

As a proof of concept for the translational validity of these results and to evaluate the reproducibility of the proposed imaging framework, we adapted the MRI protocol to a human 3T Connectom scanner (25) and acquired data from a healthy cohort at high

resolution (2 mm isotropic). As shown in Fig. 5, the multicompartiment model (MCM) applied to these data returned values for the within-subjects coefficient of variations (CoV) in the range of 1.5 to 8% and between-subjects CoV in the range of 2.6 to 15%, which are in the range of conventional MRI measures routinely used in the clinics with diagnostic value. Last, we took advantage of the known heterogeneous distribution of microglial cell densities across brain regions in humans to test the ability of our framework to quantify microglial cell populations *in vivo*. We found that the patterns of microglial cell density measured postmortem in humans across different gray matter regions (26) can be explained by two microglia-related MRI parameters, the stick fraction and the stick dispersion parameter. A multiple linear regression showed a significant correlation between histological and MRI measures ($P = 0.03$; Fig. 6).

DISCUSSION

Diffusion MRI signal has great potential to reveal the inflammatory component in numerous brain conditions (27), and several efforts have been made to provide microstructural models able to capture features belonging to distinct tissue subcompartments, for example, by including dendrite dispersion (28, 29) or a compartment for the

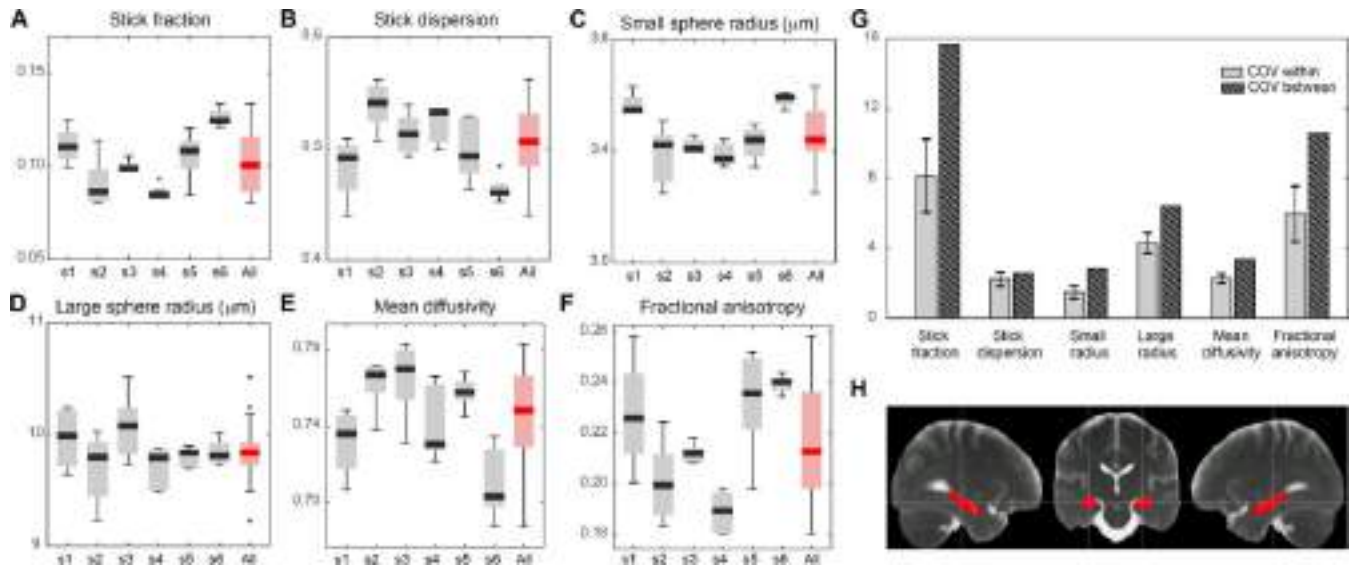


Fig. 5. Feasibility of the framework translation to human and MR parameter reproducibility analysis. (A) Boxplot of stick fraction as measured separately in the hippocampus of six subjects scanned five times (s1 to s6) and pooling all subjects together (red). The same is shown for the stick dispersion parameter (B), small sphere radius (C), large sphere radius (D), mean diffusivity (E), and fractional anisotropy (F). (G) Average coefficient of variation calculated within subject (light gray) and between subjects (striped). (H) Region of interest (ROI) in the hippocampus used for the reproducibility analysis, defined according to (56).

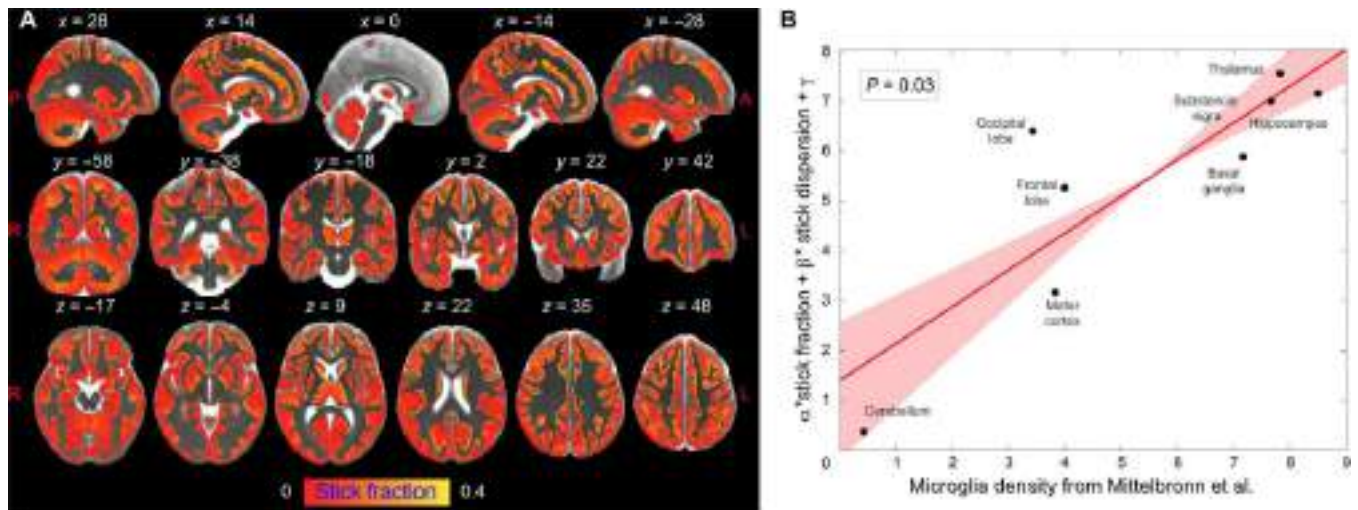


Fig. 6. Correlation between the stick fraction and microglia density in human brain. (A) Stick fraction according to the MCM normalized to the brain template defined in (56), masked for gray matter tissue, and averaged across subjects. (B) Multiple linear regression using stick fraction and dispersion to explain microglia density measured using histological staining of postmortem human tissue in eight gray matter regions (hippocampus, cerebellum, substantia nigra, basal ganglia, thalamus, motor, frontal, and occipital cortices) as reported in (26). Regression confidence intervals are calculated using bootstrap.

soma of neurons (30). While specificity to glia can be achieved, to some extent, by looking at diffusion of brain metabolites using diffusion-weighted magnetic resonance spectroscopy (31), to date, no imaging framework is available to specifically look at the cellular signature of glia activation. Here, we propose and validate a strategy to image microglia and astrocyte activation in gray matter using diffusion MRI and demonstrate its translational validity to humans. By taking advantage of the different activation windows of glia in an LPS-driven immunological challenge in rats, and by using pharmacological tools to deplete microglia in the brain, we were able to

dissect the MRI signatures of specific glia responses. We identified three MRI parameters, namely, the stick fraction, the stick dispersion, and the small sphere size, which, combined, provide sensitivity to, and only to, microglia activation. Similarly, the large sphere size is sensitive to astrocyte activation. In addition, using injections of ibotenic acid, we demonstrate that the framework can distinguish between glia activation and proliferation, independently of an underlying neurodegenerative process. Glia proliferation is an important aspect of the inflammatory reaction and a major component in the evolution of chronic neurodegeneration (32). Modulating

ibotenic acid–induced neurodegeneration with anti-inflammatory pretreatments, we further unveil an MRI parameter with capacity to monitor neuronal loss. The possibility of teasing apart the contribution of inflammation and neuronal loss has direct implications for understanding the contribution of the brain innate immune response to disease progression, where both components are key players in the pathophysiology and can be targeted by disease-modifying treatments.

Last, we tested the robustness of the developed biomarker set for inflammation in a condition of demyelination. We found that, even in a condition of severe demyelination only comparable to multiple sclerosis, microglia-associated MRI parameters such as the stick dispersion parameter and the small sphere size, and the astrocyte-associated big sphere size, were not confounded. This result, which allows differentiating demyelination and inflammation, is expected not only from basic geometric reasoning but also from our *in silico* simulation (Supplementary Materials). The MRI stick fraction was, however, decreased by demyelination. This result was expected as myelin is invisible to diffusion-weighted sequences, but its loss causes an increase in the extracellular water fraction. This reweighting of the volume fractions is well characterized in white matter, where the restricted fraction is used as an index sensitive to demyelination in multiple sclerosis (33, 34), and can be easily corrected by including myelin-specific sequences (35). This result provides important previously undisclosed information for the interpretation of the volume fractions in dw-MRI.

Our results are supported by quantitative cell morphology analysis. The validation of MRI results is challenging due to several factors, including the need to co-register regions of interest (ROIs) with very different sizes and properties and the need for tissue fixation in histological preparations (36). To overcome these limitations, here, we relied on measuring changes rather than absolute magnitude of quantities. We demonstrate that there is a very high correlation between the changes found in injected versus control regions, as measured using MRI and histology in the rat hippocampus, suggesting that our imaging measures truly capture the hallmark of glia activation with high sensitivity. Future work is needed to confirm this finding in the whole brain, possibly exploring the combined use of different antibodies (e.g., NDRG2 and S100-beta for astrocytes) (37, 38) and of other compounds/conditions eliciting inflammation. Furthermore, while the present methodology can detect morphological changes that indicate a status of LPS- or ibotenic-induced activation, future work is needed to dissect the functional status of the different glia populations (39).

The proposed MRI methodology was adapted to a human MRI scanner, and healthy subjects were recruited to perform a reproducibility study, demonstrating that the glia biomarkers are highly reproducible between different MRI sessions and in line with CoVs calculated for conventional MRI parameters routinely used in clinical settings (40). *In vivo* variability of MRI-derived microglia biomarkers can explain known patterns of cell density measured postmortem in humans across several regions of the brain parenchyma. While further work is needed to test the model in the presence of, e.g., a neurodegenerative condition, the results establish the value of the developed MRI framework to quantify glial reactions noninvasively in humans.

Our results have implications in the interpretation of several imaging studies published so far. On one hand, we propose that since diffusion MRI signal is sensitive to glia activation, the biological

substrate of some of the alterations reported in numerous brain conditions could be driven by changes in glia morphology, rather than the conventional interpretation as “neural damage or degeneration.” For example, multiple sclerosis causes not only demyelination and neuronal damage but also inflammation (2), which, according to our results, is likely contributing to the observed differences in MRI parameters between control and patients. On the other hand, our results obtained with traditional MRI, like the mean diffusivity, show that conventional parameters are sensitive to morphological changes due to inflammation, but cannot disentangle the different populations or compartments involved (microglia, astrocytes, neurons, and myelin) (41). This implies that the biological substrate of the observed changes is invisible to conventional MRI.

This study has some limitations. The MCM does not explicitly differentiate between microglia processes and neuronal dendrites. However, basic geometrical reasoning supports the idea that axon and dendrite reorganization would affect the stick dispersion parameter in a different way than microglia process retraction and would thus be easily distinguished from a microglia activation. We support this idea using *in silico* simulations, included as the Supplementary Materials (fig. S10), which show that while microglia process retraction leads to significant increase in the dispersion parameter k , dendrite loss leads to a significant decrease. Further experimental data will be required to validate this result. Nevertheless, the MRI results obtained in the animal cohort, which received injection of ibotenic acid, demonstrated that the proposed framework is already capable of distinguishing between glia activation with and without neuronal loss, the fundamental pathological feature of neurodegenerative diseases.

Water exchange between compartments has not been taken into account in the model under a slow exchange assumption, supported by recent literature (42). While future work is needed to confirm this assumption, or possibly refine the model through the use of more advanced acquisition and analysis protocols (43, 44), the strong association found between histology and MRI indicates that the contribution of exchange between compartments has to be little in our experimental paradigms.

The injection procedure used to deliver the toxins or saline in the brain is expected to induce a low-grade inflammation just by mechanical trauma. While all precautions have been taken to minimize such damage (inserting slowly the syringe and let it rest before injecting, analyzing a large volume around the injection), we cannot exclude that the area adjacent to the injection scan in both control and experimental hemispheres presents a light inflammatory phenotype. However, all the results are reported as changes in experimental versus control hemispheres, rather than absolute values; this highlights the net effect of the toxin (toxin + injection versus injection alone).

Last, the voxel size for human imaging, while much smaller than most dw-MRI studies (2 mm versus 2.5 to 3 mm), still allows for certain partial volume effects with adjacent structures, which we, however, mitigated by eroding by one voxel the ROIs, by parcellating the brains into gray and white matter, and by retaining only the voxels with negligible white matter content. In general, given the caveats of implementing dw-MRI experiments with varying diffusion time in humans (fundamental to estimate compartment sizes) in regular clinical scanners, future studies addressing translation of the experimental protocol for different hardware configurations are needed.

To conclude, we proposed here a new generation of noninvasive glia-centric biomarkers, which are expected to transform the study of many diseases associated with a glial response: those where inflammation is as a known or possible cause, as well as those in which the glial reaction can serve as a powerful early diagnostic and/or prognostic marker.

MATERIALS AND METHODS

Animal preparation

All animal experiments were approved by the Institutional Animal Care and Use Committee of the Instituto de Neurociencias de Alicante, Alicante, Spain, and comply with the Spanish (law 32/2007) and European regulations (EU directive 86/609, EU decree 2001-486, and EU recommendation 2007/526/EC). Rats were housed in groups (4, 5), with 12-hour/12-hour light/dark cycle, lights on at 8:00, at room temperature ($23 \pm 2^\circ\text{C}$) and free access to food and water. Glia activation was achieved by intracranial injection in the dorsal hippocampus (coordinates: bregma, -3.8 mm; superior-inferior, 3.0 mm; 2 mm from midline in the left hemisphere) of $2 \mu\text{l}$ of saline and LPS at a concentration of $2.5 \mu\text{g}/\mu\text{l}$. The opposite hemisphere was injected with the same amount of saline. In a cohort of animals, microglia depletion was achieved by administering the CSF1R inhibitor PLX5622 (Plexxikon Inc.) in two ways: as a dietary supplement in standard chow at 1200 ppm (Research Diets) and with an intraperitoneal injection of 50 mg/kg in vehicle with a dose volume of 10 ml/kg once a day for 7 days. Another cohort of rats received the same chow without enrichment and was injected intraperitoneally once a day with the same doses of vehicle. Less than 24 hours after the last injection, all the rats were injected LPS according to the procedure described above. Neuronal death was achieved by injecting $1 \mu\text{l}$ of saline and ibotenic acid at a concentration of $2.5 \mu\text{g}/\mu\text{l}$ in the dorsal hippocampus (same coordinates). The opposite hemisphere was injected with the same amount of saline. A subgroup of animals underwent minocycline treatment [45 mg/kg dissolved in phosphate-buffered saline (PBS) at a concentration of 13.5 mg/ml; Sigma-Aldrich, Madrid, Spain] according to (19). Minocycline was administered intraperitoneally 12 hours before the surgery, 30 min before the surgery, and once a day for 3 days at 24-hour intervals. Demyelination was achieved by injecting $1 \mu\text{l}$ of saline and lysolecithin at a concentration of 1% in the dorsal hippocampus (same coordinates). The opposite hemisphere was injected with the same amount of saline.

After different post-injection delays, the rats were scanned in the MRI scanner and immediately perfused for ex vivo MRI immunohistological analysis of Iba-1⁺ and GFAP⁺. A total of 43 rats were used, with weights in the range of 250 to 300 g, divided in six groups. Sample size was chosen on the basis of power calculation performed using, as expected effect size, the mean diffusivity changes reported in rat GM in a previous study looking at inflammation (45).

Group 1 ($n = 6$) received the LPS injection and was scanned and perfused after 8 hours. Group 2a ($n = 7$) received the LPS injection and was scanned and perfused after 24 hours. Group 2b ($n = 4$) was treated with control chow and injected with vehicle for 7 days, then received the LPS injection, and was scanned and perfused after 24 hours. Group 3 ($n = 7$) was treated with PLX5622 for 7 days, then received the LPS injection, and was scanned and perfused after 24 hours. Group 4 ($n = 5$) received the LPS injection and was scanned and perfused after a minimum of 15 days or more if the ventricular enlargement was not reabsorbed. No statistically significant differences were detected between groups 2a and 2b (control for PLX5622 chow),

so they were merged into a single group for the rest of the analysis. Groups 5a and 5b ($n = 9$) received an ibotenic acid injection and were scanned and perfused at 14 days after surgery. Group 5b ($n = 6$) was treated with minocycline for 5 days. Last, group 6 ($n = 5$) received lysolecithin injection and was scanned and perfused within 2 to 3 weeks. Experimental design is reported in fig. S1.

MRI experiment

Rats

MRI experiments on rats were performed on a 7-T scanner (Bruker, BioSpect 70/30, Ettlingen, Germany) using a receive-only phase array coil with integrated combiner and preamplifier in combination with an actively detuned transmit-only resonator. Dw-MRI data were acquired using an Echo Planar Imaging diffusion sequence, with 30 uniform distributed gradient directions, $b = 2000$ and 4000 s/mm², diffusion times 15, 25, 40, and 60 ms with four images without diffusion weight ($b = 0$, called B0), repetition time (TR) = 7000 ms, and echo time (TE) = 25 ms. Fourteen horizontal slices were set up centered in the hippocampus with field of view (FOV) = 25 mm \times 25 mm, matrix size = 110×110 , in-plane resolution = 0.225 mm \times 0.225 mm, and slice thickness = 0.6 mm. In addition, three relaxometry sequences were acquired with the same geometry of the dw-MRI scan: a gradient echo sequence with TR = 1500 ms, 30 TE equally spaced between 3.3 and 83.4 ms, and 3 averages; a T₁-weighted sequence with TR = 300 ms, TE = 12.6 ms, and 2 averages; and a T₁-weighted sequence with TR = 3000 ms, TE = 7.7 ms, and 4 averages. Last, a high-resolution anatomical scan with full brain coverage was acquired with TR = 8000 ms, TE = 14 ms, 4 averages, FOV = 25 mm \times 25 mm, matrix size = 200×200 , in-plane resolution = 0.125 mm \times 0.125 mm, and 56 slices of thickness = 0.5 mm. Total scan time including animal positioning was around 2 hours.

Humans

Six healthy subjects were scanned five times in a 3T Siemens Connectom scanner, for a total of 30 acquisitions. The study was approved by the local Institutional Review Board. Dw-MRI data were acquired using an Echo Planar Imaging diffusion sequence with the following parameters: TE = 80 ms; TR = 3.9 s; diffusion times 17.3, 30, 42, and 55 ms; b values of 2000 and 4000 s/mm², each with 30 and 60 uniformly orientated gradient directions, respectively; and six B0 images per diffusion time, yielding a total 384 images. Additional parameters used were as follows: flip angle, 90° ; slice thickness, 2 mm; in-plane voxel size, 2 mm; FOV, 220 mm \times 220 mm; matrix size, 110×110 . Total scan time was around 40 min per subject.

MRI analysis and statistics

Rat MRI data were processed as follows. Preliminary data were used to verify the reach of a $2\text{-}\mu\text{l}$ injection, confirming that the liquid filled the whole dentate gyrus. So, ROIs for the analysis were manually drawn in the dentate gyrus of the dorsal hippocampus; the injection trace was used to locate the central slice, and ROIs were drawn from two slices before the injection, and up to two slices after, for a total length of 3 mm covered. Visual check assured that the injection scar was limited to the central slice only and excluded from the analysis heavily damaged brains and/or brains with enlarged ventricles (one animal was excluded from group 1, one from group 2, one from group 5b, and one from group 6).

Raw dw-MRI data were nonlinearly registered to the T₂-weighted scan to correct for Echo-planar Imaging distortions, corrected for

motion and eddy current distortions using affine registration, and then fed to a custom routine written in MATLAB (R2018a, the MathWorks), which fits the signal to an MCM of diffusion. The MCM is inspired by the AxCaliber model for white matter (15) but is adapted to gray matter morphology. The model comprises one compartment of water undergoing restricted diffusion in cylindrical geometry (representing water trapped into cell ramifications and axons) with negligible radius; a main orientation and a Watson dispersion term (29); two spherically restricted compartments (46); one extracellular space matrix, aligned with the main cylinder orientation and modeled as a tensor; and one free water compartment, modeled according to (23, 29). The main cylinder orientation is necessary to pick up the small degree of anisotropy present in gray matter due to axons (47). Hence, the signal is expressed by the following expression:

$$S = f_{IC} \times S_{IC}(k) + f_{SS} \times S_{SS}(R_{SS}) + f_{LS} \times S_{LS}(R_{LS}) + f_{EC} \times S_{EC} + (1 - f_T) \times S_{FW}$$

where f_{IC} is the fraction of water undergoing restricted diffusion in cylinders, called stick fraction throughout the paper; S_{IC} is the signal in Watson-dispersed cylinders expressed according to equation 2 of (26); k is the Watson dispersion parameter, called stick dispersion parameter throughout the paper; f_{SS} and f_{LS} are the fractions of water undergoing restricted diffusion in the two spherical compartments; S_{SS} and S_{LS} are the signals of water undergoing restricted diffusion in spheres expressed according to equation 18 of (46), which depend on the radii of the two spherical compartments R_{SS} and R_{LS} , respectively; f_{EC} is the fraction of water hindered in the extracellular space; S_{EC} is the signal in the extracellular space modeled as a tensor with radial symmetry, whose main orientation is linked to the main orientation of the cylindrical compartment; $1 - f_T$ is the fraction of free water (defined as one minus the tissue fraction f_T to help the discussion); and S_{FW} is the free water signal, defined as in (23). The fitting parameters are f_{IC} , f_{SS} and f_{LS} , k , R_{SS} and R_{LS} , the extracellular tensor diffusivity, and f_T . Water diffusivity inside restriction is assumed to be $1 \times 10^{-9} \text{ mm}^2/\text{s}$ (29), but no tortuosity assumption is made. The convergence of two different sphere radii is ensured by different initializations (4 and 8 μm , respectively) and nonoverlapping variability range. The fitting algorithm is based on the lsqnonlin routine available in MATLAB. Average processing time per voxel is 5.9 s. The MCM is illustrated in fig. S2.

The low b value shell was used to fit the conventional tensor model and produce maps of the mean diffusivity. T_1 - and T_2 -weighted maps were also used to calculate the T_1/T_2 ratio, which is considered a proxy for myelination (48). T_2^* maps were calculated by fitting an exponential decay to the T_2^* -weighted images acquired at different echo times. In addition, for illustration purposes, the high-resolution anatomical scans were nonlinearly registered to a rat brain template (49) using an advanced normalization approach (50). Repeated-measures analysis of variance (ANOVA) was used to check for significant effect of the injection and of the group. Following significant effect, posthoc t tests were used to compare injected versus control hemisphere and corrected for multiple comparisons.

Similarly, human MRI data were preprocessed as follows. Motion, eddy current, and EPI distortions were corrected using FSL TOPUP and EDDY tools (51). Correction for gradient nonlinearities (52), signal drift (53), and Gibbs ringing artifacts (54) was also performed.

All diffusion data were then registered to a skull-stripped (55) structural T_1 -weighted image using EPIREG (51). B_0 scans were nonlinearly registered to a high-resolution human brain template (56) using an advanced normalization approach (50); then, the inverse transformation was applied to bring the Desikan GM parcellation in the single subject space. All masks were eroded by one voxel using the FSL command `fslmaths` to mitigate possible contamination from adjacent white matter. In addition, for each subject, the B_0 scan was used for brain parcellation into gray and white matter, and only voxels with minimal white matter contamination (<5%) were retained for the analysis. Both intra- and intersubject coefficients of variations were calculated for each MRI measure. The Desikan parcellization was used to calculate mean and SD of the stick fraction and dispersion parameter in eight ROIs (hippocampus, cerebellum, substantia nigra, basal ganglia, thalamus, motor, frontal, and occipital cortices), which were correlated with postmortem histological staining for microglia, as reported in (26).

Tissue processing and immunohistochemistry

Rats were deeply anesthetized with a lethal dose of sodium pentobarbital, 46 mg/kg, injected intraperitoneally (Doletal, E.V.S.A. laboratories, Madrid, Spain). Rats were then perfused intracardially with 100 ml of 0.9% PBS and 100 ml of ice-cold 4% paraformaldehyde (PFA; BDH, Prolabo, VWR International, Lovaina, Belgium). Brains were immediately extracted from the skull and fixed for 1 hour in 4% PFA. Afterward, brains were included in 3% agarose/PBS (Sigma-Aldrich, Madrid, Spain) and cut in vibratome (VT 1000S, Leica, Wetzlar, Germany) in 50- μm -thick serial coronal sections.

Coronal sections were rinsed and permeabilized three times in $1 \times$ PBS with Triton X-100 at 0.5% (Sigma-Aldrich, Madrid, Spain) for 10 min each. Then, they were blocked in the same solution with 4% bovine serum albumin (Sigma-Aldrich, Madrid, Spain) and 2% goat serum donor herd (Sigma-Aldrich, Madrid, Spain) for 2 hours at room temperature. The slices were then incubated for one night at 4°C with primary antibodies for Iba-1 (1:1000; Wako Chemicals, Osaka, Japan), GFAP (1:1000; Sigma-Aldrich, Madrid, Spain), myelin basic protein (1:250; Merck Millipore, Massachusetts, USA), neurofilament 360Kd medium (1:250; Abcam, Cambridge, United Kingdom), and NeuN (1:250; Sigma-Aldrich, Madrid, Spain) to label microglia, astrocytes, myelin, neuron processes, and nuclei, respectively. The sections were subsequently incubated in specific secondary antibodies conjugated to the fluorescent probes, each at 1:500 (Thermo Fisher Scientific, Waltham, USA) for 2 hours at room temperature. Sections were then treated with 4',6-Diamidino-2'-phenylindole dihydrochloride (DAPI) at 15 mM (Sigma-Aldrich, Madrid, Spain) during 15 min at room temperature. Last, sections were mounted on slides and covered with an anti-fading medium using a mix solution of 1:10 propyl-gallate:Mowiol (P3130, Sigma-Aldrich, Madrid, Spain; 475904, Merck Millipore, Massachusetts, USA). For myelin labeling, antigen retrieval was performed in 1% citrate buffer (Sigma-Aldrich, Madrid, Spain) and 0.05% Tween 20 (Sigma-Aldrich, Madrid, Spain), warmed to 80°C for protein unmasking. The rest of the steps were done as described above.

Imaging and data extraction

The tissue sections were then examined using a computer-assisted morphometry system consisting of a Leica DM4000 fluorescence microscope equipped with a QICAM Qimaging camera 22577 (Biocompare, San Francisco, USA) and NeuroLucida morphometric software (MBF,

Biosciences, VT, USA). Microglia were visualized and reconstructed under Leica HC PLC APO objective 20×/0.5, and astrocytes were visualized under Leica HC PLC APO objective 40×/0.75. Five cells per hippocampus per hemisphere were randomly selected for a total of 820 cells included for analysis (410 microglia, 410 astrocytes). Only cells that displayed intact and clear processes were included. Areas close to the injection scar were avoided. Cells were traced through the entire thickness of the sections, and trace information was then saved as three-dimensional (3D) reconstructions or rendered into a 2D diagram of each cell following analysis requirement.

Metric analysis of reconstructed cells was extracted using NeuroLucida Explorer software (MBF, Biosciences, VT, USA) and Imaris (Bitplane, Belfast, United Kingdom): cell body perimeter, number of primary processes, number of nodes (branch points), complexity ($[\text{Sum of the terminal orders} + \text{Number of terminals}] * [\text{Total dendritic length} / \text{Number of primary dendrites}]$), fiber density and dendograms, cell size, and polar plots (fig. S5). Polar plots were analyzed to extract fiber orientation and the dispersion parameter in a plane parallel to the microscope, where higher values mean more uniform distribution of the fibers around the cell body. 3D convex analysis was performed to estimate astrocyte volume and overcome the limitations of GFAP labeling (57–59). The volume estimation in the analysis is defined as the area of the polygon created from straight lines connecting the most distal points of the astrocyte processes.

Density analysis was performed on 12-bit gray scale pictures acquired with the described system. ROIs were manually delineated following the Franklin and Paxinos rat brain atlas (49), covering the complete hippocampus in each hemisphere, for at least five slices per rat. Analysis was performed using Icy software (59) in a semi-automatic manner. The threshold for detection of positive nuclei was set for each condition, setting a average nuclei size and a signal/noise ratio higher than 23%, according to Rayleigh criterion for resolution and discrimination between two points.

Myelin, neurofilament, and neural nuclei fluorescent analysis was also performed on pictures acquired with the described system and analyzed using Icy software (59). Two ROIs of 200 μm^2 were placed per hippocampus per hemisphere in at least five slices per rat to obtain the corresponding intensity values.

Data analysis and statistics

The statistical analysis was done using GraphPad Prism 7 software (GraphPad Software Inc., La Jolla, CA, USA) and RStudio (RStudio 2015 Inc., Boston, MA). The presence of outlier values and parametric distribution were checked. We applied paired *t* tests for comparing for each time point, control hemisphere versus injected hemisphere. Pearson's correlation was used for regression analysis, and coefficients were transformed to apply Fisher's 1925 test (60) for significant values. Polar analysis and dispersion estimation were performed to obtain the dispersion parameter (61).

REFERENCES AND NOTES

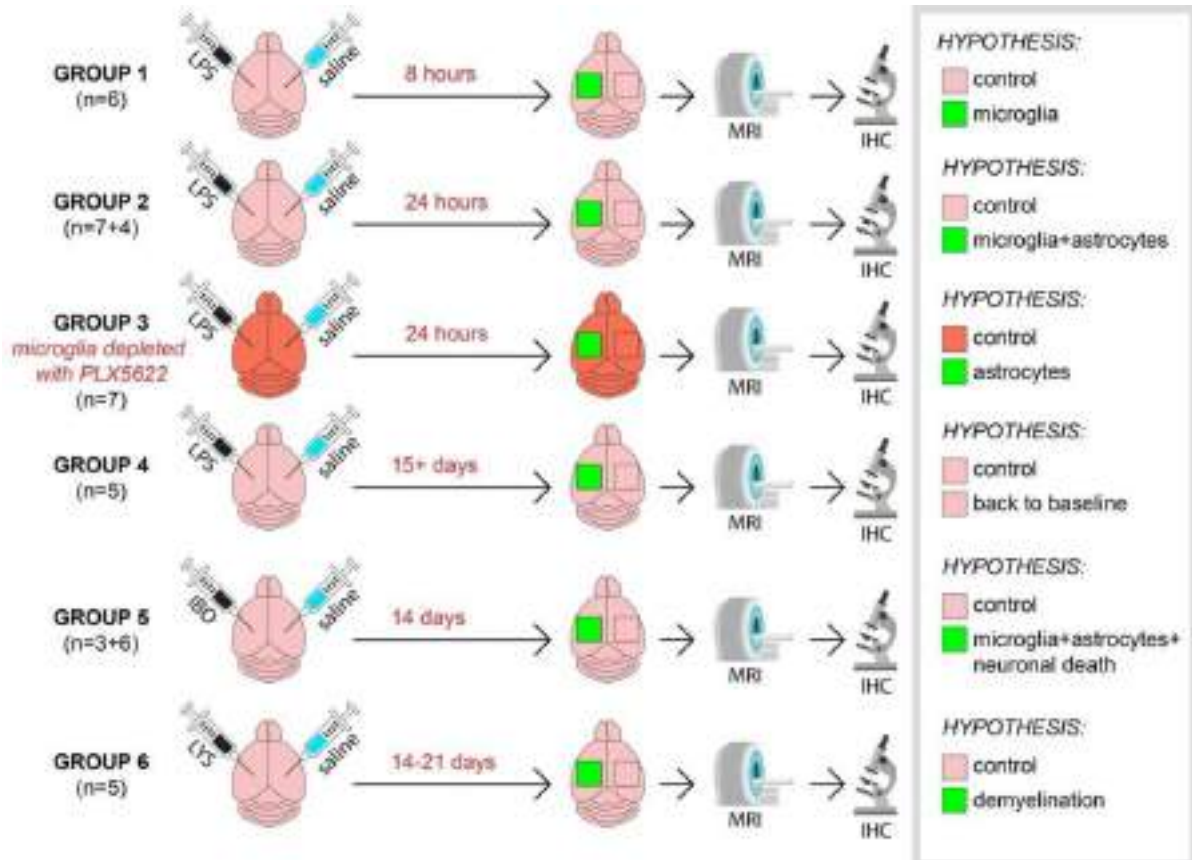
1. R. M. Ransohoff, How neuroinflammation contributes to neurodegeneration. *Science* **353**, 777-783 (2016).
2. H. Lassmann, J. van Horssen, D. Mahad, Progressive multiple sclerosis: Pathology and pathogenesis. *Nat. Rev. Neurol.* **8**, 647-656 (2012).

3. C. K. Glass, K. Saijo, B. Winner, M. C. Marchetto, F. H. Gage, Mechanisms underlying inflammation in neurodegeneration. *Cell* **140**, 918-934 (2010).
4. C. Janus, J. Pearson, J. McLaurin, P. M. Mathews, Y. Jiang, S. D. Schmidt, M. A. Chishti, P. Horne, D. Heslin, J. French, H. T. J. Mount, R. A. Nixon, M. Mercken, C. Bergeron, P. E. Fraser, P. St George-Hyslop, D. Westaway, A β peptide immunization reduces behavioural impairment and plaques in a model of Alzheimer's disease. *Nature* **408**, 979-982 (2000).
5. N. Yahfoufi, C. Matar, N. Ismail, Adolescence and aging: Impact of adolescence inflammatory stress and microbiota alterations on brain development, aging, and neurodegeneration. *J. Gerontol. Ser. A.* **75**, 1251-1257 (2020).
6. B. Wilbanks, L. Maher, M. Rodriguez, Glial cells as therapeutic targets in progressive multiple sclerosis. *Expert Rev. Neurother.* **19**, 481-494 (2019).
7. M. Zella, J. Metzendorf, F. Ostendorf, F. Maass, S. Muhlack, R. Gold, A. Haghikia, L. Tönges, Novel immunotherapeutic approaches to target alpha-synuclein and related neuroinflammation in Parkinson's disease. *Cell* **8**, 105 (2019).
8. S. Amor, F. Puentes, D. Baker, P. van der Valk, Inflammation in neurodegenerative diseases. *Immunology* **129**, 154-169 (2010).
9. D. R. J. Owen, R. N. Gunn, E. A. Rabiner, I. Bennacef, M. Fujita, W. C. Kreis, R. B. Innis, V. W. Pike, R. Reynolds, P. M. Matthews, C. A. Parker, Mixed-affinity binding in humans with 18-kDa translocator Protein ligands. *J. Nucl. Med.* **52**, 24-32 (2011).
10. T. R. Guilarte, TSP0 in diverse CNS pathologies and psychiatric disease: A critical review and a way forward. *Pharmacol. Ther.* **194**, 44-58 (2019).
11. P. J. Basser, C. Pierpaoli, Microstructural and physiological features of tissues elucidated by quantitative-diffusion-tensor MRI. *J. Magn. Reson. Ser. B* **111**, 209-219 (1996).
12. S. Y. Yi, B. R. Barnett, M. Torres-Velázquez, Y. Zhang, S. A. Hurley, P. A. Rowley, D. Hernandez, J.-P. J. Yu, Detecting microglial density with quantitative multi-compartment diffusion MRI. *Front. Neurosci.* **13**, 81 (2019).
13. H. N. Noristani, H. Boukhaddaoui, G. Saint-Martin, P. Auzer, R. Sidiboulouar, N. Lonjon, E. Alibert, N. Tricaud, C. Goze-Bac, C. Coillot, F. E. Perrin, A combination of ex vivo diffusion MRI and multiphoton to study microglia/monocytes alterations after spinal cord injury. *Front. Aging Neurosci.* **9**, 230 (2017).
14. M. Taquet, A. Jankovski, G. Renonnet, D. Jacobs, A. des Rieux, B. Macq, S. K. Warfield, B. Scherrer, Extra-axonal restricted diffusion as an in-vivo marker of reactive microglia. *Sci. Rep.* **9**, 13874 (2019).
15. D. Barazany, P. J. Basser, Y. Assaf, In vivo measurement of axon diameter distribution in the corpus callosum of rat brain. *Brain* **132**, 1210-1220 (2009).
16. A. M. Espinosa-Oliva, R. M. de Pablos, A. J. Herrera, in *Microglia*, B. Joseph, J. L. Venero, Eds. (Humana Press, 2013), vol. 1041 of *Methods in Molecular Biology*, pp. 295-305.
17. H.-K. Jeong, I. Jou, E. Joe, Systemic LPS administration induces brain inflammation but not dopaminergic neuronal death in the substantia nigra. *Exp. Mol. Med.* **42**, 823 (2010).
18. J. Han, R. A. Harris, X.-M. Zhang, An updated assessment of microglia depletion: Current concepts and future directions. *Mol. Brain* **10**, 25 (2017).
19. J. Drouin-Ouellet, A.-L. Brownell, M. Saint-Pierre, C. Fasano, V. Emond, L.-E. Trudeau, D. Lévesque, F. Cicchetti, Neuroinflammation is associated with changes in glial mGluR5 expression and the development of neonatal excitotoxic lesions. *Glia* **59**, 188-199 (2011).
20. R. H. Woodruff, R. J. M. Franklin, Demyelination and remyelination of the caudal cerebellar peduncle of adult rats following stereotaxic injections of lysolecithin, ethidium bromide, and complement/anti-galactocerebroside: A comparative study. *Glia* **25**, 216-228 (1999).
21. A. Verkhratsky, A. Butt, *Glial Neurobiology* (John Wiley & Sons Ltd., 2007).
22. J. Morrens, W. Van Den Broeck, G. Kempermann, Glial cells in adult neurogenesis. *Glia* **60**, 159-174 (2012).
23. O. Pasternak, N. Sochen, Y. Gur, N. Intrator, Y. Assaf, Free water elimination and mapping from diffusion MRI. *Magn. Reson. Med.* **62**, 717-730 (2009).
24. S. Cheng, J. Hou, C. Zhang, C. Xu, L. Wang, X. Zou, H. Yu, Y. Shi, Z. Yin, G. Chen, Minocycline reduces neuroinflammation but does not ameliorate neuron loss in a mouse model of neurodegeneration. *Sci. Rep.* **5**, 10535 (2015).
25. D. K. Jones, D. C. Alexander, R. Bowtell, M. Cercignani, F. Dell'Acqua, D. J. McHugh, K. L. Miller, M. Palombo, G. J. M. Parker, U. S. Rudrapatna, C. M. W. Tax, Microstructural imaging of the human brain with a 'super-scanner': 10 key advantages of ultra-strong gradients for diffusion MRI. *Neuroimage* **182**, 8-38 (2018).
26. M. Mittelbronn, K. Dietz, H. J. Schlusener, R. Meyerann, Local distribution of microglia in the normal adult human central nervous system differs by up to one order of magnitude. *Acta Neuropathol.* **101**, 249-255 (2001).
27. S. De Santis, S. Canals, Non-invasive MRI windows to neuroinflammation. *Neuroscience* **403**, 1-3 (2019).
28. S. N. Jespersen, C. D. Kroenke, L. Østergaard, J. J. H. Ackerman, D. A. Yablonskiy, Modeling dendrite density from magnetic resonance diffusion measurements. *Neuroimage* **34**, 1473-1486 (2007).

29. M. Palombo, A. Janus, M. Guerrerri, D. Nunes, D. C. Alexander, N. Shemesh, H. Zhang, SANDI: A compartment-based model for non-invasive apparent soma and neurite imaging by diffusion MRI. *Neuroimage* **215**, 116835 (2020).
30. C. Ligneul, M. Palombo, E. Hernández-Garzón, M.-A. Carrillo-de Sauvage, J. Flament, P. Hantraye, E. Brouillet, G. Bonvento, C. Escartin, J. Valette, Diffusion-weighted magnetic resonance spectroscopy enables cell-specific monitoring of astrocyte reactivity in vivo. *Neuroimage* **191**, 457-469 (2019).
31. D. Gomez-Nicola, N. L. Franssen, S. Suzzi, V. H. Perry, Regulation of microglial proliferation during chronic neurodegeneration. *J. Neurosci.* **33**, 2481-2493 (2013).
32. S. De Santis, T. Granberg, R. Ouellette, C. A. Treaba, E. Herranz, Q. Fan, C. Mainero, N. Toschi, Evidence of early microstructural white matter abnormalities in multiple sclerosis from multi-shell diffusion MRI. *Neuroimage Clin.* **22**, 101699 (2019).
33. S. Collorone, N. Cawley, F. Grussu, F. Prados, F. Tona, A. Calvi, B. Kanber, T. Schneider, L. Kipp, H. Zhang, D. C. Alexander, A. J. Thompson, A. Toosy, C. A. G. Wheeler-Kingshott, O. Ciccarelli, Reduced neurite density in the brain and cervical spinal cord in relapsing-remitting multiple sclerosis: A NODDI study. *Mult. Scler.* **26**, 1647-1657 (2020).
34. N. Stikov, J. S. W. Campbell, T. Stroh, M. Lavelée, S. Frey, J. Novek, S. Nuara, M.-K. Ho, B. J. Bedell, R. F. Dougherty, I. R. Leppert, M. Boudreau, S. Narayanan, T. Duval, J. Cohen-Adad, P.-A. Picard, A. Gasecka, D. Côté, G. B. Pike, In vivo histology of the myelin g-ratio with magnetic resonance imaging. *Neuroimage* **118**, 397-405 (2015).
35. A. Horowitz, D. Barazany, I. Tavor, G. Yovel, Y. Assaf, Response to the comments on the paper by Horowitz et al. (2014). *Brain Struct. Funct.* **220**, 1791-1792 (2015).
36. G. Flügge, C. Araya-Callis, E. Garea-Rodriguez, C. Stadelmann-Nessler, E. Fuchs, NDRG2 as a marker protein for brain astrocytes. *Cell Tissue Res.* **357**, 31-41 (2014).
37. Z. Zhang, Z. Ma, W. Zou, H. Guo, M. Liu, Y. Ma, L. Zhang, The appropriate marker for astrocytes: Comparing the distribution and expression of three astrocytic markers in different mouse cerebral regions. *Biomed. Res. Int.* **2019**, 1-15 (2019).
38. R. M. Ransohoff, A polarizing question: Do M1 and M2 microglia exist? *Nat. Neurosci.* **19**, 987-991 (2016).
39. T. V. Veenith, E. Carter, J. Grossac, V. F. J. Newcombe, J. G. Outtrim, V. Lupson, G. B. Williams, D. K. Menon, J. P. Coles, Inter subject variability and reproducibility of diffusion tensor imaging within and between different imaging sessions. *PLoS ONE* **8**, e65941 (2013).
40. S. De Santis, M. Drakesmith, S. Bells, Y. Assaf, D. K. Jones, Why diffusion tensor MRI does well only some of the time: Variance and covariance of white matter tissue microstructure attributes in the living human brain. *Neuroimage* **89**, 35-44 (2014).
41. H.-H. Lee, A. Papaioannou, D. S. Novikov, E. Fieremans, In vivo observation and biophysical interpretation of time-dependent diffusion in human cortical gray matter. *Neuroimage* **222**, 117054 (2020).
42. M. Nilsson, J. Lätt, D. van Westen, S. Brockstedt, S. Lasić, F. Ståhlberg, D. Topgaard, Noninvasive mapping of water diffusional exchange in the human brain using filter-exchange imaging. *Magn. Reson. Med.* **69**, 1572-1580 (2013).
43. M. Afzali, M. Nilsson, M. Palombo, D. K. Jones, SPHERIOUSLY? The challenges of estimating sphere radius non-invasively in the human brain from diffusion MRI. *Neuroimage* **237**, 118183 (2021).
44. S. De Santis, A. Cosa-Linan, R. Garcia-Hernandez, L. Dmytrenko, L. Vargova, I. Vorisek, S. Stopponi, P. Bach, P. Kirsch, F. Kiefer, R. Cicocioppo, E. Sykova, D. Moratal, W. H. Sommer, S. Canals, Chronic alcohol consumption alters extracellular space geometry and transmitter diffusion in the brain. *Sci. Adv.* **6**, eaba0154 (2020).
45. C. H. Neuman, Spin echo of spins diffusing in a bounded medium. *J. Chem. Phys.* **60**, 4508-4511 (1974).
46. M. B. Hansen, S. N. Jespersen, L. A. Leigland, C. D. Kroenke, Using diffusion anisotropy to characterize neuronal morphology in gray matter: The orientation distribution of axons and dendrites in the NeuroMorpho.org database. *Front. Integr. Neurosci.* **7**, 31 (2013).
47. M. F. Glasser, D. C. Van Essen, Mapping human cortical areas in vivo based on myelin content as revealed by T1- and T2-weighted MRI. *J. Neurosci.* **31**, 11597-11616 (2011).
48. J. Buttner-Ennever, The rat brain in stereotaxic coordinates, 3rd edn. By George Paxinos and Charles Watson. (Pp. xxxiii+80; illustrated; f\$69.95 paperback; ISBN 0 12 547623; comes with CD-ROM.) San Diego: Academic Press. 1996. *J. Anat.* **191**, 315-317 (1997).
49. A. Klein, J. Andersson, B. A. Ardekani, J. Ashburner, B. Avants, M.-C. Chiang, G. E. Christensen, D. L. Collins, J. Gee, P. Hellier, J. H. Song, M. Jenkinson, C. Lepage, D. Rueckert, P. Thompson, T. Vercauteren, R. P. Woods, J. J. Mann, R. V. Parsey, Evaluation of 14 nonlinear deformation algorithms applied to human brain MRI registration. *Neuroimage* **46**, 786-802 (2009).
50. J. L. R. Andersson, S. N. Sotiropoulos, An integrated approach to correction for off-resonance effects and subject movement in diffusion MR imaging. *Neuroimage* **125**, 1063-1078 (2016).
51. M. F. Glasser, S. N. Sotiropoulos, J. A. Wilson, T. S. Coalson, B. Fischl, J. L. Andersson, J. Xu, S. Jbabdi, M. Webster, J. R. Polimeni, D. C. Van Essen, M. Jenkinson, The minimal preprocessing pipelines for the human connectome project. *Neuroimage* **80**, 105-124 (2013).
52. S. B. Vos, C. M. W. Tax, P. R. Luijten, S. Ourselin, A. Leemans, M. Froeling, The importance of correcting for signal drift in diffusion MRI. *Magn. Reson. Med.* **77**, 285-299 (2017).
53. E. Kellner, B. Dhital, V. G. Kiselev, M. Reisert, Gibbs-ringing artifact removal based on local subvoxel-shifts. *Magn. Reson. Med.* **76**, 1574-1581 (2016).
54. S. M. Smith, Fast robust automated brain extraction. *Hum. Brain Mapp.* **17**, 143-155 (2002).
55. R. S. Desikan, F. Ségonne, B. Fischl, B. T. Quinn, B. C. Dickerson, D. Blacker, R. L. Buckner, A. M. Dale, R. P. M. Maguire, B. T. Hyman, M. S. Albert, R. J. Killiany, An automated labeling system for subdividing the human cerebral cortex on MRI scans into gyral based regions of interest. *Neuroimage* **31**, 968-980 (2006).
56. J. Haseleu, E. Anlauf, S. Blaess, E. Endl, A. Derouiche, Studying subcellular detail in fixed astrocytes: Dissociation of morphologically intact glial cells (DIMIGs). *Front. Cell. Neurosci.* **7**, 54 (2013).
57. P. M. Kulkarni, E. Barton, M. Savelonas, R. Padmanabhan, Y. Lu, K. Trett, W. Shain, J. L. Leasure, B. Roysam, Quantitative 3-D analysis of GFAP labeled astrocytes from fluorescence confocal images. *J. Neurosci. Methods* **246**, 38-51 (2015).
58. F. de Chaumont, S. Dallongeville, N. Chenouard, N. Hervé, S. Pop, T. Provoost, V. Meas-Yedid, P. Pankajakshan, T. Lecomte, Y. LeMontagner, T. Lagache, A. Dufour, J.-C. Olivo-Marin, Icy: An open bioimage informatics platform for extended reproducible research. *Nat. Methods* **9**, 690-696 (2012).
59. R. A. Fisher, in *Breakthroughs in Statistics*, S. Kotz, N. L. Johnson, Eds. (Springer New York, 1992), pp. 66-70.
60. J. Mollink, M. Kleinnijenhuis, A.-M. van Cappellen van Walsum, S. N. Sotiropoulos, M. Cottaar, C. Mirfin, M. P. Heinrich, M. Jenkinson, M. Pallegage-Gamaralage, O. Ansong, S. Jbabdi, K. L. Miller, Evaluating fibre orientation dispersion in white matter: Comparison of diffusion MRI, histology and polarized light imaging. *Neuroimage* **157**, 561-574 (2017).
61. I. E. Papageorgiou, A. F. Fetani, A. Lewen, U. Heinemann, O. Kann, Widespread activation of microglial cells in the hippocampus of chronic epileptic rats correlates only partially with neurodegeneration. *Brain Struct. Funct.* **220**, 2423-2439 (2015).
62. G. M. Arisi, N. Garcia-Cairasco, Doublecortin-positive newly born granule cells of hippocampus have abnormal apical dendritic morphology in the pilocarpine model of temporal lobe epilepsy. *Brain Res.* **1165**, 126-134 (2007).

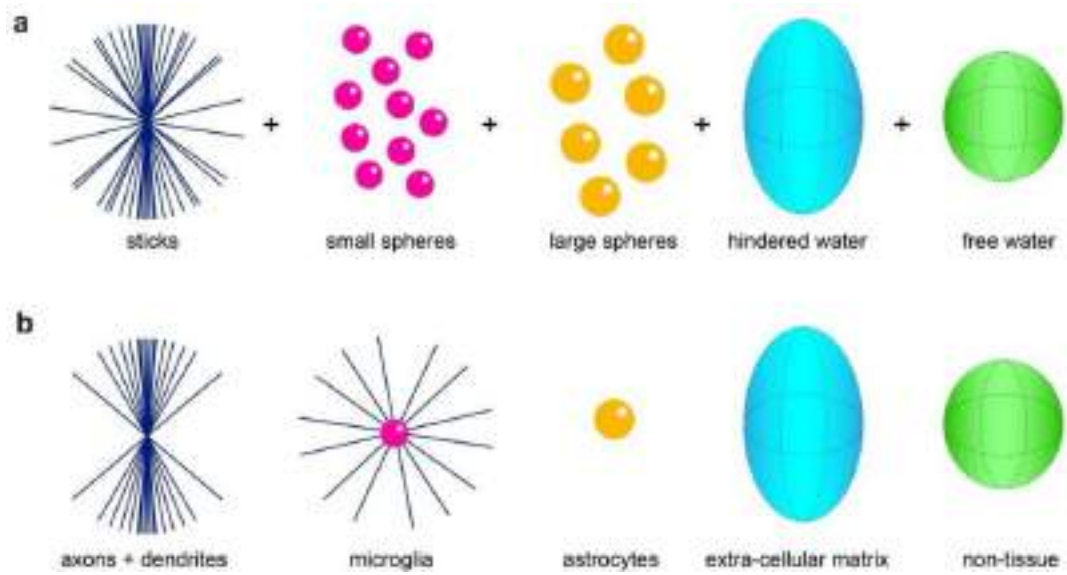
Supplementary Materials for
Mapping microglia and astrocyte activation in vivo using diffusion MRI

Fig. S1: Experimental design and hypothesis based on previous literature



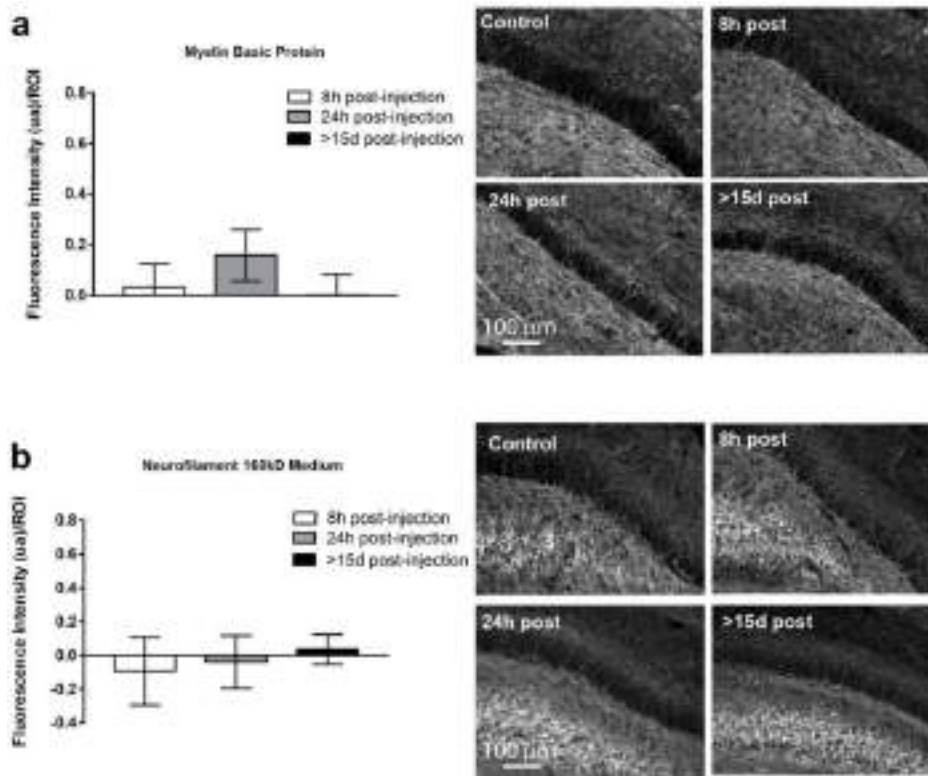
Experimental scheme showing bilateral stereotaxic injection of LPS (left hemisphere) / saline (right hemisphere) and the composition of the six groups: 6 animals were scanned 8 hours post-injection, 11 animals were scanned 24 hours post-injection, 8 animals were treated with PLX5622 for 7 days before the injection and then scanned 24 hours post-injection, and 5 animals were scanned 15 days or more post-injection. The last two rows show stereotaxic injection of ibotenic acid / lysolecithin (left hemisphere) or saline (right hemisphere) in a group of animals. Some (n=6) of the animals injected with ibotenic acid were previously treated with minocycline.

Fig. S2: Multi-compartment model



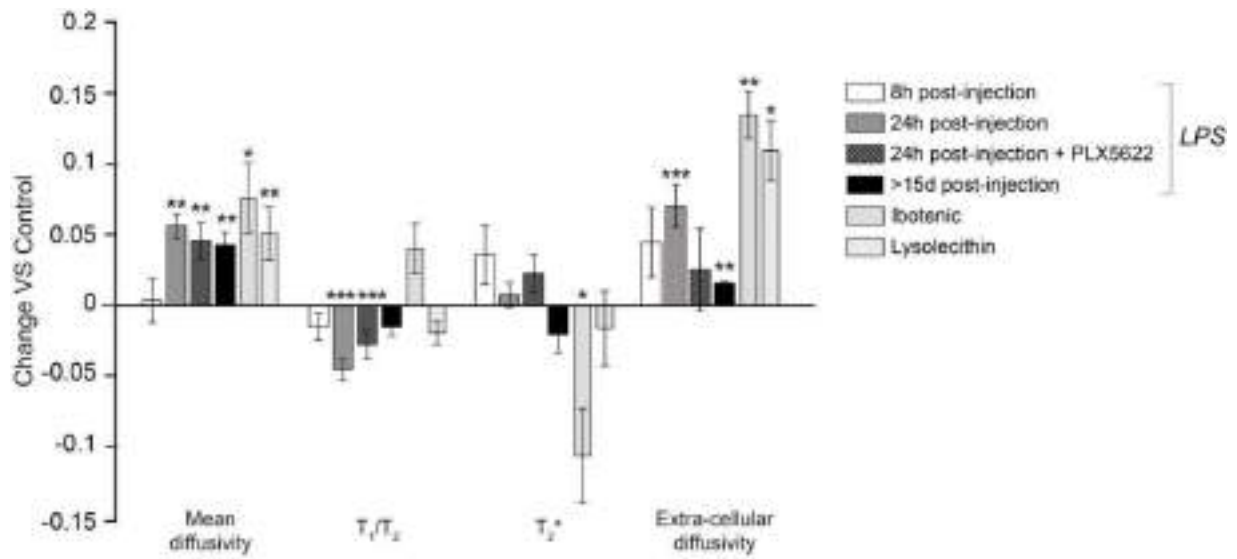
a, Multi-compartment tissue model comprising one compartment of water undergoing restricted diffusion in cylindrical geometry (representing water trapped into cell ramifications) with a main orientation and a Watson dispersion term, two spherically restricted compartments, one extracellular space matrix, aligned with the main cylinder orientation and modelled as a tensor, and one compartment of water undergoing free diffusion. **b**, The compartments defined in **a** are combined to visually represent the different cell types constituting the parenchyma in our model: microglia, astrocytes, neurons, extracellular space.

Fig. S3 : Histology of myelin basic protein and neurofilament



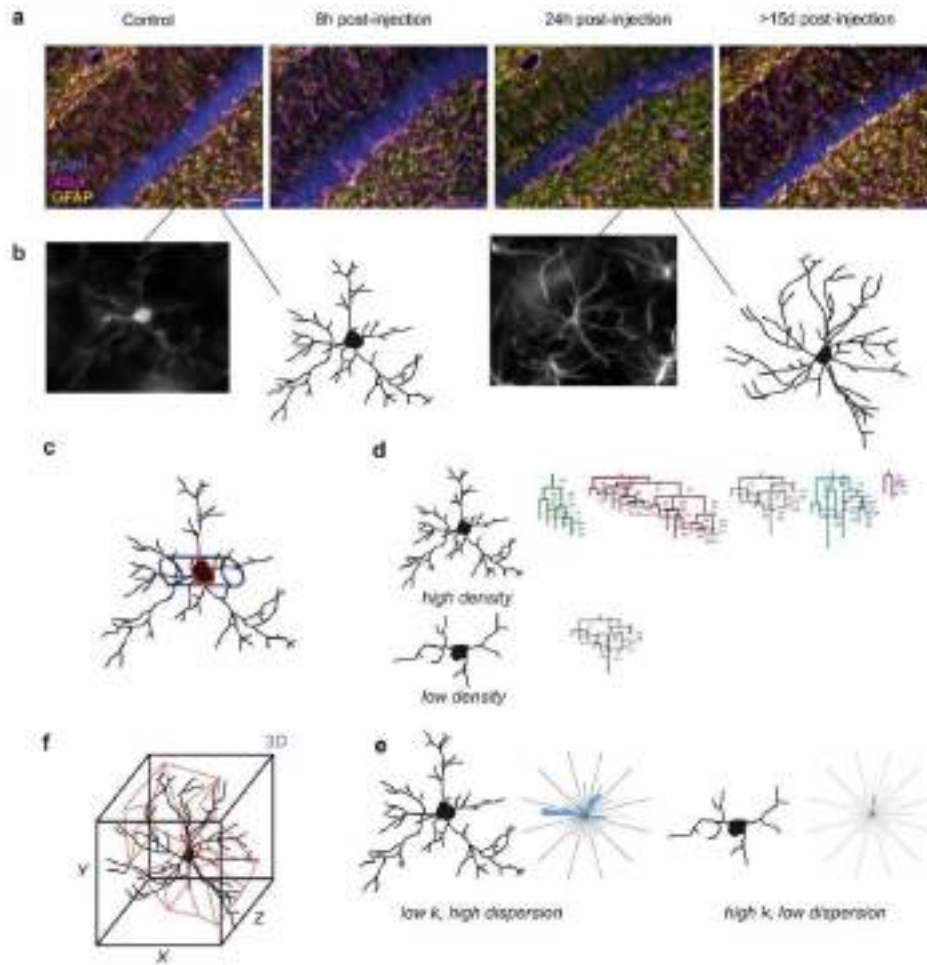
a, Myelin basic protein quantification results, plotted as mean and standard deviation, accompanied by representative microphotographs of the histological labelling at the different time points. b, same for Neurofilament. Scale bar=100 μ m.

Fig. S4: conventional MRI parameters in LPS-injected hemisphere versus control



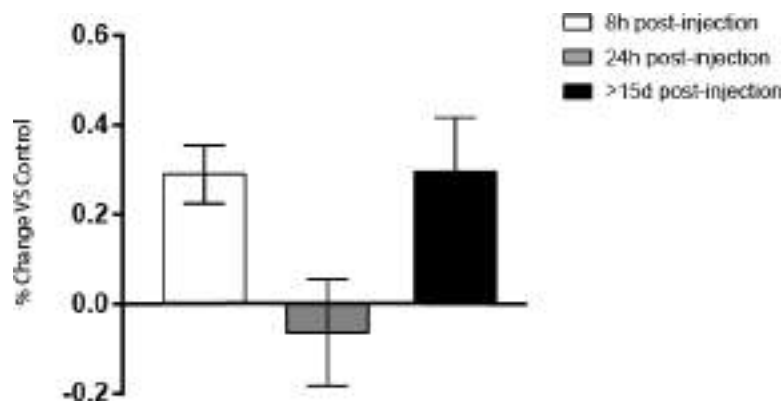
Normalized change $(P_{\text{injected}} - P_{\text{control}}) / P_{\text{control}}$ between MRI-derived mean diffusivity, T_1/T_2 , T_2^* and extracellular diffusivity from the multi-compartment model, calculated in the injected vs control hemisphere for the astrocyte compartment (shown in the insert). Asterisks represent significant paired difference between injected and control. Error bars represent standard deviation.

Fig. S5: Histology main methods and morphometric features obtained



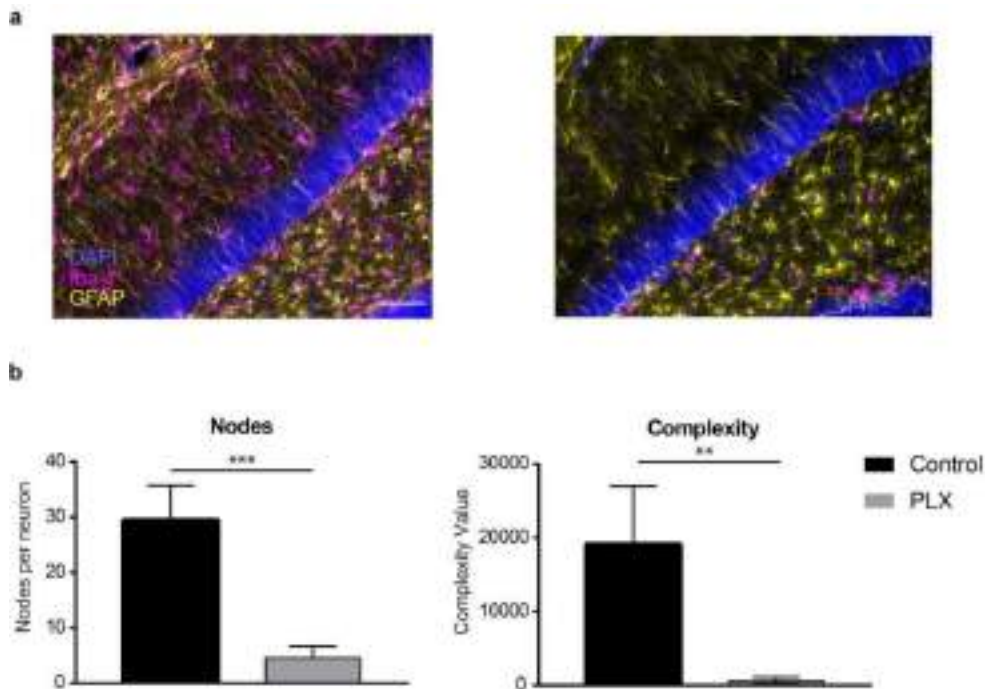
a, Representative microphotographs of the histological labelling at the different time points. Green= Iba1 (microglia), red= GFAP (astrocytes), Blue= DAPI (Cell nuclei). Scale bar= 100 μm **b**, zoom in of a microglia and astrocyte and their 3D reconstruction for morphometric analysis. **c**, microglia cell size extraction by cross-sectional area determination. **d**, Microglia's fiber density extraction, showing two representative cases of high and low densities. **e**, Astrocyte's convex hull extraction. **f**, Microglia's polar plots for fiber orientation analysis, showing two representative cases of low Watson dispersion parameter k (indicating high fiber dispersion along the main orientation) and high k (indicating low fiber dispersion).

Fig. S6: Microglia density at the different timepoints after LPS injections



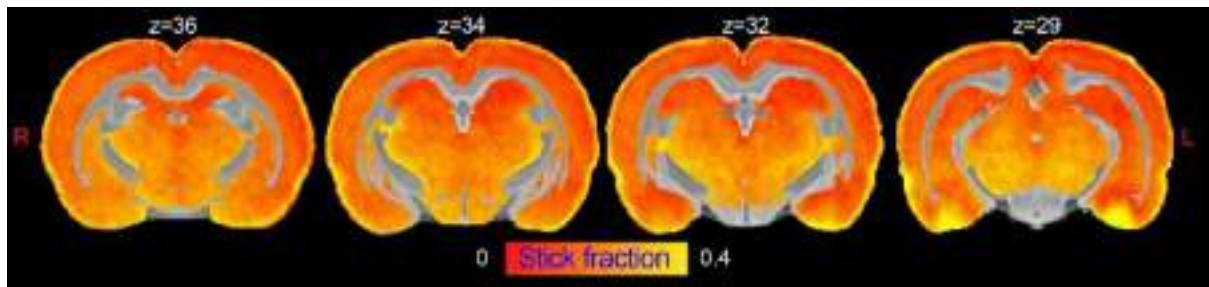
Normalized change $(P_{\text{injected}} - P_{\text{control}}) / P_{\text{control}}$ in microglial density at the different time points, calculated in the LPS-injected vs control hemisphere for the whole hippocampus. Error bars represent standard deviation.

Fig. S7: Microglia depletion in PLX5622-treated versus control animals



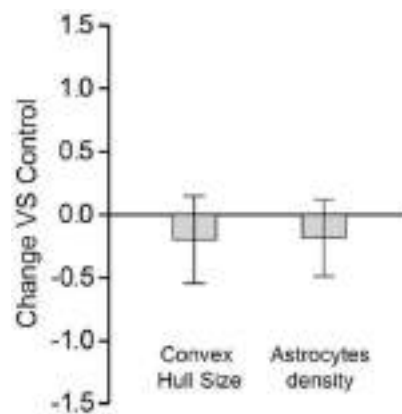
a, Representative microphotographs of a control rat and PLX5622-treated rat, respectively. Green= Iba1 (microglia), red= GFAP (astrocytes), Blue= DAPI (Cell nuclei). Scale bar= 100 μm **b**, Nodes number and complexity quantifications of microglia in both cases, plotted as mean and standard deviation. Asterisks represent significant t-test difference between injected and control.

Fig. S8: Whole GM average maps of stick fraction in rats



Stick fraction according to the multi-compartment model normalized to the rat brain template defined in (49), masked for grey matter tissue, and averaged across subjects.

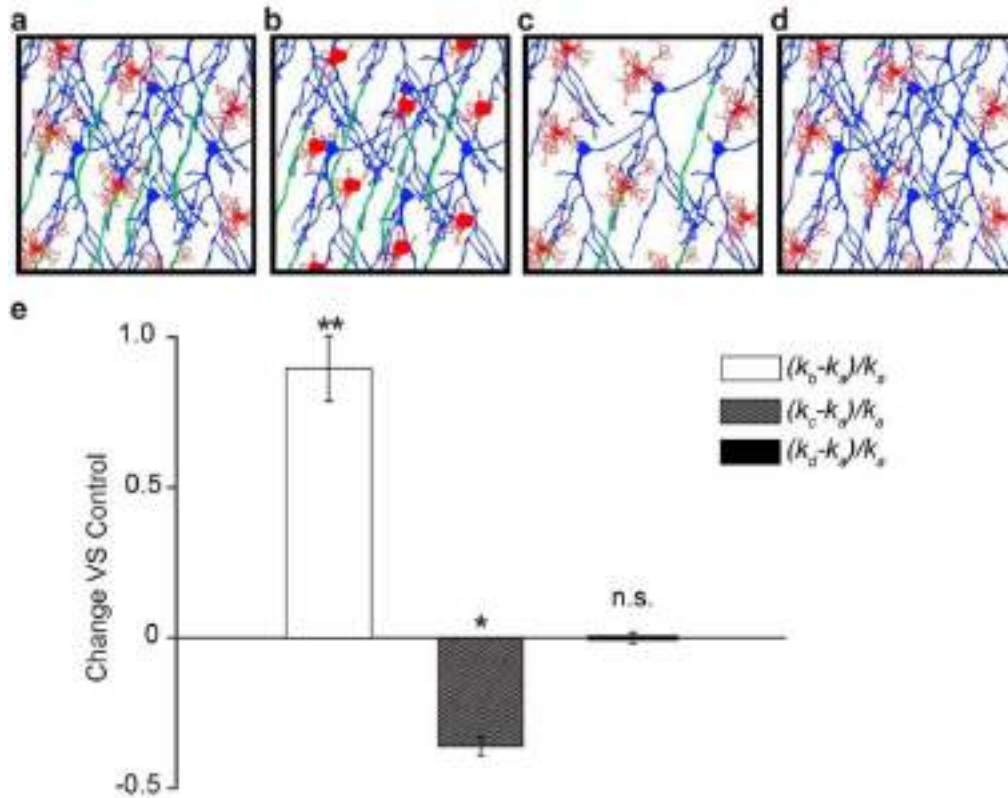
Fig. S9: GFAP staining in rats injected with ibotenic acid



Normalized change $(P_{\text{injected}} - P_{\text{control}}) / P_{\text{control}}$ in GFAP convex hull size and density, calculated in the ibotenic-injected vs control hemisphere for the whole hippocampus. Error bars represent standard deviation.

Fig. S10: Dispersion parameter k in condition of microglia activation, neuronal loss and demyelination

MRI synthetic signal was generated for a geometry composed by microglia, astrocytes and neurons. Microglia and dendrites



were characterized by size and processes/dendrite dispersions as measured in (62) (microglia) and (63) (neurons), as schematized in panel a. A myelin compartment was also included, with a g-ratio of 0.7. MRI synthetic signal was generated in a similar substrate, but with a 50% reduction of microglia ramification, and a 10% increase in cell body size as schematized in panel b. A third substrate, instead, simulated a 50% reduction of dendrites, as illustrated in panel c. Finally, a fourth substrate was generated with no myelin and increased extra-axonal diffusivity. $2 \cdot 10^3$ noisy repetitions (Rician noise) were generated, and the resulting signal was fitted using the MCM to extract the dispersion parameter k . Normalized difference in k ($(k_x - k_a)/k_a$, where $x=b,c,d$) are reported in panel e. Asterisks represent significant differences in the 1-sample t-test (*= $P < 0.05$, **= $P < 0.01$).

REFERENCES AND NOTES

1. R. M. Ransohoff, How neuroinflammation contributes to neurodegeneration. *Science* **353**, 777–783 (2016).
2. H. Lassmann, J. van Horssen, D. Mahad, Progressive multiple sclerosis: Pathology and pathogenesis. *Nat. Rev. Neurol.* **8**, 647–656 (2012).
3. C. K. Glass, K. Saijo, B. Winner, M. C. Marchetto, F. H. Gage, Mechanisms underlying inflammation in neurodegeneration. *Cell* **140**, 918–934 (2010).
4. C. Janus, J. Pearson, J. McLaurin, P. M. Mathews, Y. Jiang, S. D. Schmidt, M. A. Chishti, P. Horne, D. Heslin, J. French, H. T. J. Mount, R. A. Nixon, M. Mercken, C. Bergeron, P. E. Fraser, P. St George-Hyslop, D. Westaway, A β peptide immunization reduces behavioural impairment and plaques in a model of Alzheimer's disease. *Nature* **408**, 979–982 (2000).
5. N. Yahfoufi, C. Matar, N. Ismail, Adolescence and aging: Impact of adolescence inflammatory stress and microbiota alterations on brain development, aging, and neurodegeneration. *J. Gerontol. Ser. A* **75**, 1251–1257 (2020).
6. B. Wilbanks, L. Maher, M. Rodriguez, Glial cells as therapeutic targets in progressive multiple sclerosis. *Expert Rev. Neurother.* **19**, 481–494 (2019).
7. M. Zella, J. Metzendorf, F. Ostendorf, F. Maass, S. Muhlack, R. Gold, A. Haghikia, L. Tönges, Novel Immunotherapeutic approaches to target alpha-synuclein and related neuroinflammation in Parkinson's disease. *Cell* **8**, 105 (2019).
8. S. Amor, F. Puentes, D. Baker, P. van der Valk, Inflammation in neurodegenerative diseases. *Immunology* **129**, 154–169 (2010).
9. D. R. J. Owen, R. N. Gunn, E. A. Rabiner, I. Bennacef, M. Fujita, W. C. Kreisl, R. B. Innis, V. W. Pike, R. Reynolds, P. M. Matthews, C. A. Parker, Mixed-affinity binding in humans with 18-kDa translocator Protein ligands. *J. Nucl. Med.* **52**, 24–32 (2011).
10. T. R. Guilarte, TSPO in diverse CNS pathologies and psychiatric disease: A critical review and a way forward. *Pharmacol. Ther.* **194**, 44–58 (2019).
11. P. J. Basser, C. Pierpaoli, Microstructural and physiological features of tissues elucidated by quantitative-diffusion-tensor MRI. *J. Magn. Reson. Ser. B* **111**, 209–219 (1996).
12. S. Y. Yi, B. R. Barnett, M. Torres-Velázquez, Y. Zhang, S. A. Hurley, P. A. Rowley, D. Hernando, J.-P. J. Yu, Detecting microglial density with quantitative multi-compartment diffusion MRI. *Front. Neurosci.* **13**, 81 (2019).
13. H. N. Noristani, H. Boukhaddaoui, G. Saint-Martin, P. Auzer, R. Sidiboulouar, N. Lonjon, E. Alibert, N. Tricaud, C. Goze-Bac, C. Coillot, F. E. Perrin, A combination of ex vivo diffusion MRI and multiphoton to study microglia/monocytes alterations after spinal cord injury. *Front. Aging Neurosci.* **9**, 230 (2017).

14. M. Taquet, A. Jankovski, G. Rensonnet, D. Jacobs, A. des Rieux, B. Macq, S. K. Warfield, B. Scherrer, Extra-axonal restricted diffusion as an in-vivo marker of reactive microglia. *Sci. Rep.* **9**, 13874 (2019).
15. D. Barazany, P. J. Basser, Y. Assaf, In vivo measurement of axon diameter distribution in the corpus callosum of rat brain. *Brain* **132**, 1210–1220 (2009).
16. A. M. Espinosa-Oliva, R. M. de Pablos, A. J. Herrera, in *Microglia*, B. Joseph, J. L. Venero, Eds. (Humana Press, 2013), vol. 1041 of *Methods in Molecular Biology*, pp. 295–305.
17. H.-K. Jeong, I. Jou, E. Joe, Systemic LPS administration induces brain inflammation but not dopaminergic neuronal death in the substantia nigra. *Exp. Mol. Med.* **42**, 823 (2010).
18. J. Han, R. A. Harris, X.-M. Zhang, An updated assessment of microglia depletion: Current concepts and future directions. *Mol. Brain* **10**, 25 (2017).
19. J. Drouin-Ouellet, A.-L. Brownell, M. Saint-Pierre, C. Fasano, V. Emond, L.-E. Trudeau, D. Lévesque, F. Cicchetti, Neuroinflammation is associated with changes in glial mGluR5 expression and the development of neonatal excitotoxic lesions. *Glia* **59**, 188–199 (2011).
20. R. H. Woodruff, R. J. M. Franklin, Demyelination and remyelination of the caudal cerebellar peduncle of adult rats following stereotaxic injections of lyssolecithin, ethidium bromide, and complement/anti-galactocerebroside: A comparative study. *Glia* **25**, 216–228 (1999).
21. A. Verkhratsky, A. Butt, *Glial Neurobiology* (John Wiley & Sons Ltd., 2007).
22. J. Morrens, W. Van Den Broeck, G. Kempermann, Glial cells in adult neurogenesis. *Glia* **60**, 159–174 (2012).
23. O. Pasternak, N. Sochen, Y. Gur, N. Intrator, Y. Assaf, Free water elimination and mapping from diffusion MRI. *Magn. Reson. Med.* **62**, 717–730 (2009).
24. S. Cheng, J. Hou, C. Zhang, C. Xu, L. Wang, X. Zou, H. Yu, Y. Shi, Z. Yin, G. Chen, Minocycline reduces neuroinflammation but does not ameliorate neuron loss in a mouse model of neurodegeneration. *Sci. Rep.* **5**, 10535 (2015).
25. D. K. Jones, D. C. Alexander, R. Bowtell, M. Cercignani, F. Dell’Acqua, D. J. McHugh, K. L. Miller, M. Palombo, G. J. M. Parker, U. S. Rudrapatna, C. M. W. Tax, Microstructural imaging of the human brain with a ‘super-scanner’: 10 key advantages of ultra-strong gradients for diffusion MRI. *Neuroimage* **182**, 8–38 (2018).
26. M. Mittelbronn, K. Dietz, H. J. Schluesener, R. Meyermann, Local distribution of microglia in the normal adult human central nervous system differs by up to one order of magnitude. *Acta Neuropathol.* **101**, 249–255 (2001).
27. S. De Santis, S. Canals, Non-invasive MRI windows to neuroinflammation. *Neuroscience* **403**, 1–3 (2019).

28. S. N. Jespersen, C. D. Kroenke, L. Østergaard, J. J. H. Ackerman, D. A. Yablonskiy, Modeling dendrite density from magnetic resonance diffusion measurements. *Neuroimage* **34**, 1473–1486 (2007).
29. H. Zhang, T. Schneider, C. A. Wheeler-Kingshott, D. C. Alexander, NODDI: Practical in vivo neurite orientation dispersion and density imaging of the human brain. *Neuroimage* **61**, 1000–1016 (2012).
30. M. Palombo, A. Ianus, M. Guerreri, D. Nunes, D. C. Alexander, N. Shemesh, H. Zhang, SANDI: A compartment-based model for non-invasive apparent soma and neurite imaging by diffusion MRI. *Neuroimage* **215**, 116835 (2020).
31. C. Ligneul, M. Palombo, E. Hernández-Garzón, M.-A. Carrillo-de Sauvage, J. Flament, P. Hantraye, E. Brouillet, G. Bonvento, C. Escartin, J. Valette, Diffusion-weighted magnetic resonance spectroscopy enables cell-specific monitoring of astrocyte reactivity in vivo. *Neuroimage* **191**, 457–469 (2019).
32. D. Gomez-Nicola, N. L. Franssen, S. Suzzi, V. H. Perry, Regulation of microglial proliferation during chronic neurodegeneration. *J. Neurosci.* **33**, 2481–2493 (2013).
33. S. De Santis, T. Granberg, R. Ouellette, C. A. Treaba, E. Herranz, Q. Fan, C. Mainero, N. Toschi, Evidence of early microstructural white matter abnormalities in multiple sclerosis from multi-shell diffusion MRI. *NeuroImage Clin.* **22**, 101699 (2019).
34. S. Collorone, N. Cawley, F. Grussu, F. Prados, F. Tona, A. Calvi, B. Kanber, T. Schneider, L. Kipp, H. Zhang, D. C. Alexander, A. J. Thompson, A. Toosy, C. A. G. Wheeler-Kingshott, O. Ciccarelli, Reduced neurite density in the brain and cervical spinal cord in relapsing–remitting multiple sclerosis: A NODDI study. *Mult. Scler.* **26**, 1647–1657 (2020).
35. N. Stikov, J. S. W. Campbell, T. Stroh, M. Lavelée, S. Frey, J. Novek, S. Nuara, M.-K. Ho, B. J. Bedell, R. F. Dougherty, I. R. Leppert, M. Boudreau, S. Narayanan, T. Duval, J. Cohen-Adad, P.-A. Picard, A. Gasecka, D. Côté, G. B. Pike, In vivo histology of the myelin g-ratio with magnetic resonance imaging. *Neuroimage* **118**, 397–405 (2015).
36. A. Horowitz, D. Barazany, I. Tavor, G. Yovel, Y. Assaf, Response to the comments on the paper by Horowitz et al. (2014). *Brain Struct. Funct.* **220**, 1791–1792 (2015).
37. G. Flügge, C. Araya-Callis, E. Garea-Rodriguez, C. Stadelmann-Nessler, E. Fuchs, NDRG2 as a marker protein for brain astrocytes. *Cell Tissue Res.* **357**, 31–41 (2014).
38. Z. Zhang, Z. Ma, W. Zou, H. Guo, M. Liu, Y. Ma, L. Zhang, The appropriate marker for astrocytes: Comparing the distribution and expression of three astrocytic markers in different mouse cerebral regions. *Biomed. Res. Int.* **2019**, 1–15 (2019).
39. R. M. Ransohoff, A polarizing question: Do M1 and M2 microglia exist? *Nat. Neurosci.* **19**, 987–991 (2016).

40. T. V. Veenith, E. Carter, J. Grossac, V. F. J. Newcombe, J. G. Outtrim, V. Lupson, G. B. Williams, D. K. Menon, J. P. Coles, Inter subject variability and reproducibility of diffusion tensor imaging within and between different imaging sessions. *PLOS ONE* **8**, e65941 (2013).
41. S. De Santis, M. Drakesmith, S. Bells, Y. Assaf, D. K. Jones, Why diffusion tensor MRI does well only some of the time: Variance and covariance of white matter tissue microstructure attributes in the living human brain. *Neuroimage* **89**, 35–44 (2014).
42. H.-H. Lee, A. Papaioannou, D. S. Novikov, E. Fieremans, In vivo observation and biophysical interpretation of time-dependent diffusion in human cortical gray matter. *Neuroimage* **222**, 117054 (2020).
43. M. Nilsson, J. Lätt, D. van Westen, S. Brockstedt, S. Lasič, F. Ståhlberg, D. Topgaard, Noninvasive mapping of water diffusional exchange in the human brain using filter-exchange Imaging. *Magn. Reson. Med.* **69**, 1572–1580 (2013).
44. M. Afzali, M. Nilsson, M. Palombo, D. K. Jones, SPHERIOUSLY? The challenges of estimating sphere radius non-invasively in the human brain from diffusion MRI. *Neuroimage* **237**, 118183 (2021).
45. S. De Santis, A. Cosa-Linan, R. Garcia-Hernandez, L. Dmytrenko, L. Vargova, I. Vorisek, S. Stopponi, P. Bach, P. Kirsch, F. Kiefer, R. Cicocioppo, E. Sykova, D. Moratal, W. H. Sommer, S. Canals, Chronic alcohol consumption alters extracellular space geometry and transmitter diffusion in the brain. *Sci. Adv.* **6**, eaba0154 (2020).
46. C. H. Neuman, Spin echo of spins diffusing in a bounded medium. *J. Chem. Phys.* **60**, 4508–4511 (1974).
47. M. B. Hansen, S. N. Jespersen, L. A. Leigland, C. D. Kroenke, Using diffusion anisotropy to characterize neuronal morphology in gray matter: The orientation distribution of axons and dendrites in the NeuroMorpho.org database. *Front. Integr. Neurosci.* **7**, 31 (2013).
48. M. F. Glasser, D. C. Van Essen, Mapping human cortical areas in vivo based on myelin content as revealed by T1- and T2-weighted MRI. *J. Neurosci.* **31**, 11597–11616 (2011).
49. J. Buttner-Ennever, The rat brain in stereotaxic coordinates, 3rd edn. By George Paxinos and Charles Watson. (Pp. xxxiii+80; illustrated; f\$69.95 paperback; ISBN 0 12 547623; comes with CD-ROM.) San Diego: Academic Press. 1996. *J. Anat.* **191**, 315–317 (1997).
50. A. Klein, J. Andersson, B. A. Ardekani, J. Ashburner, B. Avants, M.-C. Chiang, G. E. Christensen, D. L. Collins, J. Gee, P. Hellier, J. H. Song, M. Jenkinson, C. Lepage, D. Rueckert, P. Thompson, T. Vercauteren, R. P. Woods, J. J. Mann, R. V. Parsey, Evaluation of 14 nonlinear deformation algorithms applied to human brain MRI registration. *Neuroimage* **46**, 786–802 (2009).
51. J. L. R. Andersson, S. N. Sotiropoulos, An integrated approach to correction for off-resonance effects and subject movement in diffusion MR imaging. *Neuroimage* **125**, 1063–1078 (2016).

52. M. F. Glasser, S. N. Sotiropoulos, J. A. Wilson, T. S. Coalson, B. Fischl, J. L. Andersson, J. Xu, S. Jbabdi, M. Webster, J. R. Polimeni, D. C. Van Essen, M. Jenkinson, The minimal preprocessing pipelines for the human connectome project. *Neuroimage* **80**, 105–124 (2013).
53. S. B. Vos, C. M. W. Tax, P. R. Luijten, S. Ourselin, A. Leemans, M. Froeling, The importance of correcting for signal drift in diffusion MRI. *Magn. Reson. Med.* **77**, 285–299 (2017).
54. E. Kellner, B. Dhital, V. G. Kiselev, M. Reisert, Gibbs-ringing artifact removal based on local subvoxel-shifts. *Magn. Reson. Med.* **76**, 1574–1581 (2016).
55. S. M. Smith, Fast robust automated brain extraction. *Hum. Brain Mapp.* **17**, 143–155 (2002).
56. R. S. Desikan, F. Ségonne, B. Fischl, B. T. Quinn, B. C. Dickerson, D. Blacker, R. L. Buckner, A. M. Dale, R. P. Maguire, B. T. Hyman, M. S. Albert, R. J. Killiany, An automated labeling system for subdividing the human cerebral cortex on MRI scans into gyral based regions of interest. *Neuroimage* **31**, 968–980 (2006).
57. J. Haseleu, E. Anlauf, S. Blaess, E. Endl, A. Derouiche, Studying subcellular detail in fixed astrocytes: Dissociation of morphologically intact glial cells (DIMIGs). *Front. Cell. Neurosci.* **7**, 54 (2013).
58. P. M. Kulkarni, E. Barton, M. Savelonas, R. Padmanabhan, Y. Lu, K. Trett, W. Shain, J. L. Leasure, B. Roysam, Quantitative 3-D analysis of GFAP labeled astrocytes from fluorescence confocal images. *J. Neurosci. Methods* **246**, 38–51 (2015).
59. F. de Chaumont, S. Dallongeville, N. Chenouard, N. Hervé, S. Pop, T. Provoost, V. Meas- Yedid, P. Pankajakshan, T. Lecomte, Y. Le Montagner, T. Lagache, A. Dufour, J.-C. Olivo- Marin, Icy: An open bioimage informatics platform for extended reproducible research. *Nat. Methods* **9**, 690–696 (2012).
60. R. A. Fisher, in *Breakthroughs in Statistics*, S. Kotz, N. L. Johnson, Eds. (Springer New York, 1992), pp. 66–70.
61. J. Mollink, M. Kleinnijenhuis, A.-M. van Cappellen van Walsum, S. N. Sotiropoulos, M. Cottaar, C. Mirfin, M. P. Heinrich, M. Jenkinson, M. Pallegage-Gamarallage, O. Ansorge, S. Jbabdi, K. L. Miller, Evaluating fibre orientation dispersion in white matter: Comparison of diffusion MRI, histology and polarized light imaging. *Neuroimage* **157**, 561–574 (2017).
62. I. E. Papageorgiou, A. F. Fetani, A. Lewen, U. Heinemann, O. Kann, Widespread activation of microglial cells in the hippocampus of chronic epileptic rats correlates only partially with neurodegeneration. *Brain Struct. Funct.* **220**, 2423–2439 (2015).
63. G. M. Arisi, N. Garcia-Cairasco, Doublecortin-positive newly born granule cells of hippocampus have abnormal apical dendritic morphology in the pilocarpine model of temporal lobe epilepsy. *Brain Res.* **1165**, 126–134 (2007).

